
On Mechanical Metamaterials

Zur Erlangung des akademischen Grades eines
DOKTORS DER NATURWISSENSCHAFTEN
von der Fakultät für Physik des
Karlsruher Instituts für Technologie (KIT)

genehmigte

DISSERTATION

vorgelegt von

Dipl. Phys. MPhys. Tiemo Kurt Bückmann
aus Mettmann

Tag der mündlichen Prüfung:	19. Juni 2015
Referent:	Prof. Dr. Martin Wegener
Korreferent:	Prof. Dr. Peter Gumbsch

Contents

Publications	vii
List of Abbreviations	xi
Introduction	1
1 Theory and Methods	3
1.1 Fundamentals of Continuum Mechanics	3
1.1.1 Linear Hooke's Law	3
1.1.2 Easy Modes of Deformation	8
1.1.3 Beyond Linear Elasticity	9
1.1.4 Density of a Material	12
1.1.5 Wave-propagation in Mechanics	12
1.1.6 Coordinate Transformations in Mechanics	14
1.1.7 Metamaterial Concept	16
1.2 Computational Methods	18
1.3 Experimental Methods	22
1.3.1 Geometry Creation	22
1.3.2 Direct Laser Writing	22
1.3.3 Super Critical Drying	27
1.3.4 Three-Dimensional Printing	29
1.3.5 Imaging and Microscopy	30
1.3.6 Cross-Correlation	32
2 Extremal Mechanical Materials	33
2.1 Unimode Materials	33
2.1.1 Theory of Unimode Materials	33
2.1.2 Structural Designs for Unimode Materials	36
2.1.3 Blueprint and Variables	37
2.1.4 Static Studies	40
2.1.5 Dynamic Studies	41
2.1.6 Fabrication and Measurement	47
2.2 Pentamode Metamaterials	53
2.2.1 Structural Design for Pentamode Materials	54
2.2.2 Static Studies	55
2.2.3 Dynamic Studies	65
2.2.4 Introducing Anisotropy	70
2.2.5 Changing the Density	79

Contents

2.3	Anisotropic Dynamic Density	87
2.3.1	Layered Pentamode Materials	89
2.3.2	Spring-Mass Model	90
3	Elastic Cloaking	97
3.1	Core-Shell Cloaking	98
3.1.1	Cloak Design: Core-Shell	100
3.1.2	Fabrication and Characterization Setup	100
3.1.3	Measurement and Numerical Calculations	105
3.2	Lattice Transformation Cloaking	109
3.2.1	Cloak Design: Lattice Transformation	109
3.2.2	Numerical Calculations	112
3.2.3	Fabrication and Measurement	114
3.2.4	Dynamic Tests of a Lattice Transformation Cloak	119
4	Conclusions	123
	Appendix	125
1	A - Additional Information on Dilational Mechanical Metamaterials	125
2	B - Additional Information on the Core-Shell Cloak	125
2.1	Derivation of the Core-Shell Formulas	126
2.2	Discussion of an Overcompensated Cloak and Additional Figures	128
3	C - Additional Information on the Lattice Transformation Cloak	131
3.1	Dependence of the Element's Width on its Length	131
3.2	Different Parameters for the Lattice Transformation Cloak.	132
4	D - Material Information	150
4.1	IP Photoresists	150
4.2	Full-Cure Printing Materials	152
	Bibliography	167
	Acknowledgments	169

Publications

Parts of this Thesis have already been published:

In a chapter of a Book

M. Kadic, R. Schittny, T. Bückmann, and M. Wegener, “Experiments on cloaking in optics, mechanics, and thermodynamics” in *Transformation Wave Physics: Electromagnetics, Elastodynamics and Thermodynamics*, F. Farhat, P.-Y. Chen, S. Guenneau, and S. Enoch, eds., (Pan Stanford Publishing, 2014)(in press).

In scientific Journals

- T. Bückmann, M. Kadic, M. Thiel, and M. Wegener, “Fertigung von mechanischen Metamaterialien mittels Dip-in Laserlithographie”, *Werkstoffe* **4**, 46-47 (2012) April 2012
- M. Kadic, T. Bückmann, N. Stenger, M. Thiel, and M. Wegener, “On the practicability of pentamode mechanical metamaterials”, *Appl. Phys. Lett.* **100**, 191901 (2012) 7th of May 2012
- A. Martin, M. Kadic, R. Schittny, T. Bückmann, and M. Wegener, “Phonon band structures of three-dimensional pentamode metamaterials”, *Phys. Rev. B* **86**, 155116 (2012) 9th of October 2012
- M. Kadic, T. Bückmann, R. Schittny, and M. Wegener, “On anisotropic versions of three-dimensional pentamode metamaterials”, *New J. Phys.* **15**, 023029 (2013) 18th of February 2013
- M. Kadic, T. Bückmann, R. Schittny, and M. Wegener, “Metamaterials beyond electromagnetism”, *Rep. Prog. Phys.* **76**, 126501 (2013) 5th of November 2013
- R. Schittny, T. Bückmann, M. Kadic, and M. Wegener, “Elastic measurements on macroscopic three-dimensional pentamode metamaterials”, *Appl. Phys. Lett.* **103**, 231905 (2013) 3rd of December 2013
- T. Bückmann, R. Schittny, M. Thiel, M. Kadic, G.W. Milton, and M. Wegener, “On three-dimensional dilational elastic metamaterials”, *New J. Phys.* **16**, 033032 (2014) 26th of March 2014
- T. Bückmann, M. Thiel, M. Kadic, R. Schittny, and M. Wegener, “An elasto-mechanical unfeelability cloak made of pentamode metamaterials”, *Nat. Commun.* **5**, 4130 (2014) 19th of June 2014
- M. Kadic & T. Bückmann, R. Schittny, P. Gumbsch, and M. Wegener, “Pentamode metamaterials with independently tailored bulk modulus and mass density”, *Phys. Rev. Applied* **2**, 054007 (2014) 21st of July 2014

Publications

- T. Bückmann, M. Kadic, R. Schittny, and M. Wegener, “Mechanical cloak design by direct lattice transformation”, *P. Natl. Acad. Sci. USA*, **112**, 4930-4934 (2015) 6th of April 15
- T. Bückmann, M. Kadic, R. Schittny, and M. Wegener, “Mechanical metamaterials with anisotropic and negative effective mass-density tensor made from one constituent material”, *Phys. Status Solidi B* (2015) DOI: 10.1002/pssb.201451698 7th of April 15
- M. Kadic, T. Bückmann, R. Schittny, and M. Wegener, “Experiments on cloaking in optics, mechanics and thermodynamics”, *Proc. Roy. Soc. A* (accepted)

On scientific Conferences (Presented by myself)

- T. Bückmann, N. Stenger, M. Kadic, J. Kaschke, A. Frölich, T. Kennerknecht, C. Eberl, M. Thiel, and M. Wegener, 76. Jahrestagung der DPG und DPG-Frühjahrstagung, Berlin, “*Mechanical Metamaterials-Negative Poisson’s ratio*” (2012)
- T. Bückmann, N. Stenger, M. Kadic, J. Kaschke, A. Frölich, T. Kennerknecht, C. Eberl, M. Thiel, and M. Wegener, Meta2012: 3rd International Conference on Metamaterials, Photonic Crystals and Plasmonics, Paris, “*Mechanical Metamaterials-Negative Poisson’s ratio*” (2012)
- T. Bückmann, M. Kadic, N. Stenger, M. Thiel, and M. Wegener, Metamaterials’2012: The 6th International Congress on Advanced Electromagnetic Materials in Microwaves and Optics, St. Petersburg, “*Pentamode Mechanical Metamaterials*” (2012)
- T. Bückmann, R. Schittny, A. Frölich, M. Thiel, A. Martin, M. Kadic, and M. Wegener, SPIE. Photonics West 13, San Fransisco, “*Mechanical Metamaterials - Made by Dip-in DLW*” (invited presentation) (2013)
- T. Bückmann, R. Schittny, M. Thiel, M. Kadic, Graeme W. Milton, and M. Wegener, SPIE. Photonics West 14, San Fransisco, “*Three-dimensional Dilational Mechanical Metamaterials: a 3D Printing Challenge*” (invited presentation) (2014)
- T. Bückmann, M. Thiel, M. Kadic, R. Schittny, and M. Wegener, Metamaterials’2014: The 8th International Congress on Advanced Electromagnetic Materials in Microwaves and Optics, Kopenhagen, “*Elasto-Mechanical Cloak Made of Pentamode Metamaterials*” (2014)
- T. Bückmann, M. Thiel, M. Kadic, R. Schittny, and M. Wegener, SPIE. Photonics West 15, San Fransisco, “*Mesoscale Pentamode Metamaterial Elasto-mechanical Cloak by 3D Galvo-scanner Dip-in Direct Laser Writing*” (invited presentation) (2015)

Additional work on related topics has been published in peer-reviewed scientific journals:

- T. Bückmann, N. Stenger, M. Kadic, J. Kaschke, A. Frölich, T. Kennerknecht, C. Eberl, M. Thiel, and M. Wegener, “Tailored 3D mechanical metamaterials made by dip-in direct-laser-writing optical lithography”, *Adv. Mater.* **24** 2710-2714 (2012) 12th of April 2012
- T. Frenzel, J.D. Brehm, T. Bückmann, R. Schittny, M. Kadic, and M. Wegener, “Three-dimensional labyrinthine acoustic metamaterials”, *Appl. Phys. Lett.* **103**, 061907 (2013) 8th of August 2013
- R. Schittny, M. Kadic, T. Bückmann, and M. Wegener, “Invisibility cloaking in a diffusive light scattering medium”, *Science* **345**, 427-429 (2014) 5th of June 2014
- M. Schumann, T. Bückmann, N. Gruhler, M. Wegener, and W. Pernice, “Hybrid 2D-3D optical devices for integrated optics by direct laser writing”, *Light: Science & Applications* **3**, e175 (2014) 6th of June 2014
- R. Schittny, T. Bückmann, and M. Wegener, “Im Nebel perfekt getarnt”, *Physik in unserer Zeit* **45**, 214-215 (2014) 2nd of September 2014
- R. Schittny & A. Niemeyer, M. Kadic, T. Bückmann, A. Naber, and M. Wegener, “Transient behavior of invisibility cloaks for diffusive light propagation”, *Optica* **2**, 84-87 (2015) 21st of January 2015
- A. S. Quick, A. S. Pereira, M. Bruns, T. Bückmann, C. Rodriguez-Emmenegger, M. Wegener and C. Barner-Kowollik, “Rapid Thiol-Yne mediated fabrication and efficient postfunctionalization of micro-resolved 3D macrostructures”, *Adv. Funct. Mater.* **25**, 3735-3744 (2015) 15th of Mai 2015
- M. Kadic, R. Schittny, T. Bückmann, C. Kern, and M. Wegener, “Hall-effect sign-inversion in a realizable 3D metamaterial”, *Phys. Rev. X* **5**, 021030 22nd of June 2015

Publications

List of Abbreviations

Abbreviations in alphabetical order

1D	one dimensional
2D	two dimensional
3D	three dimensional
ALD	atomic layer deposition
AOM	acousto optical modulator
CAD	computer-aided design
DiLL	dip-in laser lithography
DLW	direct laser writing
Laser	light amplification by stimulated emission of radiation
MEHQ	mono methyl ether of hydroquinone
NPR	negative Poisson's ratio
PDE	partial differential equation
RIE	reactive ion etching
SEM	scanning electron microscopy
STL	surface tessellation language
UV	ultra violet

Introduction

Looking at the pile of scripted introductions on my desk I come to appreciate the advantages of a pencil. I have written one version, erased parts again and replaced them by a different wording. Something that would have been impossible with ink seems normal to us for a lead made out of carbon. A crucial premise, however, is the layered substructure of graphite of which individual layers can easily be scraped off. Diamond for example is made of carbon as well, the same chemical element, but has a completely different mechanical behavior. What makes them distinct is the atomic structure they possess, more precisely the relative orientation of the atoms and bonds between them. A pencil with a diamond lead would be an expensive toy but worthless for writing. This example tells us that not only the constituent material, but also the substructure is important for the mechanical properties of materials. Our commonly used materials are designed by their chemical composition rather than their material substructure. Would it not be great to design materials with exciting new and optimized mechanical properties by tailoring the substructure of existing constituent materials? Mechanical metamaterials pick up this point in designing the lattice and the material distribution in a meta-atom, and thereby gain a whole new level of design freedom. Furthermore, instead of searching for materials that meet the requirement of desired applications, one can design materials that inherently have precisely that functionality.

The idea of tailoring a material property beyond the capabilities of natural materials has evolved in the field of optics, as here the concept of metamaterials was introduced in the 1990's. General material limitations known so far are not valid any more in metamaterial systems. These materials obtain effective features for wavelengths larger than the lattice period through the structuring and material distribution within a meta-atom or unit cell. The search for optical metamaterials has raised the interest of material scientists and lead to theoretical suggestions for materials and applications they could be utilized in. Optical metamaterials [1] have shown many times how one can create materials based on these concepts – concepts which can now be applied to other fields of physics as well. This was done for example in thermodynamics [2–6], acoustics [5, 7], electrical conduction [6, 8–10], magnetic flux [11–13], and diffusive light propagation [14, 15]. Within the field of mechanics related work was performed on stability considerations in truss systems [16] or composites [17, 18]. The concept of metamaterials gaining effective media properties in mechanics was mainly theoretical [17, 19, 20], but just started to emerge based on nature related structures like the honeycomb and the thereof derived bowtie elements [21–25]. As we used this structure element to fabricate three-dimensional metamaterials to tune the Poisson's ratio of a material [26], it was clear to us that there is much more to explore in the field of mechanical metamaterials.

The here presented tailoring of materials is based on essentially three different material characteristics. The first two are material moduli, namely the bulk B and the shear modulus G . These moduli define the force needed to compress a material or deform it via shearing respectively. The ratio B/G , which is linked directly to the Poisson's ratio ν , defines in which way a material can be deformed. The higher the B/G ratio, the more we approximate a liquid state of material. On the other side, a material with a low B/G ratio can only change its volume and is extremely stiff considering other deformations. Apart from the moduli of a material, the density ρ has an important role in dynamic considerations. The density of a metamaterial can be tailored by different means, which can lead to a reduction of the effective density, or dynamically even a negative or anisotropic density. This can open up novel applications and functionality like for example vibration filters implemented by direction dependent band gaps.

This thesis explores the theoretical limits of mechanics based on theoretical suggestions for mechanical metamaterials, principally proposed by our collaborator Prof. Graeme Milton from the University of Utah. The general concepts embodied within the theoretical designs are utilized and realistic blueprints for metamaterials are developed on this basis. To validate the performance of the blueprints of the metamaterials, numerical calculations are used for a detailed analysis of the materials effective properties. To compare the numerical evaluation with experimental data, three-dimensional samples are fabricated by state of the art additive manufacturing technologies. The gained expertise allows to use mechanical metamaterials and the underlying concepts to create devices which are able to create a hidden void, which is unfeelable from the outside. Such a device, called an elasto-static cloak, is realized and characterized in three dimensions for the first time.

Outline of this thesis

In Chapter 1 we introduce the theoretical background and the used numerical and experimental methods used within this thesis. Hook's law is introduced and combined with the density into a formalism to arrive at wave motion in elastic solids. After this the elastic cloaking theory and the concept of metamaterials is introduced. In the second part numerical and experimental instruments used throughout this work are described.

In Chapter 2 we discuss three cases of extreme mechanical materials. The first part evaluates the classification and the theoretical concepts of auxetic structures. Furthermore, the ideal auxetic (unimode or dilational material) is approximated. The second part presents the opposite of a unimode namely a pentamode material. This material system is alternated in its designed substructure to allow for anisotropy as well as variable densities. The third part elaborates on densities of metamaterials and evaluates the possibility of anisotropic mass densities by the use of two examples.

In Chapter 3 we employ the gained expertise on mechanical metamaterials in order to cloak an object elasto-statically with the aid of, first, a core-shell design and, second, a lattice transformational design.

In Chapter 4 we conclude the work and discuss possible future applications.

1 Theory and Methods

In the first chapter we introduce some basic theoretical concepts used in this thesis and will guide through the theoretical background needed to understand the mechanical metamaterials discussed in the later chapters. Further explaining the basic methods used throughout this work, related to the simulations based on finite elements and fabrication methods, namely direct laser writing (DLW) and three-dimensional printing (3D printing). This chapter is meant as a general introduction and thus will not discuss the individual simulations and fabrications in detail, as this will be explained in the corresponding metamaterial chapters individually.

1.1 Fundamentals of Continuum Mechanics

This section introduces the fundamental mechanical properties of elastic solids, starting of from Hook's law leading to the elasticity tensor in three dimensions. We will then simplify the elasticity tensor and describe the material properties by elastic moduli used commonly in literature. Further a discussion of the general behavior of extreme materials reveals the opportunities of mechanical metamaterials. After a discussion of linear to non-linear materials, Hook's law is generalized to define a density of a material. Here beyond a static mass density discussion, a possible direction and frequency dependence of the density are explained. Following the discussion of the elastic and mass density properties, the wave-equation for elastic solids can be explained. At last we will point out some key features of elastic metamaterials on the example of a bimode material and discuss the concepts of the elastic cloaking theory.

1.1.1 Linear Hooke's Law

Hooke's law describes the linear deformation of materials. It states a linear relation between a deformation and a force in materials. In material science the proportionality factor connecting the force and the deformation is called a modulus.

Starting from a very simple consideration of a force acting upon a spring, one can illustrate the basic principle of Hook's law. If one pulls on a spring, thereby applying a force to the system, and fixes the other end of the spring to prevent a translation, an elongation of the spring will be the result. The size of this elongation will depend on the force and the spring constant of the spring. In order to characterize the elongation normalized to the overall length of the spring a strain is defined. This strain ϵ is defined by the relative length change ΔL compared to the initial length L_0 as :

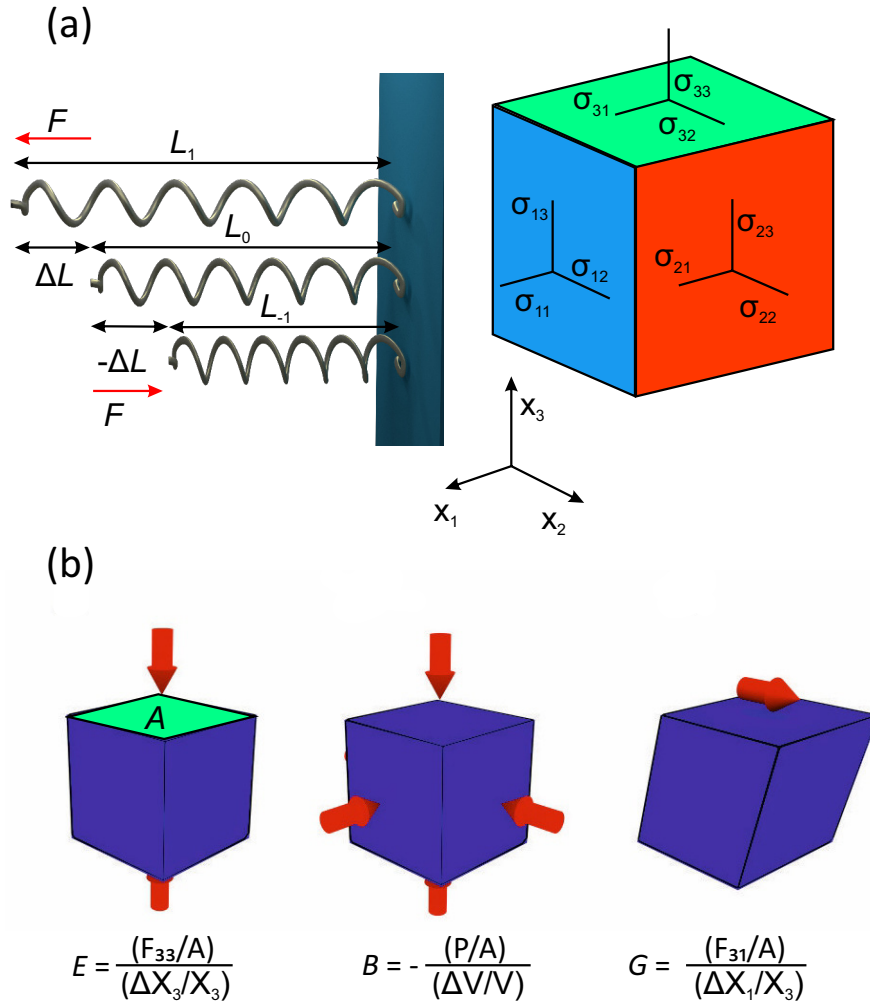
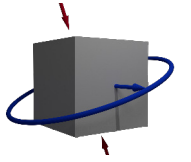


Figure 1.1: (a) Strain and different stress directions along different directions. A strain is defined as a relative length change $\Delta L/L_0$. A stress is defined as a force acting on a surface. Here the first number indicates the face whereas the second index encodes the force direction. (b) Three different moduli are shown exemplary. (Form left to right). First the Young's modulus related to a stress along one principle direction relating the length change to a force acting on a surface A . In the center the bulk modulus is represented. Here a hydrostatic pressure from all sides induces a volume change in the material. On the right a shear modulus experiment is depicted. Here the force acts along the face of the material leading to an effective shearing of the material.

$$\epsilon = \frac{\Delta L}{L_0}. \tag{1.1}$$

This strain gives an scale independent measure of deformation. To distinguish between a compression or elongation a negative or positive sign is defined accordingly. An example can be seen in Figure 1.1 (a). Here the length change is $\Delta L = L_1 - L_0$ and $\Delta L = L_{-1} - L_0$



depending on expansion or compression of the spring. One can also define the strain by a displacement \vec{u} as:

$$\epsilon = \frac{1}{2} \left(\nabla \vec{u} + (\nabla \vec{u})^T + \nabla \vec{u} (\nabla \vec{u})^T \right) \approx \frac{1}{2} \left(\nabla \vec{u} + (\nabla \vec{u})^T \right). \quad (1.2)$$

For simplicity we will mainly consider the distortion, X . To describe a force \vec{F} acting with a certain direction, thus vectorial ($F = |\vec{F}|$) onto a system, a stress σ is defined. This measure relates the force F to an area $A_0 = A$ on which this force is acting on, by

$$\vec{\sigma} = \frac{\vec{F}}{A_0} [\text{Pa}]. \quad (1.3)$$

The further discussions include only a linear relationship between the stress and strain, closely related to the simple Hook's spring model. Expressing the spring constant D of a normal Hook's spring with the stress and strain leads to $\sigma A_0 = D \epsilon L_0$. Considering a material (in the solid state), acting as a three-dimensional spring system, makes the simple one dimensional problem and the related stress-strain equation rather complex. This relation is normally denoted as elasticity tensor \mathbf{C} of rank four:

$$\boldsymbol{\sigma} = \mathbf{C} : \boldsymbol{\epsilon}. \quad (1.4)$$

This tensor has 81 entries due to the Cauchy's stress and strain tensors σ and ϵ of rank 2. The elasticity tensor can normally be simplified to a smaller representation because of its major ($C_{1122} = C_{2211}$) and minor ($C_{1233} = C_{2133}$) symmetries. But there are even some cases where 81 entries are not sufficient. This can happen in some materials when the modulus differs under compression from the one under dilatation as found in some graphene composites [27]. Neglecting this behavior and stating that the tensor is symmetric under two index exchanges (called the major and minor symmetry of the tensor as above) one can bring the tensor to a simpler form. All of the quantities can be put into a 6×6 rank X_2 using e.g. the so called Voigt notation. If forces are applied on boundaries of a material under consideration, the corresponding behavior of the material to these applied forces defines the entries of the tensor. Following this procedure one can find all entries and reconstruct the entire elasticity tensor. Usually materials show symmetries in their elastic properties. On this basis the complexity of a material description can dramatically be reduced. As a first step, the general deformation modes of such a material need to be found. This can be done by searching for eigenvalues of the elasticity matrix and considering symmetries the elasticity tensor obeys for certain material classes. Starting from the spectral decomposition of the fourth-order tensor \mathbf{C} , one can solve the eigenvalue problem [28]

$$\mathbf{C} \cdot \mathbf{N} = \vec{\lambda} \mathbf{N}, \quad (1.5)$$

where \mathbf{N} is a second-order tensor and $\vec{\lambda}$ is the column vector containing all eigenvalues. Mathematically there are six independent eigenvalues for a symmetrical fourth-order

tensor such as the stiffness tensor. Using the Voigt notation [28] the elasticity tensor can be expressed as

$$\mathbf{C} = \begin{pmatrix} C_{1111} & C_{1122} & C_{1133} & \sqrt{2}C_{1112} & \sqrt{2}C_{1123} & \sqrt{2}C_{1113} \\ C_{2211} & C_{2222} & C_{2233} & \sqrt{2}C_{2212} & \sqrt{2}C_{2223} & \sqrt{2}C_{2213} \\ C_{3311} & C_{3322} & C_{3333} & \sqrt{2}C_{3312} & \sqrt{2}C_{3323} & \sqrt{2}C_{3313} \\ \sqrt{2}C_{1211} & \sqrt{2}C_{1222} & \sqrt{2}C_{1233} & 2C_{1212} & 2C_{1223} & 2C_{1213} \\ \sqrt{2}C_{2311} & \sqrt{2}C_{2322} & \sqrt{2}C_{2333} & 2C_{2312} & 2C_{2323} & 2C_{2313} \\ \sqrt{2}C_{1311} & \sqrt{2}C_{1322} & \sqrt{2}C_{1333} & 2C_{1312} & 2C_{1323} & 2C_{1313} \end{pmatrix}. \quad (1.6)$$

It describes the whole behavior and properties for any deformation of the material. The stress and strain representations are linked by the matrix \mathbf{C} :

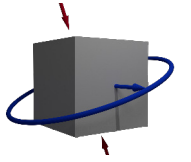
$$\begin{pmatrix} \sigma_{11} \\ \sigma_{22} \\ \sigma_{33} \\ \sigma_{12} \\ \sigma_{13} \\ \sigma_{23} \end{pmatrix} = \mathbf{C} \begin{pmatrix} \epsilon_{11} \\ \epsilon_{22} \\ \epsilon_{33} \\ \epsilon_{12} \\ \epsilon_{13} \\ \epsilon_{23} \end{pmatrix}. \quad (1.7)$$

The \mathbf{C} tensor can be diagonalized for isotropic materials, named \mathbf{C}_{iso} , to get a representation of the eigenvalues in that case. This form allows for a reduced parameter space to be taken into consideration. Due to the symmetry of an isotropic medium it is possible to describe it with only two independent parameters. The possibility to invert the matrix is another outcome of the symmetry. This states that there is an inverted matrix which relates not the strain to a stress but rather the stress to a strain also called the compliance tensor:

$$\begin{aligned} \vec{\sigma} &= \mathbf{C}\vec{\epsilon} & [\text{Pa}] &= [\text{Pa}][\text{m/m}] \\ \vec{\epsilon} &= \mathbf{C}^{-1}\vec{\sigma} = \mathbf{S}\vec{\sigma} & [\text{m/m}] &= [1/\text{Pa}][\text{Pa}]. \end{aligned} \quad (1.8)$$

$$\mathbf{C}_{iso} = \begin{pmatrix} B + 4/3G & B - 2/3G & B - 2/3G & 0 & 0 & 0 \\ B - 2/3G & B + 4/3G & B - 2/3G & 0 & 0 & 0 \\ B - 2/3G & B - 2/3G & B + 4/3G & 0 & 0 & 0 \\ 0 & 0 & 0 & 2G & 0 & 0 \\ 0 & 0 & 0 & 0 & 2G & 0 \\ 0 & 0 & 0 & 0 & 0 & 2G \end{pmatrix}. \quad (1.9)$$

Here B is the bulk modulus and G is the shear modulus. The bulk modulus is the inverse of the compressibility and thus relating a volume change to a hydrostatic pressure



as $B = -V \frac{dP}{dV}$. The shear modulus is related to a force acting along a facet and the accompanied deformation of a solid $G = \frac{F_{13}/A}{dx_1/dx_3}$. The schematics can be seen in Figure 1.1. This matrix relations can be expressed in a system of equations relating the behavior under stress to strain.

$$\begin{aligned}
 \sigma_{11} &= a \epsilon_{11} + b \epsilon_{22} + b \epsilon_{33} \\
 \sigma_{22} &= b \epsilon_{11} + a \epsilon_{22} + b \epsilon_{33} \\
 \sigma_{33} &= b \epsilon_{11} + b \epsilon_{22} + a \epsilon_{33} \\
 \sigma_{12} &= 2G \epsilon_{12} \\
 \sigma_{13} &= 2G \epsilon_{13} \\
 \sigma_{23} &= 2G \epsilon_{23}
 \end{aligned} \tag{1.10}$$

$$\text{with } a = B + \frac{4}{3} G \text{ and } b = B - \frac{2}{3} G .$$

The parts a and b come from a simple evaluation, starting from stress applied in one direction of a material. The result is the well known linear isotropic Hooke's law with the Young's modulus E in one direction: $\sigma = -E\epsilon$. Note that in a real material this is only true if either the Poisson's ratio is zero or the material is free to move along orthogonal directions. If one fixes the orthogonal expansion or contractions as it would be the case in an infinite material or by applying forces to the sides, the Poisson's ratio induces some additional forces onto the material. Consequently a force along the x -direction is accompanied with additional forces along the transverse t direction. Therefore one has to modify our equation relating the displacement to a force of $F_x - 2\nu F_t = -EA_0\epsilon$. In the transverse direction no length change is allowed, i.e. $0 = -\frac{F_t - \nu(F_t + F_x)}{EA_0}$. Solving the second equation for σ_t and evaluating the first with this result leaves a combination of bulk and shear modulus. This gives the result used for the first entry $\sigma_{11} = \left(B + \frac{4}{3} G\right) \epsilon_{11}$ [29].

The resulting form of the above mentioned matrix gives rise to diagonalize the \mathbf{C} matrix. This is done using a transformation and can directly be related to the diagonalized form of $\mathbf{C}_{\text{iso}} = \mathbf{Q}_{\text{iso}} \mathbf{\Lambda}_{\text{iso}} \mathbf{Q}_{\text{iso}}^t$ with

$$\mathbf{\Lambda}_{\text{iso}} = \begin{pmatrix} 3B & 0 & 0 & 0 & 0 & 0 \\ 0 & 2G & 0 & 0 & 0 & 0 \\ 0 & 0 & 2G & 0 & 0 & 0 \\ 0 & 0 & 0 & 2G & 0 & 0 \\ 0 & 0 & 0 & 0 & 2G & 0 \\ 0 & 0 & 0 & 0 & 0 & 2G \end{pmatrix} \tag{1.11}$$

and

$$\mathbf{Q}_{\text{iso}} = \begin{pmatrix} 1/\sqrt{3} & \sqrt{2/3} & 0 & 0 & 0 & 0 \\ 1/\sqrt{3} & -1/\sqrt{6} & -1/\sqrt{2} & 0 & 0 & 0 \\ 1/\sqrt{3} & -1/\sqrt{6} & 1/\sqrt{2} & 0 & 0 & 0 \\ 0 & 0 & 0 & 1 & 0 & 0 \\ 0 & 0 & 0 & 0 & 1 & 0 \\ 0 & 0 & 0 & 0 & 0 & 1 \end{pmatrix}. \quad (1.12)$$

As one can see we do indeed turn out to have only two distinct moduli in this case. The compression modulus B , and the shear modulus G . These two moduli are scalar for isotropic materials. This allows to calculate for example the Poisson's ratio for a material (which links the deformation of a material along one dimension to the orthogonal directions for an unidirectional induced strain) with these two scalar moduli as follows:

$$\nu = \frac{3B - 2G}{2(3B + G)}. \quad (1.13)$$

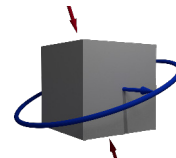
Similar to this expression one can calculate different material properties with two other known properties of the material when it is isotropic. In different communities of science different notations evolved and are used. Here the focus lies on the moduli B , G , and E as well as the Poisson's ratio ν . The elastic properties are then further related to the density ρ of a material. To make the Poisson's ratio more accessible one can describe it as a ratio of two strains. As there are in general an infinite amount of strains possible this would in general again lead to a complex tensor. To simplify this equations one considers planes regarding basis vectors of the material or of the geometry *e.g.* $\nu = \nu_{31}$.

$$\nu_{31} = \frac{-\epsilon_{33}}{\epsilon_{11}}. \quad (1.14)$$

The generally very complex description of elastic solids can be simplified to a large extend by comparing different elastic descriptions of the elasticity matrix. The symmetries of some materials allows to reduce the complexity of deformation to only two elastic moduli for an isotropic material. The less symmetric a material is the more elasticity matrix entries one has to consider. For example a cubic material has three independent elasticity matrix entries. The mechanical properties of lattices depend highly on the way they are internally connected [30], which gives an additional degree of freedom to a material design.

1.1.2 Easy Modes of Deformation

With the aid of the above mentioned equations the elastic properties (under static conditions) of a material are thus described in full. To get an intuitive feeling for the resulting materials behavior we will have a look on two extreme cases, considering only isotropic materials. Taking a closer look at the diagonalized form of \mathbf{C} named $\mathbf{\Lambda}_{\text{iso}}$ (from equation 1.11) we note that only two different entities occur, namely $3B$ and $2G$. Therefore



it seems to be promising to examine the behavior of the $3B \ll 2G$ case (a) and the $3B \gg 2G$ case (b).

(a) In the case where $3B \ll 2G$ or even considering the ultimate limit $3B = 0$ a material has lost one entry in the $\mathbf{\Lambda}_{\text{iso}}$ matrix. This translates to one stiffness constant being small or even zero meaning that a small force probing this stiffness can cause a large or even infinite deformation. In the here considered case only one of the diagonal elements of the elasticity matrix is small leading to the name unimode material (*uni* = one). As only the bulk modulus is occurring once in the matrix, the case of a vanishing bulk modulus is the only possibility how such a material can occur. The ideal unimode material is defined as ($B = 0$) with a Poisson's ratio of $\nu = -1$, setting the lower bound for a stable materials. To get a feeling for such a material one can evaluate which deformation is linked to the vanishing bulk modulus. As the bulk modulus is connected to a hydrostatic compression, a small force leads to an equal contraction from all sides. This can also be linked to the Poisson's ratio as $\nu = -1$ means that the orthogonal directions deform exactly the same way as the initial deformation direction. In short: the material can only change the volume, but cannot change the shape under any kind of force.

(b) In the case where $3B \gg 2G$ the argumentation is turned the other way around. As there are five vanishing entries in the matrix and thus five easy modes of deformation such a material is called pentamode material (*penta* = five). Now all shear moduli vanish leaving a material that is only stable under hydrostatic pressure. Relating to the Poisson's ratio again a pentamode material has ideally $\nu = 0.5$ which leads to a constant volume and can thus be compared to an ideal incompressible liquid.

A general overview of material properties is given in the following Figure 1.2 displayed in recent review articles [21, 31]. In the first panel (a) one can see that the ratio of B/G is an important key factor in characterizing a material. Some basic materials properties are displayed, allowing to compare their behavior in relation to the Poisson's ratio or B/G ratio defining the position on the plot. The plot shown is commonly known as a so called Milton map. The different regimes of this plot determine the characteristic of a material response related to the bulk and shear modulus. Further we find some general bounds imposed on the material properties. In the second panel an Ashby plot is shown [31, 32]. Here the stiffness is plotted over the density of a material. Both plots are used to compare materials and determine their characteristic features. Within this thesis we focus mainly on the Milton map and therein try to realize two extreme cases, one approaching the x -axis and one material approaching the y -axis corresponding to unimode materials and pentamode materials.

1.1.3 Beyond Linear Elasticity

In linear elasticity the material response is scalable with the stiffness or modulus of the material. This feature will be used to simplify the explanation of a metamaterial throughout this work. Accordingly only the relative difference between the different moduli will be an important number following our discussion before. In general this is not true for a large deformation, failure or special kinds of materials. There are a variety

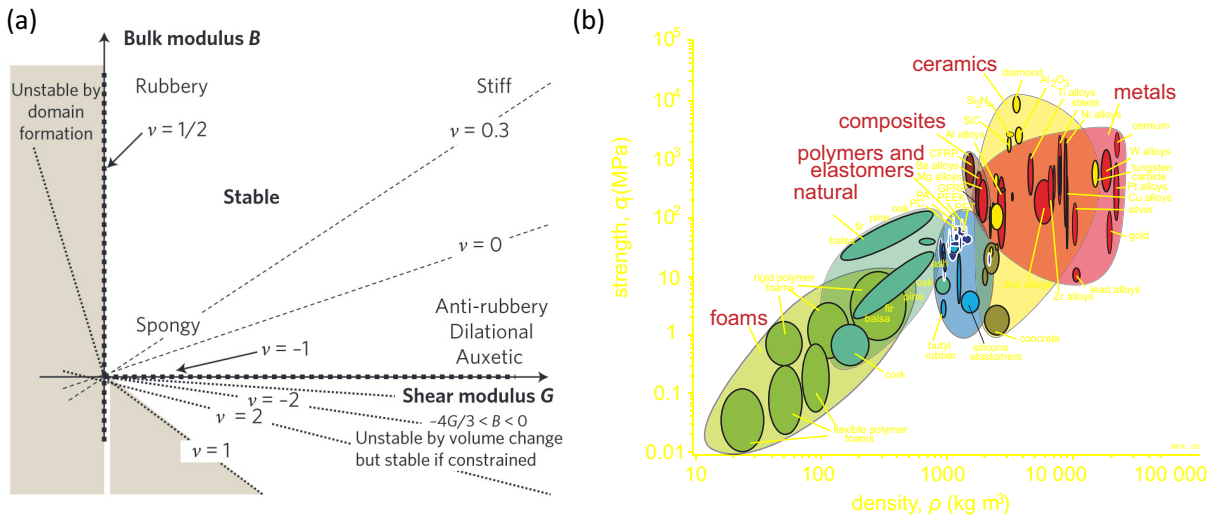


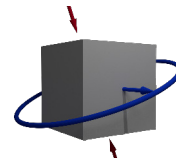
Figure 1.2: (a) The map first shown by *Milton* is commonly used to display materials stability as a function of the bulk and shear modulus, taken from [21]. (b) Plotting the stiffness of a material over the density is known as the Ashby plot, and gives insight in the the relative stiffness compared to the density, taken from [31].

of extensions to linear elasticity describing all kinds of material systems or deformation regimes better than a linear theoretical model. Only a few basic extensions are discussed here as only they are in the scope of the presented work.

Non-linear Materials

The term non-linear materials is a quite broad specification. This in general means that a material does not respond in a linear stress-strain dependence. There can be fracture and failure of a material, which we will not discuss as it is not considered within this work. Further there can be nonlinearity based on the microscopic geometry leading to a deviation of the linear dependence in the stress strain curve of a material, or the stress strain curve can depend on time called viscoelastic behavior and creep of the material. To extend the discussion on non-linear material properties one can talk about irreversible damage to a material called fatigue behavior. Here crack formation plays a key role in failure.

The general linear elasticity is based on the approximation of atomic potentials by a parabola resulting in linear restoring forces within a material. This approximation by a parabola is only valid for small deformations, and as soon as one has larger deformations, leading to a failure of this approximation, one finds a non-linear behavior of a material. Within an atomic crystalline material the Lenard-Jones potential is a better approximation, thus one finds a stiffening for extreme compression and a weakening for extreme tension. The thereon based limits for elastic properties are normally not achieved in an realistic material because of defects within the crystals. These defects lead way sooner to a failure of the material compared to the ideal values. If one reduces the material dimensions to become comparable to the atomic dimensions of the crystal, one



can have materials without any atomic defects or very few leading to a size effect of the material properties measured[32].

In polymer structures [33], mainly considered here, a dense network of connected polymer chains is building up the material rather than a crystalline structure. Here two main aspects are predominant, namely the entropy elastic deformations and the visco elastic deformations. Both deformations are mainly reversible and are linked to the polymer substructure. Entropy elasticity is based on the fact that the complex polymer chain network has initially an entropy minimized 3D orientation. If one induces a strain or stress into the material this optimized configuration can be changed and the linearity of the material is no longer a valid assumption. As the system tries to reduce the entropy, the initial state will eventually be reached again. A viscoelastic behavior is quite similar and is based on unfolding and reorganization of the molecular structure. This is generally described by an additional strain component as $\epsilon_{total} = \epsilon + \epsilon'(\sigma, t, T)$ here the ϵ' depends on the induced stress, the time t and (e.g. in polymers) also dramatically on the temperature T . These viscoelastic effects can lead to non-linear material properties. We will be using only linear constituent material properties in the numerical simulations of this thesis, but experiments might show non-linear responses due to these effects. Non-reversible deformations such as plastic deformations are not considered during the work as this would cause damage to the constituent materials.

One further occurrence of non-linear behavior is due to large strains leading to finite changes in the material and geometry which then is linked to a changed material response. These deformation modes can in principle have a large influence on the outcome of a simulation or an experiment[26]. The here considered cases assume linear responses and thus exclude these deformation dependent material parameters, as only the linear regime is considered.

Cosserat materials

Cosserat theory [34] also called micro polar theory is one extension of the normal linear elastic theory. Within this theory formally the minor symmetries of the elasticity tensor \mathbf{C} are not obeyed. This leads to additional degrees of freedom within the deformation of a material. These degrees are connected to a finite length scale of a smallest element. This can, for example, be connected to a characteristic grain of sand in the description of sand, or might be connected to the finite size of a mechanical meta-atom. The further degrees of freedom come in hand with this length scale as they are connected to a rotation of this finite cells. In the linear elasticity these rotations of points do not matter nor are correlated to a finite energy. Within a material containing finite sized elements these rotations can be related to finite energy thus rendering these deformations mechanically interesting and relevant. Materials showing this behavior have been found and studied for example in bone [35]. Inverting the general concept and designing a material, showing a certain Cosserat behavior, is way more complex and not yet explored in detail. As the additional degrees of freedom allow to extend the basic equations of mechanics under coordinate transformations, and give rise to the possibility to make them form invariant, elasto mechanical cloaking becomes possible. First simple designs start to emerge in two

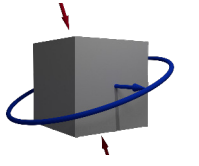
dimensions considering a swiss roll design to include rotations into the elastic behavior [36]. As the measurement of Cosserat behavior is size dependent and often only a small correction to the linear elasticity it is rather complex to evaluate parameters for given samples. These facts and the small knowledge about this material class hindered us from exploring Cosserat material parameters within this work, but might be an interesting route for future developments of mechanical metamaterials.

1.1.4 Density of a Material

The density of a material gains physical importance, once one does not only consider elastic or deformation forces, but also translations according to Newtons Law and especially once a time dependence is taken into account. Intuitively the density ρ of a material is quite easy to determine by just measuring the mass m and the volume V of a certain material and dividing one by the other $\rho = m/V$. Another way to determine the density for porous media is to scale the constituent materials density by the filling fraction of the material. These two approaches can be applied only if an isotropic and static mass density can be considered. In general the density can be frequency dependent [37, 38] and does not need to be isotropic (thus can be direction dependent) under dynamic considerations [7, 39]. A simple spring mass model can help to understand this concept of a dynamic mass density. Imagine one has a stiff matrix material with a second mass inserted into a void within the matrix. This inner mass is now connected with springs to the outside matrix. Under static considerations these inner masses are irrelevant due to their low coupling to the matrix and one only measures the matrix. In a dynamic consideration these masses will start to move and in resonance can gain a high amplitude and thus a strong influence on the measurement. As the materials stiffness is not changed, the difference in the behavior is assigned to a variable mass density, in detail resulting into a frequency dependent mass density [7]. This simple model can help to understand the concept of a changing mass density but also shows that one can not find these effects in a static consideration as there no resonance is present. Within this work we will use the concept of a static mass density as well as a dynamic mass density to design and tailor the band structure of a material and thus the wave propagation properties.

1.1.5 Wave-propagation in Mechanics

The propagation of waves in mechanics is determined by all previously discussed quantities, namely the moduli or the \mathbf{C} matrix and the density ρ of a material. The equation describing a wave propagation can be considered in various physical domains such as the time domain, Fourier domain (k space) or the here used frequency domain. The frequency domain has the advantage that it is easy to interpret and can be used for a band diagram calculation later on, relating the frequency to a wavevector. To derive the wave equations for a propagation in an elastic medium, a simple strain along one dimension is considered, e.g. ϵ_{xx} , compressing one unit cell by a certain amount. This can be translated into a displacement vector as discussed before via $\epsilon = \nabla \vec{u}$ or $(\epsilon)_{ij} = 1/2[(\nabla)_i(u)_j + (\nabla)_j(u)_i]$. This strain induces a stress, and stationary behavior is



obtained if the force density is equal to the spatial derivative of the stress, leading to [40]

$$\rho \frac{\partial^2 \vec{u}}{\partial t^2} = \nabla \cdot \sigma. \quad (1.15)$$

inserting the stress-strain relation $\sigma = \mathbf{C} \cdot \epsilon$ results in

$$\nabla \cdot (\mathbf{C} : \nabla \vec{u}) + \omega \frac{\partial^2 \vec{u}}{\partial t^2} = 0. \quad (1.16)$$

Considering a displacement vector \vec{u} with a time harmonic frequency dependence of ω we find the frequency domain version [17, 28]:

$$\nabla \cdot (\mathbf{C} : \nabla \vec{u}) + \omega \rho \vec{u} = 0. \quad (1.17)$$

To get this equation we have used plane waves as a possible solution. This is quite a general solution to the problem, as plane waves and a superposition thereof allow to generate a complex time and space dependent wave pattern and solve for a propagation thereof. A description of a wave can be done by a wave vector and a frequency, e.g., $u(x, t) \approx e^{i(kx - \omega t)}$. Herein the displacement is described for a certain point in space and time, leading to a propagating wave. The material, this wave is propagating in, can be classified mainly by the aid of a so called band structure where one plots the frequency of a propagating mode over the wave vector \vec{k} . For a one dimensional infinitely extended linear material this diagram is quite simply described by a straight line. This means that each frequency corresponds to only one wave vector. The velocity, this wave is propagating with, can be extracted by the slope of this line $v = \omega/k$. As soon as a periodicity is introduced into the material, a maximum \vec{k} limits the band diagram after which the dependence of $\omega(\vec{k})$ is periodic. This allows to represent every mode within the first periodicity called first Brillouin zone. At the edge of this zone the bands have to bend over, obeying the periodic constraints, thus two generally different velocities occur, namely the phase velocity $v_{\text{ph}} = \omega/k$ and the group velocity $v_{\text{g}} = \frac{\partial \omega}{\partial k}$. In a one dimensional space there exists only one single mode of propagation namely a longitudinal wave along this direction. Extending this concept into three dimensions allows for an additional movement out of the direction the wave is directed, or being transverse to the wave vector \vec{k} . These two transverse waves are linked to different elements within the \mathbf{C} tensor than the longitudinal waves. The different mode is connected to a different slope and thus velocity in the band diagram of a material. For an isotropic material the velocities of the modes can be linked to the moduli and the density of the material in an quite easy fashion, considering the small \vec{k} region where v_{ph} and v_{g} coincide:

$$v_{\text{L}} = \sqrt{\frac{B + 4/3 \cdot G}{\rho}} \quad (1.18)$$

$$v_{\text{T}} = \sqrt{\frac{G}{\rho}}. \quad (1.19)$$

Even for this simple infinitely extended isotropic medium a already quite complex system is found, with three modes (here two are degenerate) each with a phase and a group velocity varying with \vec{k} or ω respectively. This description is sufficient and needs no

further extension as long as we stay in this material. But as discussed before we would like to introduce a periodicity and thus need to have some kind of variation in the material properties. This leads to the need of considering an interface at which one material changes to another one. The simplest description can be obtained by considering vacuum as a second material, which leads in the first place to a finite geometry. As there is no material in vacuum no wave can be supported in this second material leading to a reflection of the wave at this interface. This brings up a quantity called impedance of a material. The impedance describes the interaction of two materials and defines the reflection and transmission properties of an interface. The impedance of a material is with regard to the assumptions:

$$\begin{aligned} Z_L &= \sqrt{(B + 4/3 \cdot G) \cdot \rho} \\ Z_T &= \sqrt{G \cdot \rho}. \end{aligned} \tag{1.20}$$

By these impedance's a transmission and an reflection coefficient for a wave impinging onto an interface can be found. The evolving expressions are in general materials quite complex, for more details see chapter 2.2 of [28]. The introduction of an interface also leads to a possible change in the mode type of a wave. In this fashion a quasi longitudinal wave propagating in a thin rod of material is dominated by the Young's modulus E rather than the term $B + 4/3 \cdot G$. The geometry factor also allows other wave phenomena[41], e.g. for flexural waves [42] as well as for surface waves [43]. With in the soil different wave types were discovered already early on [44]. This geometry dependent wave propagation is limited to some special geometries and is not considered within this thesis.

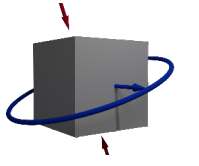
1.1.6 Coordinate Transformations in Mechanics

The theory on mechanical waves allows to predict the propagation of a wave in a elastic medium. This idea is comparable to the theory of many different physical systems such as electromagnetic waves. Within the field of electromagnetic metamaterials there has been a multitude of possible ways to influence the propagation of a wave. One example is the proposed invisibility cloak [45, 46] creating a void in space which is not detectable from the outside due to a coordinate transformation (mapping a point to a finite region), and a consecutive mapping of material parameters in the transformed space which renders the void invisible. This is done by transforming Maxwell's equations with the coordinate transformation and then assigning new material parameters to bring the equations back to the initial form. If one tries to do just the same in mechanics, one realizes that the basic equations 1.16 are generally not form invariant under coordinate transformations [45, 46] and thus can not be brought back to the initial form. This originates from the tensor form of the elasticity matrix \mathbf{C} and the resulting tensor contraction rather than a simple multiplication as it is the case in electrodynamics. How the elasticity tensor and the elastodynamic wave equation transform has been shown by Milton [47] and is here reproduced in short. Starting from the wave equation

$$\nabla \sigma = -\omega \rho \vec{u}, \quad \sigma = \mathbf{C} : \nabla \vec{u}, \tag{1.21}$$

or arranged into one equation

$$\nabla \cdot (\mathbf{C} : \nabla \vec{u}) - \omega \rho \vec{u} = 0 \tag{1.22}$$



a coordinate transformation is performed. This transformation maps coordinates and thus displacements, as the differences of coordinates, to a new set of coordinates in a transformed space. The transformed coordinates are labeled by primed values such that the mapping can be written as $\vec{x} \rightarrow \vec{x}'(\vec{x})$ and consecutively $\vec{u} \rightarrow \vec{u}'(\vec{u})$. After the transformation done for the primed coordinates, in order to map the changed coordinate system into material parameters, one should be able to write down an equation with the same form as above just with primed coordinates like:

$$\nabla' \cdot (\mathbf{C}' : \nabla \vec{u}) + \omega \rho' \vec{u} = 0 \quad (1.23)$$

Milton has though shown that by maintaining the symmetry of the elasticity tensor, the equations do not recover the above form but rather obtain additional terms. Further the scalar mass density turns into a tensor.

$$\nabla' \cdot (\mathbf{C}' : \nabla \vec{u} + \mathbf{S}' \vec{u}') - \mathbf{D}' : \nabla' \vec{u}' + \omega \boldsymbol{\rho}' \vec{u}' = 0 \quad (1.24)$$

With the Jacobian of the harmonic transformation \mathbf{J} one can express first the density and the elasticity matrix in the new coordinates:

$$\boldsymbol{\rho}'_{pq} = \frac{\rho}{\det(J_{ijkl})} J_{pi}^T J_{qj} + \frac{1}{\det(J_{ijkl})} J_{pi}^T J_{pj} \mathbf{C}_{ijkl} J_{qk}^T J_{ql} \quad (1.25)$$

$$\mathbf{C}'_{pqrs} = \frac{1}{\det(J_{i,j,k,l})} J_{pi}^T J_{qj} \mathbf{C}_{i,j,k,l} J_{rk}^T J_{sl}, \quad (1.26)$$

and further find the expressions for the newly appearing terms:

$$\mathbf{S}'_{pqr} = \frac{1}{\det(J_{i,j,k,l})} J_{pi}^T J_{qj} \mathbf{C}_{i,j,k,l} J_{rk}^T J_{rl} \quad (1.27)$$

$$\mathbf{D}'_{pqrs} = \frac{1}{\det(J_{i,j,k,l})} J_{pi}^T J_{pj} \mathbf{C}_{i,j,k,l} J_{qk}^T J_{rl}. \quad (1.28)$$

As the later terms do not vanish for any normal consideration the result is that the elastodynamic wave equations are not form-invariant under coordinate transformations. This means that in general no simple transformation of space can be mapped onto material properties obeying the same physical equations.

There are though a few concepts which allow to come back to a form-invariance of the equations, or at least to map general material properties to the transformed equations. Milton does give one solution to the problem which presents the main focus in this thesis [47] which has been also evaluated by [48]. His solution is to reduce the elasticity tensor to have only one non singular eigenvalue of the elasticity tensor. The required materials are called pentamode metamaterials. These materials allow to bring the then reduced form of the elasticity equations back to its original form. Still one is left with

a density matrix rather than a scalar value, but the problem has enormously reduced its complexity. Only a spatially varying elasticity eigenvalue and a density matrix, in general depending on space have to be tailored. A different approach is to neglect the symmetries of the elasticity tensor and obtain Cosserat materials. This second general concept is summarized in a simple example by Brun et al. [36]. Here more independent eigenvalues of the elasticity tensor are considered to be able to map the transformed material properties. Unfortunately it is not clear how to map these material properties onto a micro-structure.

1.1.7 Metamaterial Concept

Material properties or moduli are often bounded, limiting the design freedom in material science and engineering. First of all one can only use the chemical elements accessible in the laboratories or in nature. This already gives a huge range to combine them and create composites of materials. For a normal composite one can only tune the mixture and no underlying functional structures. The idea underlying metamaterials is to structure materials on demand and make designed composites to achieve a behavior which can be tuned to a parameter given beforehand. The resulting structure is described as an effective material, when we can consider the elements of the structure much smaller than the wavelength properties are observed with. To fulfill this requirement the wavelength has to be larger than the structural parts or characteristic length scale of the periodic material.

$$\lambda \gg \text{period.} \quad (1.29)$$

This means in the quasi static regime, $f \approx 0$, that a material response is expected to always be in the homogenization regime since the corresponding wavelength would be infinite, and thus larger than the lattice period.

The metamaterial concept evolved in optics as effective media and their effective properties are discussed. These materials gain unusual optical properties by the substructure of two materials [49–51]. The metamaterial concept was first discussed to get effective parameters for composite materials, considering the electromagnetic responses. Here the wavelength of the light under consideration averaged over the material and reacted to the effective properties of the material. This was used in many optical publications in e.g. the microwave regime [46, 52] until the optical regime [51, 53]. Recently, this concept was used in other parts of physics, e.g., in the acoustical regime considered for mechanics and elastodynamics [42, 54] and even thermodynamics [4, 40]. This shows that the concepts of metamaterials is a powerful tool to create effective media.

To explain the concepts of a metamaterial, one simple example is given here. Considering a simple two-dimensional structure as shown in Figure 1.3 with a lattice period of a as a bimode metamaterial. To be able to discuss the effective metamaterial properties, the band structure along the ΓX direction is plotted on the right hand side (see blue labels). As the periodicity of the unit cell is the lattice constant a the Brillouin zone edge if momentum space is thus $k = \frac{\pi}{a}$. Actually the Brillouin zone is in the interval of $[-\frac{\pi}{a}, \frac{\pi}{a}]$ but as it is symmetric (as long as materials obey no different properties after

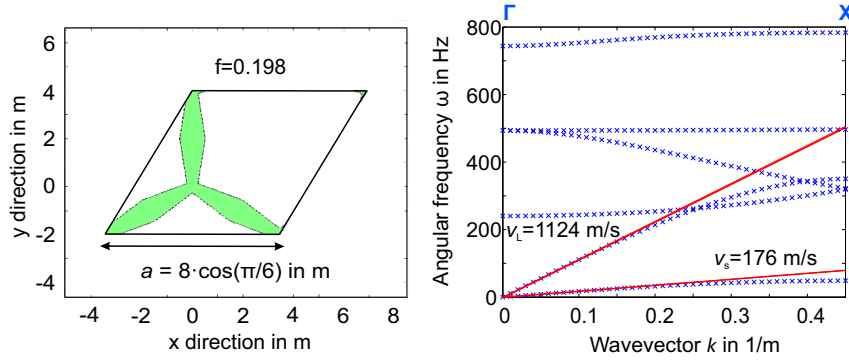
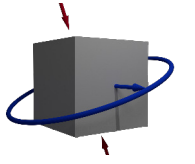


Figure 1.3: Schematic of a two-dimensional metamaterial a so called bimode material. The effective material is shown on the left, accompanied by a phonon bandstructure on the right. The band structure allows to retrieve effective material properties.

a space inversion) around the Γ point one usually only plots half of the Brillouin zone. The density is obtained by simply taking the initial density and calculating the filling fraction f of the material within the real space cell. To extract a shear or bulk modulus from the structure, one can take a closer look at the band structure of the material. As there are two branches emerging from the Γ point at zero frequency, these branches are the fundamental modes of the system. Here the wave vectors are very small and thus the wavelength in real space is very long. This leads to the conclusion that the metamaterial concept is valid in this case and one can extract the slopes of the branches leading to a velocity of this mode (the group and phase velocity are equivalent in this regime). This is done by fitting the band structure in a linear fashion around the Γ point as displayed by the red lines in Figure 1.3. The hereby obtained velocities can be used to retrieve the moduli assuming a frequency independent density obtained by the filling fraction and the constituent material properties. Here the constituent material has a Young's modulus of $E = 3 \text{ GPa}$ and a Poisson's ratio of $\nu = 0.4$. The real space unit cell is chosen to have a lattice constant of $a = 8 * \cos(\pi/6) \text{ m} \approx 6.93 \text{ m}$ along the x -direction. This leads to wavevector at the X point of $k \approx 0.45 \text{ m}^{-1}$. The resulting velocities v_s and v_L from the shear and the longitudinal modes are obtained via $v = \omega/k$. In order to retrieve the elastic moduli, we still need the effective density which is given here by the constituent density of $\rho_{\text{constituent}} = 1000 \text{ kg/m}^2$ and the filling fraction of $f = 0.198$. The multiplication of these leads to $\rho = 198 \text{ kg/m}^2$. This allows to retrieve first the shear modulus $G = v_s^2 \rho = 6.1 \text{ MPa}$ and thereafter find the bulk modulus in the same manner $B = v_L^2 \rho - 4/3G = 242 \text{ MPa}$. These moduli leads to an B/G ratio of 39. In this fashion one can obtain the effective metamaterial properties from any kind of band structure. As the velocity and the filling fraction do not depend on the actual size of the material, the retrieved parameters are scale invariant. This procedure is used throughout this work and this special example is used again in the lattice transformation, see Section 3.2. To determine the bounds of the metamaterial concept, one has to set a certain limit on either the wavelength to lattice period (normal numbers are about $\lambda > 10a$), or one can also set a limit within a band structure. In the later case one can determine at which k one leaves the linear regime of the material, and thus the linear red fits deviate significantly from

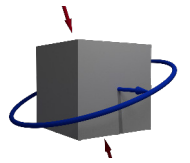
the bands. In this case one can estimate that the bands deviate significantly for k values higher than about half of the Brillouin zone thus a wavelength that is twice as large as the lattice period. In practice these bounds depend on the problem and the required accuracy, as well as on the band structure of the material. For higher k values than our bound, the effective material description is not valid any more, and the actual band structure needs to be taken into account. In this regime one finds a deviation between the group and phase velocities and thus dispersion of a wave packet. At the other extreme value $k \rightarrow 0$ the static regime is approximated. Here the metamaterial concept is valid, and one can approximate the material response and retrieve the effective materials with a very good accuracy.

1.2 Computational Methods

Within this work numerical simulations are used to estimate and verify the measurements and the mechanical metamaterial behaviors. This is done using a commercial software package called COMSOL Multiphysics. This software uses a finite-element method to solve a partial differential equation (PDE) in weak formalism and thereby simulates the physical behavior of a set real problem. Herein a geometry is used to set the problem to be solved. The geometry is then divided into smaller pieces which cover the whole geometry the so called mesh. This mesh is used as a basis to define the physical properties. In this fashion a basic physical equation is used as a basis for the computation linking the individual mesh points. This is normally a partial differential equation which is considered by the included solver sequences. In order to define the variables within this equation, one needs to define the material which is present at each mesh point. This defines the physical situation, which in combination with a set problem, normally defined by the boundary conditions, gives the required input for the solver to find a solution for a differential equation. The solver uses a matrix based system representing the mesh element and boundary conditions to solve for the solution searched for. The results can then be visualized in various fashions and resulting physical quantities can be extracted. Within this work mainly the solid mechanics module of the software is used to predict the behavior of a certain mechanical metamaterial.

The first step within a computation is to define a mesh for a given geometry. A mesh representing the geometry allows to define the computational domain and is thus of high importance. The discretisation of the geometry and the connections within the mesh need to be designed in the right fashion, to not impose errors by under representation of the physical behavior. The mesh is generated by Comsol based on a few parameters defining settings of the mesh-engine. The mesh-engine can be used with certain default values (Extremely coarse, Extra coarse, Coarser, Coarse, Normal, Fine, Finer, Extra fine, Extremely fine), or one can set the mesh parameters manually. The individual parameters are:

- Maximum Element size
This value determines the maximum size of an element normalized to the overall size of the geometry.



- **Minimum Element size**
The minimum element size determines the smallest element within the mesh. It is again normalized to the geometry and should be small enough to resolve the smallest features within a domain.
- **Maximum Element growth rate**
The growth rate defines, by how much a neighboring cell can grow with regard to the adjacent one. This defines how rapid the smaller areas are connected to the larger ones with regard to the mesh.
- **Curvature factor**
The curvature factor defines how well the mesh resolves a curvature within the system. The value defines how large a mesh cell can be for a certain curvature factor. So a lower value means that the maximum element for a certain curvature gets smaller, so the curvature is better resolved.
- **Resolution of narrow regions**
This value defines the resolution of a narrow region within the geometry. It thus control's how many layers are added in a small region.

These mesh parameters need to be evaluated for different geometries and a check needs to be performed, whether one finds a mesh representing the geometry to a high enough degree to not impose an error on the result. Normally one uses a coarse as possible mesh still fulfilling this requirement to decrease computation time. Sometimes one also intentionally wants to fix the maximum or minimum mesh size to obtain a homogeneous mesh. Furthermore, if one uses periodic boundary conditions it is sometimes useful to copy a mesh from the source to the target domain, which allows to define a direct relation for each mesh point between the source and target face, and no interpolation is necessary imposing the boundary conditions. This emphasizes that attention has be exerted not only on the geometry but also on the boundary conditions.

The boundary conditions define the problem to be solved for a given geometry. This means that one can examine many different physical systems by the aid of only a few boundary conditions. The most common and here used boundary conditions for the solid mechanics module are explained in the following:

- **fixed boundary conditions**
This option fixes the mesh elements with regard to any movement they could possibly undergo. This means for a three-dimensional simulation that all displacement vector components $\vec{u} = (u, v, w)^T$ are set equal to zero. This condition can be exerted onto points, lines, faces or whole domains.
- **prescribed displacement**
Prescribing a fixed displacement means that one can set individual components of \vec{u} to a fixed value during the solving procedure. With the aid of this condition one can for example impose sliding boundary conditions, by fixing only one or two of the components and leaving the third to be free. If one fixes all components to zero fixed boundary conditions can be mimicked.

- prescribed force

Complementary to prescribing a fixed displacement, a force onto the mesh can be prescribed. This force then will lead to a movement corresponding to the geometry and the other boundary conditions. The two methods are in general equivalent as long as they are numerically converged and set precisely.

- periodic boundary conditions

Periodic boundary conditions can be used for various physical arrangements. Here it is in general possible to mimic a periodicity of a material under static conditions or even time resolved. There are different ways of imposing these boundary conditions as described in references [55, 56]. The boundary conditions directly available in COMSOL are limited to some basic periodicity conditions. A simple condition is continuity, where the displacement vectors are set equal for the mesh points from the source and the target destination. This boundary condition allows to mimic a periodicity but does not necessarily mimic a fixed center of mass and does not allow for any contraction or expansion of the sample. To allow for this the periodicity can be set manually corresponding to the Taylor (Voigt) assumption in [55, 56]. This means that the geometry can change its size but still mimics a infinite geometry array by allowing a sign change in the displacement vector during the projection from source to the target. This does not yet mean that the center of mass is fixed as there might be an additional displacement along the direction which adds up on the deformation of the periodic boundaries. By setting this additional displacement to zero one also fixes the center of mass as it will be used further on in Chapter 2.1. One important and special case of a periodic boundary condition is the so called Floquet-Bloch boundary condition. Herein the displacement vectors of the source and the target are not set equal to each other but an additional phase difference is imposed to allow for a propagating wave. The vectorial connection for each point is given by:

$$\vec{u}_{\text{source}} = \vec{u}_{\text{target}} \times \exp(-i\vec{k}(\vec{r}_{\text{source}} - \vec{r}_{\text{target}})). \quad (1.30)$$

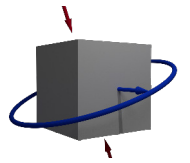
Herein the vectors \vec{r} define the position of the points related to each other, and the vector \vec{k} is the wave vector of the wave imposed. With the aid of this boundary it is possible to compute a band structure for a given unit cell, by searching for the eigenfrequencies of the system with a given wave vector \vec{k} . This scheme will be used in the following Chapters.

The last step of the preparation of a simulation is the definition of the constituent material. Here one assigns a material to the geometry and thus the mesh points. In the solid mechanics module one can set in principle the full elasticity matrix and a scalar density. In this thesis we consider the constituent material to be isotropic leading to only two moduli and the density. As the simulation is defined now with the mesh boundary conditions and materials, a solver to evaluate the PDE's has to be selected. The solver can be set to find solutions for different basic ways of solving the problem. Here are the most used ones within this work:

- stationary solution

Within this mode the solver searches for a stationary solution of the set problem. Regarding the mechanical point of view, this corresponds to a solution where no

1.2. Computational Methods



net forces exist, so that the mesh points do not change their position any more. This can for example be used to exert a certain force onto a geometry and find the resulting deformation of the sample under static conditions.

- eigenvalue solver

If the solver searches for eigenvalues of the system the result mimics the eigenmodes of the structure depending on the boundary conditions imposed. This allows in mechanics to find, for example, the principle eigenfrequencies of the system or one can determine the phonon band structure applying floquet-bloch boundary conditions.

- time dependent solver

An examination of the time dependent behavior of a system can be done using this type of solver. To find the state of a system at a given time, the static solution are calculated for each time step taking the material densities into account. This allows to examine the behavior of a system under time dependent loading, or to send pulses or waves through a material domain.

Before starting the simulation one can consider only the linear regime of the geometries deformation, or one can also include the geometries non-linearity into the solving process. This means that the calculations are done with the real deformations and are not rescaled during the solving. This can lead to non-linear behaviors of the structures even though the constituent material is strictly linear.

At last the solver can be started and after finishing the solving procedure the results can be visualized and exported in the desired fashion. This can give an input for the experimental realization and allows for comparison to an experiment.

1.3 Experimental Methods

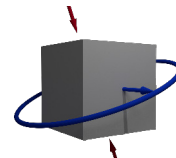
This section explains the main steps and procedures used throughout this work related to the experiments performed. Starting from the creation of geometries and pre-processing of the geometry data to the two used fabrication methods.

1.3.1 Geometry Creation

The general procedure within this thesis is to create a structure, based on theoretical suggestions, which exhibits a certain mechanical behavior. To start of with the creation, two main methods have been used: direct programming of the trajectory with Matlab and the creation of STL (Surface Tessellation Language) files followed a slicing and hatching step afterwards. The creation of the STL files can either be done with the simulation software COMSOL Multiphysics, where a direct comparison to the results from the simulations is possible, or it can be performed in a computer-aided-design (CAD) software, e.g., the freely available ray-tracing software named Blender. Both options have been used individually or in combination. For very large structure arrays it is necessary to duplicate a certain basic motive such as a unit cell. All of the considered structures are based on a rather simple unit cell. This unit cell consists of a distinction of two materials, here one constituent material and vacuum (or air). It is thus sufficient to define one material. To build up a structure only a few simple primitive geometries are used. For the examples discussed here simple cones or polygons are arranged into a certain pattern in space and are connected via a union operation. These simple basic cells can be reproduced into arrays, or be arranged by other simple operations (e.g. mirrored, translated, rotated...) into a metamaterial. By this means it is possible to generate complex micro-structures by the aid of only a few simple geometry parameters. The selected method of choice for the geometry processing depends on the sample, software and the fabrication method. Normal direct laser writing can be programmed as coordinate sets to a very large extend and lead to the best writing times for this method, whereas scanning direct laser writing as well as 3D printing procedures require a slicing along at least one dimension for optimal performance, achieved ideally by post-processing of STL files.

1.3.2 Direct Laser Writing

The technique called direct laser writing (DLW) [57] allows for the fabrication of nearly arbitrary three-dimensional structures by localized polymerization of a liquid photoresist to a solid polymer. This method of polymerization is unique as the final structure of the polymerized volume is created in a sequential fashion and build out of the same underlying feature called a voxel. The voxel consists of a three-dimensional volume in which the photoresist is exposed in order to polymerize. To create an arbitrary structure, this voxel is scanned connecting the individual voxels to a larger structure. The resulting structure can have an arbitrary three-dimensional geometry, fulfilling the resolution and linewidth constraints opposed onto the voxel[58].



This technique uses a focused pulsed laser source to polymerize a photoresist in the focal point. The laser is focused via a microscope objective and reaches an intensity in the focus that is sufficient to induce non-linear effects. This non-linear effect is called two-photon absorption and was discovered first by Maria Goeppert-Mayer [59]. This effect allows to polymerize a resist although the fundamental wavelength of the laser beam does not cause a polymerization. Exposing a photoresist to light in order to structure the resist is commonly done in two-dimensional patterning, for example in the silicon industry, but is gaining in DLW a selectivity and resolution in the third dimension. As it is sufficient to expose a resist through a mask for two-dimensional patterns, the third dimension is microscopically only available via stereo lithography[60] and consecutive steps of 2D lithography. In order to find a way of patterning in three dimensions and with a suitable resolution direct laser writing was invented.

Here the volume inscribed by an iso-intensity contour of the focal intensity is high enough to polymerize the resist. The resulting voxel is bound by a threshold behavior of the photoresist. Within the radical polymerization used here, free radicals are created with an photoinitiator which further link the individual monomer molecules (a multi-functional acrylate) together and can form thus a cross-linked solid polymer. To create a defined volume this polymerization is stopped at some point. Therefore the radicals need to be inhibited and bound. Within the photoresist the radical binding is done by ambient oxygen or an added inhibitor such as, e.g., Mono Methyl Ether of Hydroquinone (MEHQ). This scheme, in principle, works with a one photon absorbing process, but is very hard to set the power to a level in which the resist only gets enough exposure in the smallest voxel, to not polymerize the resist at unwanted sites. Further a possible memory-effect of the photoresist is admissible, remembering the previous deposited dose and thus accumulating the exposure. To be able to structure the photoresist in a three-dimensional well defined manner a second non-linear processes is utilized for polymerization. In stead of a one photon process a two-photon absorption process allows to expose the resist only in a small volume. In order to do this a tight focussing of the laser light is needed in the resist. This resist is ideally index matched and has a refractive index close to an immersion oil with an index of $n = 1.515$. The normal IP-L resist sold by Nanoscribe has a refractive index of $n = 1.48$. The index matched versions allow for the smaller focusing and local polymerization. Two versions of this index matched resist are used, the IP-Dip and the IP-S sold by Nanoscribe [61]. The constituents of the resists are only known by the selling company but some main features of the two resists can be compared. Ip-Dip has a high resolution of the individual voxel's whereas Ip-s has an intentionally reduced resolution to be able to write lines of a block with a higher spacing and thus effectively save time still obtaining a good polymer surface quality. Both resists are optimized for two-photon absorption. To polymerize the resists two photons need to be within a short time range in the area of one initiator molecule. This creates a certain possibility that the energy of two photons is available and then the combined energy is high enough to expose the resist. One can think about one photon with the energy of $E = \hbar\omega$. Two photons can have twice the energy if they have the same frequency ω and if they have the same spacial and temporal distribution, or within an error related to Heisenberg's uncertainty principle. This allows to treat them with a combined energy of $E = \hbar 2\omega$.

The absorbed photon can now expose the (for other frequencies) transparent photoresist by triggering a photoinitiator molecule. In other words the sum of the energy's is now big enough to bridge a gap via a virtual state in the energy diagram of the initiator molecule and start the polymerization. The two-photon absorption can be described as a nearly pure second order mechanism as the resist is transparent for the first order light. The change in the intensity of light passing through a medium is the absorption as stated in Beer's law. The first order term is proportional to the intensity I thus the second term of Beer's law has a proportionality to I^2 . If one looks deeper into what causes the absorption one finds [62–64]

$$\frac{dI}{dx} = -\beta \cdot c \cdot I^2. \quad (1.31)$$

The concentration of absorbing molecules c as well as the normally small second order absorption coefficient β are mainly determining this absorption. So the iso-intensity curve proportional to I^2 is the important factor resulting in a more localized voxel. Figure 1.4 shows an intensity profile for an objective with NA=1.3 and the refractive index of the IP-Dip resist, which both have been used in this thesis. The x,y -plane, x,z -plane and y,z -plane are projected to envision the evolving voxel and its rough dimensions¹.

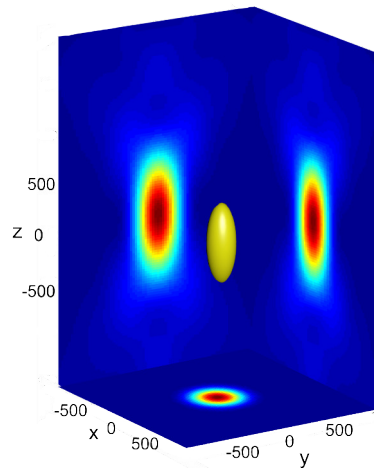


Figure 1.4: Projections of calculated intensities in x -, y -, and z -direction. A iso-intensity curve is selected and represents a voxel. The maximum intensity is normalized to one and scales are in nm.

A so called aspect ratio defines the elongation along the z -direction compared to the x - or y -direction. The elongation is dependent on the numerical aperture of the focussing lens and the refractive index of the focusing medium used and is proportional the Rayleigh length of the objective. As the aspect ratio is normally larger than one, typical values range from 2-4 (NA =1.4 leads to about 2.5), the voxel is elongated in the focusing direction. For further information about the focussing and resolution limit imposed on the lateral and axial resolution see [62].

¹The exact dimensions and shape depend further on the power relative to the threshold of the polymer. This determines which iso-intensity line one has to choose to represent the fabricated voxel.

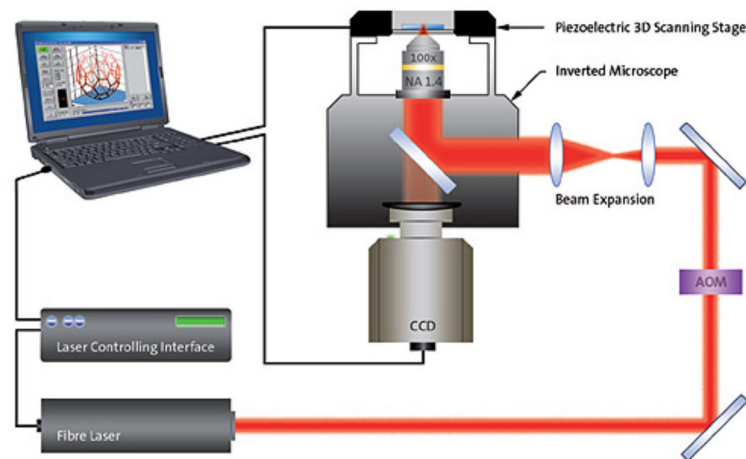
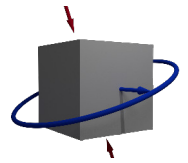


Figure 1.5: Direct laser writing setup with all key features. Figure is taken from [61].

This ratio can only be reduced by a rather complex set-up based on STED (Stimulated Emission of Depletion) inspired direct laser writing [58]. This method is not used within this work, but could possibly be an advantage considering smaller structures and higher resolution lithography. Reducing the voxel size has the drawback of an increased writing time for a given volume of desired material.

A reference setup is shown in Figure 1.5. The laser output power is modulated with an acousto-optic modulator (AOM) and focused by an objective into a resist. The laser focus is scanned via a three-dimensional linear stage and a piezoelectric stage. The consecutive polymerization of small volumes is used to build up a larger structure. A computer software which can control the laser power and address the right positions of the stages is used to automate the writing process. To be able to attach the written structure to a substrate the interface between the substrate and the photoresist is determined. This tool is called a interface-finder and is implemented within the software by imaging the reflection of a projection of a slanted grid. Focusing a femtosecond laser pulse (the laser source used is an erbium doped fiber laser with a repetition rate of 40 MHz and a pulse duration of 90 fs at 780 nm wavelength) with a high numerical aperture objective (here used: 100 \times or 63 \times , NA = 1.4, 100 \times , NA = 1.3, or 25 \times , NA = 0.8, by Zeiss) generates very high intensities in the focus. This allows to induce the two-photon polymerization and create polymer structures. The exposed polymer can withstand a treatment with a solvent such as isopropanol whereas the unexposed is solved and can thus be removed.

It turns out, that the applications and the measurement of mechanical metamaterials is mainly limited by the volume of the final geometry and thus by the possibility to write as large as possible and as fast as possible. During this thesis huge progress has been made on both aspects in collaboration with Nanoscribe. They have incorporated two main changes to the conventional DLW setup: the dip-in laser lithography (DiLL) technology and the galvanometric scanning of the laser beam.

To explain the working principle of the DiLL DLW, a conventional DLW arrangement is shown in Figure 1.6 (a) next to the DiLL configuration in (b). In panel (a) the laser light

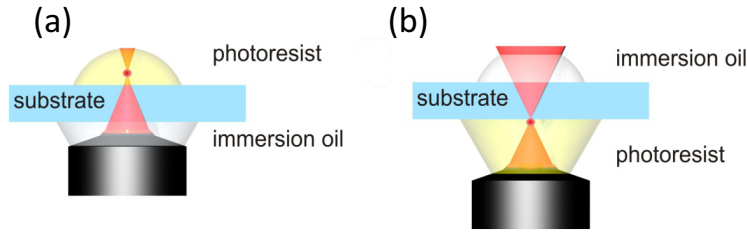


Figure 1.6: (a) Normal DLW using immersion oil and focusing through the substrate. (b) DiLL technology focusing directly into the photoresist. Reproduced after [26].

is coupled incident from the objective, through an index matched immersion oil, to the substrate and finally forming a focus within the photoresist. In this configuration three interfaces have to be passed by the light before the actual focal point. The first in the direction of light is not to be considered as critical since the immersion oil's refractive index is adjusted to match the objectives. This is also fulfilled for the substrate as one uses the same kind of glass for the substrate as one uses for the objective. This causes the substrate thickness of $170\mu\text{m}$ to have a negligible influence on the light path as most of the objectives are even corrected for the cover-glass. At last the refractive index of the photoresist is close but not perfectly matched with the beneath laying substrate. Those slight deviations from the perfect non-refractive case cause the focus to vary in its shape. The lateral size of the voxel and the aspect ratio of the voxel increase due to the index mismatch leading to a higher power needed for polymerization and a reduced resolution. Especially as for high structures one does not want to write close to the photoresist substrate interface, further referred to as the interface, aberrations occur and cause the voxel to be elongated thus the aspect ratio to increase. The compensation of this effect requires a higher power to still have the same intensity per volume. This reduces the height of the structure to be limited to a few tens of micrometer and suffering from severe distortions as one goes away from the interface. This problem can be tackled by the aid of the so called DiLL technology developed by Nanoscribe and first published in [26]. The basic principle underlying this procedure is to dip the objective directly into the photoresist. This scheme can be seen in Figure 1.6 (b). Using this method gives in general rise to aberrations by the mismatch of the index of refraction between the objective's correction and the photoresist, but the aberrations are not dependent any more on the height of the structure. Adjusting the index of refraction of the photoresist allows to minimize these aberration and good focal energy distributions can be obtained with the two used photoresists IP-Dip and IP-S. The DiLL technology gives rise to another improvement essential within this work namely the elimination of the upper bound for the sample height imposed by the working distance of the objective. In the normal DLW configuration one would be finally limited by the working distance of the objective as one touches the substrate at one point with increasing sample height. In the DiLL configuration this limitation is not valid any more as one moves away from the substrate with increasing sample height.

The second main development during the time of this theses is the galvanometric scanning technology used to move the focus relative to the substrate. In this scheme instead of moving the sample with its holder by a piezoelectric stage one fixes the sample and scans

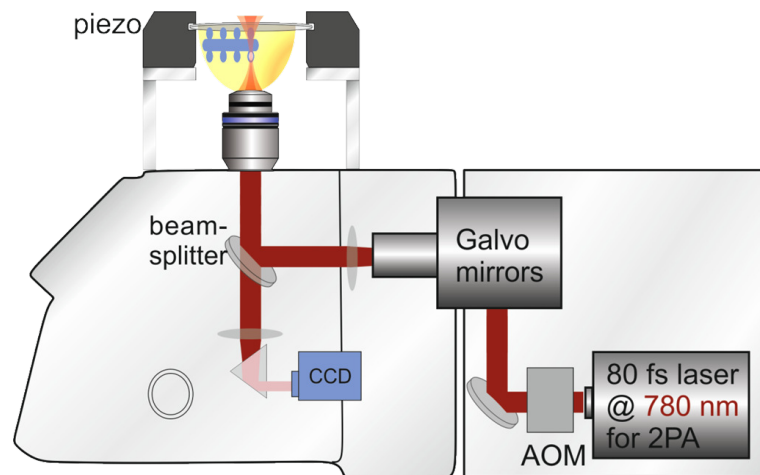
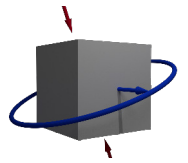


Figure 1.7: DLW setup using galvanometric mirrors to scan the laser beam rather than the substrate. The here depicted graphic represents the Nanoscribe Professional GT in DiLL mode and is taken from [61].

the laser beam. To achieve this some important key features need to be taken into account. As only a movement in the x- and y-direction are wanted one needs to change only the incident angle and not the position of the laser beam onto the back side of the objective. This is possible with the aid of two galvanometric mirrors and at least one lens. Thereby the voxel is scanned in the x-, y-plane if the objective is corrected for a flat image area. As the galvanometric mirrors, named after Luigi Galvani, are a lot lighter than the sample-stage and thus can be accelerated with less force and thus faster, this technology increases the writing speeds tremendously². The basic scheme of the set-up can be seen in Figure 1.7.

The galvanometric scanning allows to write on scan fields up to about 500 μm . These scan fields can be stitched (positioned next to each other) and a larger area can be processed. In the vertical or axial direction two possible stages can be used. The more precise one is the piezo-stage allowing for a movement of up to 300 μm . If one would like to have higher structures the linear microscope drive needs to be used. Here much larger heights can be addressed but the repeatability and precision of the stage are lower as for the piezo-stage. Depending on the structure both stages or both in combination have been used in this thesis.

1.3.3 Super Critical Drying

In order to develop a sample after the direct laser writing process the remaining unpolymerized photoresist needs to be dissolved. This is done by either Isopropanol, Aceton or mr-Dev 600 (MRTBerlin). It takes about 15 minutes to 2 hours to solve the remaining monomer out of the structures depending on the porosity of the samples. To actually transfer the sample from the solvent into air, small and mechanical stable

²Usual writing speed are 10 – 100 μm for the piezoelectric scanning and 10000 – 100000 μm for the galvanometric scanning technique.

structures can be washed in purified water. Larger and more fragile structures can suffer severe damage during this process due to capillary forces. The remaining droplets within the structures reduce their size changing from the liquid state to the gas state and thereby 'pull' on the polymer structure. This problem can be circumvented by a procedure called super critical drying. Here the sample is transferred into liquid acetone, and placed within the transport container. This transport container is then inserted into a high pressure chamber, wherein the acetone is cooled to 8°C and is exchanged with liquid CO₂ at 50 bar pressure.

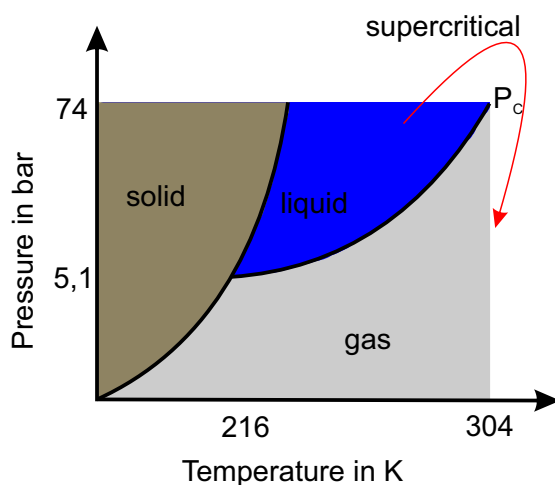


Figure 1.8: Phase diagram of CO₂ after [65].

After this step the chamber is sealed and heated to 42°C. Meanwhile the pressure rises above the critical Point of CO₂ at 31°C and 74 Bar. The liquid is now in the state of a supercritical fluid. Now the pressure can be reduced and the gas can leave the chamber. As the pressure is ambient, the sample chamber can be opened, and the sample is dried without ever performing a phase transition in the solvent. This path is indicated with the red arrow in Figure 1.8 (b). On this path no phase boundary is crossed and no capillary forces can occur. The development of extremely sensitive structures is thus possible, without any harm during these steps.

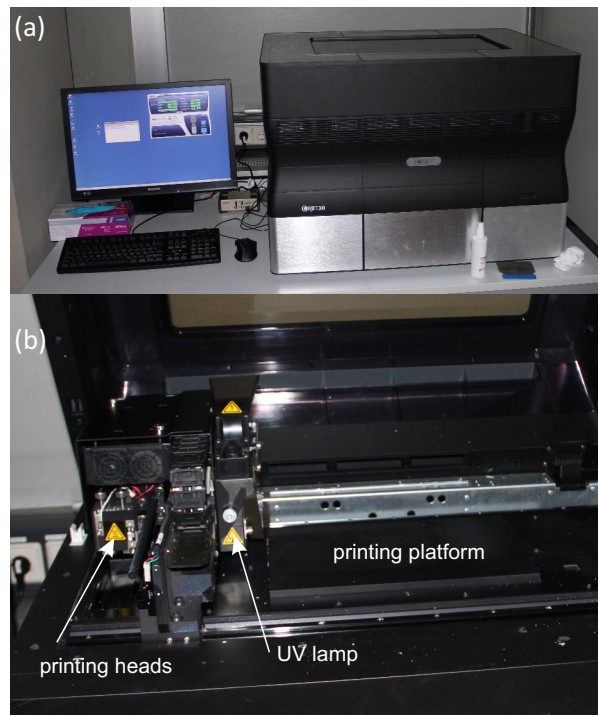
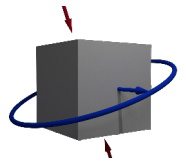


Figure 1.9: (a) Image of the Objet30 3D printer with control computer. (b) View onto the building platform of the printer with opened lid. On the left the x,y -stage can be seen. Here the here the printing heads and the UV lamp are attached to.

1.3.4 Three-Dimensional Printing

The samples on macroscopic scales have been printed using a commercially available three-dimensional printer, sold by Stratasys. The model Objet 30 used here allows to print a polymer material, namely VeroGray (for ink specifications see appendix). The printer uses an ink-jet like printing scheme with a resolution in x - and y -direction of 600 dpi (dots per inch) and in the z -direction of 900 dpi.³ The maximum specified printing volume is $294 \times 192 \times 148,6$ mm. This allows to print an object with quite high resolution. The minimum feature size, which is still stable and well resolved, is on the order of $100 - 300 \mu\text{m}$. To print truly 3D features one needs a support material, Fullcure 705, which is printed into empty volumes to allow for overhang or cantilever structural parts or around an object to stabilize it during the printing procedure. As a first step of processing a sample STL files are loaded into the software of the printer. After an automated or manual positioning step⁴ the software automatically slices the files into individual layers and decides on the basis of given printing parameters where to put which material. After this slicing has been done the procedure starts automatically and prints the desired sample. The printer and peripheral devices, as well as the building platform, and x,y -stage can be seen in the Figure 1.9. The actual printing is done by adding small droplets

³The printer resolution corresponds to $42 \mu\text{m}$ in x,y -direction and $28 \mu\text{m}$ along the z -direction.

⁴The angle and position dependent placement of the samples is necessary to minimize printing time and material consumption, and use the optimal resolution of the printer.

of the preheated ink onto the sample and curing the printed layers partially with an UV (Ultra Violet) lamp. In this fashion one layer after the other is printed, whereas they are cured consecutively to maximize the adhesion between the layers. The thereby used support material also influences the occurrence of a surface roughness on the sample walls. If no support is printed on the surface a smooth surface can be obtained. Support structure attached to the surface causes the two materials to overlap slightly and after the removal of the support structure leads to a rough surface. This can partially be avoided on the side walls and the top surface if one sets the properties of the printer to not add support material next to these surfaces. In order to remove the support structure from the samples there are three possible ways. Apart from manual cleaning it with a hard object like a metal blade, one can use a pressure washer to remove the softer support material. This is inserting quite high forces onto the sample though and can possibly damage fragile samples with complicated geometries. The alternative to this methods is the etching base. Here the manufacturer of the 3D printer recommended a 4 – 10% NaOH base. This solves the support structure and one can get the sample out without damage. One has to mention though that the base also attacks the VeroGray material making it soft during the base bath and more brittle after drying. This means one has to exert attention on the drying step to not deform the sample and the elastic material properties vary during the drying procedure of the sample. To avoid the contamination of the samples with the NaOH a rinsing in water for several hours is performed after the base bath. After these steps the samples are in general ready for use.

1.3.5 Imaging and Microscopy

The structures fabricated need to be tested for the conformity with the design and their properties characterized. To do so various different imaging techniques are used. As for the 3D printed macroscopic samples an inspection by eye or a normal digital camera is efficient, the microscopic samples needed a higher imaging magnification and resolution. Here an optical microscope with magnifications ranging from 5× to 100× allowed to get a first impression of the structure quality and even allowed to resolve smaller features down to a few microns in size. To be able to resolve even smaller features, or to check for variations within the structure a scanning electron microscope (SEM) is used. Here one can obtain a higher resolution, and/or can have a much higher depth of focus, allowing to look deep into an open structure. The presented SEM images within the later chapters are mainly taken with a Zeiss Supra operated by Johannes Kaschke. After a sputtering of a gold film with about 10 nm thickness, the images are normally taken at 1 – 5 keV to reduce charge accumulation on the structures. To improve image quality first a higher scan speed is used for an individual image, hereafter an averaging of 10-80 frames lead to satisfying images. These images could then be used to measure the geometry parameters of the fabricated samples. While evaluating the dimensions the perspective has to be taken into account.

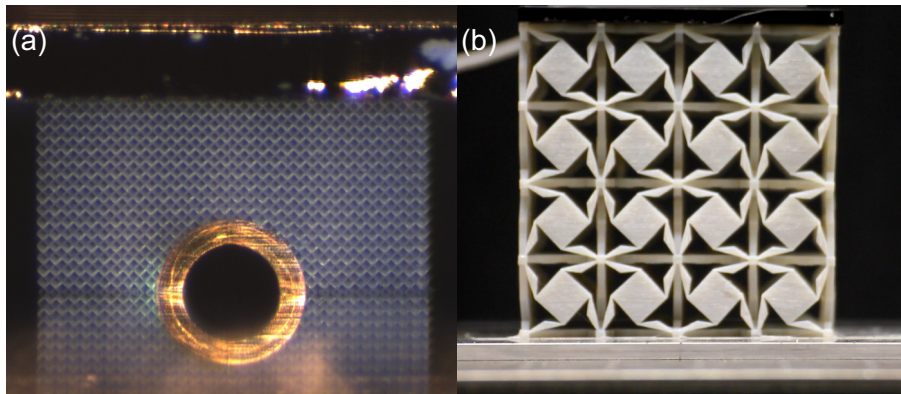
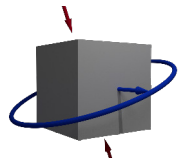


Figure 1.10: (a) Measurement image of a microscopic sample taken with the Sony camera and the Leica objective. (b) Image of a macroscopic sample taken with the Canon camera and the Tamron objective.

During the measurements normal cameras⁵ are used, combined with changing objectives⁶, to obtain the optimal image concerning resolution, field of view, depth of focus, and perspective. The first optical constraints are trivial to solve, as one would like to have a high as possible resolution still imaging the whole sample at a time. The depth of focus is more complicated to understand. In some measurements one would like to image just one facet of a sample, whereas some mechanical metamaterials under consideration have quite complex and extended unit cells, where not only one plane, but rather the first layer of the material needs to be in focus. This is linked to the perspective argument. If one considers a measurement of strain on a facet of a material, one would ideally have no perspective to the image and rather use an telecentric imaging to avoid any influence of the perspective onto the results. As this is very complex and requires special optics one can though approach this ideal by a large distance to the object compared to the object dimensions themselves. This allows to minimize the influence of the imaging optics on any measurement. Combining these general considerations, different optics are chosen to image the samples depending on their size and structure given in the corresponding chapters. For more detailed information on optical systems various literature can be consulted, e.g. [63, 66]. Here only two exemplified images from a measurement are given. In one case, the panel (a) of Figure 1.10, a microscopic sample is shown. Here the depth of focus is about the size of one unit cell. This means that one can see the full 3D cell in focus. Panel (b) is taken on a macroscopic scale with a very long focal length. This reduces the perspective of the image to not influence a measurement any more. Both of the images show an excellent imaging quality to allow for a precise measurement.

⁵Canon EOS550D, Sony GigE Vision XCG-5005CR

⁶For the Canon camera: Tamron SP 70-300 mm f/4-5.6 Di VC USD, Canon 50mm F/1.4. For the Sony camera: Leica Mz 125 and a 0.5× adapter to c-mount, Edmund optics 35mm

1.3.6 Cross-Correlation

During the measurements videos of the structures are taken while the strain rate is increased. To be able to track a displacement in these videos a cross-correlation approach is utilized allowing to track predefined areas of a certain size throughout the measurement. This allows to track individual parts of the structures and find deformations within the structures as well as global movements within the measurement setup. The software used is a free software package [67] used with the commercial software Matlab. Herein a certain sub-part, defined by the location and the dimension in pixel of one initial image, is tracked throughout a set of images based on cross-correlation. The basic principle of the here used correlation is based on a convolution of the whole image with the selected sub part defined in the beginning. In a mathematical one dimensional sense this is defined as:

$$(f * g)(\tau) = \int_{-\text{inf}}^{\text{inf}} f^*(t)g(t + \tau)dt. \quad (1.32)$$

This correlation function of τ gives a peak where the functions f and g are similar to each other and else has only a small noise due to accidental self similarities. In contrast to a auto-correlation the functions f and g do not need to be defined in the same interval, translating in a discrete manner to not having the same length as vectors. Within the code used, a slightly different implementation of this principle is used. Here the two vectors are multiplied with each other and then summed up to give one element of the output vector. The next element is then obtained by a permutation of the vector which has to be correlated. This results into a vector peaking where the two input vectors are self similar returning thus a cross correlation for discrete inputs. This basic principle can also be applied in a two-dimensional manner and thus be used to correlate images. Using periodic structures can in principle cause some problems, and thus a peak closest to the position in the last image needs to be selected, causing a necessity to have only small movements (less than a periodicity of the structure) between two images. One nice thing about the cross correlation is that one can use the correlation output and fit a function to the curves determining the actual position much better than the pixel resolution would allow for. With this at hand we can define the properties of our correlation and use it throughout this work. The tracing is performed with markers of the size of 25×25 pixel and they are tracked with a precision of 1/1000th of a pixel. These settings are found to result in a good data quality and return an accurate tracking. The returned positions of the markers throughout the stack of images can then be used for further evaluation of strains and thus deformations during the measurement. In short a cross correlation approach can be used to track predefined marker regions of an image throughout a measurement stack of images and the positions of these markers can be found for each measurement image to allow for further evaluation.

2 Extremal Mechanical Materials

Extreme material properties help to exploit the limits of material science. The materials discussed within this chapter are extreme in the sense that they are showing material properties approaching the bounds of the Poisson's ratio ν for isotropic media. This is done on the basis of mechanical metamaterials in the long wavelength limit. Here the materials are a composite of one constituent material and air/vacuum only. The mechanical properties are solely based on the structure (though scaling with the constituent material). In the first part of the chapter the lower bound of the thermodynamically allowed range of the Poisson's ratio is approximated. The ideal structure thus has only one allowed mode of deformation naming the material a unimode material with $\nu = -1$. Thereafter the upper limit $\nu = 0.5$ approached by pentamode materials. As the upper and the lower limit can be tailored allowing to control the elastic moduli of the structures, the mass density is tailored. Herein a static as well as dynamic mass density is explored. The combination of these allows for full direction dependent control of the elastic wave propagation with regard to wave velocity and impedance.

2.1 Unimode Materials

Unimode or dilational materials are one kind of auxetic materials also sometimes called the perfect auxetic. This refers to the property of an isotropic negative Poisson's ratio of $\nu = -1$, leaving only one easy mode of deformation, and thus naming the material unimode material. In this section we will discuss how one can approach this idealized material and what special behavior this property implies. We will see how such a material can be implemented and what problems can arise during a mechanical characterization. Further we find a way to overcome these problems by comparing finite-element simulations to the experimental measurements and thereby retrieve the effective material properties. Parts of the chapter have been published and figures are in accordance to or taken from the publications: [68].

2.1.1 Theory of Unimode Materials

As we have seen in Chapter 1 the underlying physics and especially the complexity of the equations describing linear elasticity depend on the dimensionality of the considered problem. In one dimension there is no definition of a Poisson's ratio as it links a strain in one direction to an induced strain in an orthogonal direction. So discussing the properties of an auxetic material needs to take at least a two dimensional system into consideration.

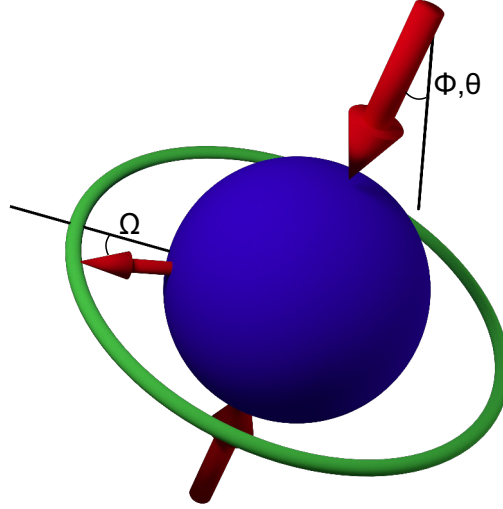


Figure 2.1: Poisson's ratio for a general material (blue). The two opposing red arrows depict the initial strain, whereas the other arrow depicts one strain direction within the orthogonal plain indicated by the green torus. The relative angles are indicated.

As discussed in the Chapter 1 the Poisson's ratio is defined as :

$$\nu_{12} = -\frac{\epsilon_{11}}{\epsilon_{22}}. \quad (2.1)$$

Herein the strains ϵ are defined along two orthogonal directions. This simple definition leads in general media to a very complex description, as for any initial strain direction an orthogonal plane exists, where for each orthogonal vector a Poisson's ratio is defined. This would lead to a Poisson's ratio depending on three variables namely the azimuthal angle ϕ , and polar angle θ for the first strain and at last the angle of the vector in the plane Ω . This dependence can be seen in the schematic of Figure 2.1.

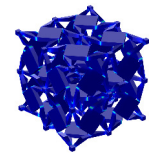
This very complex evaluation can be simplified in many cases depending on the symmetry of the material. For cubic materials this relation can already be simplified by averaging over the orthogonal strain plane. This helps to display an average Poisson's ratio for each of the spherical directions. This was calculated using the [69] material properties of the cubic material so one needs all independent entries of the \mathbf{C} matrix. One can get these entries from the velocities along the ΓM direction of the Brillouin zone:

$$C_{44} = \rho \left(v_{110}^{T,z} \right)^2, \quad (2.2)$$

$$C_{12} = \rho \left(v_{110}^L \right)^2 - C_{44} - \rho \left(v_{110}^{T,xy} \right)^2, \quad (2.3)$$

$$C_{11} = 2\rho \left(v_{110}^{T,xy} \right)^2 + C_{12}. \quad (2.4)$$

$$(2.5)$$



2.1. Unimode Materials

These relations are valid for any cubic material, where one needs three different material parameters for a full description of the linear elastic material properties. The first three modes need to be investigated propagating along the face diagonal in the band diagram. The mode characteristic (longitudinal L , transversely in z or in x, y polarized) and the corresponding velocities define the linear properties of the material assuming a scalar density. The elasticity matrix entries can be translated into material properties such as the moduli, which can be expressed with the elasticity tensor elements [70, 71]:

$$B = \frac{C_{11} + 2C_{12}}{3}, \quad (2.6)$$

$$G = C_{44}, \quad (2.7)$$

$$E = \frac{C_{12}^2 + C_{12}C_{11} - 2C_{12}^2}{C_{11} + C_{12}}. \quad (2.8)$$

These moduli lead to a Poisson's ratio for the cubic directions given by:

$$\nu = \frac{C_{12}}{C_{11} + C_{12}} \quad (2.9)$$

To find the Poisson's ratio for other directions we use the averaged Poisson's ratio for any compression direction as described above. The relations are based on [72].

$$\nu(\phi, \theta) = -\frac{Ar_{12} + B(r_{44} - 2)}{16[C + D(2r_{12} + r_{44})]} \quad (2.10)$$

Herein the ratios r , extracted from the compliance tensor $\mathbf{S} = \mathbf{C}^{-1}$, and the abbreviations $A - D$ are defined the following way:

$$r_{12} = \frac{S_{12}}{S_{11}}, \quad (2.11)$$

$$r_{44} = \frac{S_{44}}{S_{11}}, \quad (2.12)$$

$$A = 2 \left[53 + 4\cos(2\theta) + 7\cos(4\theta) + 8\cos(4\phi) \sin^4(\theta) \right], \quad (2.13)$$

$$B = -11 + 4\cos(2\theta) + 7\cos(4\theta) + 8\cos(4\phi) \sin^4(\theta), \quad (2.14)$$

$$C = 8\cos^4(\theta) + 6\sin^4(\theta) + 2\cos(4\phi) \sin^4(\theta), \quad (2.15)$$

$$D = 2 \left[\sin^2(2\theta) + \sin^4(\theta) \sin^2(2\phi) \right]. \quad (2.16)$$

Here, ϕ and θ are the azimuthal and polar angle, respectively, in spherical coordinates. Plotting the absolute of the Poisson's ratio as a radial component over these two angles gives a possibility to evaluate the isotropy and the absolute magnitude of the Poisson's ratio for a cubic material.

A further and more intuitive insight into auxetic materials can be obtained by the help of a few simple relations for isotropic media. If one expresses the moduli of a material with the Poisson's ratio one can directly conclude some boundaries for ν , see also section 1.1.2. There we find that in the case of a vanishing bulk modulus the material was easy to compress but hard to deform in any other way. Translating this into a Poisson's ratio results in $\nu = -1$. This is also the lower limit for an isotropic Poisson's ratio as a material with negative bulk modulus is not stable without any further constraints. As a side remark we mention that the considerations done here are in the long wavelength limit or quasi-static meaning that resonant effects, possibly leading to a negative bulk modulus [73–77], are not considered and irrelevant at this point. If one has a closer look onto the terms in equation 2.9 one finds that only the bulk modulus is taken into account within this equation as the elasticity entry C_{44} is not occurring within the definition. The assumption of a Poisson's ratio of $\nu = -1$ directly leads to the relation of $C_{11} = -2C_{12}$ which is representing an isotropic material. An equivalent result can be obtained from the assumption $B = 0$. This result needs not to be mixed up with a Poisson's ratio of $\nu = -1$ along any direction as described in equation 2.10. If the Poisson ratio is $\nu = -1$ for the cubic axis the Poisson's ratio is isotropic and $\nu = -1$ for all directions, we will call this ideal an dilational material. Whereas in general the Poisson's ratio for a certain direction can be lower than $\nu = -1$. Thereby is though has to be larger along other directions still maintaining $\nu > -1$ for the principle cubic directions [78, 79]. As a simple example one could think of a simple leverage structure, which translates a small strain along one direction into a large strain orthogonal to it. If one inverts the directions in such a structure, the effect would be inverted as well, leading to the before mentioned asymmetry.

2.1.2 Structural Designs for Unimode Materials

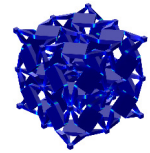
The question on how to obtain a material that exhibits a low Poisson's ratio approaching $\nu = -1$ is tackled on various different approaches. The research on auxetics can be divided into three main fields, namely:

1. Natural materials

Some natural materials exhibit a negative Poisson's ratio right from the start. Especially cubic metal crystals can show a highly negative Poisson's ratio along certain directions [80, 81]. But natural materials are used because of their Poisson's ratio even in normal life. An example is cork, as it allows with its Poisson's ratio close to zero to be pushed into a bottle without expansion [82].

2. Auxetic foams

Auxetic foams are one of the oldest systems in which a negative Poisson's ratio was obtained. The pioneering work of Lakes and his coworkers in 1987 [83] has shown that foams can show a negative Poisson's ratio after a certain treatment. In this treatment a foam is compressed before heating it up to a certain temperature where the initial foam material is starting to relax and reform such that the compressed state is now nearly stress free. After cooling the samples back down the compression is released. The resulting foam now has a negative Poisson ratio depending on



2.1. Unimode Materials

the compression ratio imposed beforehand. This procedure can be done in many material systems [21, 84–86] and one can even treat the compression directions independently resulting in an an-isotropic behavior. Although this method is quite universal and samples can be fabricated in large quantities and at low cost, it is not intuitively clear how one can reach extremely low values approaching the ideal of $\nu = -1$. The lowest value achieved so far is showing a Poisson's ratio of $\nu \approx -0.8$ [87].

3. Structure based fabrications

A very different approach is based upon the underlying concepts of an auxetic structure. Here different ways how to obtain a negative Poisson's ratio are identified and a structure showing these features is designed. As this field was mainly dominated by the theory of mechanical systems several mechanical models for dilational or auxetic materials were discussed [19, 86, 88–92]. Lately some more structures could be designed via numerical optimisation [93–95] or based on the so called buckling concept [96–100]. Both of these concepts have mainly been realized by 3D printing as this technique allows to fabricate even very complex micro structures and is easy to handle.

As the most promising approach regarding the flexibility of the design and performance of the final structure seems to be the structure based fabrication we will focus on this general procedure within this thesis. We will use the metamaterial concept to design a material that exploits its mechanical properties based on the underlying structure of a material.

2.1.3 Blueprint and Variables

Dilational materials can be obtained in various fashions as discussed in References [19, 86, 88, 90–92]. Some are based on idealized sliding elements others are constructed of rotating cubes [92, 101–104]. To choose one of these theoretical ideas as a design, we are limited by some basic constraints. As these complicated structures need to be fabricated using a rapid prototype method as 3D printing or DLW, we are currently limited to one constituent material. Further a smallest feature size compared to the overall volume limits the complexity of a design. Within these constraints the most promising idea is chosen introduced by Milton in [19]. This as well as the other approaches still contain elements like 'perfect joints' or 'rigid bars' within a two dimensional model cell. The basic design is depicted in Figure 2.2.

Within this design there are three main features to be considered. The cell is centered around a square element which is held by four triangle elements at its corners. These elements are then connected by small bars. All the elements are perfectly rigid and can not be deformed. The connections though are ideal joints meaning that no force is needed to obtain a rotation in this point-connection joint. The behavior of the cell under any force can only be a dilation, meaning that it can just change its size. If one for example inserts a force from the top onto the cell the central square will start to rotate and pull all holding elements in. the small connecting bars prevent the cell from a possible shearing

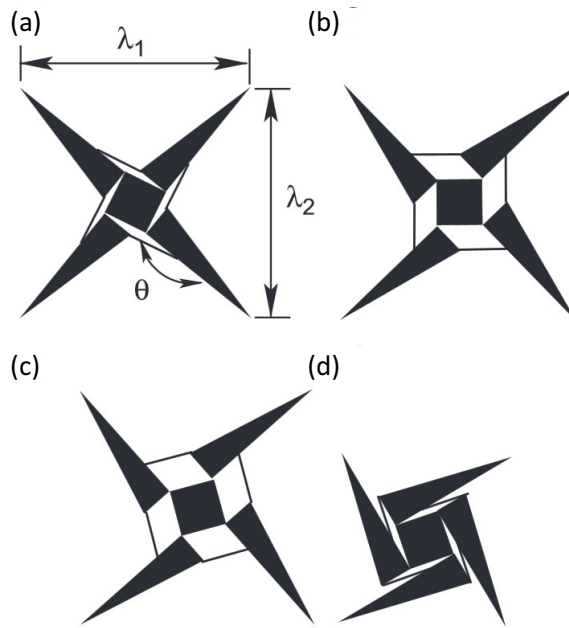


Figure 2.2: Basic dilational cell containing the principle basic elements following [105]. Here a central square rotates and thereby pulls the connected triangular parts inwards. The line connections hinder the design to shear and thus leave only one deformation possible.

leaving only a contraction equally from all sides open as a response to a force. This is only working perfectly in an idealized system and is still limited to a two dimensional design. Our work starts at this point taking this idealized model and translating it into a feasible three-dimensional design without losing too much of the performance. As a first step we have to transfer all connections between elements from a point like connection to a finite sized connection. This step is especially important at the connection of the square to the holding elements. This connection is defined by an overlap resulting from a distance d , which is defined starting at the corner of the square and reaching a distance d into the square, pointing to the square's center. The micro-structure with the appropriate dimension labels can be seen in Figure 2.3.

Within the unit cell of size a the size of the innermost block b needs to be set and the initial rotation of the block fixed, resulting into a holding element length h . The next design step is to ensure the rigidity of each element in an actual micro structure. For one constituent material two opposing properties are needed. On the one hand a stiff connection between elements is required, whereas on the other hand easily deform-able joints should connect the different parts of the structure. Especially the holding elements need to be stiff enough to withstand the forces induced into the structure, but on the other side small enough to deform easily at the joints. A width w was chosen such that the elements are still stable enough concerning our connection to the block d . At last the line-like rigid connections would have to be implemented into the design, preventing a possible shear deformation of the structure. The constraints for these elements could not

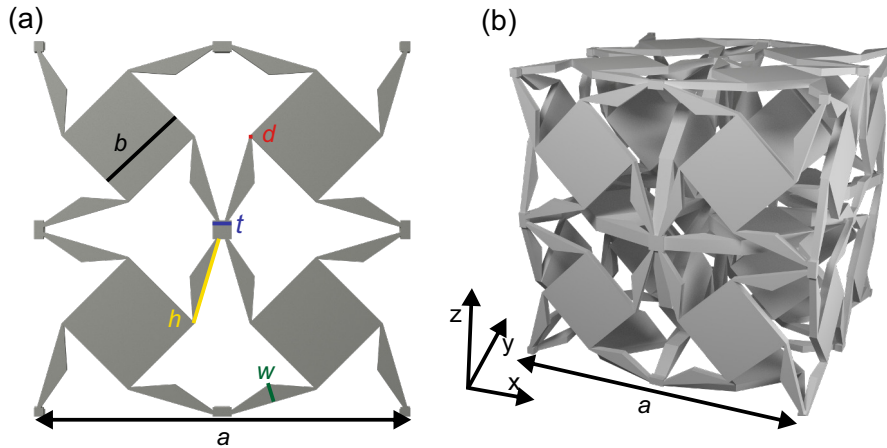
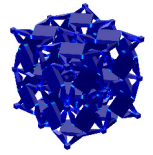


Figure 2.3: (a) The basic design shown in Figure 2.2 is adjusted and simplified to obtain a reasonable structural layout for fabrication. The structural parameters are indicated and as follows: Cubic lattice constant a , block size $b/a = 0.25$, width of the holding element $w/a = 0.048$, layer thickness $t/a = 0.05$, holder length $h/a = 0.235$, and the connection size d (here $d/a = 0.5\%$). (b) Blueprint of a 3D micro-structure representing a dilational unit cell. Here the faces of panel (a) have been copied and rotated to result into a voluminous cell. Reproduced in accordance to [68].

be fulfilled within the size and rigidity needed. As a result they are left away, causing the shear deformation to be a possible deformation. To prevent this and obtain a unimode material, the basic cell is mirrored along both axis to result in the scheme seen in Figure 2.3 panel (a). Here two neighboring cell elements rotate in the opposite fashion to prevent the cell from shearing. With this step the 2D design is finished and we need to extend this design into the third dimension. To create this 3D structure based on the basic motive, the design needs to get a finite thickness t . At the corners of each sub cell small blocks of side length t are added in order to connect the sub cells in a precise fashion and to allow for a tracing area during a measurement. Further we copy the cell orthogonal to the normal of the former layer and rotate the array along two axis resulting into the unit cell seen in Figure 2.3 (b). This basic unit cell now can be arranged in a simple cubic transnational lattice. One has to note that the underlying unit cell does not fulfill the cubic symmetry but rather is part of the symmetry group D_{2h} (Schoenflies notation). This is because the crystal has inversion symmetry, three mirror planes normal to the principle cubic axis, and only two fold rather than four fold rotational symmetry along these axis. This reduced symmetry is though only present in the structure and not in its properties as we will find with the aid of simulations. To evaluate the mechanical behavior of this structure and to make sure only one mode of deformation exists, at least in first order, numerical simulations have been performed in the dynamic regime to gain insight into the mechanical behavior and in the static regime to compare to the experiments.

2.1.4 Static Studies

We have performed static calculations on the basic unit cells using the software package COMSOL Multiphysics with the static solver for linear mechanics. The geometry is created using the build in CAD Comsol kernel and also the mesh is created using the internal meshing algorithm. The parameters of the geometry are as explained above (see Figure 2.3) and we have used the connection d at the inner block as a design parameter. To be able to find the behavior of the crystal we have imposed anti-symmetric boundary conditions mimicking an infinite extended crystal but allowing for a contraction or expansion orthogonal a direction with induced strain ϵ . Thereby we can find the Poisson's ratio of the infinite crystal along the simple cubic directions. This boundary conditions are realized by prescribing a displacement of two opposing facets to be the inverse of each other. This fixes the center of mass and still allows for a Poisson's ratio induced deformation. The prescribed displacement normal to the facet is assigned with a probe at one point of the geometry very close to the facet, measuring the displacement and assigning it to the whole facet. This is done for both pairs of facets orthogonal to the prescribed strain direction. This probe is directly used to find the Poisson's ratio of the structure by evaluating the prescribed strain and the induced strain in the two orthogonal directions. We find that the deformations induced are depending in the size of the connection d as one would have expected. Decreasing the relative connection dimension d/a comes closer to an ideal joint described in the theoretical design. We find that the results with a mesh size of about 90000 tetrahedral elements (with meshing parameters set to normal) show an error of only about 1% regarding the accuracy of the simulation and the direction dependence of the design. The deformation can be seen in the Figure 2.4 (a) for a $2 \times 2 \times 2$ array of the unit cell. The black arrows indicate the local displacement vector and the color coding represents the local absolute strain on the surface of the structure. The induced contracting strain modulus into the structure is $\epsilon = 0.01$ along the vertical direction. We can clearly see that the displacement vectors are pointing inwards from all directions just with a slightly changing modulus. The displacement vectors on the rotating cubes are actually not pointing to the center but rather have a certain angle to the center showing that the blocks rotate on top of the inward movement just as they are meant to do by the design. This simulation with a relative connection of $d/a = 0.75\%$ leads to a Poisson's ratio of $\nu = -0.79$ showing already a very negative value for the Poisson's ratio in these crystals. To compare to an experiment, where one is limited to a finite number of unit cells, we can find that sliding boundary conditions on the top and the bottom surface can be used to compare to a measurement on a finite cell still not preventing the only left mode of deformation, namely contraction. If one would fix the top and bottom's in-plane movement this mode would be suppressed and the structure would be hindered in its deformation probably leading to a reduced Poisson's ratio or even a fatal failure in an experiment.

In order to investigate a finite structure the above performed simulations have been repeated with changed boundary conditions. The facets where the strain is induced are set to be sliding and displaced only in the vertical direction, whereas the orthogonal directions are set to be free. To be able to compare the deformation to a measurement the vertical central and horizontal outer most cubes are taken as a deformation indicator

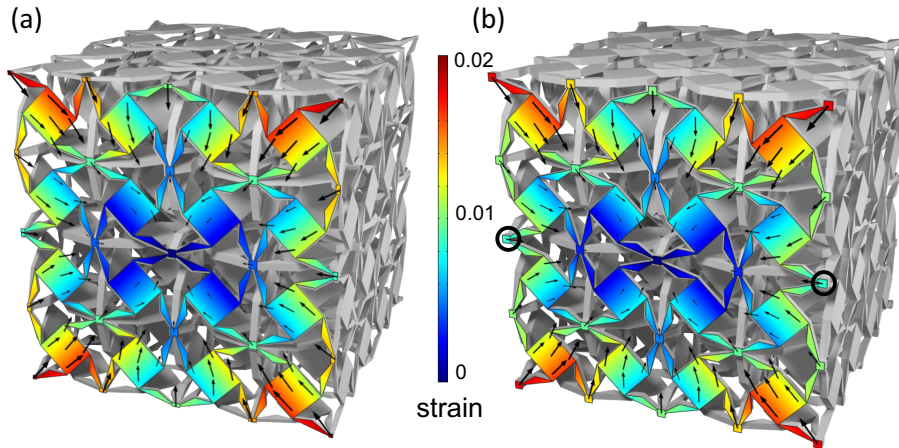
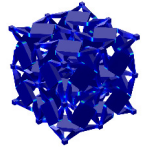


Figure 2.4: (a) Results of a static calculation imposing periodic boundary conditions onto an array of $2 \times 2 \times 2$ unit cells of a dilational material with $d/a = 0.75\%$ and $a = 4.8\text{cm}$. The arrows represent a scaled displacement vector of selected points on the front surface whereas the color scale represents the induced Strains. (b) The same but for a finite sized crystal with sliding boundary conditions on the top and the bottom and free boundaries on the sides. The black circles mark the tracking areas in the measurement. Reproduced in accordance to [68].

(see black circles in Figure 2.4 (b)). The here induced strains are again used to compute a Poisson's ratio leading to a slightly increased value of $\nu = -0.76$. This value is still very close to the infinite crystal and can be compared to measurement later on in this section. The dependence of the connection d/a with the resulting Poisson's ratio has been computed in the infinite crystal case for one unit cell and can be seen in Figure 2.9, where the Poisson's ratio retrieved from the static simulations is compared to the dynamic retrieval discussed next. One can already see a decrease in the Poisson's ratio with decreasing relative connection size d/a reaching very low and approaching the ideal dilational material ($\nu = -1$).

2.1.5 Dynamic Studies

In order to determine the dynamic behavior of this material and thereby we find the Poisson's ratio along the non cubic axis, we have performed dynamic band structure calculations. From these band structures we can determine the elastic constants of the material. These calculations allow for the phonon band structure of the dilational material to be determined and the wave-propagation along various directions to be observed. In order to obtain the band structures COMSOL Multiphysics is used and floquet-bloch periodicity is assigned to the boundary. The wavevector is used as a parameter to sweep through the brillouin zone and for each wavevector \vec{k} the first eigenfrequencies are searched. As the lowest bands carry the most important information for our purposes, the six lowest eigenvalues for each \vec{k} are computed. This allows to plot the band structure

as a typical tour through the k -space for cubic materials¹. Figure 2.5 shows two typical band structures for changing connection size d . The connection size is increased from $d/a = 0.5\%$ in (b), to $d/a = 5\%$ in panel (c). The constituent material used here has a Young's modulus of 1 GPa, a Poisson's ratio of $\nu = 0.4$, and a density of 1200 kg/m^3 corresponding to the experimental materials below.

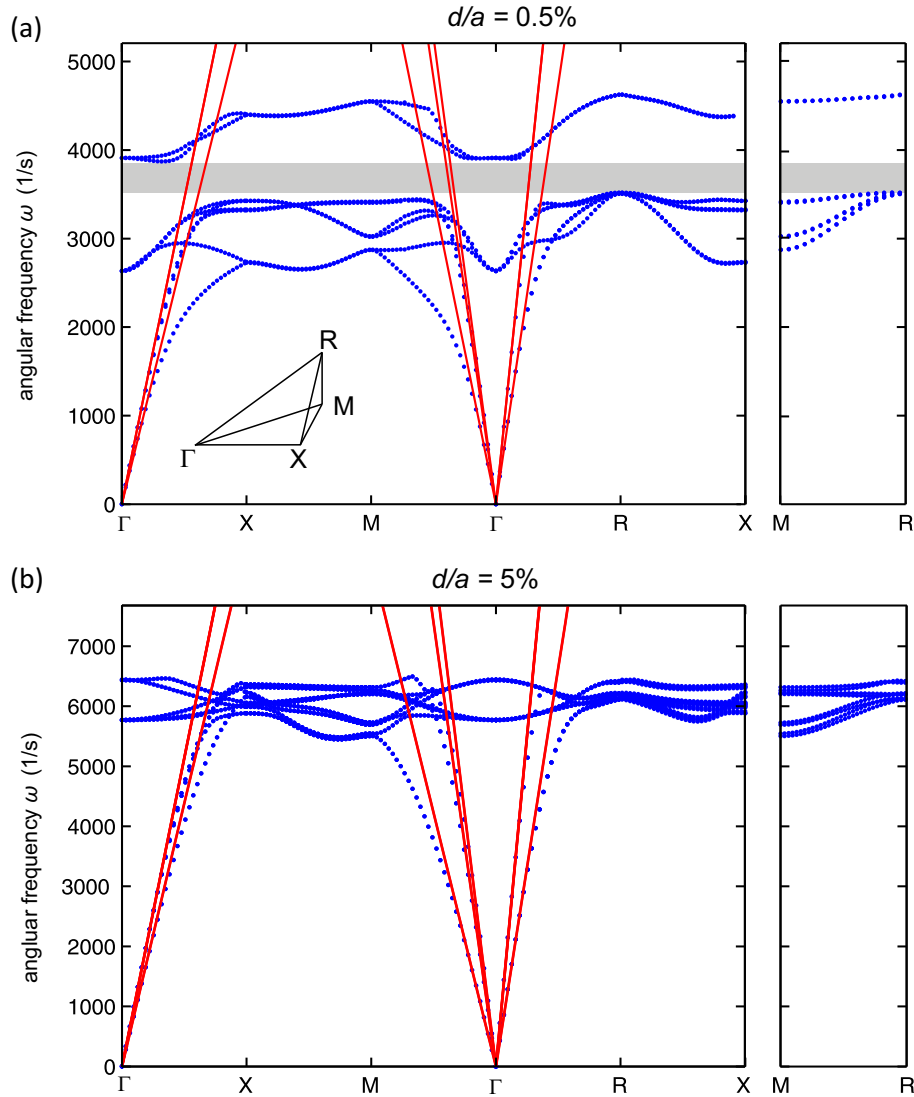


Figure 2.5: band structure calculations obtained for different connection sizes. The tour through the Brillouin zone (inset in panel (a)) is indicated on the x axis the obtained frequencies are indicated on the y axis corresponding to a unit cell size of $a = 4.8 \text{ cm}$ as in the experiments. The connection sizes are (a) $d = 0.5\%$ and (b) $d = 5\%$. In panel (a) a grey area is indicating a region, where no modes are present resulting in a complete three-dimensional elastic band gap. The red lines correspond to calculations for an effective medium with the retrieved material parameters. Reproduced in accordance to [68].

¹Here are only the lowest six eigenfrequencies evaluated.

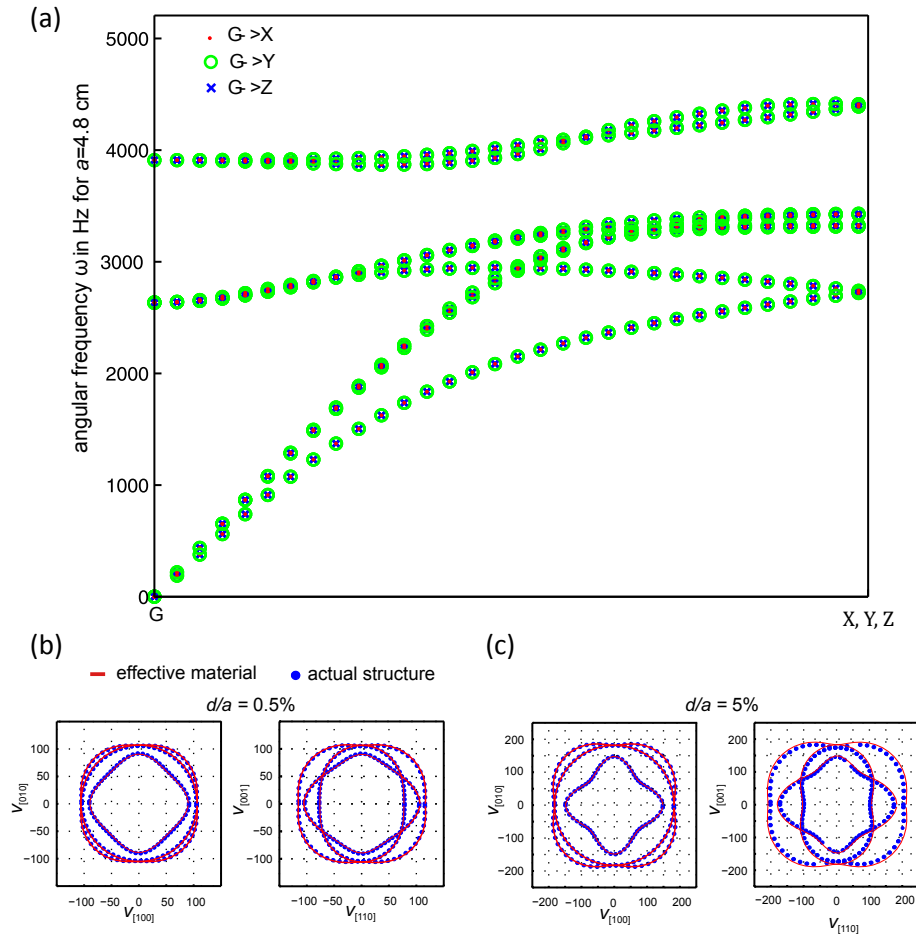
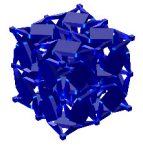


Figure 2.6: (a) Band structure calculations obtained along the three different cubic directions. One can see that no significant change in the band structure can be detected hinting onto the fact that the properties of the whole crystal obey cubic symmetry. (b)-(c) Velocity plots in different cubic plots for constant modulus of the wave vector $|k| = 0.01/a$ given in m/s. The blue dots are taken from a micro structure calculation and the red lines correspond to retrieved effective material descriptions. The radial length represents the velocity in the spanned plane. On the left the xy -plane is shown whereas on the right the plane spanned by the $[111]$ and the $[110]$ direction is depicted. (b) is for $d/a = 0.5\%$ and panel (c) is for $d/a = 5\%$. Reproduced in accordance to [68].

As the unit cell is not necessarily cubic in its properties (reminding ourselves that the crystal does not show cubic symmetry), we have performed band structure calculations along the basic simple-cubic directions to be able to determine possible deviations in the band structure depending on the direction. A deviation in the band structure would be linked to a difference in the elastic properties, and thus to an anisotropy. Figure 2.6 gives a good impression on how the cubic axis deviate in their behavior. As one can see in panel (a) the deviation in the behavior is nearly not detectable even for higher modes. This leads to the conclusion that although the crystal does not have cubic symmetry the underlying elastic properties do obey this symmetry within the evaluated precision. In the

panels (b)-(c) velocities for a certain wave vector modulus are plotted depending on the direction. The simple cubic directions coincide in their velocity profile and only directions not along these directions show deviations from these velocities. The red lines indicate a comparison with the effective medium description for the retrieved parameters. The agreement is extremely good leading to the conclusion that the material can be described by a effective cubic material. We can see that the deviation between the different directions gets less for the smaller connection hinting at a more isotropic behavior of the material for smaller connection sizes. As no significant deviations from a cubic material could be detected in the band structures, we can treat the material as a cubic material in the further considerations.

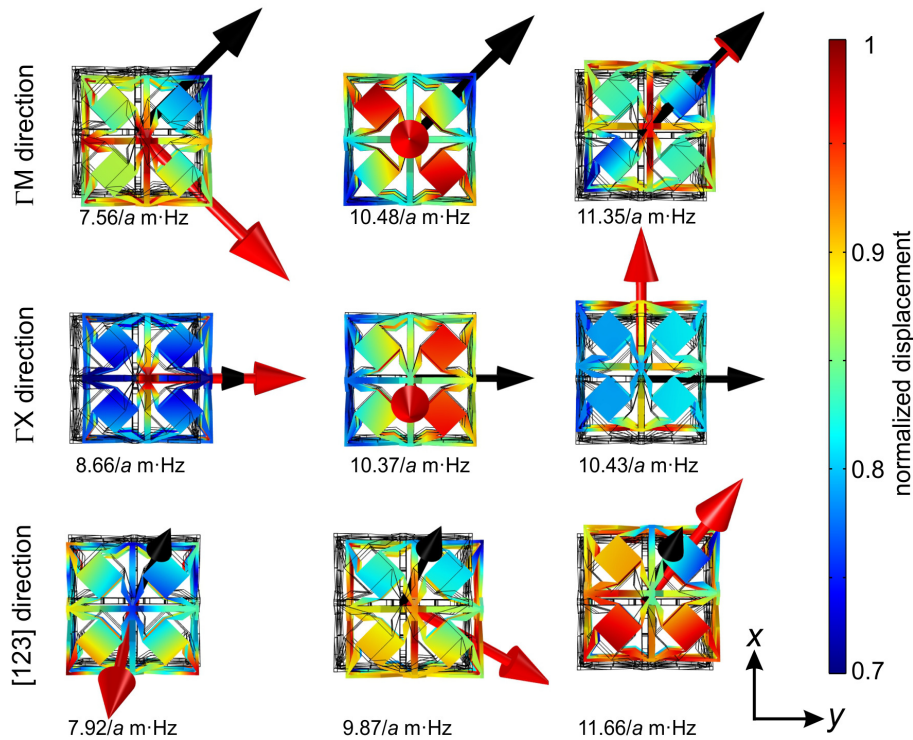


Figure 2.7: Mode shapes extracted from the band structure calculations at $k = 0.2/a$. The wave vector is indicated by the black arrow whereas the averaged displacement vector is given by the red arrow. The first three modes are depicted for a wave-propagation along three different directions namely the ΓM direction corresponding to the face diagonal used for retrieving the velocities, the ΓX direction along a simple cubic axis and the direction given by the Miller indices [1 2 3]. The deformation within one unit cell is represented by a color scale of which the average movement of the cell is subtracted. The corresponding frequencies are given below each mode. Reproduced in accordance to [68].

With the aid of these band structures we are able to find the velocities along the different directions and, taking into account the mode-shapes (see Figure 2.7), we use the retrieval of the entries of \mathbf{C} introduced at the beginning of this chapter. This allows to return to the elastic moduli and the Poisson's ratio along the cubic axis as well as for any desired

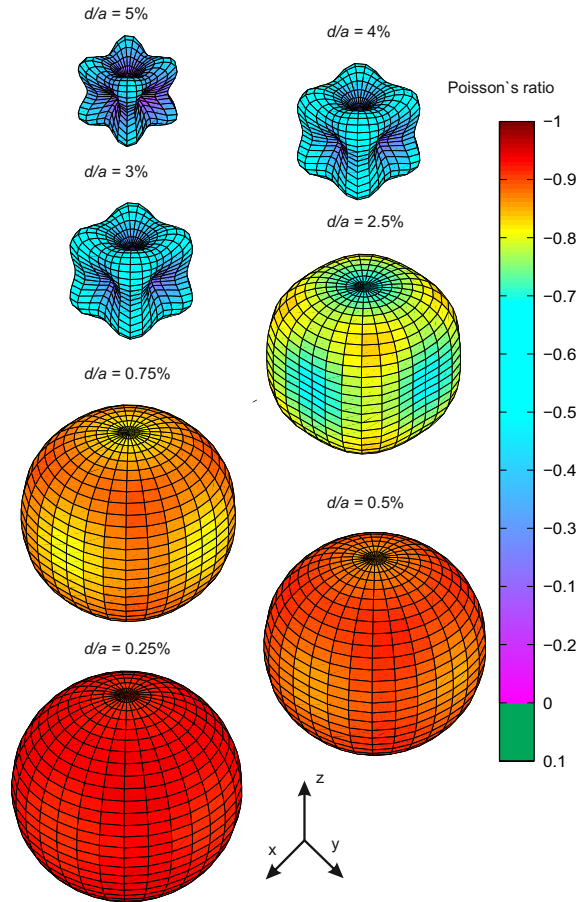
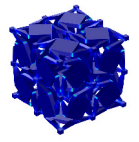


Figure 2.8: Polar diagram representing the effective Poisson's ratio as a radial component over the spherical angles representing the strain direction. As one can see the Poisson's ratio gets larger in the modulus approaching $\nu = -1$ with decreasing connection size d/a . The amplitude difference for one connection size of the Poisson's ratio gets smaller for decreasing d/a indicating a more isotropic behavior for smaller connections. Reproduced in accordance to [68].

direction. The table in the Appendix 1 gives the retrieved components of the elasticity matrix \mathbf{C} and the most common moduli.

With this information about the different materials, changing only the connection d , the Poisson's ratios can be found. A few different ratios of the connection size d/a are selected and illustrate the dependence of the Poisson's ratio on the direction. As we have already seen in panels (b)-(c) of Figure 2.6, the materials are not isotropic for larger connections but are getting more isotropic for smaller connections. This general trend is expected for the Poisson's ratio as well, especially as isotropy is forced as one approaches the ultimate value of $\nu = -1$ along the cubic axis (see section 2.1.1). In order to make the data interpretation easy we have plotted the direction dependent modulus of the Poisson's ratio as a radial component in a polar plot, where the polar direction represents the initial strain direction. This representation can be seen for different connection sizes in Figure 2.8. If one has a closer look onto the structure of the Poisson's ratio plots one finds

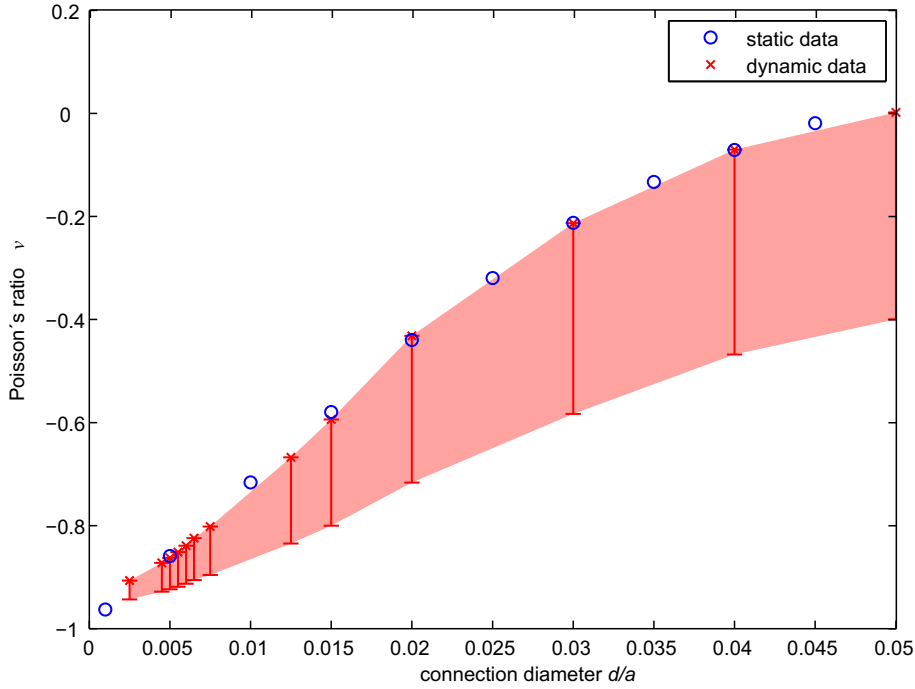
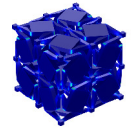


Figure 2.9: Poisson's ratio span indicating the maximum and minimum plotted over the connection size d/a as evaluated from the direction dependent Poisson's ratios. The red area indicates the Poisson's ratios possible along various directions. The blue circles are representing the static data. The upper bound of the red bars indicates the Poisson's ratio along a cubic direction extracted from the band structures. Reproduced in accordance to [68].

that the Poisson's ratio along the cubic axis (along x , y , or z) is actually the highest one. This means that if one applies a strain not along the cubic directions one finds even lower values than we could find in the static calculations. The isotropy of the structure can in this fashion be easily determined and one can intuitively estimate that a connection size less than $d/a = 1\%$ is needed for a modest isotropy. To get a better feeling for the actual Poisson's ratios obtained for the different connections we have extracted the maximal and minimal value for each connection size. This gives a hint on the span of Poisson's ratios within the structure and a better comparison to the static calculations. The obtained data is plotted in Figure 2.9. Here the static data is comparable to the dynamic evaluation of the Poisson's ratio. The Poisson's ratio decreases for both computations with decreasing relative connection size d/a and we can obtain benchmark values with Poisson's ratio values below $\nu = -0.8$ for connections smaller than $d/a < 0.75\%$ in an infinite crystal. As the static data seems to extrapolate towards $\nu = -1$ the dynamic data rather seems to bend over and does not reach this minimum. We assume this is to the finite thickness of the layers t which hinders a perfect connection and thus obtaining perfect dilations. To compare the values obtained from the static calculations for an infinite crystal with the ones obtained by the aid of the band structure calculations we have picked one example corresponding to the measurements (see below). For a connection size of $d/a = 0.75\%$ The static calculations lead to a Poisson's ratio for the crystal of $\nu = -0.79$ whereas the



2.1. Unimode Materials

minimum of the dynamic calculations returns a value of $\nu = -0.895$ along the $[1\ 1\ 1]$ direction as can be seen already in Figure 2.8. This shows that a direction dependence of the Poisson's ratio is still present and the material is still not isotropic. For a comparison of the simulated data to a measurement, finite-sample calculations have been performed returning an effective Poisson's ratio (considering only the encircled cubes in Figure 2.4 (b)) of $\nu = -0.76$. This value is smaller than for the infinite crystal leading to the conclusion that one needs more than $2 \times 2 \times 2$ unit cells to obtain the infinite crystal behavior. Additional calculations have shown that the convergence is very slow, as one needs at least a few ten cells in each direction which could neither be simulated nor fabricated at the time. This shows that only a simulation of the infinite crystal and a structure corresponding to the actual sample, obeying the boundaries obtained in the measurement, can reveal the performance of an actual material design.

2.1.6 Fabrication and Measurement

In order to fabricate the structures presented above we used two different methods of 3D fabrication. For macroscopic samples we used 3D ink-jet printing method whereas we used a DLW approach for the microscopic samples. Both of these fabrication techniques require additional post-processing steps to achieve the desired samples.

3D printing

In this section we will discuss the fabrication of the macroscopic samples of the dilational metamaterial with a 3D printer. We used the commercially available 3D printer Objet30 as described in the section 1.3.4. The samples are printed with the ink 'FullCure850 VeroGray' for the structural elements of the printed sample and the support material 'FullCure 750 Support' for structures, supporting the geometry while printing. As determined in additional measurements the constituent polymer has a Young's modulus in the range of $E = 0.7 - 2$ GPa [106]. The support structure preset has been changed, to only print support material rather than a mixture. This is necessary as it turned out to not be possible to remove the composite in complex and fragile samples completely, and only the Support material can be etched from the samples. For our structures no influence in the stability while printing and no further influence on the resulting quality of the samples themselves is observed. The structures are fabricated based on a STL files directly exported from the simulations performed in COMSOL Multiphysics. The dimensions of the structures is chosen to exploit a unit cell size of $a = 4.8$ cm. This allows to resolve the connection d while using the optimal geometry size for the printer. The other geometry parameters are as given in Figure 2.3, and the connection size is chosen to be $d/a = 0.75\%$, limited by the resolution of the 3D printer. A finalized structure can be seen in Figure 2.10. The structure is then detached from the build tray and cleaned in a bath of NaOH base until all the left over support material is dissolved. To improve the cleaning process the sample is immersed into the base within a beaker glass approximately the size of the sample, and on a small post to allow for stirring the base using a magnetic stirrer. After the base the sample is transferred into a water bath and flushed there for

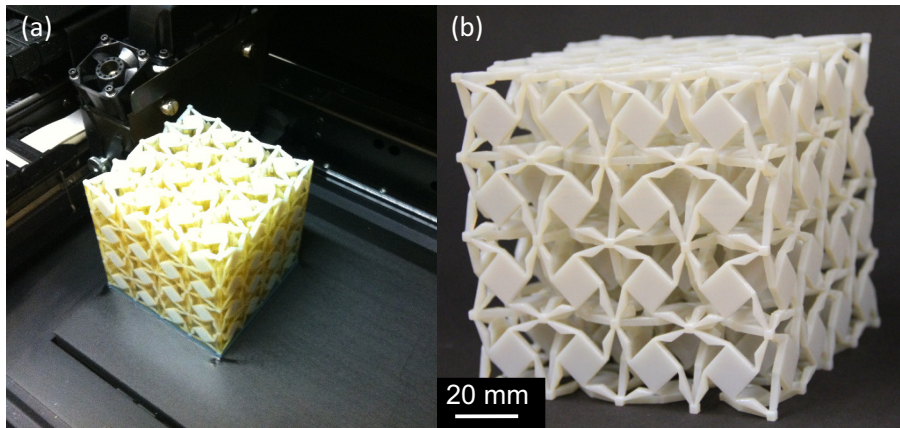
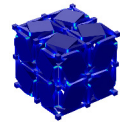


Figure 2.10: (a) Macroscopic sample directly after the printing process. The structure is still embedded in the support structure and attached to the building tray. (b) Sample after the cleaning process.

several hours to make sure no residual base is left on the sample surface. After a final rinse-of with water the sample is measured directly, as it turns out that the underlying polymer hardens significantly and turns into a more brittle material reducing the elastic regime of the material after a few hours. Apparently the NaOH base does not only resolve the support material but also attacks the plasticizer in the VeroGrey to some extent. The finalized structure can be seen in panel (b) of Figure 2.10.

The sample is then placed between two metal plates and a linear stage is used to exert a displacement and thus a resulting strain onto the sample along the vertical direction. During the measurement a force cell attached below the linear stage and the upper metal plate recorded the exerted force. The whole process is monitored by a camera setup recording a movie for later evaluation using the cross-correlation approach. The camera used is a Canon EOS 550D taking movies in Full HD quality (1920×1080 pixel with 24 frames per second) with an objective lens Tamron SP 70-300 mm f/4-5,6 Di VC USD. The camera is placed at a distance of about 1.5m in order to get the best resolution and still have a small amount of perspective in the image to approach a telecentric image. This reduces aberration errors due to distortions of the lens. The wet sample is placed between the two metal plates to reduce friction on the stamp and the bottom plate allowing for a contraction of the sample and mimicking the sliding boundary conditions simulated before. While lowering the stamp towards the fixed plate the force data as well as the movie are recorded. After the experiment the movie is used to evaluate the displacements of the corners with the cross-correlation approach explained in the introduction. The displacements along the two different directions are then evaluated like in the simulations. The strain along the vertical direction could be obtained by tracking the top and the bottom of the structure. To compare the measurement to the simulations the strain at the central outer blocks is taken as a measure. For each of the strains multiple markers are tracked and averaged afterwards. The measurements are performed in a consecutive fashion and consisted of a step-wise increasing strain amplitude and releasing steps to the initial position. The result of the strain measurement can be seen



2.1. Unimode Materials

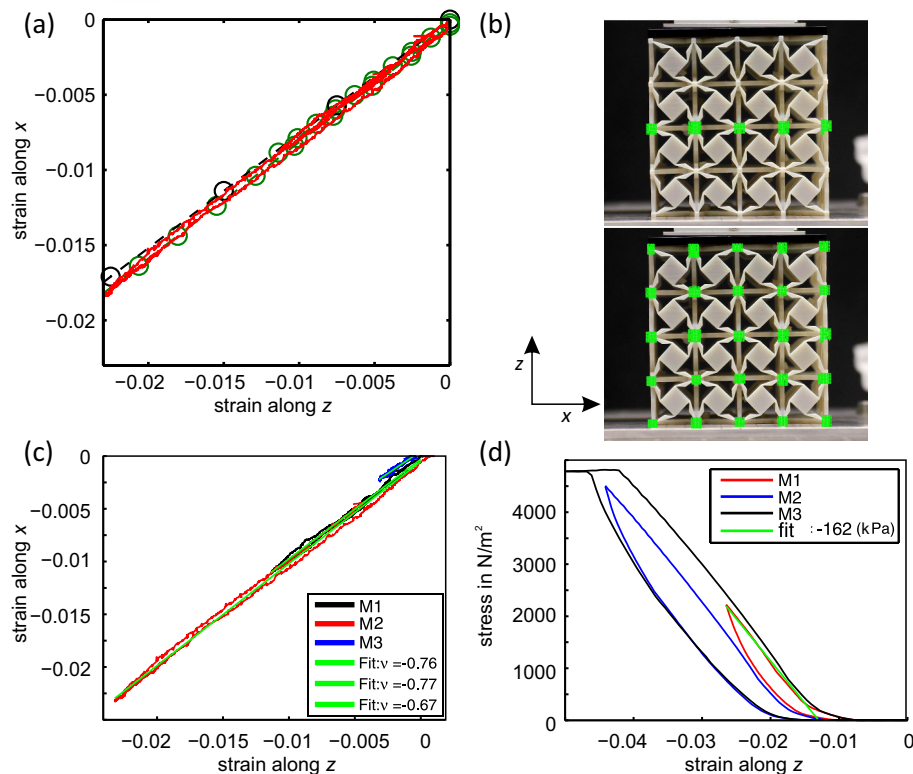


Figure 2.11: (a) Measurement of the strain relations along the two measured directions. As the strain is employed along the z -direction the induced strain along the x -direction is evaluated. (b) Measurement images with an overlay of the marker positions. The images are evaluated in the x -direction in the upper image and along the z -direction in the lower image. (c) The same measurement data as shown in (a) but with two additional measurements added. (d) The stress curves corresponding to the data shown in (c). Reproduced in accordance to [68].

in Figure 2.11. Here the strain along the x -direction is plotted over the strain along the z -direction. The measurement (red lines) is taken in two cycles each consisting of one loading and one unloading ramp. One can clearly see that no significant deviation can be found within the measurements. The green circles correspond to a fit to the red lines leading to a Poisson's ratio of $\nu = -0.76 \pm 0.02$. This data fits to the expected value for a connection size of $d/a = 0.75\%$ as one can deduce from the simulation results depicted in black. A comparison to a Poisson's ratio for the infinite crystal yields $\nu = -0.79$. Plotting the measured stress over the measured strain, one obtains the Young's modulus of the effective material (see Figure 2.11 (d)). Here three different measurements with increasing strain rate are shown. As the experimental setup is readjusted every time the strains do not match at their starting points. As the strain rate increases the stamp is at first not in contact with the sample, then at some finite strain starts to make contact until all of the structure is touched, and finally the whole structure is subject to one given strain. This is why the curves start at zero force and have a region with slowly increasing force until the stress strain curve gets linear. A fit to the data corresponding to the measurement discussed beforehand (M1) is fitted, and results in an effective Young's

modulus of $E = 0.16$ MPa. Comparing this to the evaluation done based on the band structure calculations leads to a Young's modulus of $E = 0.33$ MPa as can be seen in Table 1. There is some significant deviation in the Young's modulus but one has to keep in mind that the properties of the constituent material show some significant uncertainty and change while drying, leading to an approximate agreement between the simulation and the measurements. We have thereby shown that dilational or unimode materials can be approximated and tailored by this means and that an actual experiment yields extremely low values for the Poisson's ratio of this metamaterial.

Direct Laser Writing

The macroscopic samples shown beforehand validate the dilational behavior of our blueprint and could be measured with satisfying accuracy. Unfortunately although the effects are size independent one would call a crystal of only 2 cells along each direction and with a cm lattice constant not quite a material jet. This brings up the question whether one could fabricate many more cells and lattice constants few orders of magnitude smaller. Therefore, we have utilized a fabrication technique called direct laser writing introduced in section 1.3.2 of this thesis. There we use the commercially available system Photonic Professional GT. Here a liquid phototresist is drop-casted onto a substrate made out of silicon which has been diced to a size of 22×22 mm. The used resist is called 'IP-Dip' and is sold by the same company. To build up a structure the galvanometric mirror scanning technique is used to scan a laser beam impinging from different angles on the rear side of the objective, leading to a lateral scan of the focused beam in the focal plane of the objective. The objective lenses have a numerical aperture of $NA = 1.3$ for lens 1 and $NA = 0.8$ for lens 2 by Carl Zeiss, see also section 1.3.2. The structural data is taken from the COMSOL files again but is replicated using the software Blender. The tracking blocks are removed from the geometry. The writing speed is set to be 20 mm/s and the structure is written in skywriting mode switching the laser on and off during the continuous scanning rather than writing each line-segment individually. The geometries are programmed for different unit cell sizes and different structure's aspect ratios. For the samples written with the lens 1 a slicing of 200 nm in the lateral direction and 300 nm in the axial direction is used to fabricate samples with a unit cell size of 35 μ m. Structures written with lens 2 have a slicing of 400 nm and 800 nm respectively with a unit cell size of 180 μ m. All samples have been developed in isopropanol and acetone and have been dried with the super-critical point dryer avoiding extensive forces while drying. The resulting structures can be seen in the Figure 2.12. Here the good sample quality can be seen, and within the large overall dimensions even small features are fabricated in a reproducible fashion.

Nevertheless the microscopic samples could not be measured accurately enough to extract a Poisson's ratio. As sliding boundaries could not be imposed on this length scale fixed boundary conditions would have to be assumed excluding the pure dilational deformations of the cells. Simulations on this level could not be obtained for all three dimensions due to memory size limitations of the server systems used. Also one would have to resolve the unit cells and actually the corner-points of the unit cells to be able to trace a sens-

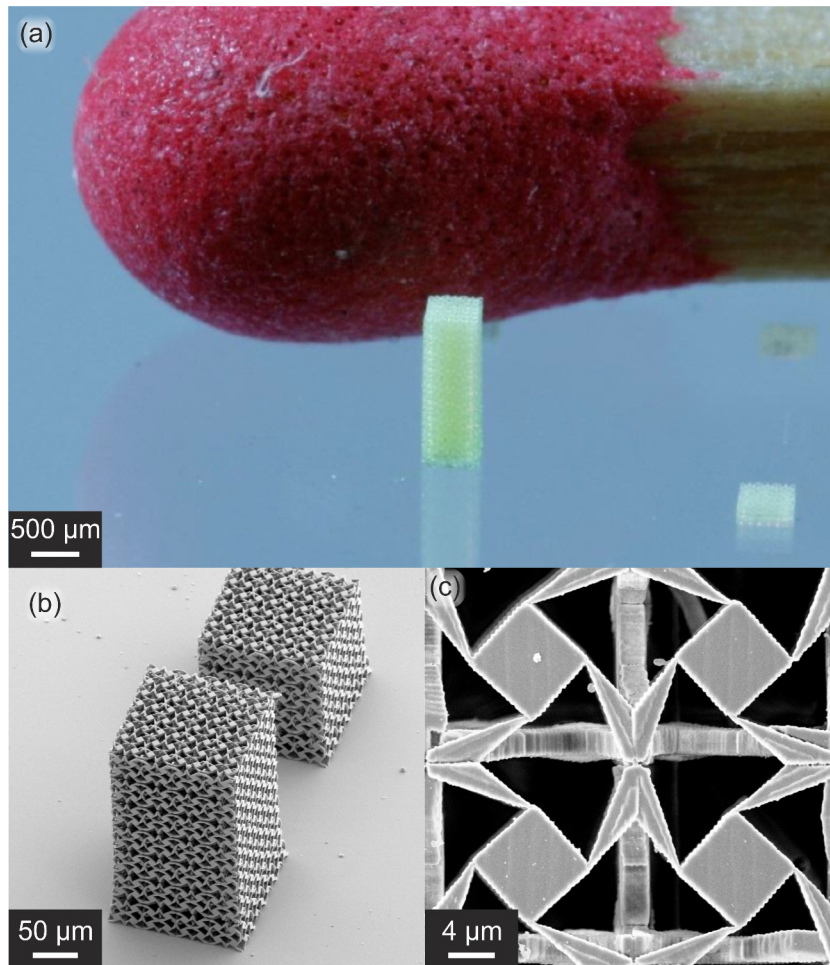
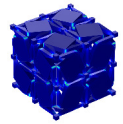


Figure 2.12: (a) Photograph of a microscopic sample fabricated with the DLW setup using the lens 2. Here the structure consists of $3 \times 3 \times 9$ unit cells each with a lattice constant of $a = 180\mu\text{m}$. (b) SEM image of a samples fabricated with lens 1 and a lattice constant of $a = 35\mu\text{m}$ The two structures have a aspect ratio of 1:1 and 2:1 allowing to estimate the change in properties depending on the height and the aspect ratio. (c) Zoom into the structure seen in (b). Here the accuracy as well as the substructure can be seen and determined. Clearly the central blocks as well as the holding elements can be identified and the size of the connecting elements can be estimated. Reproduced in accordance to [68].

full movement or deformation at all. As these requirements could not be fulfilled, the microscopic samples still give hope for the future as fabrication techniques improve. This techniques could allow to fabricate large quantities of of the metamaterial and approach a dilational material consisting of thousands of cells. This could be used in various ways starting from packaging and improved protection of sensitive objects over shrinkable devices not changing their shape to adjustable and reusable filters in micro-fluidics.

To sum up this section we have used a theoretically proposed two dimensional blueprint of a dilational material and have reduced the design to be fabricated out of one material. This basic design is then transferred into three dimensions and numerically proven to tailor

a dilational material approaching $\nu = -1$ with decreasing a geometrical parameter, the connection dimension d , towards zero. Simulations performed dynamically lead to band structures and a procedure is incorporated to retrieve all independent elasticity matrix entries. This elastic information is used to evaluate the angle dependent Poisson's ratio. These simulations could be verified with static simulations and have shown a Poisson's ratio gaining isotropy as well as approaching $\nu = -1$. Static simulations have helped to compare the infinite crystal properties to a finite sized sample. This sample could be fabricated using a commercially available 3D printer and measured imposing a finite strain into the sample. Via a cross correlation approach the deformation and Poisson's ratio of the material is determined. A value of $\nu = -0.76$ is measured and a comparison to the infinite crystal leads to a Poisson's ratio of $\nu = -0.79$ for this structure. Microscopic samples are fabricated using a novel DLW approach allowing for structures with as many as 81 unit cells and a structure height of 1.6mm.



2.2 Pentamode Metamaterials

The previous section has discussed dilational materials that have only one easy mode of deformation. Within this section, we will present a mechanical metamaterial which is in some fashion just the opposite of the dilational material. Instead of one easy mode of deformation, it has five of them and only one principle deformation under which it is stable as discussed in section 1.1.2. This is why it is called pentamode material [107]. This material can be seen as the solid mechanical equivalent of a liquid, as the only stable loading configuration is hydro-static compression. All deformation modes related to a shear deformation are unstable. The origin of this behavior is the vanishing shear modulus of this material.

During this section the theoretical background of this material class in the ideal form is discussed and a feasible design to tailor the ideal pentamode metamaterial is presented. The evolving blueprint can be validated using numerical simulations in the static as well as in the dynamic regime. It is shown that it is possible to fabricate these structures and tailor not only their B/G ratio but also introduce anisotropy into these structures. At last it is shown how to reduce the filling fraction in order to achieve ultra lightweight structures and tailor the mass density and the bulk modulus independently. Parts of the chapter have been published and figures are in accordance to or taken from the publications: [106, 108–110]. Some of the data shown has been obtained by Muamer Kadic, Aude Martin, and Robert Schittny working in our group.

Bimode Materials

Let us start the discussion with a the two dimensional case of a pentamode material, the so called bimode material². For such a material, due to the reduced dimensional space, two of the three modes of deformation are considered easy. The bimode material can be easily deformed in two shear deformations and only the remaining compression mode is stable. The corresponding elasticity is described by the following equation just as in 3D.

$$\sigma = \mathbf{C}\epsilon \quad (2.17)$$

Here the \mathbf{C} tensor can be written in a matrix form, described by:

$$\begin{pmatrix} \sigma_{11} \\ \sigma_{22} \\ \sqrt{2}\sigma_{12} \end{pmatrix} = \frac{E}{1-\nu^2} \begin{pmatrix} 1 & \nu & 0 \\ \nu & 1 & 0 \\ 0 & 0 & (1-\nu)/2 \end{pmatrix} \begin{pmatrix} \epsilon_{11} \\ \epsilon_{22} \\ \sqrt{2}\epsilon_{12} \end{pmatrix}. \quad (2.18)$$

In this equation, \mathbf{C} can be expressed by the bulk and shear modulus and be diagonalized leading to[107]:

$$\mathbf{C} = \begin{pmatrix} 1/\sqrt{2} & -1/\sqrt{2} & 0 \\ 1/\sqrt{2} & 1/\sqrt{2} & 0 \\ 0 & 0 & 1 \end{pmatrix} \cdot \begin{pmatrix} 2B & 0 & 0 \\ 0 & 2G & 0 \\ 0 & 0 & 2G \end{pmatrix} \begin{pmatrix} 1/\sqrt{2} & 1/\sqrt{2} & 0 \\ -1/\sqrt{2} & 1/\sqrt{2} & 0 \\ 0 & 0 & 1 \end{pmatrix}. \quad (2.19)$$

²For an illustration and a discussion on the properties see Section 1.1.7.

This diagonal form allows us to determine the modes of deformation. In the case of vanishing shear modulus two entries within this matrix are purely shear dominated and thus vanish, whereas one entry is linked to the bulk modulus, and stay's finite.

This behavior has been discussed e.g. on honeycomb lattice structures [111, 112] as well as in a metal lattice mimicking the behavior of water [113]. Here the combination of a metal lattice and air is tailored to have the effectively same elastic moduli and density as water. Into this layout anisotropy, depending on the design parameters used [112], can be induced. These structures have in principle the same behavior than a pentamode material except for the dimension. Bimode materials can be classified in the same sense as pentamode materials, and thus are not discussed in detail. Within this thesis bimode materials occur in the lattice transformation cloak discussed in Section 3.2.

2.2.1 Structural Design for Pentamode Materials

The proposed ideal design [107] for a three dimensional pentamode structure is consisting of cones arranged in a fashion, that they are connected by point connections at the atomic sites of a diamond lattice. An extended fcc unit cell can be seen in Figure 2.13 (a). The connections of these cones are defined to translate only forces along the directions of the bars and can not support any other forces. For a compressive deformation the bars and connecting tips have to be deformed, leading to a finite force and thus a finite bulk modulus. Bending one of the cones at the connection with respect to the other cones takes ideally zero force and thus no shear force and no shear modulus is present for this material. The blueprint of the unit cell translates to an effective material which is only mechanically stable under hydrostatic compression. A material is called stable if a finite force leads to a finite deformation in the material. Every other kind of force, except for a homogeneous pressure from all sides, will lead to an infinite translation as an ideal pentamode material has strictly zero shear modulus. The effective behavior can thus be described only by the bulk modulus. In principle it is possible to generate any arbitrary elasticity tensor as a superposition of many different pentamode materials (allowing for mode couplings of these) [17, 107]. The perfect pentamode material is not stable as even a unidirectional force, e.g. gravity, would lead to an unstable deformation, thus the material would simply flow away. To overcome this instability, the initial suggestion [107] proposed is to fill the voids between the cones with a softer material and thus generate a shear modulus to effectively stabilize the material.

The abstract proposal for an ideal pentamode structure cannot be simply fabricated as it is impossible to realize point connections supporting only one force along one connection. This brings us to the consideration of what happens if one makes the connection finite with regard to the modes within the material. To achieve this we have come up with a design as shown in Figure 2.13.

The double cones of length h connect two lattice sites of the diamond lattice and have a larger diameter in the center of the connection of size D . The connections at the lattice sites is made finite and has a diameter of d . The left panel shows the ideal version of the extended fcc (face-centered-cubic) unit cell which can be translated along the simple



2.2. Pentamode Metamaterials

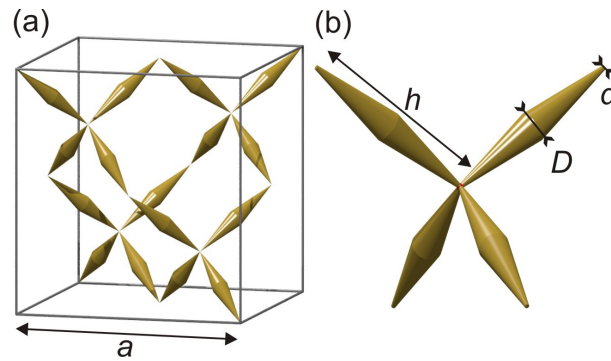


Figure 2.13: (a) Ideal design of a pentamode metamaterial. Here the double cones are arranged to touch each other at points on the atomic sites of a diamond lattice. (b) Our design of a pentamode metamaterial. The double-cones touch each other at finite sized connections d and have a larger diameter of size D in the center between two lattice points. Previously published in [108].

cubic axis to build up a crystal. This means that the relation between the length of the double cones and the unit cell size is fixed and given by:

$$h = \frac{\sqrt{3}}{4}a, \text{ or } a = \frac{4 \cdot h}{\sqrt{3}}. \quad (2.20)$$

The reduced unit cell and thus the primitive cell as shown in Figure 2.21 contains only four of the double cones. Both unit cells will be discussed in this section as some principles are easier to understand in one or the other description. In this blueprint we have two independent variables to consider for a certain lattice period a , namely the larger diameter D and the smaller connection diameter d . Both parameters in relation to the lattice period have an influence on the material properties as the stiffness of the material is determined by the thickness of the cones. The main key feature is the ratio of the two diameters though. The smaller the connection diameter is compared to D and the lattice constant a , the more pronounced the pentamode behavior will be as it approaches the ideal proposal with zero connection size d . All of these considerations take only one constituent material into account. Changing the underlying material properties the results can be scaled by e.g. the constituent material's Young modulus.

2.2.2 Static Studies

We have already given a general explanation on how this material design might work and why it has a pentamode-like behavior. To get a better feeling on how well this concept works and how close one can get to the ideal pentamode behavior we have performed numerical simulations testing the material properties in a static fashion. The simulations have been performed in COMSOL Multphysics in the static mechanics module. We have assumed finite connections d and have varied both parameters d and D . As a constituent material we have used a Young's modulus of $E = 3 \text{ GPa}$ and a Poisson's ratio of $\nu = 0.4$. The Poisson's ratio of the constituent material is nearly not influencing the result of the

simulations, whereas the Young's modulus can be scaled to any desired value and the results scale in the same fashion. This is a direct result of the linear equations taken into account. The ratio of the resulting bulk and the shear modulus is considered as the figure of merit (FOM) concerning our achievement of pentamode materials. This consideration even cancels out the Young's modulus dependence to first order and only the design determines the FOM.

To be able to determine the bulk modulus of the material, the definition of the modulus and thus the volume change under hydro-static pressure is applied. Therefore we have exerted a force on all six sides of a cube along the normal of the faces. Within the cube a crystal consisting of $N \times N \times N$ fcc unit cells is placed and intersected, so that forces act only on the pentamode material. The simulations are performed with up to $N = 5$ unit cells along one direction, resulting into a total of 125 unit cells for the full crystal. There have been nearly no differences between the $N = 1$ and the $N = 5$ case such that we are confident that we compute the bulk properties of the material. The mesh has been chosen such that the convergence of the results is sufficient, resulting in about 10^6 tetrahedral elements. The shear moduli have been obtained by a shear loading, fixing the displacement vectors on one face of the cube to $\vec{u} = 0$ and loading the material at the opposing facet with a force orthogonal to the normal, so along a simple cubic direction not coinciding with the normal. The resulting displacement leads to the shear modulus via its definition. The resulting dependence on the small connection of the bulk and shear modulus is depicted in Figure 2.14. One can clearly see that both moduli decrease as one reduces the connection size d in panel (a). The reduction of the bulk modulus is less severe compared to the shear modulus. In the limit of $d \rightarrow 0$ the shear modulus approaches $G \approx 0$ whereas the bulk modulus stays finite. This is just what we have expected from the theoretical design. In the second panel the ratio of the bulk and the shear modulus is plotted. The trend that the ratio is larger for smaller connections d can now clearly be seen. The B/G ratio actually increases dramatically for $d \rightarrow 0$ resulting in a nearly perfect pentamode material. To be able to estimate the performance by the absolute numbers of the B/G ratio we have to compare them to the values of normal materials. Gold has for example a $B/G = 13$ and some rubber materials, being the closest to pentamode materials, get into the range of $B/G \approx 30$ [114]. Our design can beat this values even for nearly rod-like cylinders ($d \approx D$) rather than cones. For realistic and possible to fabricate values of d we can reach values between $[10^2 < B/G < 10^4]$. Even smaller values are hard to fabricate and will resemble the ideal pentamode design to such a high degree that they would literally flow away and be destroyed by small forces. The black line in panel (b) is a fit revealing the proportionality of $B/G \propto 1/d^2$ for small d .

To evaluate the dependence of the double cone's larger diameter we have performed corresponding simulations for a specific choice of d . The results are shown in Figure 2.15. Here, the bulk and shear modulus as well as their ratio are plotted versus the larger cone diameter D on a logarithmic scale. One can see in panel (a) that the material gets softer for smaller connections D but the effect is less pronounced than for a changed d . Also the difference in the dependence between the bulk modulus and the shear modulus is smaller. Plotting the ratio of the moduli brings up the dependence of the FOM with regard to D .

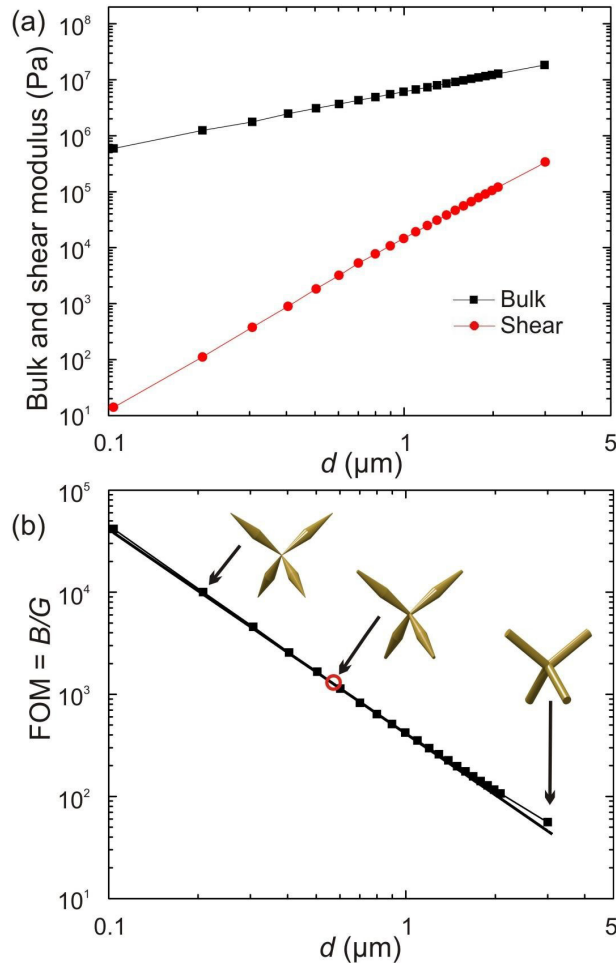


Figure 2.14: Results of the static calculations for changing connection diameter d , plotted on a double logarithmic scale. (a) Effective bulk and shear modulus for a geometry of $a = 37.3 \mu\text{m}$ and $D = 3 \mu\text{m}$. (b) The figure of merit B/G as a function of the connection size d . The black lines are corresponding to the fit given in equation 2.21. Previously published in [108].

A fit returns a proportionality of $B/G \propto 1/\sqrt{D}$. One reason why the two moduli change in a comparable manner is that one does not only change the larger diameter, but rather also the angle of the cone at the smaller diameter leading to a reduction or an increase of stress concentration in the tips. Using the data to find a global fit with the two already determined dependencies, one can find that the B/G ratio roughly scales like

$$FOM = B/G \approx 0.63 \left(\frac{h}{d}\right)^2 \sqrt{\frac{h}{D}}. \quad (2.21)$$

The simple formula can be used to tailor a material in which one chooses e.g. the B/G ratio needed for a certain application and can find a design fulfilling this equation. To further evaluate the dependence of the constituent material on the B/G ratio, various tests have been performed, for example changing the Poisson's ratio of the constituent from 0.4 to 0.1. The resulting B/G ratio increases by about 20%. Changing the Young's

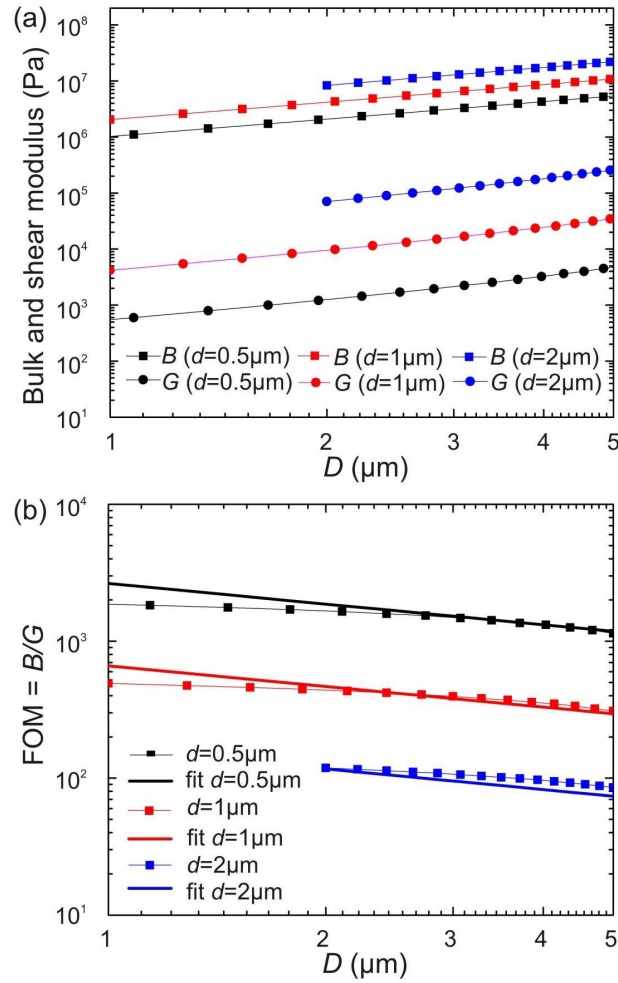


Figure 2.15: Evaluations of the numerical calculations performed on the static pentamode materials. (a) Bulk and shear modulus over central connection diameter D for three choices of connection diameter d . (b) FOM as a ratio B/G for the same connection diameters d as in panel (a). Previously published in [108].

modulus and the Poisson's ratio (e.g. $E = 1220$ GPa and $\nu = 0.2$) results in no more than a 10% change on the B/G ratio. This shows how stable the design is with regard to changing the constituent material revealing the universality of the approach.

In order to prove that such structured materials can be manufactured by the aid of state-of-the-art DLW, we have fabricated pentamode materials using DiLL DLW. Here, cones are programmed individually using MATLAB as closed spirals changing their diameter along the spiral axis. These cones are then assembled to fcc unit cells in three dimensions. A specific tour through the fcc cell had to be applied in order to connect the double-cones at their tips, reducing the possible drift and offset while writing. This procedure led to the most accurate structures and smallest feature sizes. An NA = 1.3 objective and the piezoelectric stage are used to scan the voxel. The samples are developed after the writing procedure in acetone and dried using the super critical-point drying procedure. The resulting SEM micrographs can be seen in Figure 2.16 and Figure 2.17. In Figure 2.16

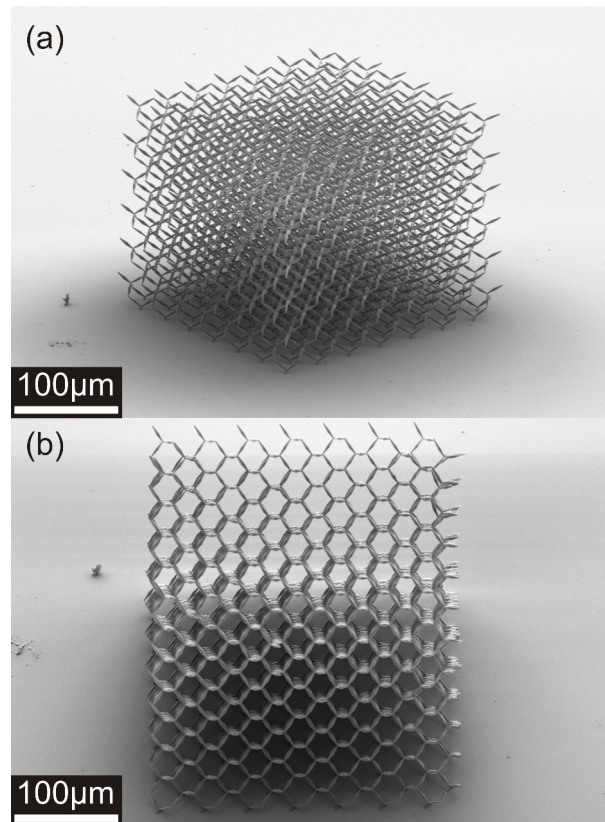


Figure 2.16: SEM of a pentamode metamaterial. The crystalline material consists of $7 \times 7 \times 6$ fcc unit cells. The resulting dimensions are $261 \mu\text{m} \times 261 \mu\text{m} \times 224 \mu\text{m}$. (a) Oblique-view of the structure revealing the structure of the metamaterial. (b) View along one of the face diagonals revealing the hexagonal substructure. This view also allows to determine the accuracy of the fabrication and the periodicity of the structure. Previously published in [108].

a whole crystal structure is shown consisting of 294 unit cells. The structure parameters are $a = 37.3 \mu\text{m}$, $D = 3 \mu\text{m}$, and $d = 1 \mu\text{m}$. The crystal has a high accuracy as can be revealed by the view along the $[0\ 0\ 1]$ -direction in panel (b). Here the hexagonal substructure of the crystal can be seen and the periodicity can be estimated. There are no visible fabrication errors³ within the structure and even the free hanging unit cells at the corners are mainly aligned and did not deform during the writing or drying process. Taking the structural parameters to estimate a filling fraction one reaches a value of $f = 1.5\%$ resulting in a total weight (neglecting the air inside) of the shown material cube of 270 ng or effectively $\rho = 0.015 \text{ g/cm}^3$, compare to the normal material on the Ashby map in Figure 1.2. This means that 1 m^3 of this materials would weight about 15 kg (for a constituent material density of $\rho = 1000 \text{ kg/m}^3$)⁴. By this estimate, we can already see that the here presented material has a remarkably small filling fraction and

³Meaning that all connections are attached, and no defects of the crystal are visible.

⁴The ultralight materials shown in [18] would lead to about 0.6 kg/m^3

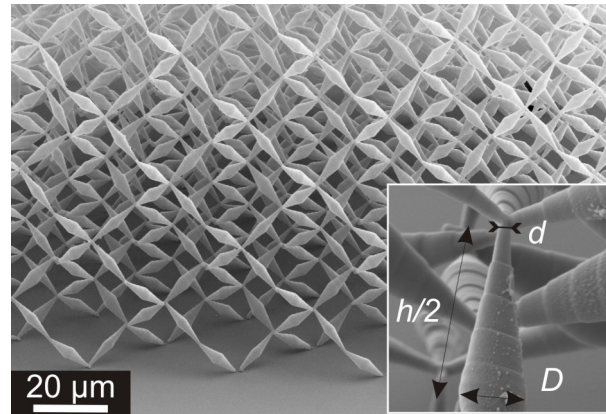


Figure 2.17: Zoom into a different structure revealing the double cone features the material is made of. The very low filling fraction allows to view inside the structure and measure the dimensions of the cones and connection points. The inset is a top view of one of the conical elements revealing the dimensions obtained, namely: $h = 16.15 \mu\text{m}$, $D = 3 \mu\text{m}$, and $d = 0.55 \mu\text{m}$. Previously published in [108].

can thus be considered as a light-weight material further discussed below, see section 1.1.7.

A fabricated structure with even smaller connections can be seen in Figure 2.17. Here, a connection diameter of $d = 0.55 \mu\text{m}$ could be fabricated maintaining the other dimensions. Reducing the connection even further would lead to a not cylindrical symmetric structure as the aspect ratio of the voxels would cause a significant difference in the x , and y -direction compared to the z -direction. In the inset one can also see the writing strategy as the spirals of the programmed trajectory are visible. The resulting value for the B/G ratio is highlighted as a red circle in Figure 2.14 and is on the order 10^3 .

To create larger structures for an easier measurement and sample handling, the scalability of the underlying physics is used. To do so, Robert Schittny has build structures on the scale of about $a = 1 \text{ cm}$ using a 3D printer [106]. The used printer (Objet30, Stratasys USA) is described in the experimental methods part (section 1.3.4). The structures are printed with a plate on the top and the bottom to clamp them while drying and during the measurement. To measure the moduli of the structures software-controlled linear stages combined with a force cell are used to exert a certain strain and measure the related forces. The fabricated macroscopic samples can be seen imaged in Figure 2.18 with connection diameters reaching down to about $d/a = 2\%$ compared to $d/a \approx 1.5\%$ in the DLW samples.

,

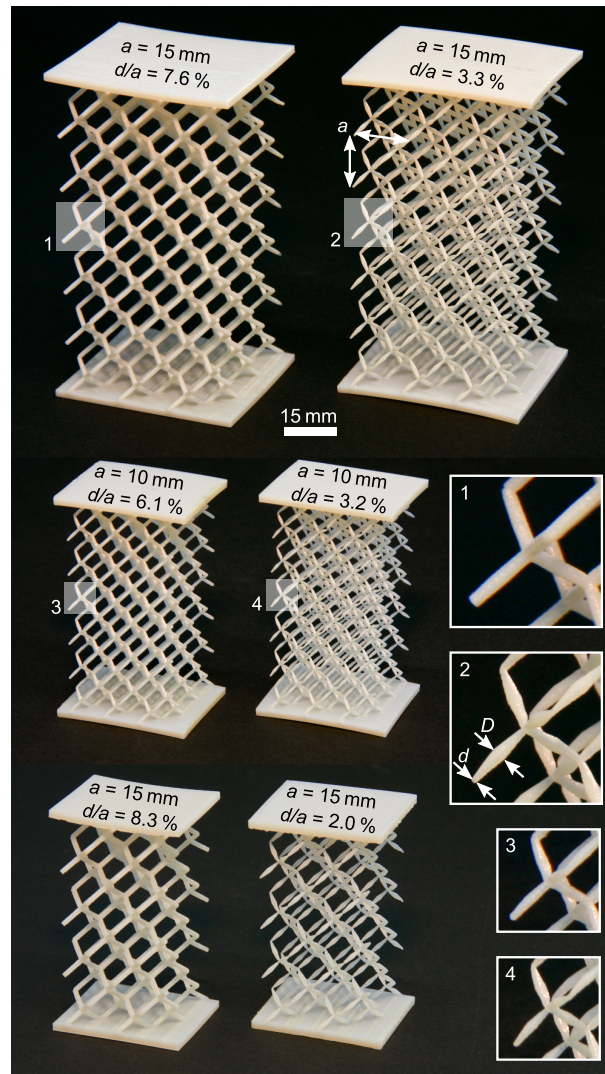


Figure 2.18: Macroscopic samples fabricated by 3D printing. Various different parameter sets are fabricated to evaluate the dependence of the material properties on the design parameters. Previously published in [106].

Measurement

In order to characterize the elastic moduli of the structures, the intrinsic property of very low shear modulus is an important barrier. As a measurement along only a single direction is linked to the Young's modulus rather than the bulk modulus, the material is soft under this deformation. This can be seen by the relation of the Young's modulus with regard to bulk and shear modulus.

$$E = \frac{9BG}{3B - G}. \quad (2.22)$$

Considering the shear modulus of in ideal pentamode material with $G = 0$ effectively also reduces the Young's modulus $E = 0$. The finite shear modulus of the presented

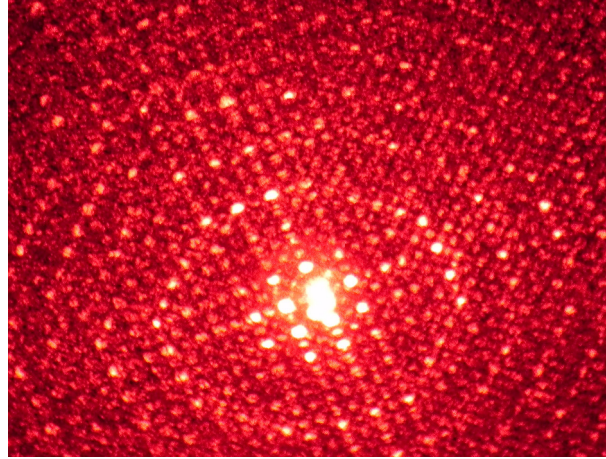


Figure 2.19: Scattered intensity profile of a HeNe laser incident on a pentamode structure.

pentamode materials will prevent this but reduces the Young's modulus considerably. A measurement of the bulk modulus would require at least sliding boundaries on four sides which are very difficult to achieve especially as the material has only very small surface area of the actual constituent material compared to the area of a facet. To estimate the B/G ratio one can use the Poisson's ratio following

$$\nu = \frac{1}{2} \left(1 - \left(\frac{B}{G} \right)^{-1} \right). \quad (2.23)$$

Based on this method one can estimate the Poisson's ratio and relate this to the B/G ratio without any force measurement. In order to obtain a Poisson's ratio, a direct approach based on image correlation seems reasonable. There in a deformation along two orthogonal directions has to be measured under a uniaxial strain. This could in principle be done, but would require a high accuracy of the measurement, allowing to resolve large B/G ratios⁵, which could not be obtained on the by DLW fabricated small samples. We have also tried to find the displacements within the structure based on a different approach using light scattering based on the periodicity of the structure. If one illuminates the sample with coherent light, for example a HeNe (Helium Neon) laser, scattering of the different features takes place and a pattern in the transmitted light appears like the one shown in Figure 2.19.

This scattering behavior is based on the periodic features of the pentamode material, and can in principle be used to determine the periodicity of the crystal along different axes within the sample. The periodicity change is related to the Poisson's ratio, as it changes for two orthogonal directions as one exerts a strain along one direction. The diffraction patterns are changing on a macroscopic scale, whereas small changes in the microscopic geometries can be translated into a macroscopic deviation of the diffraction pattern. Here the distances of the peaks as well as their intensity changes for a deformed structure.

⁵A B/G ratio of 1000 leads to a Poisson's ratio of $\nu = 0.4995$. To resolve this one would need at least a precision up to the fourth digit, which could not be obtained in previous measurements [26, 68]



2.2. Pentamode Metamaterials

Unfortunately, one has to know what the precise origin of the scattered points is to be able to distinguish between a periodicity change and a form-factor change of an individual cell. The form-factor in this context is the origin and spacial distribution of the scattering parts of the geometry. As e.g. the angle of a double cone to the incident light changes, the scattering sites position might differ. To be able to compute the light scattering pattern of a pentamode material one would have to compute the scattering of a structure that has a many times larger unit cell and thus periodicity than the actual wavelength of the light incident. Further multiple scattering events of the light take place within the structure complicating the calculations even further. Clemens Baretzky has tried to find a precise prediction of the scattered patterns by computing the scattered light intensities in his bachelor theses but could not reach an acceptable accuracy with the current technology in an acceptable time. The only promising pathway is to scale the geometry up to a level where a direct measurement of forces becomes possible. As we have seen the basic working principle is scalable and does not critically depend on the constituent material.

The measurement of the 3D printed samples is performed using an automated stage with a three axis force sensor. Therefore the samples are attached to the force sensor on one side and a breadboard on the other side. To measure the elastic constants, first a the shear deformation is induced into the sample, and the resulting shear forces are tracked. This leads to a shear modulus of the structure. Example data sets can be seen in Figure 2.20. The hysteresis on the data is known to appear on viscoelastic materials. The fit to the data reproduces the linear elastic regime and can be transferred into a modulus for the structure. Various samples are fabricated and characterized for changing geometry parameters. To be able to compare the measurements to numerical calculations, the constituent materials Young's modulus can be found by fitting the measured data for the various samples and comparing it to the calculations for exactly the same geometries. As the Poisson's ratio does not influence the result at first order, a typical value for polymers of $\nu = 0.4$ has been implemented. The provider quotes a Young's modulus of $E = 2 - 3$ GPa, but a measurement in collaboration with Professor Wilhelm (KIT) has returned $E = 0.7 - 2$ GPa. The fit to the measured data allows to determine a Young's modulus of $E = 1.4$ GPa. A scaling of the constituents Young's modulus does not change the results as all values are obliged with a simple scaling, not changing any considered ratios as shown before.

Evaluating the bulk modulus has to be done in an indirect way, as no hydrostatic pressure can be applied with our setup. Therefore a measured axial force over strain is compared to numerical simulations, corresponding to a Young's modulus measurement just with fixed boundary conditions in x and y on the top and bottom. This procedure allows to return the Young's modulus of the material. As we are interested in the bulk and the shear modulus, linear elastic relations are used to compute the bulk modulus with the Young and shear modulus. The resulting moduli are plotted in the panel (c) of Figure 2.20. The error-bars on the diameter show the variations obtained within one sample. To compare the samples to the design features, the measured connections d are plotted over there design values in panel (d).

Comparing the experiments to the simulations allows to return an approximate value for the bulk modulus. In combination with the measured shear modulus a B/G ratio can

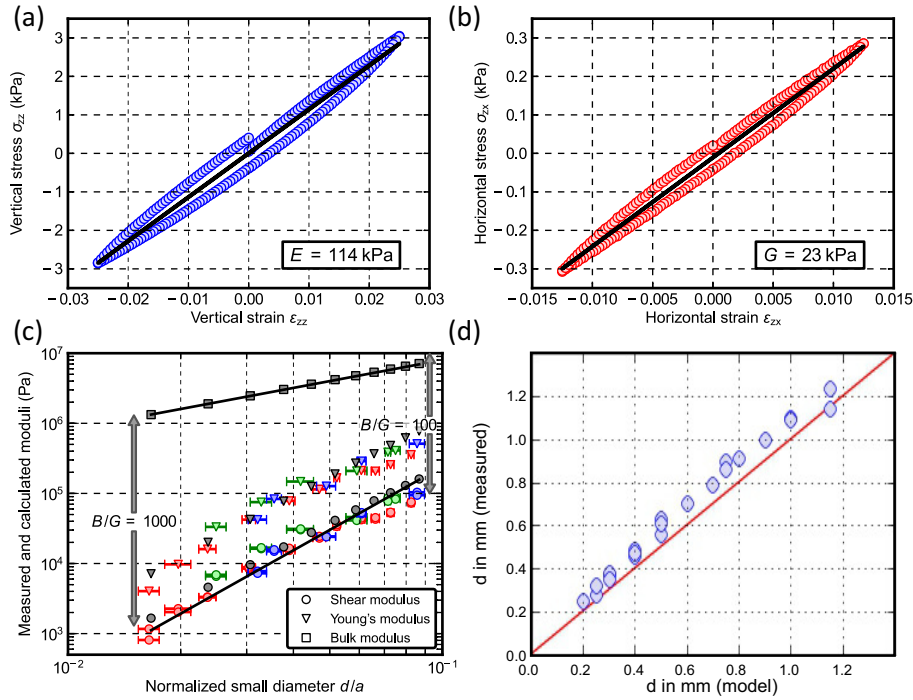


Figure 2.20: (a)-(b) Stress-strain measurements of one fabricated pentamode material with $2 \times 2 \times 2$ cells and parameters: $a = 15$ mm, $D = 1.32$ mm, and $d = 0.71$ mm. (a) Measurement of the shear modulus. The straight line is a fit to the data returning the shear modulus of $G = 23$ kPa. (b) Young's modulus measurement returning $E = 114$ kPa. (c) Measured and retrieved elastic moduli over the normalized connection diameter d/a . The shear moduli as circles, the Young's moduli are plotted as triangles, and the retrieved bulk moduli as squares. The samples are consisting of: $a = 1.5$ cm and $2 \times 2 \times 4$ cells (red), $a = 1.5$ cm and $3 \times 3 \times 6$ cells (green), and $a = 1$ cm with $3 \times 3 \times 6$ cells (blue). Grey markers correspond to the numerical simulations used as comparisons. (d) The fabrication tolerance estimation comparing the model files used and the actual measured sample dimension with regard to the most critical feature, the connection diameter d . Only small deviations can be found increasing the size of the sample with regard to the design slightly. Figure reproduced in accordance to [106]

be stated for the measured samples. The here fabricated and measured samples show a B/G ratio ranging from about 100 to 1000. Robert Schittny has thus shown that a macroscopic measurement of this metamaterial is possible and that one can obtain large ratios of $B/G > 100$ qualifying the fabricated samples to be a pentamode material.



2.2.3 Dynamic Studies

The pentamode metamaterials have been introduced and fabricated on two length scales and characterized on macroscopic samples. To be able to find the dynamic behavior and to estimate the wave propagation in these materials dynamic studies have to be performed. The here shown calculations have mainly been performed by Aude Martin and have been published in [109]. There are a few aspects which are still unclear from static considerations, e.g., how does the dynamic mass density relate to the static one obtained by simple filling fraction scaling of the constituent mass density? Further, it is not clear until which frequency the pentamode behavior is present, or in how far it changes its nature. These dynamic elastic properties of the material can best be extracted with the aid of a phonon band structure calculation. The band structure plots the frequency ω of an eigenmode over the corresponding wave vector \vec{k} . The phonon band structure is determined by numerical calculations performed by COMSOL Multiphysics searching for an eigenfrequency of a structure under Floquet-Bloch periodic boundary conditions for a given k . Comparable simulations have already been performed on bimode materials in two dimensions based on honeycomb structures [111], see also Section 1.1.7. To be able to compare the results to the static data the constituent materials are chosen corresponding to the static calculations on the microstructures with $E = 3$ GPa, $\nu = 0.4$, $a = 37.3 \mu\text{m}$ and a density of $\rho = 1190 \text{ kg/m}^3$. Considering the primitive unit cell of the lattice shown by the black box in Figure 2.21 in real space, one has to consider the body-centered-cubic (bcc) unit cell for the Brillouin zone in k space [115]. To determine the full phononic behavior one would have to find the band structure along every possible direction which is impracticable and in reality simply impossible. The band structure calculation is based on a wave propagating along a certain direction in space and finds the eigenmodes for a certain modulus of the wave-vector k along this direction. Corresponding to normal crystals, characteristic points in k space are used to define a tour through the Brillouin zone which is assumed to represent the crystal behavior in an appropriate manner. The center of the Brillouin zone for $k = 0$ is called the Γ point. At this point the band diagram has its origin and the lowest propagating modes have zero frequency at this point. A wave propagating in the positive x -direction in real space will lead to a band structure in the ΓX direction in k space. The characteristic points are well established for the here considered crystal and shown in panel (b) of Figure 2.21. A standard tour representing this crystal is given by $\Gamma \rightarrow X \rightarrow W \rightarrow L \rightarrow \Gamma \rightarrow K$.

This tour is directly transferred to the x axis of Figure 2.22. The vertical scale is represented in two different fashions. On the left a comparison to the standard velocity in air of 343 m/s is given as a/λ . This axis allows to compare the actual lattice dimensions to a wavelength in air independently of the lattice dimension itself. This universal scale allows a scale independent discussion of the properties of the material. The vertical scale on the right side of the band structures is the actual frequency corresponding to a lattice period of $a = 37.3 \mu\text{m}$. Figure 2.22 shows the band structures for three different real space structures changing the connection size d from (a) $d = 3 \mu\text{m}$ over (b) $d = 0.55 \mu\text{m}$ to (c) $d = 0.2 \mu\text{m}$. The Γ point is the origin and the ΓX direction relates to a wave propagation along the x -direction in real space. This direction shows three bands emerging from zero frequency at the Γ point, as expected from the discussion before. The two shear bands,

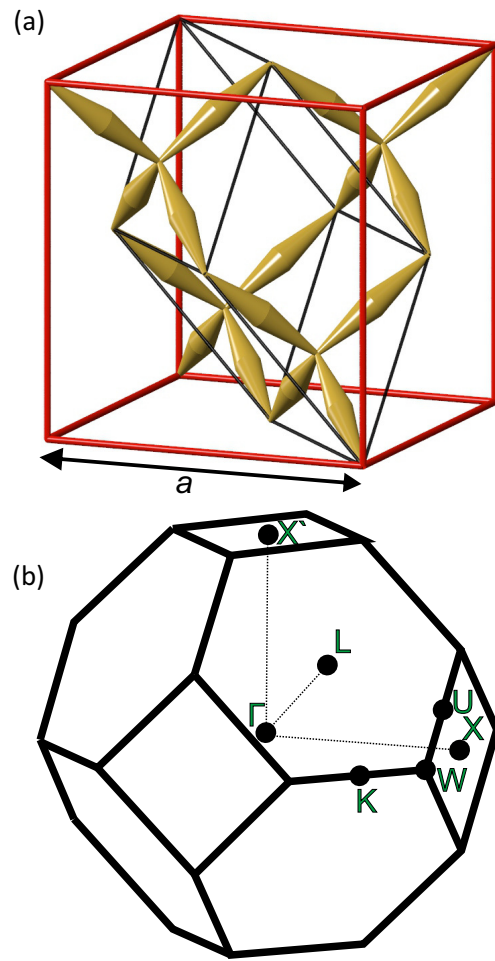


Figure 2.21: (a) Pentamode material in the cubic fcc cell. The black lines outline the primitive cell including only four double cones. (b) The Brillouin zone corresponding to the momentum space. Here, the direction of the \vec{k} is defined and the high symmetry points of the crystal are displayed. Previously published in [109].

being the lower bands identified by the mode shape, are in this case degenerate and have the same frequencies. The higher band corresponding to a longitudinal wave is just one mode. The mode type (longitudinal or transverse) can be found by comparison of the wave vector \vec{k} with the displacement vector averaged over one unit cell $|\vec{u}|$. If the vectors are orthogonal to each other, the wave is considered transverse corresponding here to a shear wave, whereas if the vectors are parallel, the wave is a longitudinal wave here called bulk wave⁶. To be able to compare the different velocities of the wave propagation, the slopes can be fitted with MATLAB in a linear fit evaluating data points close to the Γ point. The fitted slopes are marked as red straight lines in Figure 2.22, and are called c_L for the longitudinal wave velocity and c_T for the transverse wave velocity. In the long wavelength limit the phase and group velocity do not differ significantly. Comparing the different panels one can find that the difference in slope changes and gets larger upon

⁶Precisely the latter is connected to $B + 4/3G$ in an isotropic medium.

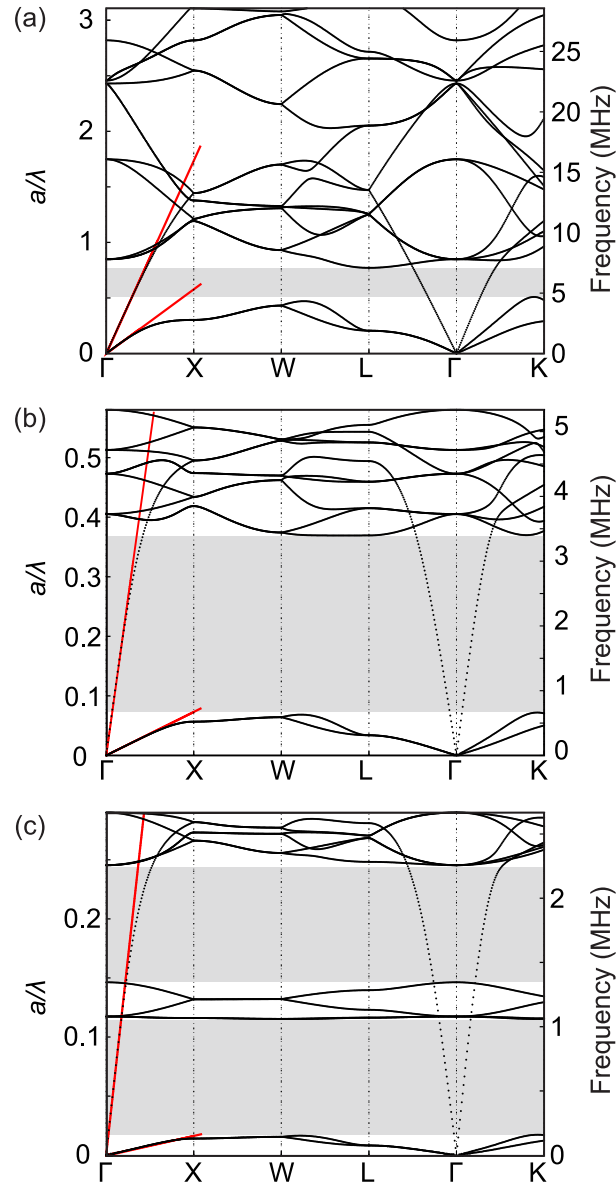


Figure 2.22: Band structure calculations for changing connection size d . (a) $d = 3 \mu\text{m}$, (b) $d = 0.55 \mu\text{m}$, and (c) $d = 0.2 \mu\text{m}$. On the x axis, the usual tour through the Brillouin zone is plotted. The y axis is corresponding to the frequency or the reduced frequency a/λ . The grey areas correspond to pure longitudinal wave motion. The red lines are fits to the long wavelength wave velocities in the Γ X direction. Figure reproduced from [109].

decreasing the connection size. This means that the wave speeds for longitudinal and transverse waves differ by a larger amount. The grey areas in Figure 2.22 correspond to an frequency regime where only longitudinal waves exist and no shear waves are present. This could be called the region where the material behaves purely pentamode like, as only compression waves are supported. The grey area starts at a relative wavelength of about $a/\lambda = 0.1$ on the lower end and is limited on the higher end at $a/\lambda = 0.4$ leading

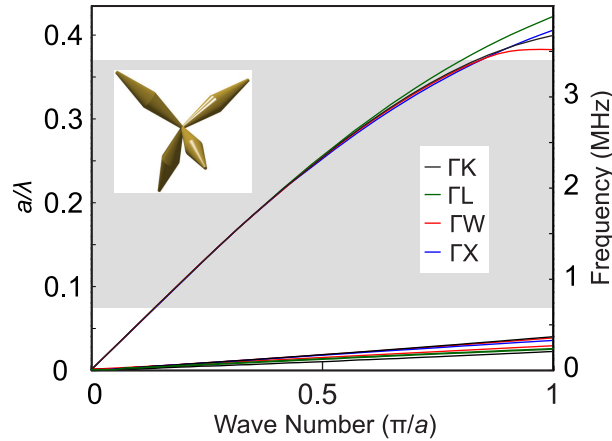


Figure 2.23: Band structure along various directions. One can see that the longitudinal modes are isotropic, hence have the same dependence of $\omega(k)$. The shear modes show more change in velocities and the degeneracy of transverse modes is lifted along some directions. Previously published in [109].

to about 2.5 lattice periods per air wavelength. In panel (c), the grey region is intersected by nearly horizontal modes. These modes correspond to localized vibrations in real space and can generally not be coupled to. This is why one calls them deaf modes. Reducing the connection diameter towards the ideal pentamode structure reveals the occurrence of the deaf bands. Each single double-cone is only connected to the matrix by a very small and point like connection. As it has a finite mass, a resonance of one single element would occur at very low frequencies. This expectation can help to explain the shift towards lower frequencies of the deaf modes in panels (a)-(c). As the connection size d decreases, these modes reduce their frequency and are shifted downwards in the band structure. The higher bands are a mixture of various polarizations and higher order phonon modes which will not be considered here. To be able to estimate the isotropy of our pentamode material a band structure for different directions in the Brillouin zone is calculated and plotted on the same scale. Such a plot is shown in 2.23. There, a calculation along four different directions is shown corresponding to the parameters in Figure 2.22 (b). One can see that the longitudinal modes coincide up to a wave vector of about $k = 0.5\pi/a$. The corresponding shear modes though show slight deviations between them, depending on the direction. We can already see that the shear modes are not isotropic comparing the ΓX direction and the ΓK direction in Figure 2.22. The degeneracy of the transverse modes in the ΓX direction is lifted in the ΓK direction and two bands showing different velocities are emerging. To compare the velocities of the longitudinal wave and the transversal waves the velocities along the ΓX direction are extracted and summarized in a simple table, see Figure 2.24.

The shown matrix is displaying a parameter variation of the connection diameter d along the horizontal direction of the matrix and the larger cone diameter D along the vertical. The corresponding structures are depicted for each combination. The velocity of the longitudinal wave c_L is given in black. The ratio of the velocities c_L/c_T is given in red. In green a filling fraction f of the constituent material with regard to the unit cell is given



2.2. Pentamode Metamaterials

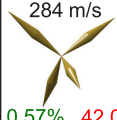
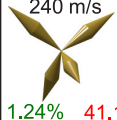
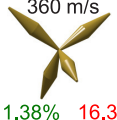
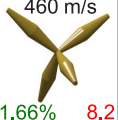
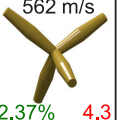
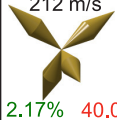
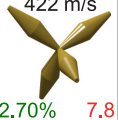
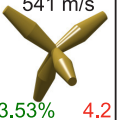
	$d = 0.2 \mu\text{m}$	$d = 0.5 \mu\text{m}$	$d = 1 \mu\text{m}$	$d = 2 \mu\text{m}$
$D = 2 \mu\text{m}$	 284 m/s 0.57% 42.0	 413 m/s 0.67% 16.8	 512 m/s 0.89% 8.5	 570 m/s 1.47% 4.4
$D = 3 \mu\text{m}$	 240 m/s 1.24% 41.1	 360 m/s 1.38% 16.3	 460 m/s 1.66% 8.2	 562 m/s 2.37% 4.3
$D = 4 \mu\text{m}$	 212 m/s 2.17% 40.0	 324 m/s 2.35% 16.0	 422 m/s 2.70% 7.8	 541 m/s 3.53% 4.2
$D = 5 \mu\text{m}$	 194 m/s 3.37% 37.7	 292 m/s 3.59% 15.3	 397 m/s 4.00% 7.7	 521 m/s 4.96% 4.1

Figure 2.24: Matrix resulting from a parameter sweep in d and D . The corresponding geometries can be seen in the insets. Resulting properties are the filling fraction (green), the longitudinal wave speed c_L (black) and the ratio of wave speeds c_L/c_T (red). Previously published in [109].

in %. As one can see the velocity c_L is decreasing with decreasing d and increasing with decreasing D . As expected from the static calculations, the influence of the connection diameter has a higher influence on the velocity and especially on the ratio of velocities. The filling fraction of the material is dominated by D as long as $D > d$ is fulfilled. To compare the ratio of the velocities to the B/G ratio discussed before a simple calculation relating the velocities to the elastic moduli is done. As the velocities are given by (for an isotropic medium)

$$c_L = \sqrt{\frac{B + 4/3G}{\rho_B}} \approx \sqrt{\frac{B}{\rho_B}}, \quad (2.24)$$

considering a $B/G \gg 1$ in the last step and

$$c_T = \sqrt{\frac{G}{\rho_G}}. \quad (2.25)$$

To directly relate the dynamic data to the static considerations, we can assume constant density's and express the B/G ratio with the velocities. A simple reasoning would be that the mass densities ρ_B and ρ_G are comparable and are directly related to the density obtained when one scales the density by the filling fraction, leading to the static filling fraction ρ_0 . This simple reasoning is dangerous though as it neglects the substructure of the metamaterial. As already discussed, the mass density in a dynamic experiment can vary from a static mass density. A slightly more sophisticated approach using the Berryman formula [116] has been shown to fail under these consideration even in some very simple cases [117]. Mass densities common to both modes do drop out when considering the ratio c_L/c_T . In comparison to the static experiments one would assume a scaling

proportional to: $c_L/c_T \propto 1/(dD^{1/4}) \propto 1/d$. Fitting the data in Figure 2.24 leads to a good fit concerning the connection diameter d . We obtain:

$$\frac{c_L}{c_T} \approx 0.5 \frac{h}{d}. \quad (2.26)$$

To compare the B/G ratios or the c_L/c_T ratios of the static and dynamic calculations, one can pick a geometry comparable to the microscopic samples ($a = 37.3 \mu\text{m}$, $D = 3 \mu\text{m}$, and $d = 0.55 \mu\text{m}$). Here the static data lead to $c_L/c_T = 35$ and $B/G = 1260$ compared to the dynamic data of $c_L/c_T = 16$ and $B/G = 256$. Considering the anisotropy of the shear modes and the potential differences in the densities the result can be interpreted as agreeing fairly well.

In summary, we have been able to compute the band structures for pentamode metamaterials and found a separation in the longitudinal and the transverse wave velocities exceeding those of normal materials. We have also found a frequency region in the band structures where only longitudinal modes are present leading to a decoupling of shear related and bulk related waves. To be able to guide a wave in this regime one needs to introduce anisotropy in the material and thereby control the wave propagation.

2.2.4 Introducing Anisotropy

We so far have tried to influence the wave propagation independent of the propagation direction of the material assuming isotropy of the longitudinal polarized waves. To guide an elastic wave differently depending on the direction of the wave, as needed for example in an dynamic elastic cloak[47], we need an anisotropy of the material properties. By changing the dimensions of the cones the wave velocities can be tuned and the coupling of longitudinal and transverse wave can be adjusted by changing the B/G ratio. To be able to influence the wave propagation depending on the direction and thus to make it anisotropic one has to change the design of the unit cell or build up gradients assembling multiple different cells. Further, an anisotropy can be introduced within the unit cell by changing one of the position of the connection points p of the double cones [107] even for an ideal pentamode material. The discussion of such anisotropic materials gets a little tricky at this point. In an anisotropic case the mechanical modes are mixed and one returns formally at an anisotropic bulk modulus. This tensor should in general only be a scalar bulk modulus⁷ rather than a tensor, causing a difficult discussion. This formal problem disappears as a finite shear modulus occurs in the material as the additional modes can be related to a combination of shear and bulk modulus. Here we pick two out of the numerous possibilities of changing the design, namely moving the connection point P 's position along the space diagonal and along a cubic axis. The calculations have mainly been performed by Mumer Kadic.

Figure 2.25 shows the resulting geometries within a unit cell. In the left column the connection point P is displaced along the space diagonal $[1 \ 1 \ 1]$, and the right column

⁷The bulk modulus is defined by a volume change compared to a hydrostatic pressure. Within this definition it does not matter if the volume change is direction dependent or not. It could though happen, that the volume is mainly changed along one direction not reflected within the bulk modulus.

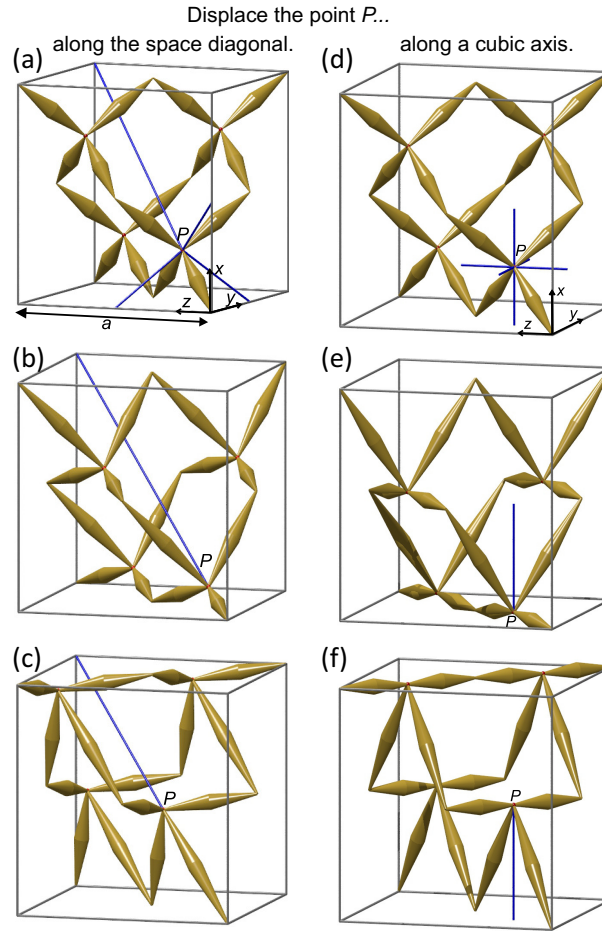


Figure 2.25: Unit cells resulting from moved connection points P within the unit cell. The left column (a)-(c) corresponds to a displacement along the space diagonal, whereas the right column (d)-(f) corresponds to a displacement along one cubic axis. Previously published in [110].

along the cubic axis $[1\ 0\ 0]$. The uppermost panels (a) and (d) show the initial structures and the axis orientation with regard to the fcc unit cell. To define a changed unit cell we have chosen to give a position of the point P percentage wise in units of the basis vectors. This means that the position vector of the isotropic structure is defined in (a) as a percentage value, here $p = 25\%$, multiplied with the axis vector such that the resulting vector for the position is defined as $\vec{P} = (pa, pa, pa)$. Following this procedure the resulting position vector for the cubic axis displacement is $\vec{P} = (pa, 0.25a, 0.25a)$. Displacing P less than for the isotropic structure ($p = 15\%$ in panel (b)) or more ($p = 42\%$ in panel (c)) than for the isotropic material, changes not only the connection point but rather also the individual double cone length h within the unit cell. This gives a direct hint that the structure will get anisotropic as the isotropic behavior is seen to depend on the relations h/d and h/D , see also equation 2.21. Further, we also change the angles between two connected elements resulting in stiffer (angles approaching 180°) and weaker connections (angles approaching 90°) even in the ideal pentamode case as long as one

neglects buckling of the structures. As only the connections within the unit cell get displaced, the connections at the faces of the fcc unit cell are not affected in the position of the connections and keep the translational lattice the same. This is important for the calculation of the properties of a structure as the primitive cell does not change its shape or size by the here considered alterations of the material. Using layered structures consisting of e.g. two different isotropic pentamode materials, changing for example d , D or a , the lattice would not be the same and the primitive cell would increase in size. The constant dimensions of the primitive cell allow us to use the basic simulation setup for the isotropic pentamode material and change the geometry with regard to P within this unit cell. The parameters are again: $E = 3 \text{ GPa}$, $\nu = 0.4$, $\rho = 1190 \text{ kg/m}^3$, $a = 37.3 \text{ }\mu\text{m}$, $D = 3 \text{ }\mu\text{m}$, and $d = 0.55 \text{ }\mu\text{m}$. As before the periodic Floquet-Bloch periodicity is used and a mesh is generated within COMSOL. To still have a mesh that represents the actual structure to an extent that leads to converged results is now more demanding, as the relative angles of the double cones can get very small. The parameters used for the mesh have a maximum element size of $0.025a$ and a minimum element size of $0.0008a$ resolving the small connections and leading to about 10^5 tetrahedral elements. To be able to compare the results to the isotropic structures, band structure calculations along two principle directions, as well as angle-velocity plots are plotted in Figure 2.26 and Figure 2.26. For the angle-velocity plots, a direction-sweep through a plane is performed, which is spanned by vectors orthogonal to the vector along which the point P is moved. Longitudinal polarized modes are indicated by red color, whereas transverse polarized modes are colored in green. The velocities are also indicated as fit lines to the bands in the long-wavelength limit within the band structure plots. Figure 2.26 shows this data for different changed connection points P moving along the space diagonal of the fcc cell. The same data but for the displacement of P along a cubic axis can be seen in Figure 2.27. Especially the velocity plots give an insight into the properties of the material, as they reveal the change in the type of the connections. The geometry in panel (c) of Figure 2.25 has for example the connections in the plane orthogonal to the $[1 \ 1 \ 1]$ direction at a large angle, approaching the situation where all cones lie in this plane. As there are now three stiffer directions, applying the considerations discussed before, an anisotropy shows three-fold symmetry. Comparing this reasoning to the velocity plots seen in Figure 2.26, we see that a three-fold symmetry is indeed visible. Finding a circle in the orthogonal velocity plane and changing velocities along the $[1 \ 1 \ 1]$ direction compared to the plane's velocities would correspond to a uniaxial anisotropy. This situation is approximately fulfilled in the structure seen in Figure 2.26 panel (a). For all data shown the transverse modes are well separated from the longitudinal ones indicating that the pentamode general behavior is maintained.

The same plots as in Figure 2.26 for the displacement of the point P along the cubic axis $[1 \ 0 \ 0]$ can be seen in Figure 2.27. In contrast to the before-mentioned three-fold symmetry, we find a two fold symmetry instead. The two fold symmetry of the velocity profile can be explained by considering the resulting geometry for this movement seen e.g. in panels (e)-(f) in Figure 2.25. Here we see that two cones get aligned with respect to each other, stiffening this direction compared to the others. By these means the symmetry of the anisotropy can be controlled, which changes the materials crystal axis properties to be a uniaxial, biaxial or even more axes.

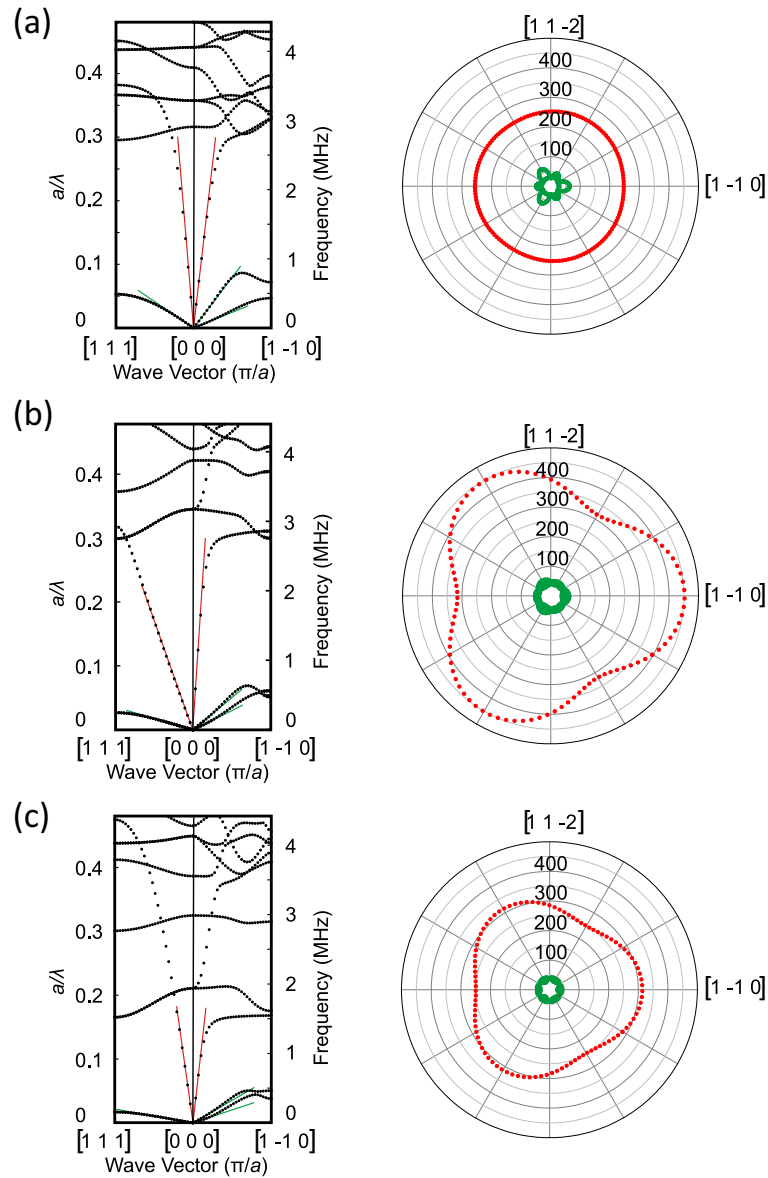


Figure 2.26: Band structure calculations (left column) and phase velocity plots (right column) for different positions of P on the space diagonal $[1 1 1]$. Panels (a)–(c) correspond to $p = 15\%$, $p = 31\%$, and $p = 42\%$, respectively. The red lines correspond to the longitudinal long-wavelength fits and the green lines to transverse polarized modes. The related velocities in a plane orthogonal to the space diagonal are shown in the right column with the same colors denoting the polarization state and are given in m/s. Previously published in [110].

The position of the point P seems to influence the material properties in various ways. To be able to understand the change in properties a little better, we have performed a sweep through the percentage p defining the position of P for both geometry possibilities discussed here. For each geometry the wave speeds for the longitudinal and the transverse modes along two principal directions are extracted. For the structures with a moved

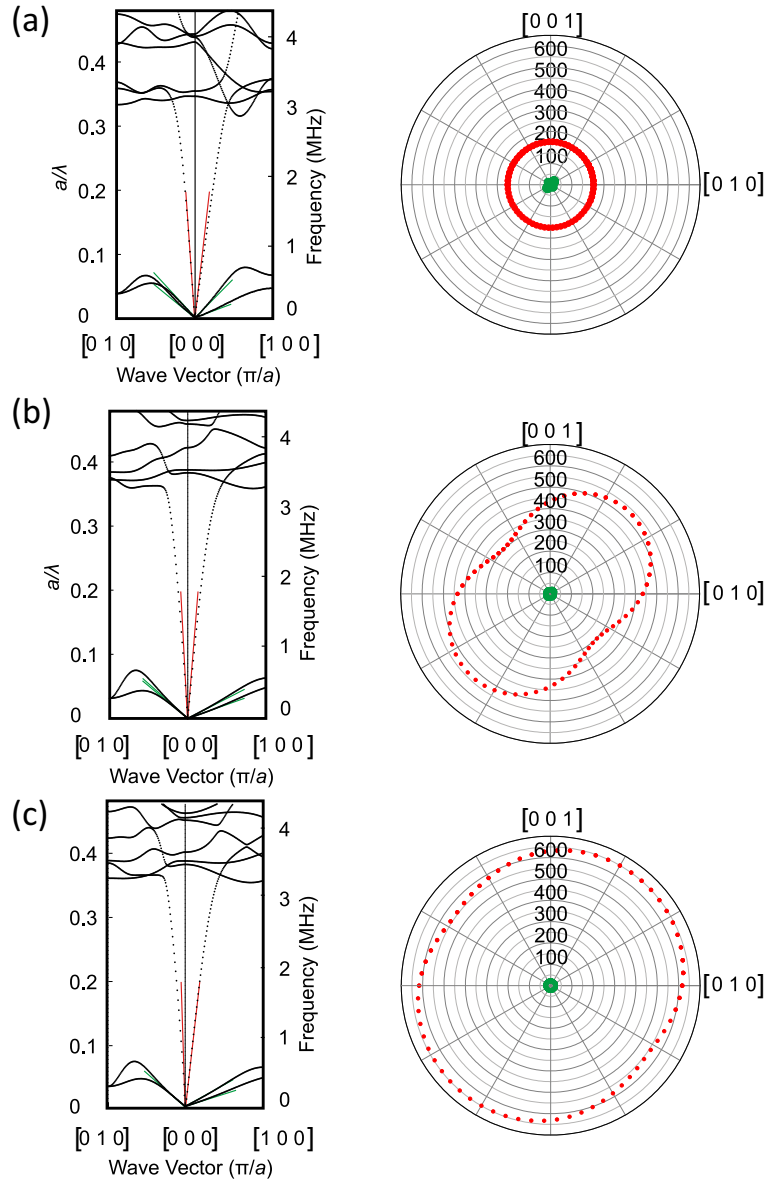


Figure 2.27: The same plot as in Figure 2.26 but for displacing the point P along a cubic axis, here the $[1\ 0\ 0]$ direction. The displacement in panels (a)-(c) are $p' = 14\%$, $p = 30\%$, and $p = 42.5\%$, respectively. Previously published in [110].

P along the space diagonal, we have used the velocities along the $[1\ 1\ 1]$ direction (actually along the space diagonal) and one orthogonal to this, namely $[1\ -1\ 0]$. For the samples moved along the cubic axis we have chosen the directions $[1\ 0\ 0]$ and $[0\ 1\ 0]$. Resulting velocity values for changing connections, color coded as before with regard to the polarization, are shown in Figure 2.28.

The data shown give an insight into the anisotropy comparing e.g. the longitudinal wave speeds (red) with respect to the position of the connection point. We find that the anisotropy is increasing for values smaller than the isotropic value of 25%. Further increasing the percentage shows a strange behavior, see panel (a). Enlarging



2.2. Pentamode Metamaterials

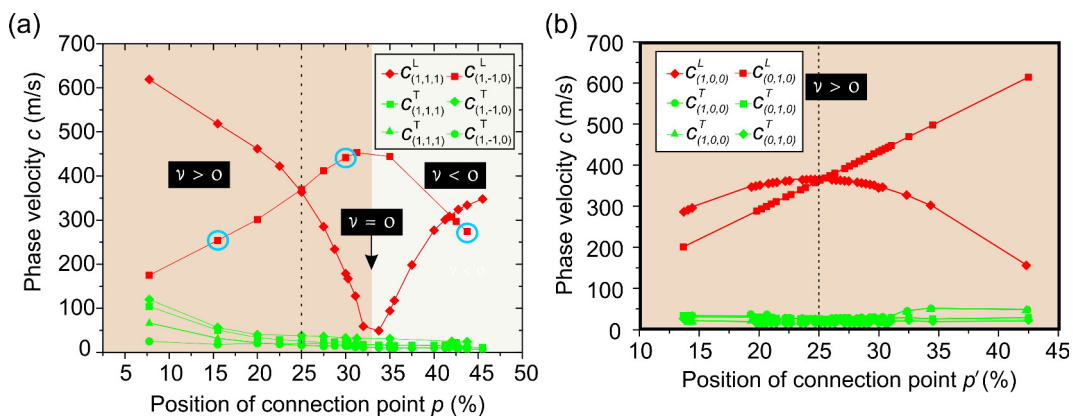


Figure 2.28: (a) Velocities for the different wave polarizations plotted over the displacement of the connection point P moving along the space diagonal. (b) the same as in (a) but for a displacement along one cubic axis. Previously published in [110].

the connection first of all increases the anisotropy until a certain point is reached, from where on it gets again more isotropic at least along the directions shown here. Velocities plotted over a displacement along the cubic axis (panel (b)) do not show this behavior. For some values, we find that the ratio of the two longitudinal velocities reaches a factor of 10, compare [118]. This ratio is the largest occurring in this evaluation, and occurs at the percentage of 33.3%. There though the difference of the phase velocities of the longitudinal and the transverse modes is not large anymore reducing to comparable values, see Figure 2.28 (a). This is a sign that a possible coupling occurs between the modes limiting the pentamode behavior. In principle the decoupling via a large B/G ratio can be improved as one uses jet smaller connection diameters d^8 . This leads to a larger splitting in the longitudinal and the transverse modes. On closer consideration of point $p = 33.3\%$, we find that at this point all the three cones, oriented not along the $[1\ 1\ 1]$ direction, have orientations in one plane. To find a intuitive explanation on the influence of this point, static calculations are performed for the connection sizes indicated with the blue circles in panel (a) of Figure 2.28. Therein $3 \times 3 \times 3$ fcc unit cells are exposed to a force along the space diagonal. The resulting deformations are exemplified in Figure 2.29. We find that the Poisson's ratio component along the examined direction changes from positive over zero to being negative. This outcome can be explained by considering the displayed sub geometries. Pressing on the structure shown in panel (a) leads to a force pushing the double cones in the center out. The force component is decreasing to zero for the case shown in panel (b) and even inverts its direction going beyond this point. Now a force along the upper cone leads to an inward pointing force on the connected double cones. The special point of $p = 33.3\%$ relates to an inversion of the Poisson's ratio component along the space diagonal and thus influences the behavior of the wave propagation. The static calculations give a simple explanation to dynamic computations. Thus the anisotropy

⁸This is limited realistically to some finite size by the fabrication technology and simulation memory capacity.

has a large influence on the Poisson's ratio of the structure and influences the wave propagation as expected. Further, the splitting of the longitudinal and transverse modes (the B/G ratio) is direction dependent and can change over a broad range by introducing anisotropy.

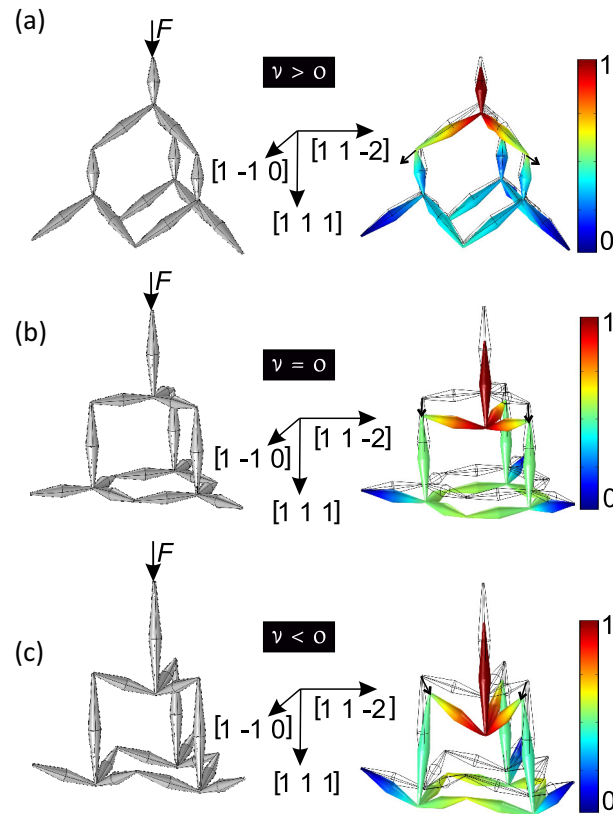


Figure 2.29: Calculation results of the static behavior of the anisotropic pentamode metamaterial for an induced strain along the $[1\ 1\ 1]$ direction. The shown structure parameters are highlighted by the blue circles in 2.28 (a). (a)-(c) correspond to the displacement of the point P by $p = 15\%$, $p = 31\%$, and $p = 42\%$. The undeformed structure is shown on the left and a deformed structure, evaluating a deformation as a result of an induced force F as indicated, is shown on the right (the actual displacement is largely exaggerated for visibility). The color scale represents the deformation modulus at each point of the structure. The three different initial geometries show a different deformation scheme. Calculating an effective Poisson's ratio for this direction, one obtains a value changing from $\nu = 0.9$ in (a) over a near zero Poisson's ratio $\nu = 0$ in (b) to an auxetic material with $\nu = -0.4$ in (c). Previously published in [110].

One advantage of the serial production of additive manufacturing is the possibility to fabricate structures in accordance to the above mentioned samples. Here, one can even change the parameters from one cell to the other. Figure 2.30 shows an example structure fabricated by DLW. There, the connection point P is moved from one layer to the other along one cubic direction, starting from the isotropic material towards the point where the top cones are aligned. The view along the diagonal reveals the change in the structure.



2.2. Pentamode Metamaterials

The lower unit cells still show the hexagonal pattern whereas the highest unit cells transfer into a square pattern. The top layer can also be seen with a higher magnification in panel (b). Here one can see the different orientation of the double cones, as compared to the isotropic structures. One can identify the aligned double cones resulting from the displacement of the connection point P normal to the substrate. Panel (c) shows a structure with isotropic unit cells, but with a change of the isotropic material properties for each adjacent unit cell. Here a checkerboard arrangement is used to build up an anisotropic material consisting of larger unit cells that consist of two different isotropic pentamode materials. This kind of anisotropy allows to tailor a material even further with regard to the direction dependent properties still keeping the B/G ratio as large as desired.

In principle, the properties can be changed even further by modifying the design in various different ways. One could for example change the connection shape by introducing different shapes for the connections and the cones. This leads to a very small difference in the direction dependence [118]. To increase the effect one could add connections between certain double cones increasing the rigidity with regard to shear, allowing to tailor the shear modulus of a structure in a direction dependent way. Decreasing the stability of the structure and translating the structure towards a six mode material can be done by interchanging the size of the double cones. For the so far discussed structures we have assumed $D > d$. If one turns this ratio around and inverts this assumption to $D < d$, one obtains cones connected at their thick end at the atomic sites of the diamond lattice. The resulting structure looks like caltrops connected at their thin ends. This structure is still stable under hydrostatic compression, but now also has easy modes related to rotations of the caltrop elements. These are just few further suggestions how one could in principle use the basic pentamode structure to tailor and design a material's elastic properties with regard to a specific need. Recent work has shown that some aspects of pentamode materials can be maintained when changing the underlying lattice symmetries to e.g. a scc crystal structure[119]. In general one does not necessarily need pentamode materials to tailor a specific material property, but it is shown [107] that one can tailor any kind of elasticity tensor (without a global scaling pre-factor due to the constituent materials stiffness) by modifications or combinations of pentamode metamaterials.

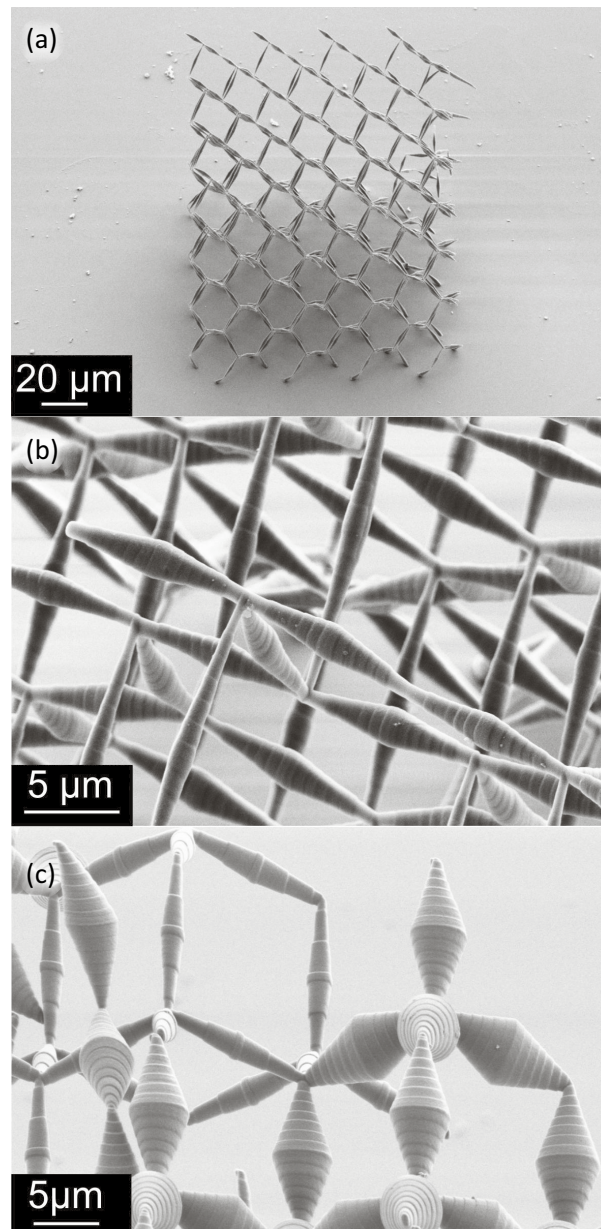


Figure 2.30: Microscopic pentamode samples with induced anisotropy. (a) A block of pentamode metamaterial with changing connections along the cubic axis. The block of material has a changed connection point P for every layer and has thus gradient anisotropic material properties. (b) Zoom into the top layer of the structure revealing the changed connection. (c) A different way of introducing anisotropy, namely by alternating the effective properties. Here the larger connection size D is changed from one unit cell to the other, introducing anisotropy in the effective material parameters.



2.2.5 Changing the Density

We have seen that it is possible to generate isotropic and anisotropic versions of pentamode metamaterials and tune the elastic properties of the effective material. One metamaterial property only slightly discussed so far is the variable density. As mentioned before, wave propagation is not only governed by the elastic properties of the material, but also by the density of the material. Apart from dynamic considerations, so called ultra-lightweight materials have recently gained a large interest in the community [18, 32, 120–124]. These materials are normally designed to have a large Young’s modulus with a low density, making them a good candidate for future high-performance materials.

Ultra-light Pentamode Materials

Changing the density of our pentamode material is generally possible as well. We have already seen that the filling fraction of the presented structures is only on the order of a few %. Our goal is thus to tune the density to extremely low values and still keep the B/G ratio large instead of the Young’s modulus. Therefore, we have used the normal pentamode design fabricated with the DLW and have chosen to set the diameter values of the cones equal and fixed to $D = d = 1 \mu\text{m}$. This structure size can be fabricated without major problems and also allows to stitch writing fields together, as $1 \mu\text{m}$ is about the precision of the translation stage of the DLW setup for repeated access. Such a stitching process of the individual writing fields allows to enlarge the overall material dimensions. Fixing the diameters generally fixes the geometry’s density for a given lattice constant. As the only free parameter is thus the lattice constant a , we use it to tailor the filling fraction. Increasing the unit cell makes the material effectively softer as the filling fraction decreases. We have tried to fabricate samples with as large as possible lattice constants and have found that lattice constants of up to $a = 200 \mu\text{m}$ can be fabricated in a reproducible fashion using DLW. These samples could then be coated using atomic layer deposition, where one atomic layer at a time is deposited homogeneously onto the samples [125]. This procedure is shown to exhibit an extremely good homogeneity of the material thickness, and no directionality. The material used here for the coating is aluminum doped zinc oxide (AZO), a high Young’s modulus ceramic. The doping, in the ratio 18 : 1, ZnO to Al_2O_3 , is used to increase the conductivity of the ceramic, needed in the following etching steps. The resulting coating had a thickness of 50 nm which could be measured by cutting open part of the structure with a focused ion beam (FIB) and imaging with a SEM. After this coating step the structure is etched open from the top by the aid of reactive ion etching (RIE) for about 5 minutes. This procedure allows to etch in a highly directional fashion. This highly selective process allows to etch only the top of the structure, exploiting the required directionality and etch rate dependence. The polymer has a significantly slower etching rate within this procedure than the coating, which is paired with a beneficial thickness ratio, such that the ceramic layer is about twenty times thinner than the polymer structure. The directionality of the etching procedure is small enough though to etch bars in the lower unit cells, which are positioned below another bar and could in principle be shaded. After the RIE step the polymer is etched out of the half shells of ceramic by an oxygen plasma for about 16 hours and 30 minutes.

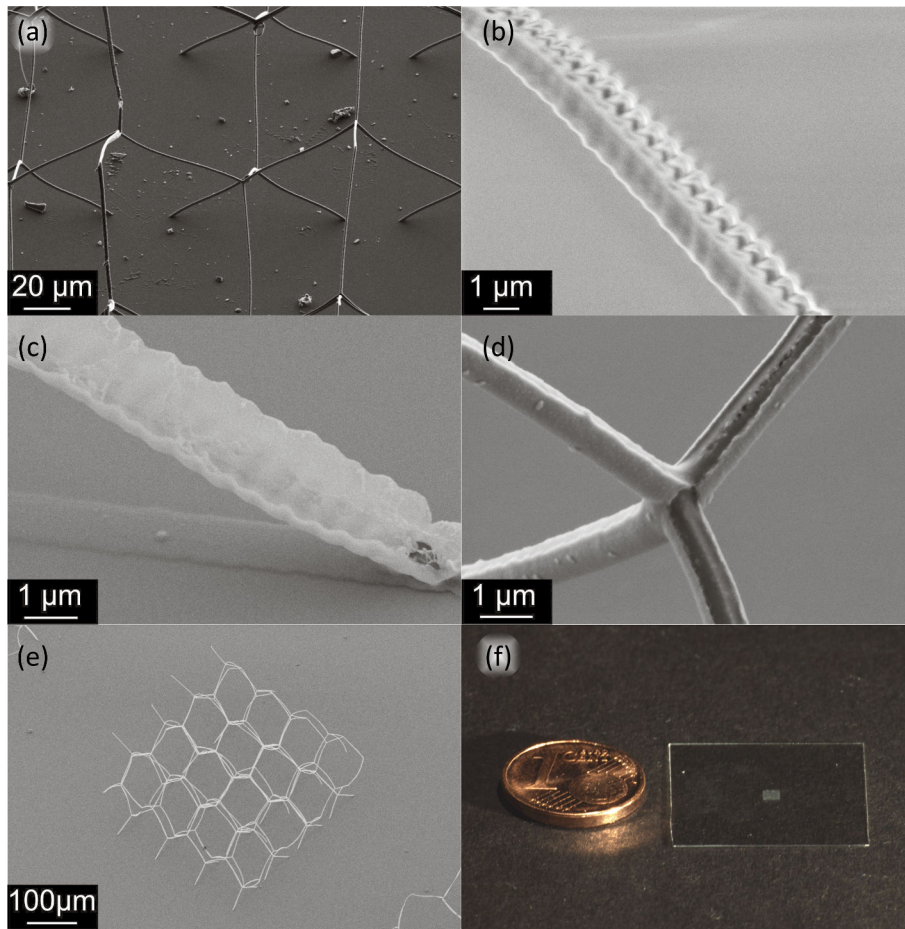


Figure 2.31: SEM micrographs of lightweight structures during the fabrication process. (a) Fabricated polymer structure with a lattice constant of $a = 200 \mu\text{m}$. (b) Zoom onto the structure after coating with AZO. (c) Same structure after etching the top part of the structure open with reactive ion etching (RIE). One can see that the polymer shields the structure such that only half of the AZO is etched away. (d) Sample after the polymer has been etched by an oxygen plasma. Only the AZO shell is left over. One can even see the etching shadow on the substrate indicating the directionality of the RIE etching procedure. (e) Structure after the polymer is removed. Although the structure is extremely light it still holds up and does not collapse. (f) A different sample after the same fabrication procedure with dimensions $5 \times 5 \times 0.28 \text{ mm}$. The comparison to a euro cent allows to compare the material in size.

This step removed the polymer without harming the ceramic. A removal of the polymer could not be obtained within a closed ceramic cylinder. Here, etching only occurred a few microns depth into the cylinders, independent of the plasma etching times⁹. After the removal of the polymer the structures are still standing up and withstanding the force acting upon them by their own weight and forces induced by handling the structures. The resulting structures resemble the design considering the complicated fabrication steps

⁹The times used here ranged from an hour to 144 hours.



2.2. Pentamode Metamaterials

within the errors estimated for the densities below. To enlarge the material dimensions we have stitched individual fields of the material together and obtained dimensions of up to $5 \times 5 \times 0.28$ mm. These main processing steps and imaged samples can be seen in Figure 2.31.

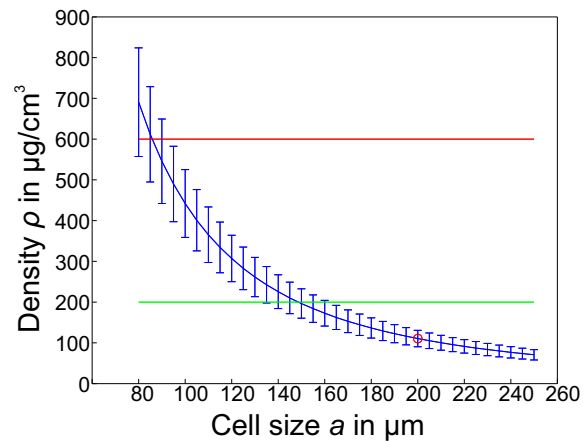


Figure 2.32: Calculated density of the effective material in vacuum depending on the lattice constant a . The horizontal lines correspond to carbon nano wall materials [126] (green) and ultralight metallic lattices [18] (red). The red circle represents the fabricated structure in Figure 2.31.

Although the material is not showing large errors with each writing field the overall sample shows some error due to the stitching of the individual fields. To be able to compare to other ultra-lightweight materials, we have estimated the density the actual material has depending on the unit cell size (always neglecting the air in the material). Therefore we have used to geometry parameters for a filling fraction and thereby scaled the density of AZO. The resulting densities can be seen in Figure 2.32. The horizontal lines correspond to recent ultra-lightmaterials, e.g. the green line corresponds to carbon nano wall materials [126] and the red line to the ultralight micro lattices reported in [18].

Even taking realistic errors¹⁰ found by measurements in the SEM on the dimensions and material properties, we can obtain materials with lower effective density, from lattice constants larger than about $160 \mu\text{m}$, than reported in literature known to us at this time. The presented structures shown in Figure 2.32 are highlighted by the red circle in Figure 2.32 and have calculated densities reaching towards $100 \mu\text{g}/\text{cm}^3$. The structures presented here could neither be measured as the densities and forces are too low for our available equipment, nor be simulated as the large aspect of the small shell to the large unit cell requires not accomplishable precision on the meshing.

¹⁰The calculations are done with the following parameters: rod radius $0.5 \pm 0.01 \mu\text{m}$, wall thickness = $0.035 \pm 0.005 \mu\text{m}$, remaining fraction of the coating 0.5 ± 0.05 , and the error on the lattice constant is considered as $2 \mu\text{m}$

Independent Control of the Density and the Bulk Modulus

To be able to control the wave propagation in full, one needs not only to control the elastic properties or the density but rather wants to control both parameters at the same time and in an independent manner. Therefore, we remember the dependencies of the pentamode behavior on the diameters d and D . There we have seen that the main effects on the B/G ratio is determined by the connection diameter d and the angle the cones have at the connection. This feature can be used to concentrate the effective stress into the tips and determine the mechanical properties by these two features. As we have seen, the stress within the thicker parts of the cones is comparably low. This allows to make use of the geometry by adding mass to the thicker parts of the double cones¹¹. The added masses can be designed in such a fashion that they have minimal influence the mechanical properties. On top of the initial double cones with parameters d_1 , D_1 and h we add a second double cone shortened by a length s on both sides and parameters $d_2 > d_1$ and $D_2 > D_1$. The design and a resulting structure can be seen in Figure 2.33.

To check for a possible change in bulk modulus and density we have performed numerical calculations. In a first step we validate our assumption that the concentration of stress into the tips is still valid for the now changed design. Therefore we have performed calculations inducing a hydrostatic force onto a primitive cell evaluating the stress concentrations obtained by this procedure. To be able to compare to the previously obtained results, we use parameters in accordance to the geometries discussed before. For convenience, they are given in units of the lattice size: $D_1/a = 0.12$, $d_2/a = 0.04$ and $s/a = 0.05$. The other two parameters namely, D_2/a and d_1/a , are used to tune the filling fraction $f = \rho/\rho_0$ and the bulk modulus B . One can see in Figure 2.33 (b) that the von Mises stress concentrates mainly within the small tip objects and the added masses do not influence the stress pattern in a significant manner. Comparing the smaller added mass with the large one in panel (b) of Figure 2.33, we can already see that the filling-fraction changes dramatically whereas the stress patterns show only minimal differences. This suggests, that our assumption is valid at first order and one can tune the density via the filling fraction of the material determined by the parameter D_2 and still preserve the scaling of the bulk modulus as before with regard to the connection size d_1 . This decoupling of the parameters will of course break down for a certain parameter set as the two parameters approach each other in size. On the other hand, in the limit of $d_1 \rightarrow 0$, the decoupling should be perfect. In order to estimate in which regime we are considering realistic parameters, the relative bulk modulus is computed. Comparing the relative bulk modulus B/B_0 for changing filling-fraction f , reveals the possible correlations of the two material parameters. Here both parameters are used in a relative fashion to the initial constituent material parameters given in %.

The outcome of the simulations performed statically, prescribing hydrostatic pressure on a fcc unit cell is shown in Figure 2.34. The simulations assume typical polymer values given by $B_0 = 5$ GPa, $\rho_0 = 1190$ kg/m³ and $\nu = 0.4$. To illustrate the parameter sweep, the normalized bulk modulus over the normalized density is plotted. The changing geometry's

¹¹This scaling allows only to add masses to the design. Here no reduction of the mass of the material is attainable.



2.2. Pentamode Metamaterials

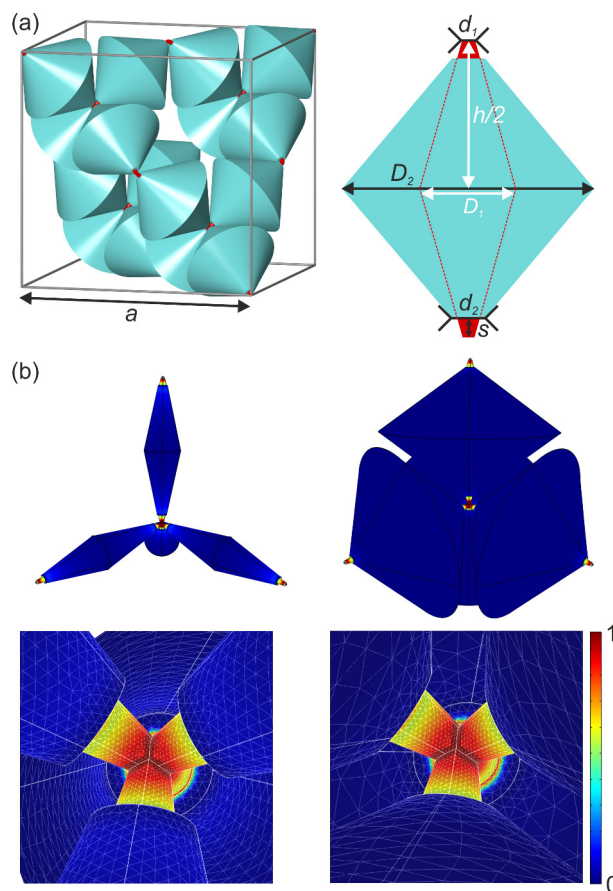


Figure 2.33: Design of a pentamode material with added masses to tune its density. (a) Exemplified structure with masses added (blue) to the initial pentamode material (red). (b) Two static numerical calculations as two examples of a material with different added masses. Here, hydrostatic pressure allows to estimate the stress concentration in the tips, mainly determining the bulk modulus of the material. Figure in accordance to [127].

given by D_2 are represented with blue lines, whereas the changing connection diameters d_1 are given as red lines. The calculated velocities obtained by simply neglecting G and using the formula $c = \sqrt{B/\rho}$ are given in black. In the ideal decoupled case one would obtain orthogonal straight lines for both scaling. As we have already pointed out, we break the assumption of independent scaling as the diameters become comparable, which is also visible in the plotted data. Especially for large values of d_1 and small values of D_2 (in the upper left corner), we get significant deviations. Evaluating the other extreme and decreasing d_1 towards zero, should lead to less coupling. As highlighted with the lowest red line, smaller d_1 lead to less change of the bulk modulus when loading the structure with more mass. To be able to estimate on how realistic these parameter combinations are, two examples are depicted indicated by number 1 and 2. To compare the values obtained by the static calculations to the ones obtained by wave propagation, the corresponding band structures for the different materials are calculated. As we expect isotropic properties of

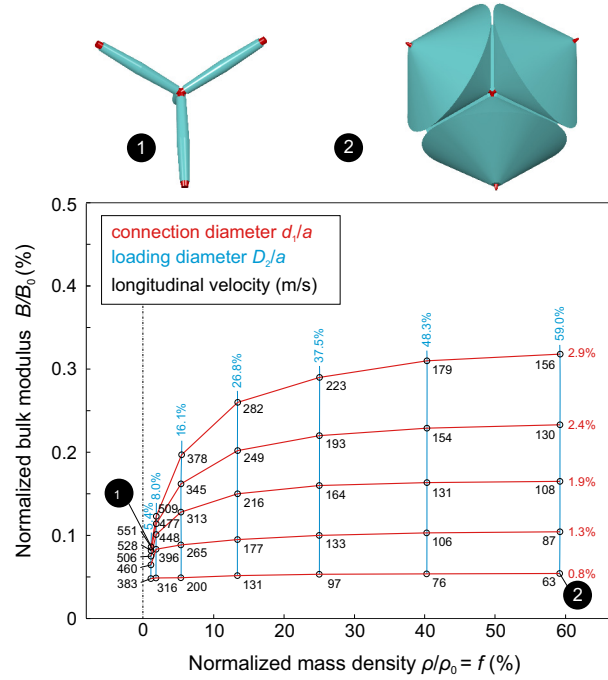


Figure 2.34: Calculated metamaterial parameters evaluating the dependence of B and ρ on the geometry parameters D_2 and d_1 . Two example structures indicating the changing geometries are depicted on top. Value of the connection diameter d_1 are shown in red whereas loading parameters D_2 are given in blue. The sound velocities calculated as $c = \sqrt{\frac{B}{\rho}}$ are given in black. Previously published in [127].

the structure, an arbitrary direction is chosen, here the ΓK direction of the band structure. Calculated representative parameter choices are depicted in Figure 2.35.

The longitudinal polarized modes are shown with a linear fit in the regime $|k| \approx 0$ represented as the red lines. Comparing the densities, resulting from the velocities obtained by the fit, with the static densities considering only the filling fraction, a very good agreement is found, as the deviations are below one percent. For the reasoning we have only considered the bulk modulus for the longitudinal polarization speed (in contrast to the expression $c = \sqrt{(B + 4/3 G)/\rho}$). One can thus tune the wave velocity as well as the wave impedance $Z = \sqrt{B\rho}$ ¹² independently and tailor both parameters as necessary for an application if control of the impedance is needed for example to avoid reflections at an interface of two materials. The shear related bands as well as the other "deaf" bands are shown in grey. As expected and seen beforehand these bands decrease for smaller d_1/a as well as for larger D_2/a . The reference wavelength used here is again corresponding to standard air with $c = 343$ m/s. In this fashion, the absolute frequencies for a given a of, for example, a unit cell size of $a = 40 \mu\text{m}$, would lead at $\lambda/a = 0.5$ to a frequency of 4.3 MHz. Scaling the results to different constituent materials (assuming negligible Poisson's ratio influence) is straightforward as well. Thus, changing from $B_0 \rightarrow \tilde{B}_0$ and from $\rho_0 \rightarrow \tilde{\rho}_0$ the corresponding angular frequency changes as $\omega \rightarrow \omega \times \sqrt{\tilde{B}_0 \cdot \rho_0 / B_0 \cdot \tilde{\rho}_0}$.

¹²Valid in the assumption $G = 0$



2.2. Pentamode Metamaterials

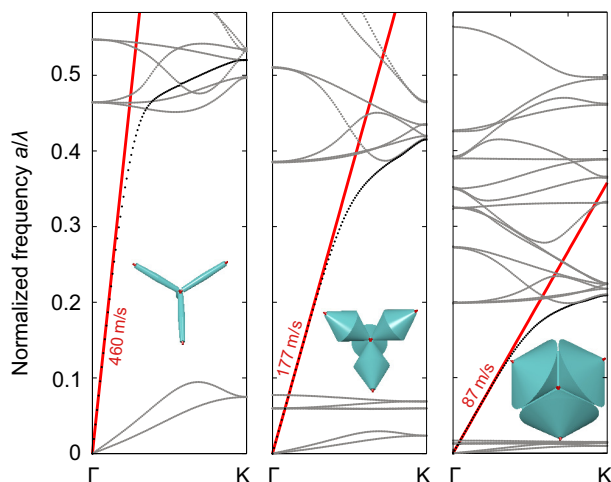


Figure 2.35: band structure calculations for different geometry parameters D_2 . The longitudinal velocities fits are indicated in red. The structures are shown as insets in each sub-panel. Previously published in [127].

To be able to estimate the buckling of these structures, hydrostatic linear buckling analysis are performed on the fcc cells. The first buckling modes occur at about 5 MPa under hydrostatic conditions and the smallest connection size. But a unidirectional load distributed throughout the structure, like gravity, can in principle lead to a much lower critical buckling load. Experimental verification of the stability against such loading of the structures is proved as the corresponding geometries are fabricated by the use of DLW. A unit cell size of $a = 40 \mu\text{m}$ is used and the connection diameter is fixed to the lowest easily obtainable value of $d_1 = 0.45 \mu\text{m}$ corresponding to $d_1/a = 1.1 \%$. To estimate the stability of a fabricated sample see Figure 2.36. As can be seen in the top panels a connection diameter of $d_1 \approx 0.45 \mu\text{m}$ is obtained and maintained for the different parameters of D_2 . The additional mass parameter is chosen to vary from $D_2/a = 13.5 \%$ to 47.5% . All of the structures could withstand the forces in the drying process and are mechanically stable. To visualize the exceptional ratios within such geometries, a structure with $D_2 = 19 \mu\text{m}$ is demonstrated and depicted in the lower left panel. Here we see that the structure holds itself up supported only by the comparably small connections. We note that this is about the largest D_2 one can obtain, as in this case the added masses are nearly touching each other on the outer sites. The lower right two panels depict a top view of the structures, illustrating the filling fraction's dramatic change by varying the loading parameter D_2 .

Within this section we have evaluated the possibilities allocated to pentamode mechanical metamaterials. Based on an ideal theoretical design [107], we have used a key parameter, the connection size d , to realize a blueprint for a tailored pentamode metamaterial. To evaluate the performance of the metamaterial, we use numerical calculations to reveal the dependence of the characteristic material properties, the B/G ratio, on the structural parameters, d/a and D/a , in the static regime. We find, that the tailored pentamode metamaterial can outperform natural materials with regard to the B/G ratio. To evaluate the behavior of the pentamode materials under dynamic conditions, band structure calculations are performed. Here the B/G ratio translates into a wave velocity

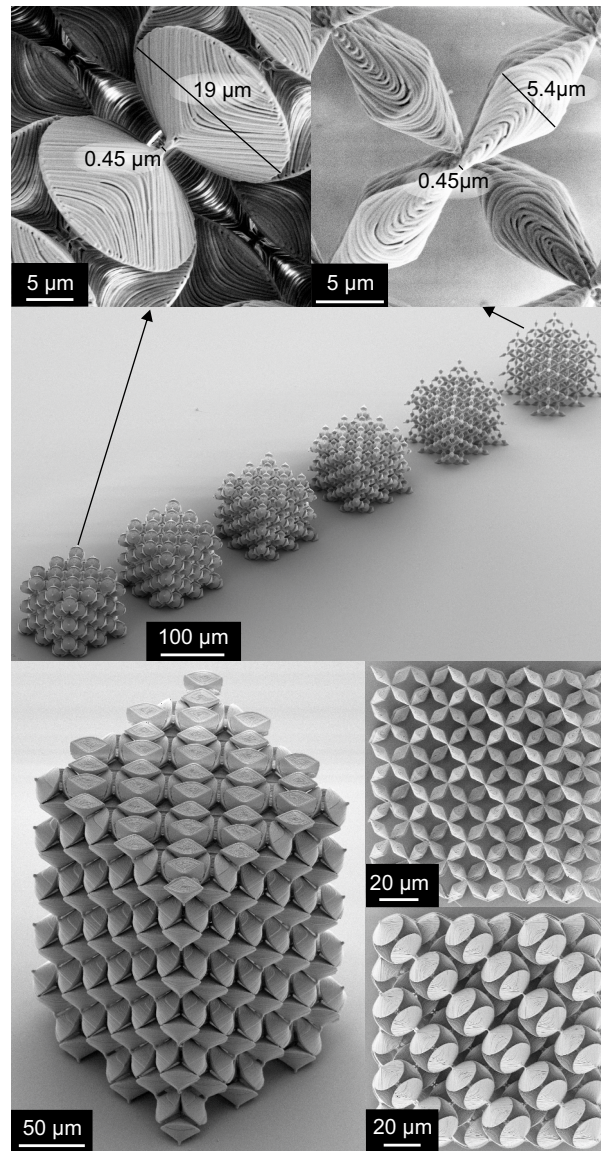
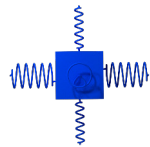


Figure 2.36: Fabricated structures for changing D_2 . The fabrication precision can be revealed by the SEM micrographs. The filling fraction as well as the stability of the effective medium can be estimated. Previously published in [127].

for the longitudinal and transverse wave polarization. Apart from a large difference in the wave velocities, related to large B/G ratios, we find a frequency region wherein only longitudinal waves can propagate. Within this region a pure pentamode behavior is present, as no coupling to shear waves is possible. After verifying the concept of pentamode metamaterials we were able to fabricate these structures on the microscopic scale by DLW and on the macroscopic scale via 3D printing. The latter could be characterized in its static properties confirming the numerical calculations.

To be able to have an space or direction dependent influence on the wave propagation with in pentamode metamaterial, needed for example to build an radial symmetric cloaking



2.3. Anisotropic Dynamic Density

assembly [47, 50], further modifications are done to the design. The first of these is using a distorted unit cell to introduce anisotropy into the properties of the metamaterial. The second modification uses the density of a pentamode material, to reduce the density towards ultra-lightweight materials, or to tailor the density and the elastic properties independent. This allows to control the wave propagation direction dependent, via the anisotropy, and tailor the impedance of a material to avoid, e.g., reflections at interfaces between two different pentamode metamaterials.

2.3 Anisotropic Dynamic Density

To be able to control the propagation of mechanical waves in elastic solids in full, we have seen that one needs to control the material's elasticity tensor \mathbf{C} and its mass density ρ . Only with both of these parameters independent control on the phase velocity and the wave impedance is possible. Generally, the effective mass density of artificial materials is frequency dependent. The resulting retrieved density can even be negative [38], or can depend on the propagation direction as well as on the polarization of the wave. This means that one needs to tailor a direction-dependent mass-density tensor for each frequency. To illustrate this, we consider a simple model illustrated in Figure 2.37. Here a spring-mass model is shown, consisting of the masses (red) and springs connecting them. In the center of each mass there is another mass, shown in blue, connected with a different spring to the first mass. Within this model the masses themselves do not deform, and the springs do not carry any mass. As a first step one consider a quasi-static deformation of a one-dimensional system. Pressing onto the chain will only lead to a contraction of the matrix springs connecting the rigid red masses. The inner masses will be displaced, but still be centered with respect to the red masses they are enclosed by. As the inner springs are not deformed, no energy is taken up by them leading to an elastic behavior only dominated by the sum of the static masses and the outer springs.

This simple reasoning is true also for small but finite frequencies until the resonance frequency of the inner mass-spring combination is met. Approaching this resonance the inner masses start to move with respect to the matrix. As the inner springs deform, this movement also carries energy and the wave propagation is influenced. When the frequency approaches the resonance frequency of the inner masses, they start to show a phase lag to the excitation, and oscillate at a phase of π for frequencies right above the resonance.

The resulting behavior can be summarized with an effective mass density describing the frequency dependent response of the spring-mass system. A normal linear spring mass system with lattice constant a , where the masses m are connected by springs with spring constant D , is described by the following dispersion relation:

$$\omega^2(k) = \frac{2D}{m}(1 - \cos(ka)). \quad (2.27)$$

A Taylor expansion for small values of ka leads to the standard expression of the phase velocity $c = \sqrt{B/\rho}$ with a bulk modulus of $B = D/a$ and a mass density of $\rho = m/a^{dim}$ with the dimension dim . To describe the previously mentioned mass-in-a-mass system,

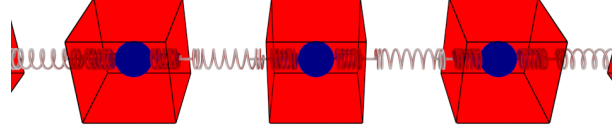


Figure 2.37: A simple mass-in-a-mass spring model. An elastic host is mimicked by the red masses and the springs connecting them. Into this host material masses, colored in blue, are added and connected to the host by different springs.

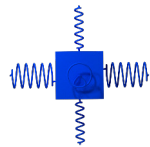
one has to consider the outer matrix masses m_m and the inner masses m_i . The inner springs have a spring constant of d , whereas the outer springs still have a spring constant of D . For this kind of spring-mass system one can introduce the concept of an effective mass given as [37, 128]:

$$M_{eff}(\omega) = (m_m + m_i) + m_i \frac{\omega^2}{\Omega^2 - \omega^2} \quad (2.28)$$

with a resonance frequency of the inner masses $\Omega = \sqrt{d/m_i}$. Herewith one can find the effective mass density

$$\rho_{eff}(\omega) = \frac{M_{eff}(\omega)}{a^{dim}}. \quad (2.29)$$

This resulting effective mass density is thus frequency dependent and becomes negative for values in the interval of $(\Omega, \Omega\sqrt{(m_m + m_i)/m_i})$. To exploit this behavior, one basically just needs to couple two masses in the above mentioned way. This one dimensional concept can be translated into three dimensions, where each direction can in principle have different springs and thus eigenfrequencies, resulting in an anisotropic, possibly negative mass-density tensor. The basic concept is not new and there have been a few suggestions how to achieve such a design strongly influenced by acoustic research[7, 129]. Within this section we will first discuss a design based on the above mentioned pentamode metamaterials. Subsequently we evaluate a design in which the simple mass-spring model is realized. The following results have partly been published in [127, 130].



2.3.1 Layered Pentamode Materials

The principle of a changing mass density can be used to tailor the band structure of pentamode metamaterials as shown in the previous section. To be able to introduce a direction-dependent mass density in this system, one can use the independent design freedom on the mass density and the bulk modulus of these materials. The easiest approach towards an anisotropic material, is to consider a layered structure with alternating properties. Here the alternating material property is the mass-density of such a bi-layer structure, where each individual layer shows an isotropic mass-density. As the pentamode materials allow to create a material with changing mass-density and constant bulk modulus, one can make this alternation only influencing the density. The basic principle of inducing anisotropy by the aid of a bi-layer structure has been shown to work in various different physical systems, such as electrical conductivity, thermal diffusion, or even in the bi-harmonic approximation for flexural waves in thin plates, summarized in [40]. Considering this approach for pentamode materials we have seen that we can change the density by about a factor of 10 from one layer to the other by still keeping the bulk modulus constant. Such a layered structure is the analogue to a model with two different masses connected by the same springs. To compare the band structure along different directions and evaluate the direction-dependent properties of the material, an extended unitcell is considered based on two different effective materials just different in their density. band structure calculations for this cell can be seen in Figure 2.38.

One has to keep in mind that the unitcell has a different elongation in real space along the z direction compared to the x and y directions leading to a smaller brillouin zone along the k_z direction. For simplicity we have colored the longitudinal modes red (along the k_z direction) and green (along the k_x direction). All the other modes occurring from transverse modes, localized resonant modes or even modes corresponding to "optical" branches resulting from the two-atom basis, are depicted in grey. In the long wavelength limit we still find an isotropic material response as the wavelength is much larger than the unitcell and no resonances are excited in the limit $|k| \rightarrow 0$. At about $|k| \approx 0.1$ the bands start to differ from each other as the longitudinal band along k_x (green) flattens whereas the band along k_z (red) only flattens out at much higher frequencies. A simple explanation for this behavior can be found by comparing the properties of the individual layers. In general, one would expect that a mode propagating in the light material is much faster and that there would be a mode splitting comparing the low and high mass density layers. The splitting would, however, only be perfect if there was no coupling by shear forces. This is not the case as the shear modulus is small, but not zero. This coupling can be described by a mass-spring model with large masses for the dense layer and a soft shear spring of the lighter layers. The mass-spring system will be in phase as long as it is driven by a frequency below the eigenfrequency, but will react with a π phase shift driven above the eigenfrequency. This behavior can be described as a negative mass density [40]. As a result we obtain a direction dependent mass density tensor, still dependent on frequency. This tensor, as we have discussed before, is isotropic in the long wavelength limit and becomes highly direction dependent as one approaches the resonance frequency of the system.

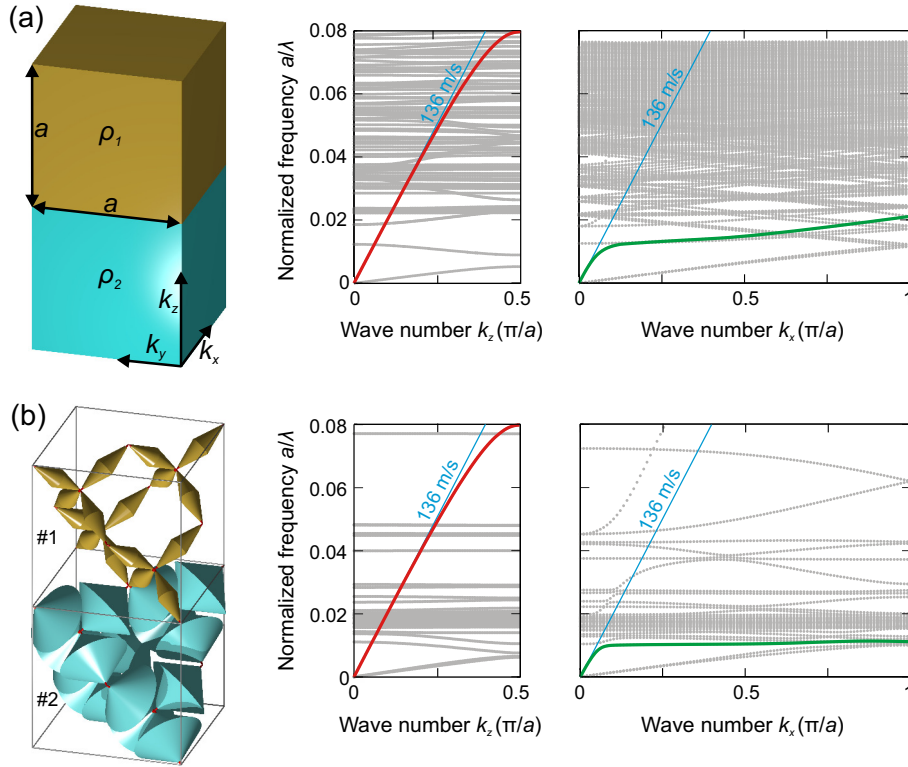
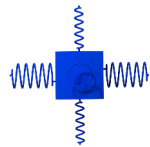


Figure 2.38: Laminate material with constant bulk modulus but changing density. (a) effective material description considering a layered structure composed of two materials with $\rho_1 = 47.4 \text{ kg/m}^3$ and $\rho_2 = 588 \text{ kg/m}^3$ and the same bulk modulus $B_1 = B_2 = 5.9 \text{ MPa}$. band structure calculations corresponding to the k_z and the k_x direction are shown on the right hand side. The longitudinal modes are depicted in red (normal to the layers, along z) and green (parallel to the layer, along xy). The corresponding velocities obtained by the long wavelength fit are shown in blue. The material properties displayed here are in correspondence to the microstructure shown in panel (b). There the microstructure corresponding to the light and heavy pentamode metamaterial are shown. The structure parameters used for layer 1 (2) are $d_1/a = 1.88\%$ ($d_1/a = 1.34\%$) and $D_2/a = 13.4\%$ ($D_2/a = 53.6\%$). The other parameters are unchanged. Previously published in [127].

2.3.2 Spring-Mass Model

To fabricate a structure which is simple to understand in three dimensions and still exhibits anisotropic and negative mass densities, a design inspired by the mass-in-a-mass model is considered. The main idea is to use just one constituent material and to fabricate a structure based on spring like elements inner masses and outer masses. A very simple design has been introduced by Wang [131] and has been explored in detail in [132]. Here a solid cuboid object is used as a spring relating the Young's and shear modulus to spring constants. This design is very simple, as it consists of a solid host material representing the outer masses and the outer springs at the same time. Into this host material periodic voids are cut creating a free space and a periodicity at the same time. This void is then



2.3. Anisotropic Dynamic Density

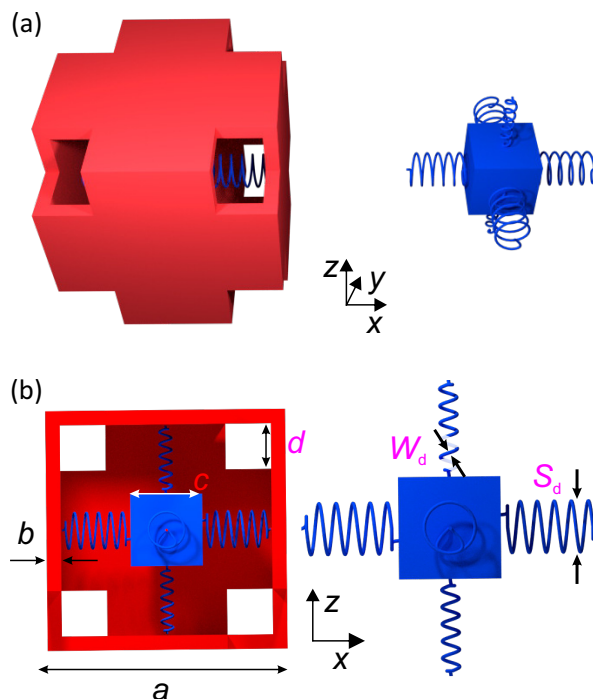


Figure 2.39: Blueprint of our design based on the simple mass-in-a-mass model. The outer matrix is shown in red, whereas the inner mass is shown in blue. Both parts are from the same constituent material. The here shown geometry parameters are: $b/a = 0.05$, $c/a = 0.3$, $d/a = 0.2$, $n = 5$, $W_d/a = 0.01$, $S_d^{x,y}/a = 0.15$, and $S_d^z/a = 0.05$. To relate to the fabricated structures shown in 2.44 we have chosen the lattice constant to $a = 50 \mu\text{m}$. However the design can easily be scaled to any other value. Previously published in [130].

filled with an inner mass and elements that act as springs. These spring-like elements are represented by small blocks of the constituent material, mimicking very stiff springs thus yielding very high resonance frequencies. To decrease the resonance frequencies, we have use a simple helix of the same constituent material as our spring instead. The spring constant of this spring can be determined in principle by

$$D = G \frac{(W_d)^4}{(8n(S_d)^3)} \quad (2.30)$$

with the wire diameter W_d , the number of coils in the winding n , and the spring diameter S_d combined with the shear modulus G of the constituent material. The constituent material is the same for all components to allow for fabrication with additive manufacturing techniques. The resulting design examined here can be seen in Figure 2.39

The outer periodic material is used as a matrix (red), which combines the outer masses and the outer springs as in the Wang design. The inner masses (blue) are connected to the outer matrix via springs which have a direction dependent design. Here we choose a bi-directional design for simplicity, but in general all directions can have a different spring constants. The spring constant can be changed by three different parameters, namely the

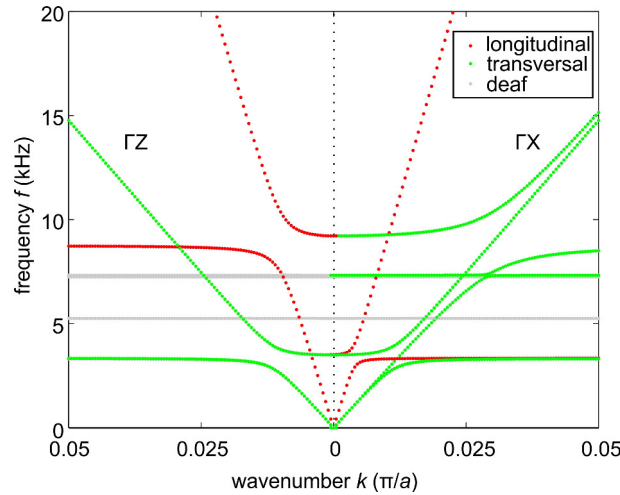
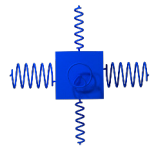


Figure 2.40: band structure calculation along two principle directions for $a = 50\mu\text{m}$. The ΓX direction relates to the softer spring constant for the longitudinal waves. Note that only a small portion of the Brillouin zone is depicted. Previously published in [130].

number of coils, the spring diameter and the wire thickness. To simplify the discussion, here only a variation of the spring diameter is considered.

A fundamental difference to an idealized spring mass system, is an effective shear modulus of the springs, which is related to an additional spring in our model. Considering small displacements, these springs influence cancels out in first order. However one must be careful, as large displacements can occur in resonance. If this is the case the orthogonal springs describing the finite shear modulus have to be considered in the spring constant of the mode. For a realistic spring, especially one made out of the same material and directly connected to the masses, this effect can not be neglected. In general this leads to a coupling of the spring constants along different directions. This coupling limits the range of possible resonance frequencies for some orthogonal wave propagation directions.

In an elastic solid there are three orthogonal polarizations. Thus we expect a longitudinal and two transverse polarization's coupling to the springs and masses. The influence of the polarization of the wave, and thereby the coupling, is rather related to the direction of the displacement vector instead of the wave vector of the elastic wave. To illustrate this, one can consider a mass in a void of the matrix material connected only by one spring to the outer matrix. Let this spring be along the x -direction and consider only waves traveling along k_x . The longitudinal wave will feel the spring constant related to the normal mode of the spring and we can use our simple formula described before. If we now consider a transverse polarization the mass should in the ideal case be isolated from the matrix and should not influence the wave propagation. But a real spring does have a finite shear spring constant related to a transverse movement. This shear spring constant will thus couple to the inner mass and influence the wave propagation just as the normal spring constant did for the longitudinal wave. Adding more springs to the system does not change this behavior, but renders it more complex to interpret.



2.3. Anisotropic Dynamic Density

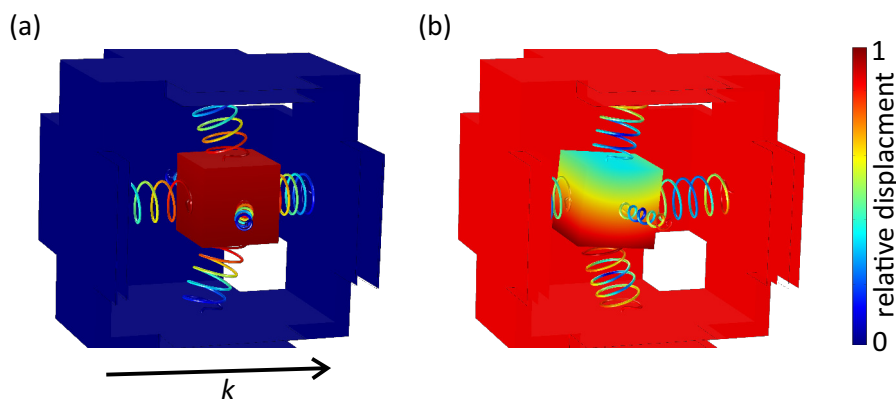


Figure 2.41: Mode shapes right below (a) and above (b) the resonance frequency at the same phase angle. One can see that the inner mass is in phase and out of phase compared to the outer matrix, in the left and right displacement graphs respectively.

To be able to find out how much this coupling influences our design we have performed numerical simulations (the underlying material parameters are: (Poisson's ratio $\nu = 0.44$, shear modulus $G = 0.13$ GPa and the mass density $\rho = 1160$ kg/m³) calculating the band structures along the principle directions. The resulting bands can be seen in Figure 2.40. Here the ΓX and the ΓZ direction are plotted. The longitudinal bands (red) show a characteristic anti-crossing where the resonances occur. One can see that the resonances are shifted in frequency for the two different directions, being related to the different spring constants along these directions. The polarization dependence of the wave can be seen as well by considering for example the longitudinal wave along the ΓX direction. Considering the anti-crossing of the resonance mode with the longitudinal wave mode (red) along this direction, we find that at the same frequency along the ΓZ an anti-crossing occurs as well. This anti-crossing is though for the transverse instead of the longitudinal polarization and colored in green. The same argumentation holds true for the longitudinal mode anti-crossing along the ΓZ direction and one finds a transverse anti-crossing in the ΓX direction at this frequency. This behavior still occurs if one considers ideal masses and is just related to the three-dimensional design. The above mentioned coupling leads to effective spring constants composed of the springs along the displacement vector of the mode and the shear contributions of the springs orthogonal to the displacement. This effective spring constants limit the frequency spacing between the longitudinal mode resonances along different directions. With our design, however, it is possible to clearly separate the two resonance frequencies. This anti-crossing can only be due to a negative mass density for the related mode, since we consider modes which are in the extremely long wavelength regime at wave vectors of about $k \approx 0.004 \times \pi/a$. This relates to a wavelength in the composite of $\lambda/a = \frac{2\pi}{k} \approx 500$ thus a few hundred times larger than the unitcell. Bragg scattering (possibly also leading to a band gap) related the periodicity of the metamaterial can be neglected in this limit. Hence only the elasticity matrix or the density can be causing this effect. A final distinction can not be done by a band structure calculation alone. Here, one would need transmission-reflection type of simulations revealing as well the wave impedance of the material. This in combination with a band structure calculation

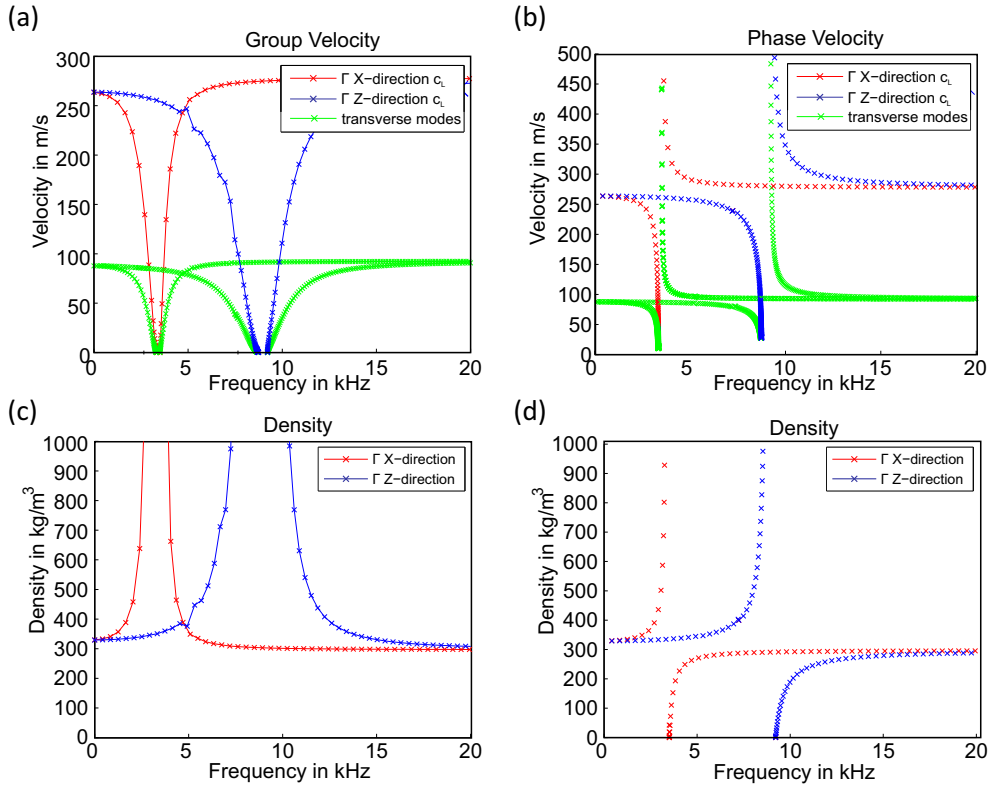
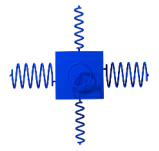


Figure 2.42: Retrieved velocities from the band structure seen in Figure 2.40. The group and phase velocity show significant dips at the resonances. Considering the group velocities one finds a divergence of the retrieved density. Considering the phase velocity to retrieve the density one can see that the mass density above the resonance is rising from zero, suggesting that it is negative at some point before this.

can then be used to distinguish between a negative elastic modulus and a negative mass-density. As effects of a negative mass density will occur only on the order of a few wavelength, thousands of the already quite complex unitcells would have to be simulated, simply not being possible by today's standards. Therefore, we can use a few hints towards a distinction of a negative mass density and a negative modulus. First of all, one can compare the design mechanism and the related geometry to various different designs, which revealed the occurrence of negative mass density [7, 40] considering smaller λ/a . The second hint is that the group velocity approaches the same value again for frequencies above the resonance. The last and most convincing consideration one can do, is to look at the mode shape right below and above the resonance (see Figure 2.41). At the resonance no modes are present thus not allowing to determine the mode shape. The inner mass is, in the case of the negative-mass-density model described above, moving out of phase with relation to the matrix. Mode shapes around this resonance do show exactly this behavior allowing for a direct comparison as the design is very close to the ideal model. The corresponding velocities and densities can be seen in Figure 2.42.

In the corresponding band structure calculations we see that the negative mass density occurs at extremely small wave vectors. This allows to operate at a long wavelength



2.3. Anisotropic Dynamic Density

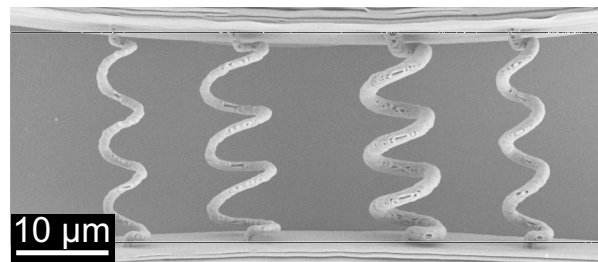


Figure 2.43: Scanning electron micrographs of microscopic springs with changing wire thickness and spring diameters.

in comparison to the lattice period. Relating to the unitcell size of $a = 50 \mu\text{m}$ and thereby gaining the absolute frequency of only a few kHz reveals an interesting feature. This means that the corresponding structures exhibit band gaps in the audible range even though the materials lattice constant is many times smaller. This feature can have interesting applications in sound guiding and canceling on small length scales. Although the design has been simplified to a large extent, fabrication still imposes high demands on precision and complexity. As we would like to fabricate the unitcells as small as possible we have used the DLW technique. Fabricated springs showing different spring and wire diameters are shown in Figure 2.43. One can clearly see that although the springs are written in a layer by layer fashion, thus only connecting the different coils at the very end, all springs show a decent structure quality.

This evaluation leads to the conclusion that it might indeed be possible to fabricate structures in accordance to our blueprint. Samples with a lattice constant of $a = 50 \mu\text{m}$ can be seen in the Figure 2.44. The cut out windows, see openings on the corners, allow to develop the structure and remove the resist from all unitcells. Furthermore, they are used to reduce the relative mass of the matrix compared to the inner mass. The springs within the structure can be seen through the top openings. Although the wire thickness of $W_d = 0.6 \mu\text{m}$ is slightly larger than the design value of $W_d = 0.5 \mu\text{m}$ and there is some significant surface roughness the springs show good overall agreement to the blueprint.

To be able to measure these materials, one would though have to produce a structure with dimensions representing at least one wavelength for an frequency of interest. As we have seen before the materials interesting features occur at wavelength about 500 times larger than one unitcell directly translating into at least 500 cells needed. As a direction dependence and thus anisotropy is the key feature of this material one has to produce these many cells along at least two, if not three dimensions. This is unfortunately still not possible given the enormous writing times resulting from this estimation. We have shown though that it is in principle possible to tune the dynamic mass density of a mechanical metamaterial and that it is even possible to do so depending on the direction. Furthermore, we are able to fabricate microscopic samples in accordance to the designed structures.

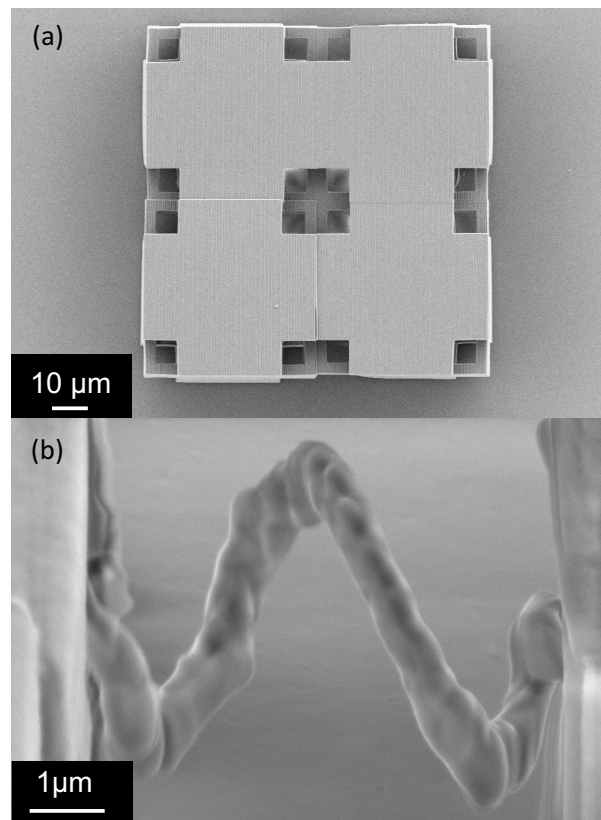


Figure 2.44: (a) Microscopic sample consisting of $2 \times 2 \times 2$ unitcells with $a = 50 \mu\text{m}$. (b) Zoom onto one of the springs revealing the fabrication tolerances. Previously published in [130].

3 Elastic Cloaking

Generally cloaking means to make an arbitrary object appear just like the surrounding by adding a cloak around the object. In fact cloaking is meant to work only with respect to a certain physical observable, e.g., an optical cloak hinders the observer to see the cloaked object. In this sense elastostatic cloaking means that no difference in the stress or strain field of an elastic solid with a cloak is measurable. To be able to achieve this, materials not found in nature are required. The theory of elastic cloaking brings forward the need for special mechanical properties and an feasible way to tailor the mechanical behavior space dependent. Within the last chapter we have seen how one can tailor the mechanical and density related properties of an elastic metamaterial.

In this section two different approaches towards elastic cloaking are discussed and it is shown how the basic design of an elastic cloak can be translated into a micro structure and a functional cloaking device. These final cloaking devices are able to render an object invisible, thus hinder to detect an object by stress strain probing. These cloaks hide an obstacle with respect to its surrounding and in this way cloak the object from detection via feeling. In other words – we fabricate and characterize an unfeelability cloak. To get an intuitive feeling what this means in elasticity a simple example is given in the Appendix B, Figure 1.

Cloaking, as discussed in the introduction chapter, has to fulfill some very complex mathematical equation systems originating in the elasticity tensors and anisotropic mass density tensors. To be able to reduce the complexity of the discussed cloaking concepts we exploit a simplification of the equations, turning both tensors into a scalar, leading to the acoustic equations. This resultant equation set is form invariant under coordinate transformations and one can use the normal procedure of mapping materials to effective parameters in order to obtain a cloaking device. This though requires a material with strictly zero shear modulus, thus a fluid. These initially spatially separated materials would rapidly intermix with each other and the design of a cloak seems impossible. However, adding a little shear modulus to the system changes the problem dramatically. Even a very small shear modulus will lead, inducing some finite deformation, to finite forces. This is distinct from liquids, as the structure would have a finite restoring force which can be used to hinder the materials from intermixing. As the underlying physics are a lot easier in the acoustic regime some cloaking devices have been presented there based on acoustic waves in water [54, 133], ground cloaks based on holey plates [134, 135], temperature gradients [136], and omnidirectional but single frequency free space cloaks designed by numerical optimization [137]. All of these cloaks are designed by a modification of the surrounding of the liquid rather than the liquid itself. By adding stiff objects the wave propagation within the liquid is essentially modified and thus a cloaking behavior is obtained. In mechanics a modification of the basic material rather

than its surrounding is needed. There have been only two preliminary results based on the actual modification of elastic properties used for cloaking. The first one uses a fibrous material system to deviate a stress wave around an object [138]. Here the direction of the stiff fibers guides the wave along the fibers and an effective anisotropy can be obtained. The design is based on a unidirectional guiding of the stress wave around a void in an object. The second example has been done in our group by Nicholas Stenger and is based on a parameter retrieval of effective material properties based on the biharmonic approximation for flexural waves in thin plates [42]. Both designs are based on very specific physical situations and are using a macroscopic assemblage of two materials.

In this section elastic cloaking is performed based on effective material parameters which are tuned and tailored by the structure rather than the composition of materials. Static cloaking can be obtained using two different approaches, leading to two different cloaking performances in different physical situations. The first one is based on a core-shell approach allowing to tailor bulk modulus values for the cloaking of a stiff inner core. The second approach is based on a direct transformation of lattice points of a former homogeneous material, allowing to cloak even voids in a material without a core. Both of these cloaking concepts require mechanical metamaterials explained in the previous chapters. The extensive knowledge gained about mechanical metamaterials can be exerted on the design of the cloaks. Parts of the chapter have been published and figures are in accordance to or taken from the publications: [139, 140].

3.1 Core-Shell Cloaking

The basic concept of core-shell cloaking has been shown by Mansfield [141] in 1952 and Kerner in 1956 [142], which have later been summarized by Milton in his book about composites [17]. The concept is based on the idea of a neutral inclusion where one radial shell compensates another shell to have effectively no impact on the surrounding medium. With regard to the elastic cloaking theory one can simplify an array of radially distributed shells to the absolute minimum, which is a core and one shell, returning to the core-shell theory. This theory states that for zero shear modulus there is an exact solution where one can find a bulk modulus B_2 for a shell to compensate a core with B_1 in that the static properties are exactly as a surrounding medium with bulk modulus B_0 . If one expresses the moduli corresponding to the fractions filling the shells, thus to the radii of the shells one finds (see Appendix for the derivation)

$$B_0 = \frac{B_1 B_2}{f(B_2 - B_1) + B_1} \quad (3.1)$$

with the filling fraction f for the cylinder design and for the spherical design

$$f_{2D} = \left(\frac{R_1}{R_2}\right)^2, \quad f_{3D} = \left(\frac{R_1}{R_2}\right)^3 \quad (3.2)$$

The radii R_1 and R_2 correspond to the geometries in Figure 3.1. The bulk moduli are indicated as well. One can find closed expressions for a cylindrical and a spherical design.

3.1. Core-Shell Cloaking

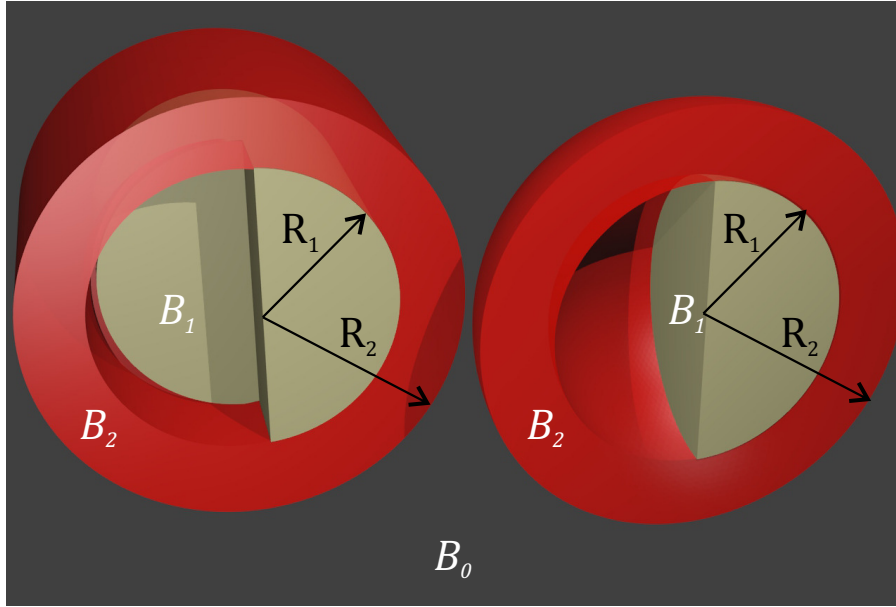
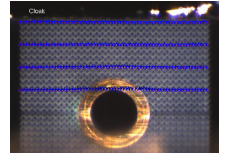


Figure 3.1: Core-shell geometries corresponding to the cylindrical (left) and spherical (right) design. The radii and bulk moduli are indicated.

In general these equations are exact. But considering for example a unidirectional deformation, the inner core deforms from a circular object into an ellipse. Consequently to cloak an object an rigid, thus not deforming, inner cylinder is required. This reasoning, leading to a rigid inner cylinder, requires $B_1 = \infty$. This constraint allows to directly relate the two radii with the two remaining bulk moduli as follows:

$$\frac{B_2}{B_0} = 1 - \left(\frac{R_2}{R_1}\right)^{-2} \quad (3.3)$$

for a cylindrical design (2D) and for the spherical design (3D)

$$\frac{B_2}{B_0} = 1 - \left(\frac{R_2}{R_1}\right)^{-3}. \quad (3.4)$$

The assumptions are exact for vanishing shear moduli for all materials. But for vanishing shear modulus neither can one create materials that do not intermix, nor can the inner part be made rigid, in the sense that deformations are prohibited ($B_1 = \infty$ and $G_1 = \infty$). To be able to create such a core-shell cloak a finite shear modulus needs to be allowed. Assuming very small shear modulus in the surrounding and cloak seems a fairly good approximation, even though perfect cloaking can not be realized for finite shear moduli. The inner core needs a large shear and bulk modulus to qualify as rigid compared to the other two layers, to not deform during any exertion of stress onto the overall structure. This further allows to leave the idea of a solid inner core, and cut a void with radius R_i into this rigid material. This void is protected from the outside by the rigid material and one can place any arbitrary object into the created space. As the design of the cloaking shell lets the inner core appear as the surrounding, the cut void into the rigid material

does not change this behavior. The above mentioned formulas allow us thus to calculate a bulk modulus for the cloaking shell surrounding the inner stiff core for all radii of the core and shell and all bulk moduli of the surrounding. Keeping in mind that the formula is a good approximation as long as the cloaking shell has a more than about one hundred times larger bulk modulus than shear modulus ($B_2/G_2 > 100$).

3.1.1 Cloak Design: Core-Shell

To be able to cloak an object and insert it into a void as well as simplifying a possible measurement, the cylindrical version of the presented cloaking possibilities is chosen. There is no general difference in the design just the resulting bulk modulus for the cloaking shell is different, and one would have to choose a different material in the cloaking shell. Fixing the radii to an arbitrary ratio of $R_2/R_1 = 4/3$, a ratio of the bulk moduli results of $B_2/B_0 = 7/16 \approx 0.44$. So following the theory two materials are needed that have a very low shear modulus compared to the bulk modulus and whose bulk moduli have the above mentioned ratios. Unfortunately no material exist in nature fulfilling this assumption, but as we have seen in the previous chapters, mechanical metamaterial, especially pentamode metamaterials, can fulfill these assumptions. The material properties of the pentamode metamaterial depends on the size of the connection diameter d and the larger double cone diameter D with respect to the lattice constant. This allows to tailor the bulk moduli and at the same time maintaining the large B/G ratios. Only one material needs to be tailored, namely the cloak, as the surrounding material is an arbitrary choice. This leaves the design of the cloaking shell with only one parameter, e.g. the connection diameter d , to be adjusted. For a choice of a lattice constant of $a = 125\mu\text{m}$ for both materials and fixing the surrounding material ($D_0 = 10\mu\text{m}$ and $d_0 = 6.6\mu\text{m}$), allows to find a connection diameter d_2 for the cloaking shell keeping $D = D_0 = D_2 = 10\mu\text{m}$. The scaling and calculations performed before lead to a connection diameter in the cloaking shell of $d_2 = 3\mu\text{m}$. The resulting design can be seen in the Figure 3.2.

The actual cloaking layer is just one unitcell thick and the radii have the relation $R_i = 2a$, $R_1 = 3a$ and $R_2 = 4a$. To reduce the overall dimensions and thus fabrication time the complete design is reduced to some finite surrounding and due to symmetry reasons it can even be reduced further by considering only one half space and thus only half of the cloak. The resulting geometric design is highlighted in Figure 3.2 (a). The blueprint is translated into the third dimension and extends the geometry. Due to the chosen cylinder design the local properties are not changed along this dimension. The final design is (for the homogeneous material) $16 \times 8 \times 8$ unitcells large corresponding to $2 \times 1 \times 1$ mm and an volume of 2mm^3 .

3.1.2 Fabrication and Characterization Setup

To fabricate such a structure with extends on the mm range, but still keeping the versatility and the resolution to below a μm could only be achieved by DLW in the dip-in galvo-scanning technique. The samples have been fabricated in collaboration with

3.1. Core-Shell Cloaking

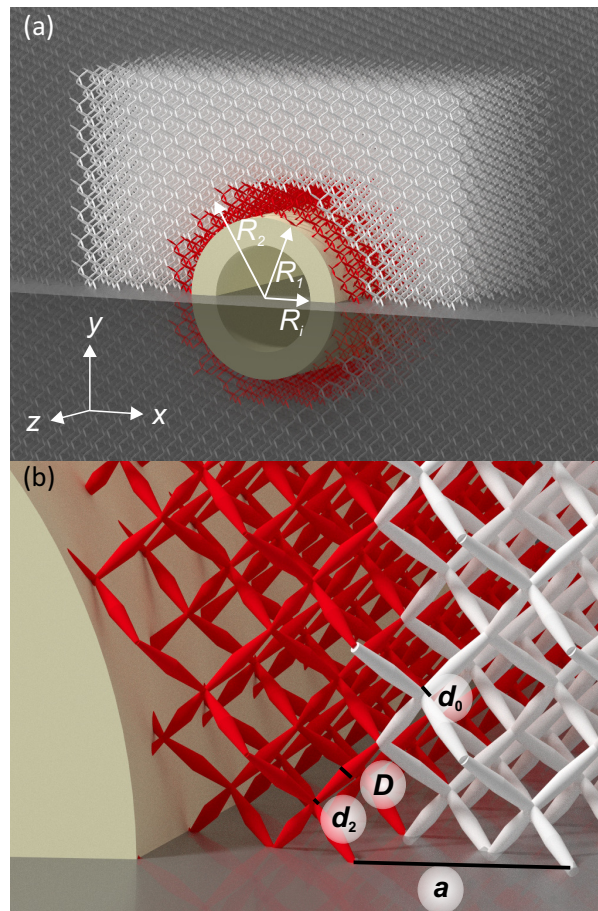
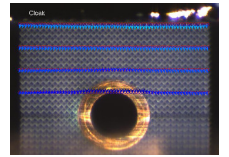


Figure 3.2: (a) Core-shell cloak design consisting of a solid inner core in an pentamode metamaterial surrounding. The cloaking shell (red) consisting of a different pentamode metamaterial effectively hides the solid core within the elastic surrounding medium from detection. (b) The underlying metamaterial parameters are indicated in the zoom onto the cloaking shell. Previously published in [139].

Nanoscribe by Michael Thiel. Here a new objective is used (Carl Zeiss, $25x$, $NA = 0.8$) to allow for scan fields of $500 \times 500 \mu\text{m}^2$. These scan fields are stitched together translating the sample by a linear stage. The splitting of the geometry can be seen in Figure 3.3. The whole geometry is subdivided into 8 scan fields. Each of the scan fields is sliced with a raster resolution in the x, y plane of $0.5\mu\text{m}$ and $1\mu\text{m}$ in the axial direction.

To be able to scan the geometry in a quasi continuous fashion along the vertical or axial direction, the scanning is split into sub-parts along this direction as well. As the precision of the microscope drive is only high enough when moving into one direction, the cloak is build up by a stepping of $10 \mu\text{m}$ on the microscope drive. The procedure is thus as follows. One starts writing one scan field and moves into the third dimension with the piezo. At a height of $10 \mu\text{m}$, the piezo returns to its original position, and the linear stages move the sample in x and y direction to the next scan field. There the piezo and the galvo scanner write the next structure part. This procedure is repeated until all of the scan fields are addressed. After this the microscope z drive is used to translate the

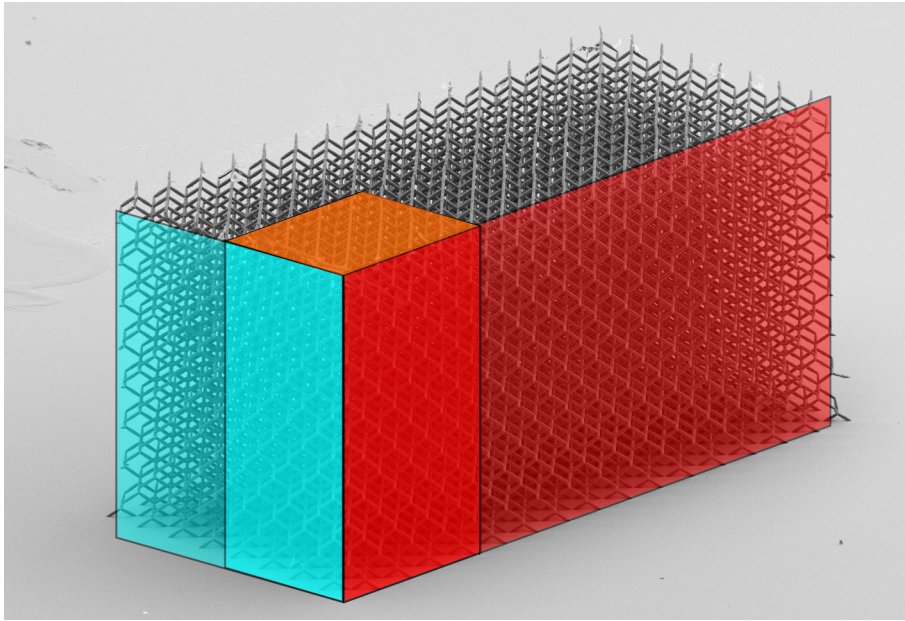


Figure 3.3: Fabricated homogeneous pentamode sample with an overlay of the splitting fields. The blue face is divided into two parts, whereas the red face is divided into 4 parts. The geometry is written quasi continuous in the vertical direction.

objective by $10\mu\text{m}$ and the whole procedure can be repeated. With this procedure effects of the neighboring fields due to aberrations can be minimized and the working distance of the objective does not play a significant role. In order to minimize the writing times, a writing speed of 5 cm s^{-1} is used. The structure is fabricated onto glass cover slips with dimensions $22 \times 22 \times 0.17\text{ mm}$. The used resist is the IP-S resist sold by Nanoscribe. After the writing procedure the undeveloped resist is solved out of the structure by mr-Dev 600 (MRTBerlin). To wash the solvent out of the structure the sample is transferred into acetone hereafter it is critical point dried. The developed sample can be characterized in the SEM and with an optical microscope. Characteristic samples can be seen in Figure 3.4. As one can see within the SEM measurements the fabricated samples actually reveal the same dimensions as the designed values, only the small diameter deviated and turned out to be about $0.3\mu\text{m}$ larger than the design values.

To test the fabricated samples regarding their performance and the functionality of our design, a uniaxial strain is applied into the structures which reveals the cloaking performance with regard to the uniformity of deformation. First of all a reference sample has been characterized. The measurements on the obstacle and the cloak sample can then be compared to the reference and with each other. To induce a uniaxial strain, the sample is placed onto a goniometer to adjust the tilt angles and on top of a linear stage. This allows to position the sample below a linear motorized stage to which a force cell and a silicon wafer are attached. The measurement setup is sketched in Figure 3.5. Here the sample is clamped between the glass substrate and the flat silicon stamp which are aligned by eye. The samples are then imaged from the side revealing the unitcells. For illustration, an optical image of a fabricated cloak is depicted in Figure 3.6. Herein

3.1. Core-Shell Cloaking

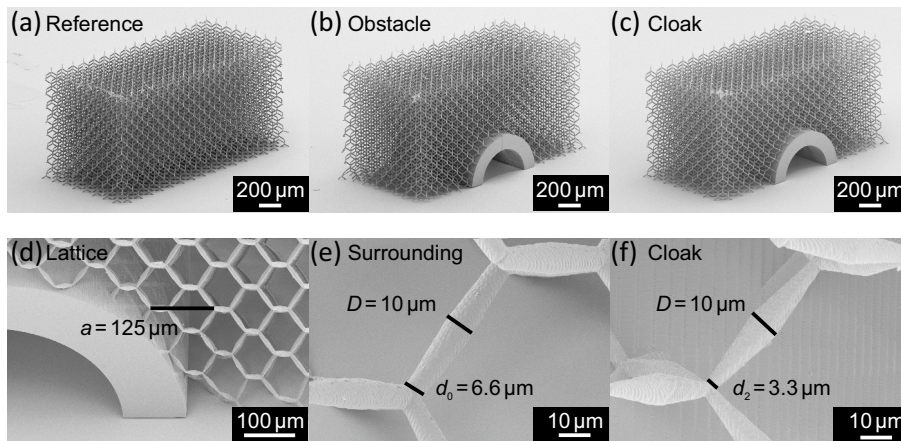
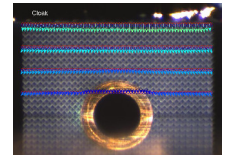


Figure 3.4: SEM micrographs of the samples fabricated. The homogeneous samples as can be seen in (a) consist of just a homogeneous pentamode metamaterial. Into the homogeneous sample a obstacle can be placed and a resulting structure can be seen in (b). At last a cloaking shell is added around the obstacle consisting of a different pentamode metamaterial. The insets in the lower row reveal the lattice period (d), the surrounding material (e) and the cloaking shell (f) dimensions. In accordance to [139].

the substructure and the reflection of the structure on the glass cover-slip can be seen. During the measurement the oblique view in Figure 3.6 is changed to be straight onto the face of the structure. The view is chosen to monitor the largest face of the structure to be able to determine the deformations of the surrounding and the cloaking shell during the measurement. After the alignment procedure, the measurement can be started. The automated linear stage is moved so that the sample is pressed onto by the silicon wafer, inducing a finite strain. The force acting upon the stamp is tracked throughout the measurement and images are taken for each step of the measurement. First the set strain is induced, then a force measurement is taken averaging over a few thousand samples. At last an image is taken, before the next strain value is addressed. The measurement is progressed by increasing the strain over 50 steps and afterwards releasing the strain again with another 50 steps. The rate is chosen to be about 2% per minute. This allows to have a quasi static measurement and not move the sample while taking an image.

After the measurement the cross-correlation approach introduced in chapter 1.3.6 is used to track individual parts over strain rate or time. Markers are chosen as a grid with a rather fine spacing allowing to track the whole of the facet in general. The resulting markers, 15×15 pixel in size, are placed in a grid spanning the whole face of the sample. This grid results in 67 markers in the horizontal and 35 markers in the vertical direction. The tracking allows to determine the displacement of each cell and part of the structure throughout the measurement. The differences between two images can be related to a displacement of the marker corresponding to a certain strain. This procedure allows to create a strain map for each image. To simplify the analysis only four equally spaced lines of markers are picked out and used to determine the cloaking behavior. The first line corresponds to the top of the sample and is used to determine the overall strain. As

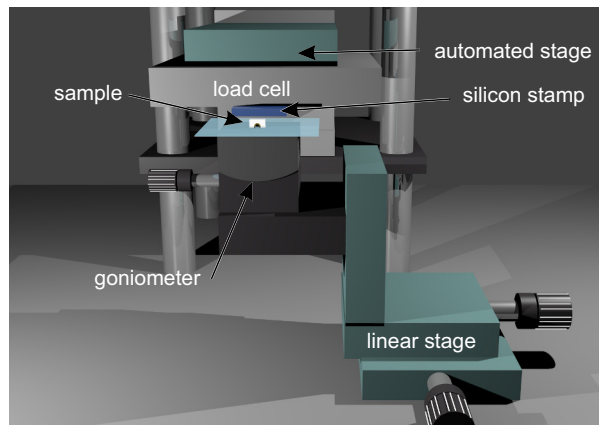


Figure 3.5: Measurement setup with all parts except for the imaging components. The sample is placed with the cover-slip on a goniometer. The goniometer is mounted to a 3D linear stage to position the sample. An automated stage with a load-cell is used as a stamp from the top. To use a flat stamp contacting the sample, a silicon wafer is attached below the force cell.

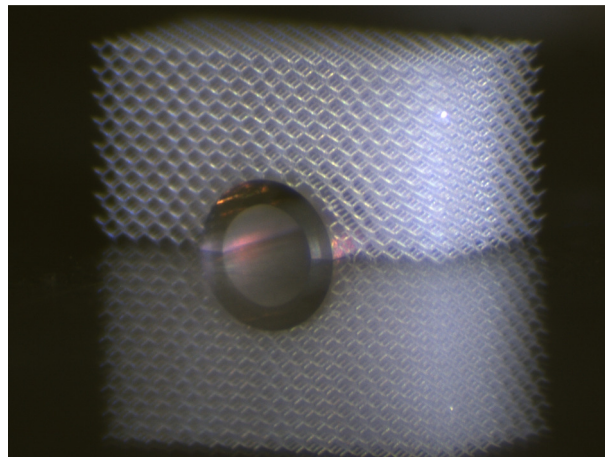


Figure 3.6: Optical image of the cloaking sample. The imaging quality is good enough to reveal the substructure of the sample and even individual double cones. In accordance to [139].

the displacement is fixed at this point of the cloak by the silicon stamp, no deviations can be expected here. The other three left lines are used for a comparison between the different samples. They are numbered 1-3 where line number 1 is the highest, thus above the cloaking shell in the surrounding medium. The line number 2 is positioned such, that the line is in the case of the cloaking sample just outside of the cloaking shell. The last line number 3 is determining the behavior of the samples next to the obstacle and cloaking shell, and is positioned at a lower height, so that it passes through the rigid core in the cloak and obstacle samples. An image with the corresponding lines and the first image of the measurement can be seen in Figure 3.7. To reduce the data to a comparable strain within the sample the stamp movement is used to determine the overall strain through

3.1. Core-Shell Cloaking

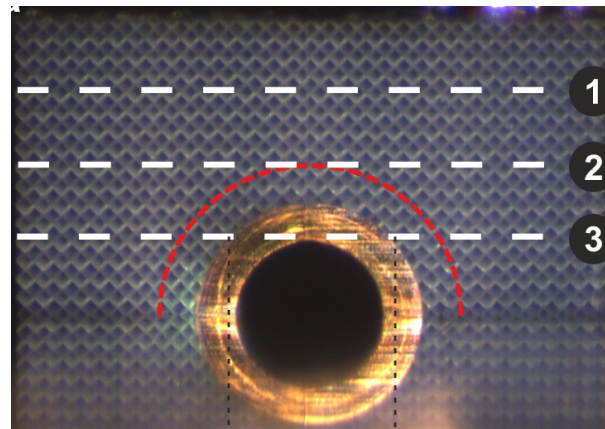
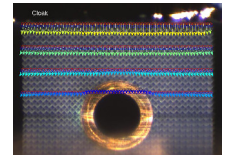


Figure 3.7: Optical image of the cloaking sample as measured. The cloaking shell is indicated as outlined by the red lines. The evaluated marker positioned are shown as line cuts in white and are labeled. In accordance to [139].

out the measurement, and a strain of 2.8% is picked out in all the measurements to compared the displacement at this overall strain. The strain is calculated by normalizing to the overall height of the sample. This procedure allows to plot the lines 1-3 into the same strain-position plots for all samples and measurements, and thereby compare them directly.

3.1.3 Measurement and Numerical Calculations

The measurement and subsequent cross-correlation allow to compare the samples with each other. To do so the absolute strain and the modulus of the displacement are evaluated and compared between the different samples. One has to keep in mind, that for the negative strain within the sample, the highest modulus of the strain occurs at the highest line. The lower modulus of the displacement the less is the structure displaced downwards. First the homogeneous sample is measured and evaluated. The resulting measurement is seen as the green lines in Figure 3.8. The lines are more or less straight for line 1-3 except for some edge effects towards the sample edges. This displacement pattern is our reference as it needs to be recovered as good as possible using the cloaking procedure. One can also estimate the deviations by the comparison between the reference and the obstacle sample. The measured deformations for the cloak are shown as red lines in Figure 3.8, whereas the obstacle lines are indicated in blue. In the panel of line number 1 the deviations are quite small relating the displacements of the cloak and the homogeneous sample. The obstacle case is though displaced less. This reveals the influence of the stiff object already at this position. In line 2, which is positioned closer to the cloaking shell, a much larger deviation is found between the displacements in the obstacle to the homogeneous sample. The changed displacement in the obstacle thus reveals the stiff inner core. The cloak recovers the displacement of the homogeneous sample to a very large extent and hides the influence of the stiff core. At line 3, the displacements outside of the cloaking shell (shaded gray area) show only small deviations. But upon closer examination the

obstacle case has a nearly constantly increasing strain moving away from the stiff object, indicated by the dashed line. The cloak shows a different elastic behavior. Here the strain is dramatically changing within the cloaking shell, whereas outside of the shell the same strain and also the same strain curve are measured as for the homogeneous sample. This means that the stiff core is compensated within the cloaking shell, and the displacement field is recovered for the surrounding material with respect to a homogeneous sample.

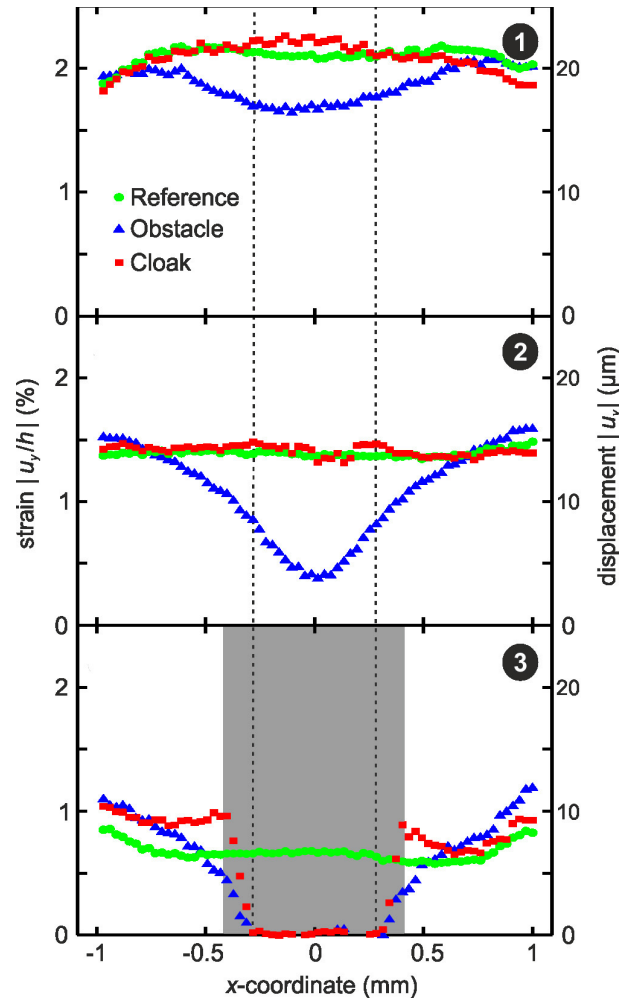
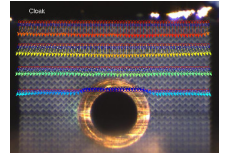


Figure 3.8: Measured strain and displacements for the selected lines of the reference, obstacle and cloak sample. The modulus of the strain is given in % and can be compared to the real displacement in μm . The cloak and homogeneous sample show nearly the same displacements for lines 1-3, whereas the obstacle deviates significantly and thus reveals the influence of the solid core. In accordance to [139].

The cloak can recover the displacement field on the surface of the block to a very good extend. This means that we can actually cloak an stiff object elastically. To be able to compare the measured performance to a numerical calculation and thereby try to estimate the dependence on the depth of the sample we have tried to compute the structure under homogeneous strain from the top. Unfortunately it is not possible to simulate the whole structure as the memory and computational resources available are not sufficient. It is

3.1. Core-Shell Cloaking



thus possible to compute a reduced geometry comparable to $16 \times 8 \times 1$ fcc unitcells, corresponding to the first layer of the structure. The boundary conditions are left free on the outer sides, and fixed at the bottom corresponding to the adhesion to the substrate. On the top boundaries the structure is displaced downwards, but is fixed in x and y to mimic a non slipping condition at this boundary. The front face is left free to move as well, but the back surface is programmed to slide along the surface corresponding to a finite but extended sample. This allows to compare the numerical calculations to the actual sample with as little deviations as possible.

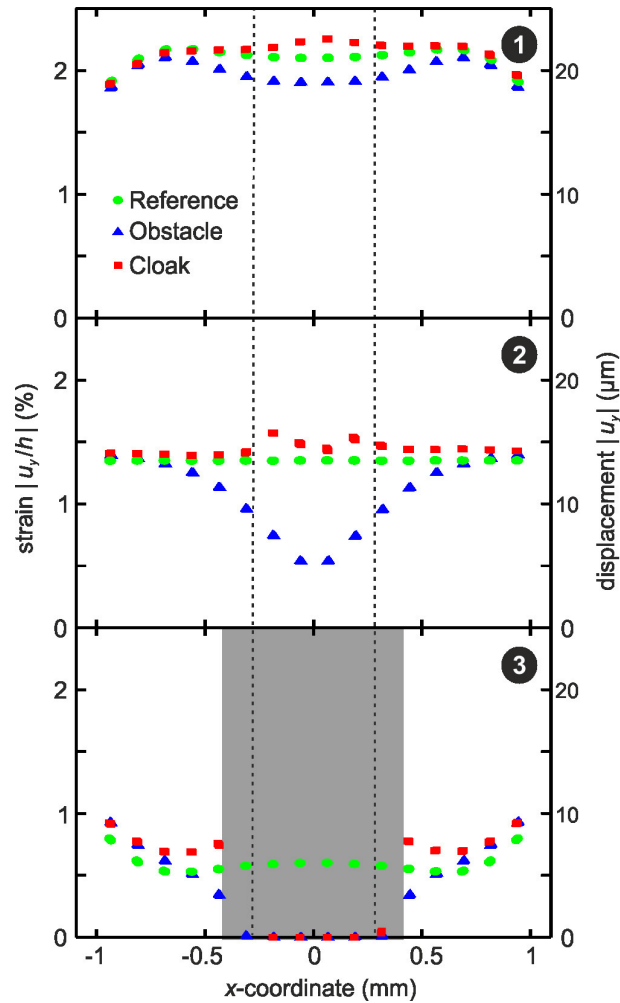
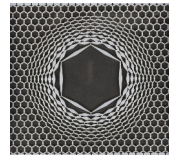


Figure 3.9: Numerical calculations evaluated in correspondence to the measurement. The same lines are evaluated and a strain and displacement is calculated and plotted over the position as in the measurement. In accordance to [139].

The results of the numerical calculations are evaluated just in the same fashion as the measurement, except, that one can use the displacements directly given from the calculations and no cross-correlation needs to be performed. The simulation can only evaluate the displacements at positions where an overlap of the evaluated line and a geometry exists. The resulting line representations are plotted just in the same fashion

as the measurement in Figure 3.9. Here again edge effects occur because of the finite samples, whereas the good cloaking performance of the core-shell design is verified. Even in these simulation small deviations from a perfect cloak are found, indicating that the deviations in the measurements are not due to measurement of fabrication errors, but due to the approximations in the core-shell design and the finite number of unitcells.

To sum up the outcome of the performed experiments we find that it has become possible to cloak a stiff object in an elastic medium in the quasi static regime and recover the displacement field outside of the cloaking shell. The elastic core-shell theory is employed to find a relation of bulk moduli of the cloaking shell compared to the surrounding material. Thereafter pentamode metamaterials are used to simultaneously tailor the bulk modulus while maintaining a bulk to shear modulus ratio large enough to decouple the shear deformation, and approximate $G \approx 0$. This allows to generate a cloaking geometry with effective material properties. This geometry is fabricated using DLW and numerically modeled corresponding to a finite sample. The samples are measured and evaluated using a cross correlation approach. Characteristic lines used to compare the homogeneous material with the obstacle and cloaking sample are tracked and a displacement as well as a strain is calculated. Different characteristic features are analyzed and the cloak is shown to recover the displacement of the reference outside of the cloaking shell. Significant deviations for the obstacle case show that a large and soft surrounding material is not enough to cloak a stiff object. The design is supposed to work in the quasi-static regime which is valid until a wavelength is approaching the size of the cloak, rendering the frequency range in the approximate interval of $[0, 100]$ kHz for the fabricated geometry dimensions.



3.2 Lattice Transformation Cloaking

We have previously seen that one can cloak a rigid elastic object in a pentamode surrounding medium. This can be done by a simple core-shell approach and can thus work with isotropic elastic media placed around the object. If one tries to exchange the inner stiff object by a void, $B_1 \rightarrow 0$, the core-shell formulas do not lead to a solution. Thus the core-shell approach cannot allow to cloak a void in this case. In general the 2D problem of uniaxial stress or strain on a hole in a plate is known as the Kirsch plate problem [143]. This leads to a stress concentration around the hole possibly leading to fracture and fatigue behavior at hole site's. Theoretical solutions exist but do not arrive at a realistic material distribution [141]. All these problems are addressed by the lattice transformation approach presented in this section.

3.2.1 Cloak Design: Lattice Transformation

To explain the concept of a lattice transformation cloak considering a different physical setting can help to understand this basic concept. Starting from a resistor network like the one depicted in Figure 3.10 a simpler electrical conduction description is used for an initial description. The basic resistor network consists, as seen on the left side, of equal resistors connected by wires (which do not embody a resistance) at lattice points. The equal resistance between each of the lattice points can be exchanged by one homogeneous material with a defined shape. If the shape is the same for all of these elements, the resistance of the network has the same pattern as before. The elements used here are double conical elements with a connection width of w at the lattice points and a central width of W in the center between two lattice points. The length of such an element is simply given by the distance between two lattice points. Here an arbitrary resistance is chosen for the homogeneous material which meets the resistance of the resistors. This leads to no change in the general behavior and the resistor network can be described as a effective material with an effective resistance.

The basic idea of a lattice transformation cloak is to transform the lattice points and to reposition them in space. As a second step, elements are inserted between the lattice points still having the same physical quantity rendering the change in geometry undetectable. As one example we exploit a Pendry transformation [45, 46] mapping a point to a finite circle and transforming the space around in a radial fashion up to a second radius. It is described by:

$$r' = R_1 + \frac{R_2 - R_1}{R_2} r \quad (3.5)$$

where R_1 is the inner and R_2 is the outer radius, setting the interval for the transformed radius $R_1 < r' < R_2$ and the initial radius $0 < r < R_2$. The angles are preserved in this transformation, and the space is left unchanged for radii larger than R_2 .

This transformation applied to the lattice points leads to a new distribution of these in the area between R_1 and R_2 . with a void in the center of radius R_1 . To relate to the undeformed space and keep the same physical properties one needs to insert the same

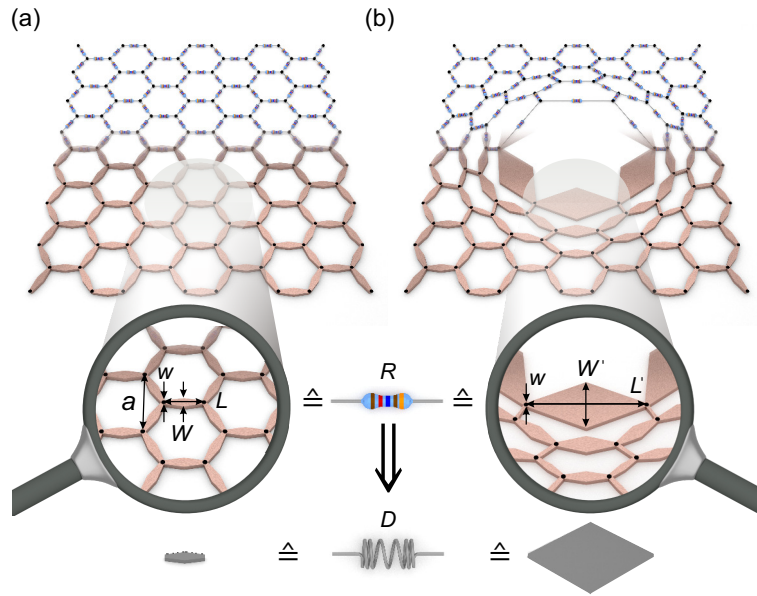


Figure 3.10: Design principle of a lattice transformation cloak. A simple resistor network, connected at black lattice points, is transformed, and afterwards the resistors are exchanged by one material. The double conical elements are designed to have the same resistance regardless of what length they have. (a) Homogeneous periodic material consisting of a resistor network. The resistors can be exchanged by a conducting elements made out of one material. The elements are determined by the connection width w , the central width W and the length L . The lattice constant a is thus connected to the length L . (b) Transformed lattice points with inserted elements of same conduction. Here the elements are changed in width $W \rightarrow W'$ corresponding to their changed length $L \rightarrow L'$ to keep the conduction of each element and thus the whole network the same. this basic principle can be transferred by replacing the conduction with a spring constant for mechanics. Previously published in [140].

physical quantity, e.g. resistance, between two lattice points. This can easily be done in the resistor network, taking the same resistors between the lattice points (the actual connecting wires have zero resistance). It is immediately clear that the new distribution of resistors will not be detectable from the outside by probing a resistance throughout the network. To be able to keep the resistance between two lattice points the same in the design consisting of one constituent material, we need to change the geometry as we change the distance between to lattice points (keeping the constituent material fixed). To do so, the central width W is changed as a function of length L of the element. The connections are kept constant in order not to change the connection behavior at the lattice points, which would lead to unconnected geometry parts and a changed resistance in the connections. As the resistance of a wire is proportional to the length and anti proportional to the cross-sectional area (in 2D to the width), one has to integrate the cross-section of the wire along the length of the wire to obtain the actual resistance. This leads to the relations (see Appendix 3.1):

$$\frac{L'}{L} = \frac{W'/W - 1}{W/w - 1} \cdot \frac{\ln(W/w)}{\ln(W'/w)}. \quad (3.6)$$

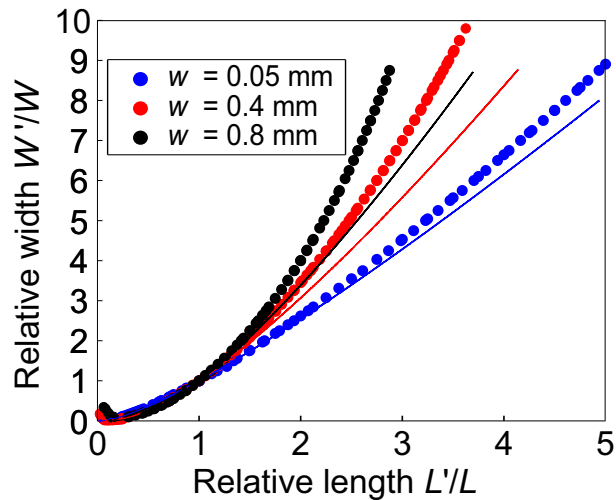
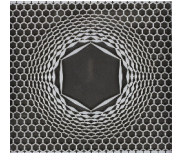


Figure 3.11: Curves of constant spring constant D or constant resistance R of the trapezoidal elements. The parameters are for an initial length $L = 4$ mm and $W = 1$ mm. The curves are shown for three different connection width w . The dotted lines correspond to numerical calculations taking a not uniform stress over a cross-section into account. Previously published in [140].

The returned solution can not be directly solved towards W' , but one can perform an indirect retrieval of the dependence as one can plot the ratio of length L'/L over the change in central width (w is fixed) W'/W , and for any change in length interpolate to get the right central width W' . Such a retrieved curve is shown in Figure 3.11.

This gives the possibility to find an element consisting only of one material which keeps the resistance R of each element fixed, and thus the overall resistance of the network constant. This renders the changed geometry and the void in the center invisible to the resistance measurement, effectively cloaking the void. This basic concept can easily be translated to other parts of physics showing the same physical equations, e.g. the electric permittivity ϵ , the magnetic permeability μ , the diffusivity D and the heat conductivity κ . The underlying physical equations and the construction concept is always the same for all of these settings, and can thus be applied in a straight forward manner. A more interesting case is mechanics. Here it is not directly clear what happens if one uses the spring constant D as a fixed parameter. The procedure stays the same though. One calculates the dependence of the spring constant of each element on the length and width. In general this leads to the same dependence than for the conduction case, but in the mechanical considerations one has to make the assumption that the stress is uniform over an cross-sectional area. This is not the case for all parameters. Thus a numerical calculation is used to find the dependence taking this deviation into account. The outcome of the calculations are plotted as dots in Figure 3.11. As the numerical calculations are assumed to be more accurate they are taken to form the geometry. The procedure can be applied just in the same fashion as before resulting into a transformed geometry. In an actual lattice it can in principle happen, that adjacent elements start to overlap with each other and thus change the geometry. To prevent this one can limit the maximum width

W' allowing for some extra space depending on the transformation. As the length scales are only changed in the radial direction, the lattice constant is also changed radially as $a' = a(R_2 - R_1)/R_2$. As the maximum width is restricted to be a lattice constant (half a width from both elements at the sides of a lattice cell), we find (allowing for 10% extra gap):

$$W'_{max}/a = 0.9 \frac{R_2 - R_1}{R_2}. \quad (3.7)$$

This limitation affects only elements at the inner most part of the structure.

3.2.2 Numerical Calculations

After the design procedure a numerical characterization of the mechanical performance is done by evaluating the deviations of the cloak from the homogeneous material prescribing different loading conditions, transformations, and initial parameters. For all these calculations we have used the same constituent material ($E = 3$ GPa and $\nu = 0.4$) with an linear elastic calculation performed in COMSOL Multiphysics. The computation are performed in a 2D calculation allowing for a reduced calculation time. As one can only take a finite surrounding into consideration, here a homogeneous sample of a fixed size is used as a reference. The transformed cloak can be compared to a homogeneous sample with a cut out hole of radius R_1 as an obstacle. As a first test a uniaxial homogeneous load with sliding boundary conditions orthogonal to the loading direction is calculated. The geometries (from top to bottom: homogeneous sample, obstacle and cloak) can be seen in the left column of Figure 3.12.

The calculations are performed by applying a total pressure (33 kPa) on the outer boundaries on the left and right side. A calculation is taking about 2.2 million mesh cells into account, slightly changing from design to design. To be able to compare the different designs of cloaks to the obstacle case and to the homogeneous reference, three characteristic measures are extracted. The first one is the stress distribution through out the structures (von Mises stress). These plots are shown in the left column of the Figure 3.12. The second measure is the resulting strain value, here split into both components ϵ_x and ϵ_y evaluated at the lattice points. The representation in the two right columns of the figure is displayed on a saturated scale stretching the scale by a factor of 5 with respect to the maximum strain occurring (normally in the obstacle ϵ_x). To give an example, if the maximum strain is 1.6% representing a colorscale value of 100, all color values are multiplied by 5 and all color values in the interval of [100, 500] are set to color value 100. Thus the maximal strain and the strain corresponding to the maximal color scale strain are given at the colorbar. The last value used for comparison is kind of a standard deviation between the cloak or obstacle strains compared to the reference, called Δ . The exact calculation is done by summing over the differences in the vector components of the displacement vectors \vec{u} , and normalizing to the homogeneous case with displacements \vec{u}^0 as:

$$\Delta = \frac{\sqrt{\sum_i (\vec{u}_i - \vec{u}_i^0)^2}}{\sqrt{\sum_i (\vec{u}_i^0)^2}}. \quad (3.8)$$

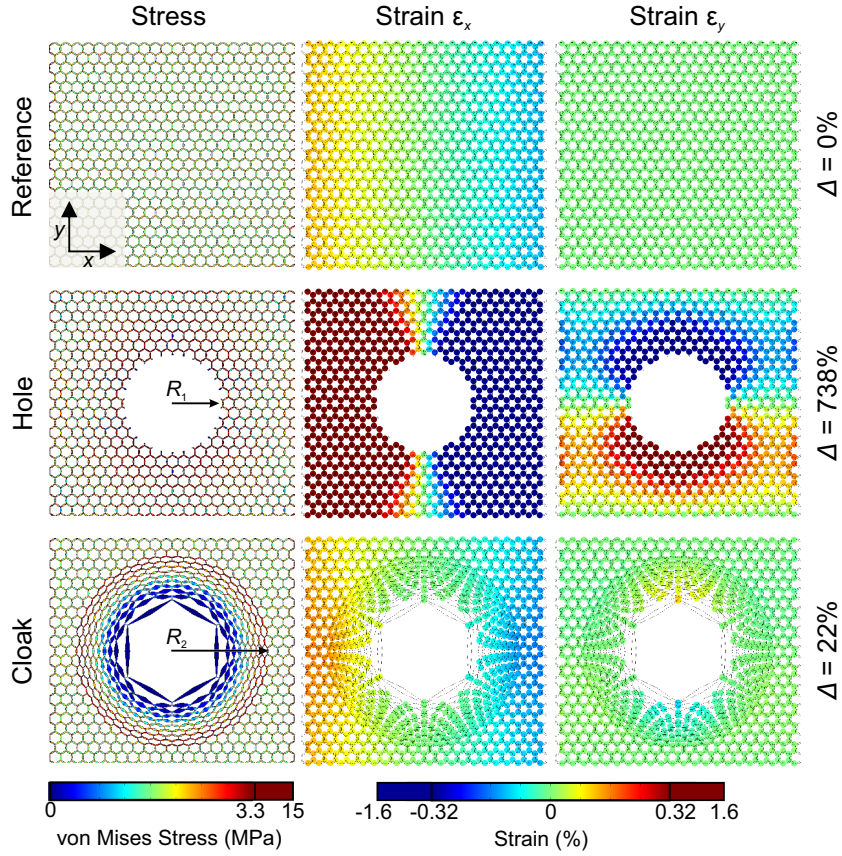
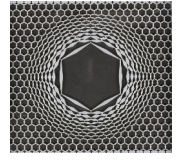


Figure 3.12: Numerical calculations for a uniform stress along the x -direction. The outer boundaries along the y -direction are set to be sliding, corresponding to $u_y = 0$. The geometrical parameters are $L = 4$ mm, $W = 1$ mm, and $w = 0.4$ mm. The transformation radii for the cloak are $R_1 = 30$ mm and $R_2 = 60$ mm. The stress and strain values are represented on a saturated scale. The strain values ϵ_x and ϵ_y are given for the lattice points. The deviations Δ for the obstacle and hole case are given on the right. Previously published in [140].

This procedure is evaluating all lattice points outside of the cloaking region R_2 . Inside of the radius R_2 the lattice points have no correspondence or are initially misplaced in comparison to the homogeneous case. The resulting deviations Δ are given in percent on the right side of each row, and thus structure. These data allow to compare the obstacle and cloak to the homogeneous material, illustrated in Figure 3.12. Here one can see that the stress is concentrated into the cloaking shell, but herein it has a distribution in the radial direction, decreasing towards the center. This means that the stress is guided around the void and is thus distinct from a hole in a plate consideration. This is transferred into the strain pattern. In the first row (homogeneous sample) only a strain along the horizontal direction is present. A comparison of the reference to the obstacle in the second row obviously shows large deviations. The strain is such, that the material moves into the central void. Comparing the cloak, this behavior is reduced immensely,

and the deformation is reduced as well in comparison to the homogeneous case. An estimation on how large this effect really is, can be found by comparing the values of Δ . Here one finds that an average deviation of $\Delta = 738\%$ is present for the obstacle whereas this deformation can be reduced to $\Delta = 22\%$ in the Cloak case, improving the performance by a factor of 34. This percentage and improvement factor are changing for a different surrounding material size. The larger the surrounding the smaller is the influence of the cloak or hole, and thus the deviations. This is why only surroundings of the same size and thus same number of lattice points are compared. To find out how general this procedure is various changes of the design and probing have been calculated, and are presented in the Appendix. It turns out that the lattice-transformation approach is able to allow for cloaking in various circumstances. The approach is neither sensitive on the transformation parameters or the initial lattice structure, nor on the loading condition or the exact dimensions of the conical elements. The data evaluated in the Appendix is summarized in the table 3.1.

Table 3.1: Summarized outcome of a parameter study for the lattice transformation cloak. The extensive calculations and discussions are given in the Appendix.

Changed Parameter	Δ_{hole}	Δ_{cloak}	Improvement Factor
90° rotated loading	684	24	29
Young type of loading	91	29	3
Shear type of loading	92	28	3
$R_1 = 15$ mm	246	6	41
$R_1 = 35$ mm	958	30	32
$R_1 = 40$ mm	1476	47	31
$R_1 = 30$ mm cut at $R_{cut} = 40$ mm	738	32	23
$w = 0.05$ mm	2368	56	42
$w = 0.8$ mm	244	19	13
Square lattice $R_1 = 30$ mm	666	28	24
Square lattice $R_1 = 15$ mm	233	14	17
$W' = 1$ mm	738	19	39

3.2.3 Fabrication and Measurement

As the numerical calculations seem to be very promising and show an excellent cloaking performance, a validation of these calculations with an actual experiment needs to be done. In order to do so the samples needed to be designed exploiting additional features, which on the one hand allow to optimize a sliding boundary condition, and on the other hand provide a way to exert a force into the sample. Blocks of solid material are added

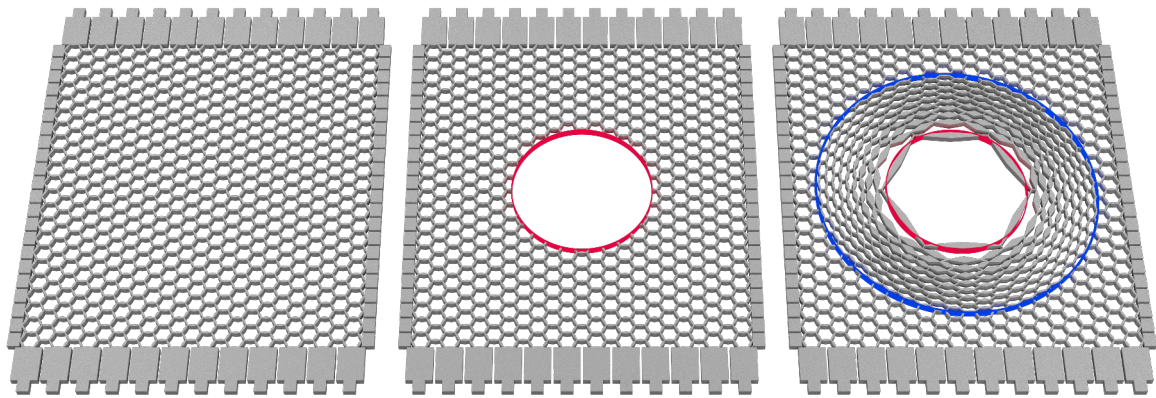
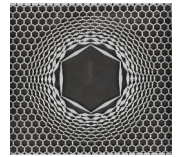


Figure 3.13: Sample designs as used in the measurement. The design from the numerical calculations is used and blocks are added on the outer boundaries. The 2D design is extruded into the third direction to gain a thickness of 3 mm. The transformation radii are indicated in red (R_1) and blue (R_2).

to all of the boundaries. Where a force needs to be exerted these blocks are elongated. The resulting sample designs can be seen in Figure 3.13. The two dimensional design is extruded to have a thickness of 3 mm. The radii R_1 and R_2 are indicated by red rings.

These designs are used and transferred to an STL file, which could be utilized to print the samples on the 3D printer. Here the samples are fabricated individually in the sizes as given above on the mm scale. The connections are thus still resolved, with a printer resolution of about 0.1 mm. To have as little supporting material as possible, no support structure is printed around or within the geometries, just on the bottom a release layer is needed to remove the structure from the building plate. After the samples are build and released from the printer, the residual support material is washed of using a jet of water supplied by a pressure washer. The afterwards dried samples are ground on the sliding sides, to minimize any sliding resistant friction.

In order to mimic the numerical calculations a setup is needed which allows to exert a constant pressure on two opposing boundaries, and have sliding boundaries orthogonal to these. The top and bottom of the three dimensional structure should have ideally no friction, and slide. To come as close as possible to these conditions, a measurement setup is build, consisting of two polished metal bars as the sliding boundaries in the y -direction. The top and bottom boundaries are consisting of "Plexiglas" plates, to still allow to monitor the deformation of the structure. The exertion of a constant pressure is done by the aid of springs. An array of springs, each one attached to one unit cell, is displaced on the far end of the spring towards the sample. The used springs (12 on each side) have a spring constant of about 7.4 N/cm. As long as the springs show a higher displacement then the sample, a constant pressure on each cell can be assumed. This

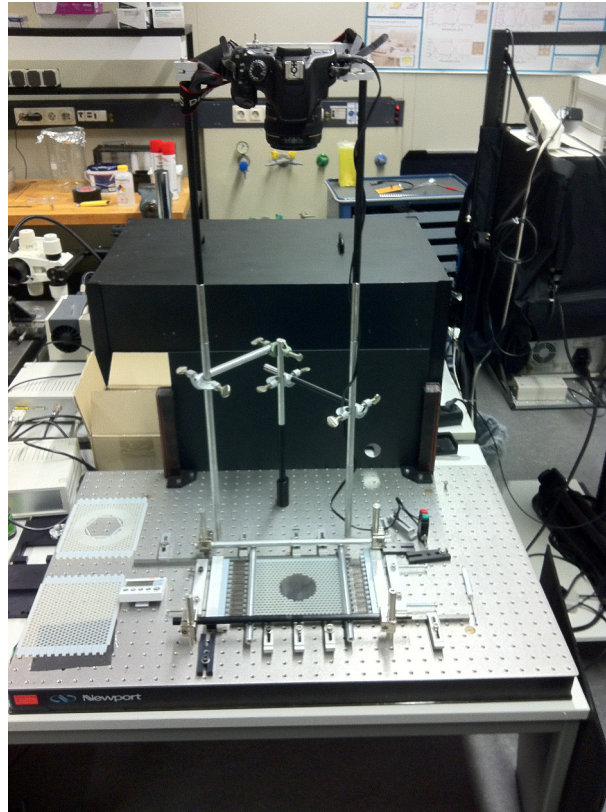


Figure 3.14: Measurement setup used to induce a strain into the samples and take images from above. Two metal bars, mounted to the base-plate mimic the sliding boundary conditions. The springs are used to translate a constant displacements into a constant pressure. The sample in the center is imaged from the top by a mounted camera.

is the case here, as the springs got compressed by about 1 cm compared to only a few mm displacement in the sample. This means that about $24 \times 7.4 \text{ N/cm} \times 1 \text{ cm} = 178 \text{ N}$ are the maximum force induced in the sample. The measurement is monitored with a camera from above at a distance of about 80 cm (Canon EOS 550d, Canon EF 50 mm, f/1.4 USM). During the measurement, the strain onto the springs is increased from both sides by turning four screws half a turn each. Then an image is taken, where after the procedure is repeated. To allow for a sliding and some settling time, a time-span of about 2 minutes between each measurement is waited for. The measurement setup is imaged in Figure 3.14. One measurement consisted of about 20 steps always starting from the same starting point. This means that the image number automatically encodes the induced strain on the springs and thus the stress onto the sample. The first raw image for all three samples is given in Figure 3.15.

These images also reveal the sample quality and the details of the measurement setup. The attachment of the springs and the sliding boundary metal bars are visible. The rods above the samples, on the right and left of the springs are used to fix the "Plexiglas" plates in the vertical direction, and hinder the samples from buckling.

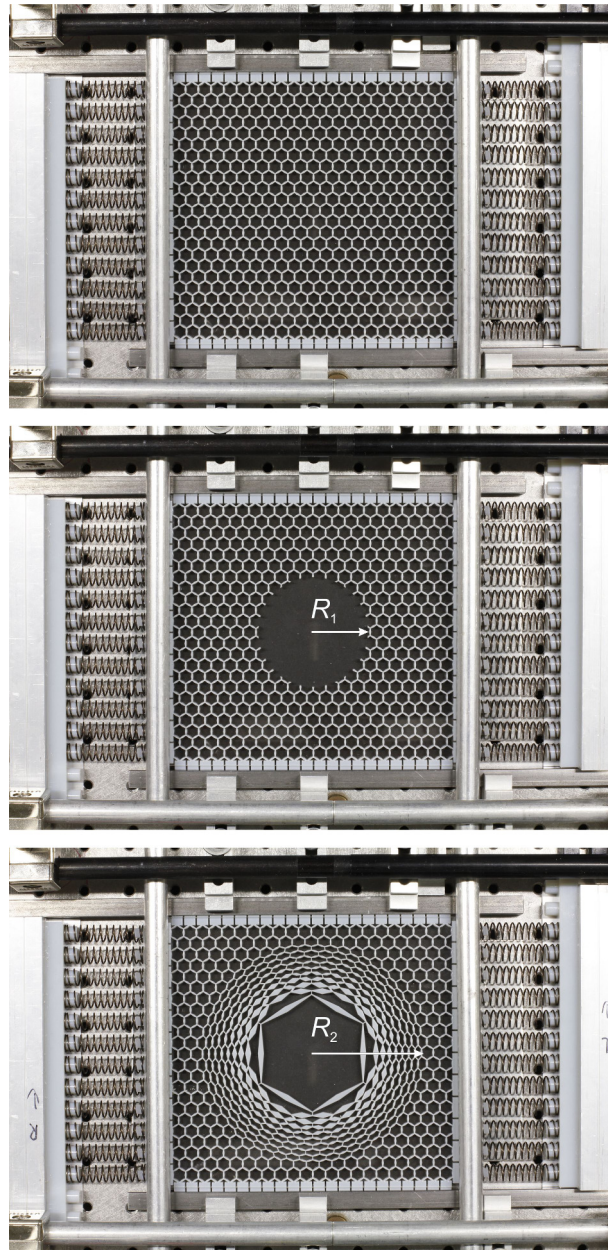
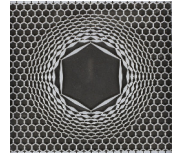


Figure 3.15: First images as measured in the experimental setup. All three samples are inserted into the setup. The radii are indicated. Previously published in [140].

To evaluate the different samples and compare them to the numerical calculations, a cross-correlation of the different image series is performed. Within the images the markers are placed on the lattice points just as in the calculations, and the displacements for all markers are traced for all samples through the image series. This data allows to directly compare the calculations to the measurements. Thus the same evaluation is performed with the measurement data. The resulting strain curves are plotted in Figure 3.16.

The strain pattern in the homogeneous sample deviates already from the numerical calculations. The strain is higher in the central region, which is linked to a not perfectly

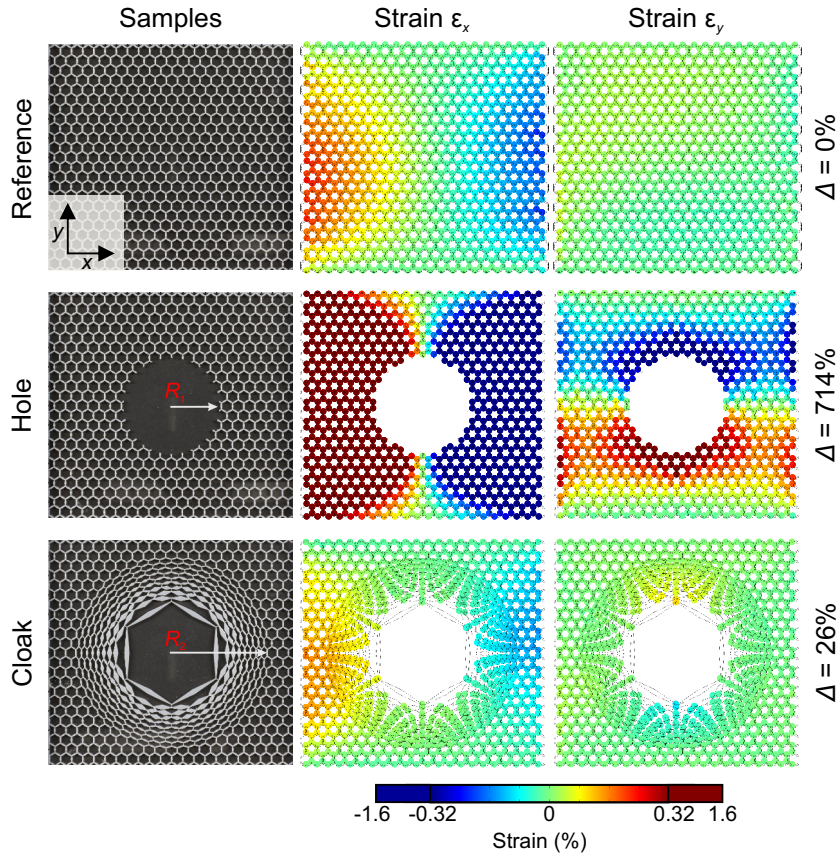
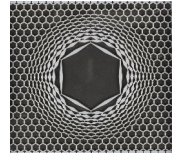


Figure 3.16: Measurement of the lattice transformation cloak. The sample parameters, and the plot are the same as in Figure 3.12. Previously published in [140].

sliding boundary condition. Nevertheless the hole case can be traced and a deviation of $\Delta = 714\%$ can be calculated. The cloak results into a much smaller deviation of $\Delta = 26\%$. These values are quite close to the numerical calculations. One has to mention, that the error on the measurement is rather complex to evaluate. A direct comparison of two different homogeneous samples can result into a $\Delta \approx 20\%$. A tracing repeated onto the same sample can result into about $\Delta \approx 5\%$ depending on the placement of the markers. Different radii R_2 have also been measured (see Appendix 19 and 20). Here the performance of the cloak is within the same error range than for the smaller R_2 . The hole sample is stiffer than before probably because the constituent material is changed (new batch of material VeroGray), between the homogeneous sample and the hole sample. This stiffer material leads to less deformation and thus smaller errors. Nevertheless we find an excellent agreement between the numerical calculations with the measurement.



3.2.4 Dynamic Tests of a Lattice Transformation Cloak

After we have shown that we can cloak an object with the lattice transformation cloak and recover the strain field to a very large extend, we have tried to find out if this general concept would work under dynamic considerations. Here we would like to mention, that the simple core shell cloak would not work, but an extension of the design to multiple shells is necessary in general. An further aspect comes into play under dynamic conditions, as discussed before, namely the mass density and the herewith connected impedance. It is required to adjust the mass density in the same manner as one has to adjust the mechanical properties. Within our lattice transformation cloak we do adjust the mass density, by changing the covered area within our cloak and thus the filling fraction. But this transformation scheme does so far not have any free parameters allowing to tailor the mass density individually. To address the question on how good the actual cloak performs, time resolved calculations can allow to address this question by sending a displacement pulse onto our structure and comparing the displacements to the hole and homogeneous case. To reveal deviations, we need to add a homogeneous material around our actual cloaking sample and calculate the whole structure, leading to a reduced meshing accuracy. To estimate the real structure, we have performed a band structure calculation, taking the dimension into account here set into the m range (see Figure 1.3). We find that we expect a nearly dispersion free propagation until an upper frequency of about 100 Hz. To probe the cloak at the maximum fidelity, we have chosen a pulse with a Gaussian envelope, center frequency of 80 Hz and a standard deviation of $\sigma_{gauss} = 0.1$. The amplitude is set to be $A = 1$ m (see Appendix Figure 21). The geometry is 8×3 times the size of the initial sample considered in the static calculations¹. The pulse is launched at a certain delay allowing to see the pulse arriving into the domain, and to have close to zero amplitude at time zero (a very small part of the Gaussian pulse is also present at this time, but is below the calculation accuracy). To compare the different samples with each other, they are plotted, with displacements encoded in color, beneath each other for specific times in Figures 3.17 to 3.19.

The pulse is propagating along the mechanical metamaterial from the left to the right as time passes on. The cloak as well as the hole are casting a shadow of the wave packet behind themselves. This means that the cloak is not working perfectly. Nevertheless the cloak shows some decent improvement and reduces the distortion of the waves after the cloak. The reflections caused by the hole have a higher amplitude and thus the scattering cross section in this direction is larger as for the cloak. The here compared times correspond to a position of the wave-packet where at first no part of the pulse has arrived at the obstacle or cloak (0.5s), at second the pulse is at the cloak or hole site (1.0s), and at last after the pulse has left the cloak or hole again (1.5s). Especially after the time of 1.0s the wave and thus the displacement is guided around the inner free part of the cloak, which although not restrained in any way does not move jet. Only at later times does the wave impinge into the central region of the cloak, causing a resonance mode to occur. This is a general problem that occurs in the transformation cloaking, as at the

¹The initial sample consisted of 22 unit cells in x-direction and $23\frac{1}{3}$ unit cells in y-direction. This leads to 176 unit cells in x-direction and 70 unit cells in y-direction for the dynamic calculations. In total 12320 cells were simulated for the pulse propagation simulations over a domain of 1219×420 m.

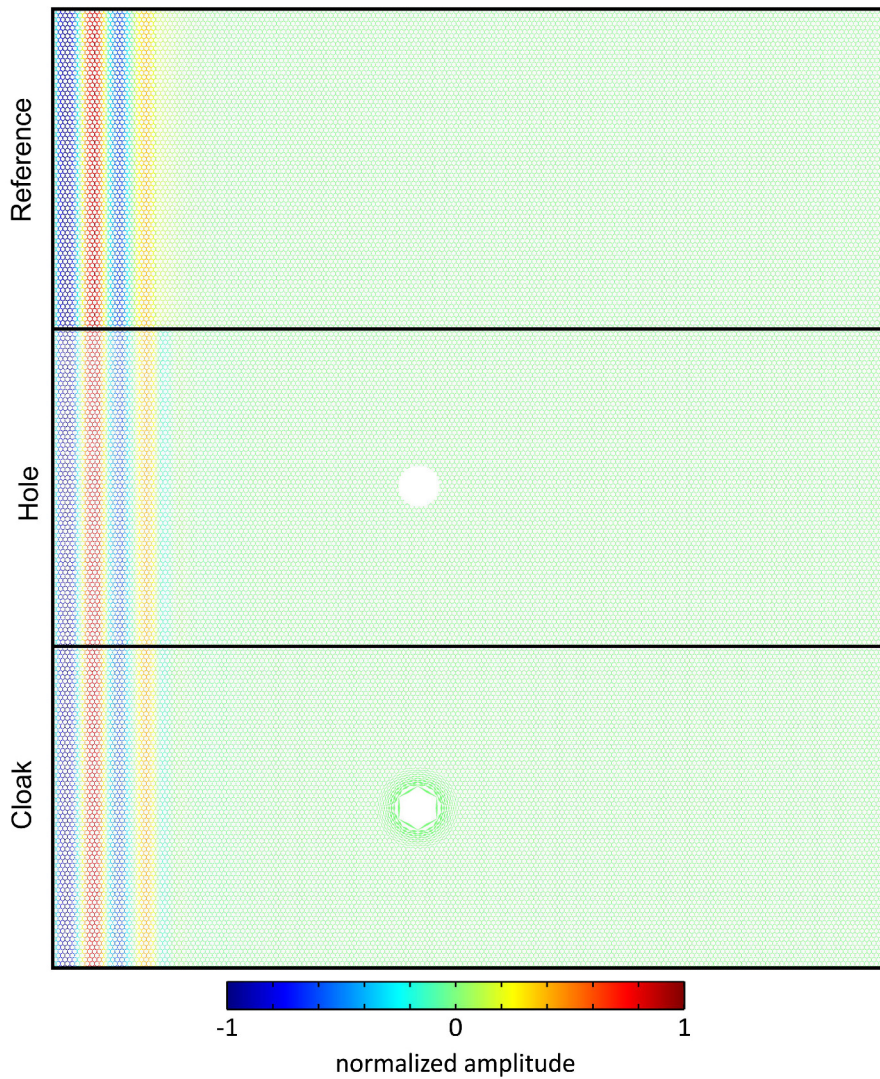


Figure 3.17: Dynamic evaluation of the lattice transformation cloak. The cloak is incident to a Gaussian pulse. The cloak, the hole, and the homogeneous material are compared at time $t = 0.5s$.

inner boundary the effective material parameters found by transforming a homogeneous material diverge to infinity, which should be the case here for the mass, but can not be reached in an realistic design.

These considerations show that there is essentially a possibility to use the lattice transformation cloak in the dynamic case, thus in elastodynamics, but a measure allowing to evaluate the performance of the cloak needs to be defined. To improve the performance of the cloak a way of influencing the mass density as well as the elastic properties needs to be established. The concept of the lattice transformation cloak has proven to work very nicely in the case of static loading for several loading condition, but it would be interesting to examine even more possibilities this concept has to offer. One could for example use different lattices, or generally different transformations. Interesting examples could be a

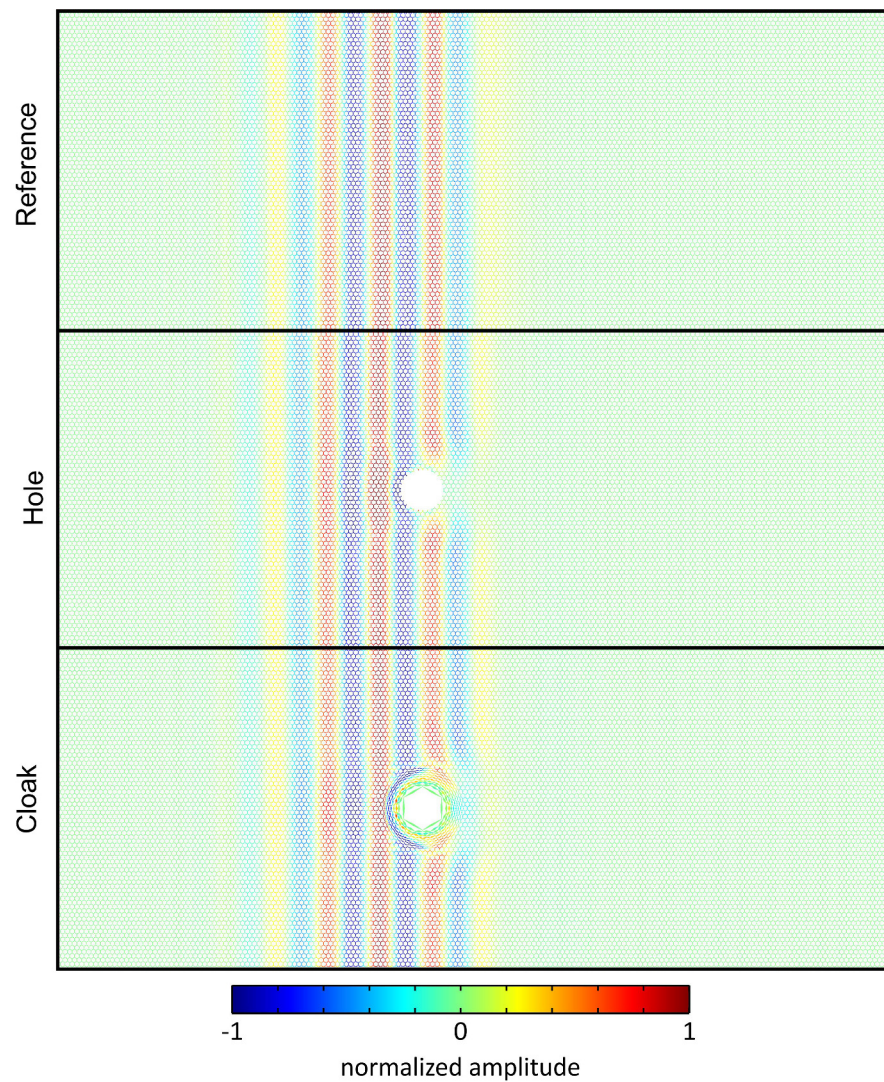
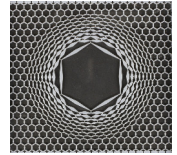


Figure 3.18: Same plot as Figure 3.17, just for the time $t = 1.0$ s. Here the pulse is at the site of the cloak and hole. The displacement is guided around the inner part of the cloak, thus preventing the pulse to enter the inner part of the cloaking structure.

three dimensional transformation, or transforming an extended lattice being optimal for a certain application, such as a bridge post, and transforming them into a more useful or smaller, or lighter lattice structure, without losing the performance of the actual lattice. This opens up new design possibilities and advanced functionality.

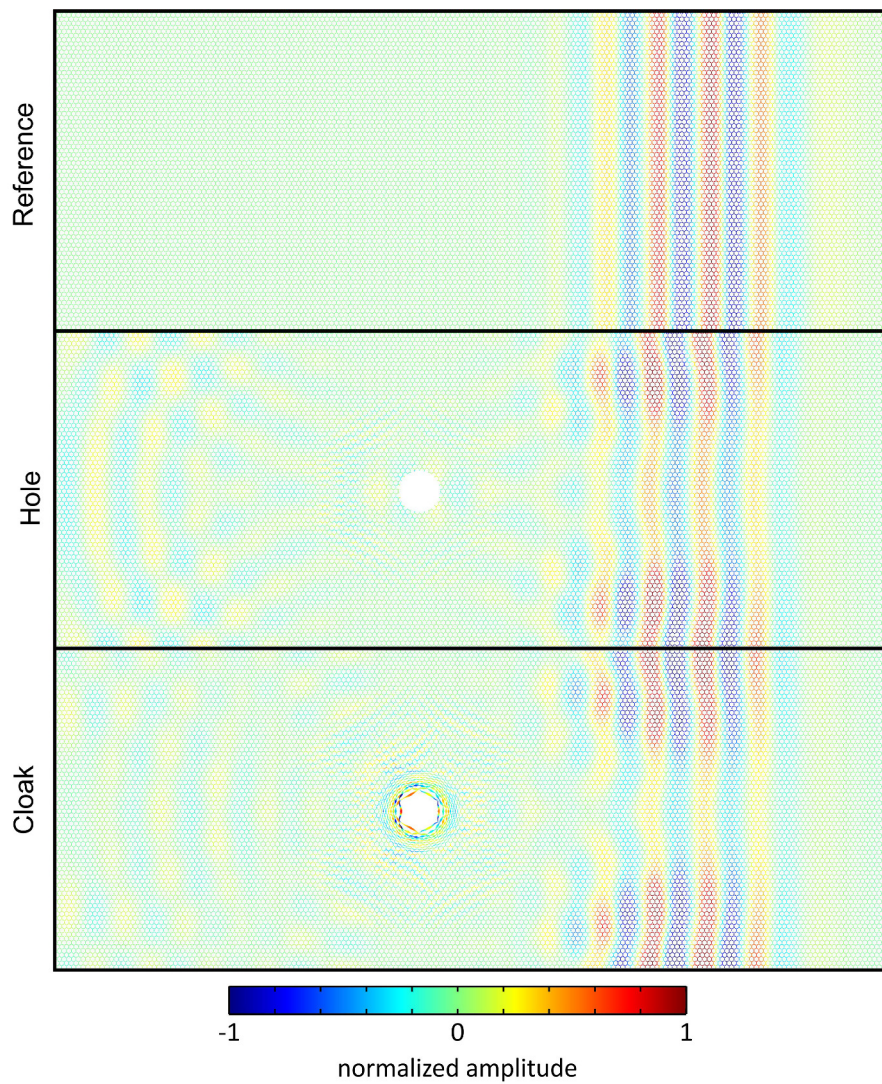


Figure 3.19: Same plot as Figure 3.17, just for the time $t = 1.5$ s. The pulse has left the cloaking site and the hole and cloak case cast a shadow. The reflections of the hole are larger in amplitude and the shadow is larger than for the cloak case.

4 Conclusions

The goal of this thesis was to perform research on mechanical metamaterials. The metamaterial concept allows for tailoring mechanical materials properties and functionality and has therefore gained an increasing interest by various scientists recently. During this thesis we have developed, fabricated and characterized different novel mechanical materials and the results have been compared with numerical calculations.

Our first experiment is based on theoretical suggestions mainly proposed by Prof. Graeme Milton from the University of Utah, mechanical metamaterials are designed, for two extreme cases of elasto-mechanical materials. The first material is based on a rotational element, combined with holding elements forming a dilational cell. This concept is transferred to a unimode material, which allows to tailor the Poisson's ratio towards the ultimate lower limit for isotropic materials, namely $\nu = -1$. Here numerical calculations in the static as well as in the dynamic regime allow to find a characteristic scaling depending on geometry parameters. The dynamic studies are used to retrieve the cubic elasticity tensor elements, and evaluate the Poisson's ratio dependent on the initial strain direction. The numerically characterized structure is fabricated on a microscopic and a macroscopic scale, the later allowing for a measurement. A cross-correlation approach is used to link a uniaxial strain imposed into a sample to a Poisson's ratio. The numerical calculations encounter good agreement with the measurement and allow to observe a Poisson's ratio, for a crystal of the auxetic material, as low as $\nu = -0.79$.

To advance in the creation of mechanical metamaterials, a further highly desirable material system was explored. The so called pentamode materials approach the upper limit bounding the Poisson's ratio for elasticity, namely $\nu = 0.5$. These materials are highly desirable, as they grant an opportunity to allow for cloaking in an elastic medium. A theoretical concept is transferred into a blueprint and the design is assessed. The performance benchmark of normal materials is overcome by far, and the perfect pentamode material is approached. To determine the performance, numerical calculations are utilized, in the static and later the dynamic regime, to find the B/G ratio, directly linked to the Poisson's ratio. The design permits B/G ratios about three orders of magnitude higher than normal materials. A fabrication of these materials is done in the microscopic regime, and later also in the macroscopic regime, where a elastic measurement are performed validating the numerical calculations.

These pentamode materials are used as a tuneable material for a three-dimensional core-shell elasticity cloak. The basic blueprint is created based on a core-shell layout. The samples are designed on the basis of pentamode mechanical metamaterials. One of these materials is employed as a surrounding medium, whereas a second cloaking shell material is tailored, to compensate for a stiff inner core. A reference, obstacle and cloaking

structure are produced by the aid of DiLL galvo-scanning DLW as a fabrication method. This allows to create sample overall dimensions of $1 \times 1 \times 2$ mm, while at the same time a micrometer resolution can be maintained. The excellent fabrication accuracy is utilized to tailor the mechanical properties of the pentamode materials. The ability to precisely tailor the metamaterials bulk modulus for the cloaking shell is essential to allow a good cloaking performance. The samples are measured under quasi-static conditions incident to a prescribed strain. Images of the sample facet are taken for each strain in the measurement. By a cross-correlation approach displacements are extracted throughout an image set of variable increased strain. An performance evaluation, within the three samples based on the strain patterns of the measurement, leads to the very good cloaking performance.

Extending the core-shell design to, e.g., a compliant core is not feasible, as the basic equations lead to no accessible shell parameter. To be able to cloak an object based on an effective medium theory, an inverse step of mapping a material parameter onto a microstructure is required. Without a comprehensive knowledge of designed materials and their adaptable properties this inverse mapping is highly complex if at all possible. A newly developed design tool, the so called lattice transformation cloak, is capable of cloaking a void without extensive material design in a lattice periodic material. Here a simple analogy to a resistor network allows to cloak an area by transforming lattice points of a periodic material and placing the same physically equivalent as a connection between these transformed points. In this fashion cloaking of a void is obtained for a lattice material under mechanical stress or strain. The approach proves to be successful for a large variation of parameters and designs. This reveals the comprehensive performance of the design concept of a lattice transformation cloak. The design principle could be exerted in two dimensions and be verified in an experimental setup.

The presented results open the way for future research on mechanical metamaterials. The possibilities to tailor a material to fulfill a specific task exploiting designed properties opens up versatile possible applications. Starting from material properties such as stiffness or Poisson's ratio, which have been shown to be tailorable to a large extend, over ultra-light weight materials [18, 124, 126] to origami type materials[144, 145] and programmable materials [146] a large research field has evolved. In the future it will be possible not only to use one type of these materials, but combine them to intricate designs and functionalities. One can also make use of different constituent materials showing different mechanical properties, and integrate them into one design. This allows to add even active functionality to a design, e.g., to have a photo-mechanical response in one of the materials, allowing to built up muscle like structures. Carbon nanotubes added to a resist could lead to stiffer and maybe even conductive polymers. Waveguides coupling temperature sensors or on chip light sources to various locations would allow to have active and sensing functional materials at the same time. Here mechanical metamaterials could play a key role in designing materials and can lead to light, functional and possibly even integrated materials. The design of complex systems can lead to advanced micro robotics and other microscopic or macroscopic devices allowing to make our live easier in the future.

Appendix

1 A - Additional Information on Dilational Mechanical Metamaterials

Within Section 2.1 we have used the band structure calculations to determine the Velocities of the different modes within the dilational materials. The following table gives the different moduli evaluated from these band structures for different structural parameters. The presented data is listing the independent \mathbf{C} tensor elements, the Young and bulk modulus for varying connection sizes d/a .

Table 1: Examples of retrieved effective parameters. The three non-equivalent non-zero elements of the elasticity tensor C_{11} , C_{12} , $C_{44} = G$, the Young's modulus E , and the bulk modulus B are given for selected values of d/a . (taken from [68])

d/a (%)	C_{11} (MPa)	C_{12} (MPa)	$C_{44} = G$ (MPa)	E (MPa)	B (MPa)
5	2.33	0.0051	3.5	2.33	0.78
4	2.33	-0.16	3.78	2.31	0.67
3	2	-0.35	3.36	1.85	0.43
2.5	1.3	-0.52	2.1	0.61	0.0867
0.75	1.14	-5.07	1.68	0.33	0.042
0.5	0.97	-4.45	1.35	0.21	0.026
0.25	0.85	-4.06	1.06	0.12	0.014

2 B - Additional Information on the Core-Shell Cloak

Within this part of the appendix additional information with regard to the core-shell elastic cloak is presented. To give a better understanding of the basic principle of a core-shell cloak, a simple analogy to the fairy-tale called "Princess on a Pea" by Hans Christian Andersen helps. In this tale the princess can not sleep during the night as a small pea is hidden under several mattresses. Translating this into a physical context means that the princess is very sensitive in detecting forces or can detect deviations in the displacement

field of a mattress to very high fidelity and low signal to noise. This allows to detect even the small pea others would not be able to detect. The elastic core-shell cloak hides this pea within the mattress such that the princess can not detect it any more, even within one thin mattress, and can sleep through the night without any disturbance. This analogy is illustrated in Figure 1.

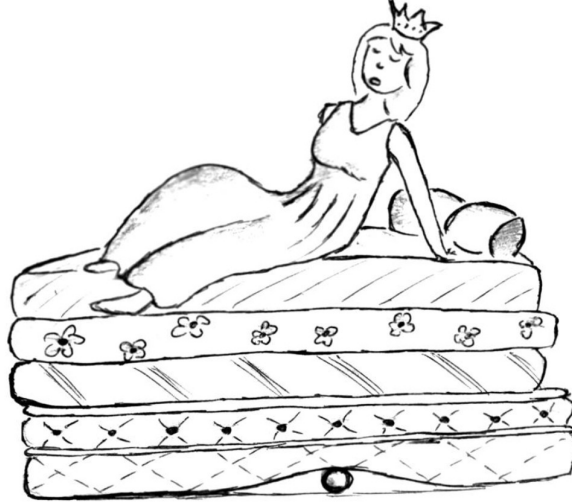


Figure 1: Illustration of the basic working principle of the core-shell cloak. The princess in the fairy-tale "Princess on a pea" by Hans Christian Andersen cannot sleep as a pea is placed under her mattresses. Here our cloak can help the princess in that it can cloak the stiff pea within just one mattress. This helps the princess to get a good night of sleep. Illustration taken from [139].

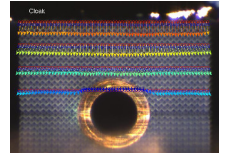
2.1 Derivation of the Core-Shell Formulas

The core-shell formulas given in [17, 142] are valid for a hydro-static compression of an inclusion within an elastic medium. Here the surrounding medium's shear modulus is not important and the core can have any shear modulus as well. This is due to the hydro-static compression, as no further deformations are allowed in this case except for a radial compression. The cloaking shell though needs a specific shear modulus, which needs to be tailored depending on the parameters of the cloak. The formula for this consideration is given in the two publications mentioned, and links the bulk moduli of the surrounding to the core's and the shell's moduli depending on the radius of the core R_1 and the shell R_2 .

$$B_0 = B_2 + \frac{(R_1/R_2)^2}{(B_1 - B_2)^{-1} + \frac{1-(R_1/R_2)^2}{(B_2+4/3 G_2)}} \quad (1)$$

As we would like to have a cloak that works under any kind of deformation and pressure, we need to fulfill that the surrounding medium only supports the hydro-static pressure, which directly links the shear moduli to be the same for all three materials and supporting

2. B - Additional Information on the Core-Shell Cloak



only the hydro-static pressure to be zero. This assumption leads to the stated case (see equation 3.1) of

$$B_0 = \frac{B_1 B_2}{f(B_2 - B_1) + B_1}. \quad (2)$$

With the filling fraction f of the radii, depending on the cylinder of spherical case. Further setting the inner core material to be very rigid ($B_1 \rightarrow \infty$), simplifies the equations to the maximum and allows to link the shell bulk modulus to the core's modulus only by the aid of the radii and the geometry (here cylinder):

$$\frac{B_2}{B_0} = 1 - \left(\frac{R_2}{R_1}\right)^{-2}. \quad (3)$$

Inserting even the ideal material parameters into a cloaking structure of homogeneous materials reveals the problem of the core-shell approach. Simulating a structure with bulk moduli according to the equations and very small and equal shear moduli for the three materials leads to very good cloaking performance outside of the cloak as can be seen in Figure 2. Here such a structure is compressed from the top and the bottom while sliding on the sides, leading to a very good cloaking performance for the two vector components along the vertical and horizontal direction. This means that the cloak effectively works very nice for small shear moduli.

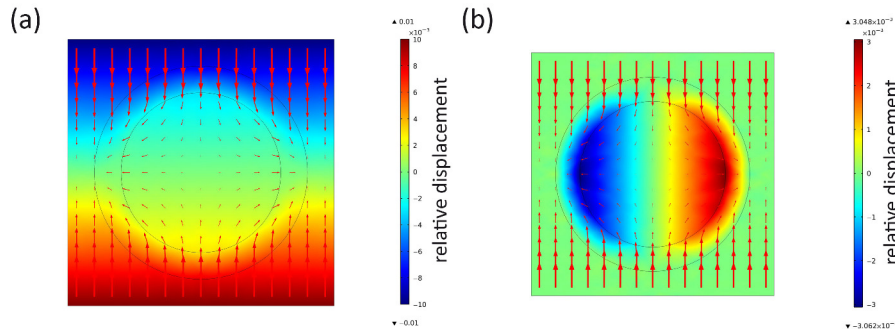


Figure 2: Homogeneous material cloak according to the equations. Parameters are $R_1 = 0.3$, $R_2 = 0.4$, $B_1 = 1000$, $B_2 = 1$, $B_0 = 2.3$, $G_1 = G_2 = G_0 = 1 \times 10^{-6}$. A displacement is prescribed along the vertical direction, whereas the horizontal boundaries are fixed. The surrounding material translates the unidirectional strain into an hydrostatic pressure. (a) Here the vertical displacement component is encoded in the false-color plot. The arrows are indicating the full displacement vector. (b) Same plot as in panel(a) but for the horizontal displacement component. One can clearly see that the displacement in the inner core is not zero, but rather has a finite and even comparable (about $\frac{1}{3}$ of the initial horizontal strain) induced strain. This means that the approach does lead to a invisible object or a neutral inclusion, but not a real cloak, where a rigid inner part is required.

On the other hand taking a closer look into the deformation of the horizontal displacement reveals a problem. The inner core is not stiff at all, but rather shows some severe displacement for this component. This means that even though the cloak works fine and

the bulk modulus of the core is much larger than for the shell (here 1000 times larger), the inner core still is not rigid. As soon as one introduces a larger shear modulus into the core it can be rendered rigid, but at the same time the cloak is not perfectly recovering the displacement field outside of the cloak any more as one has made an approximation. To hide an object within the center and thus to build a cloak rather than just an undetectable object, one needs to have a rigid inner core. This requires the cloak to be an approximation for all loading conditions except for a centro-symmetric loading with respect to the cloak, in which case the shear modulus of the core does not matter.

2.2 Discussion of an Overcompensated Cloak and Additional Figures

To give a better direct understanding of the deformations within the cloak a sample image is shown in Figure 3, indicating the key parts of the sample and measurement setup.

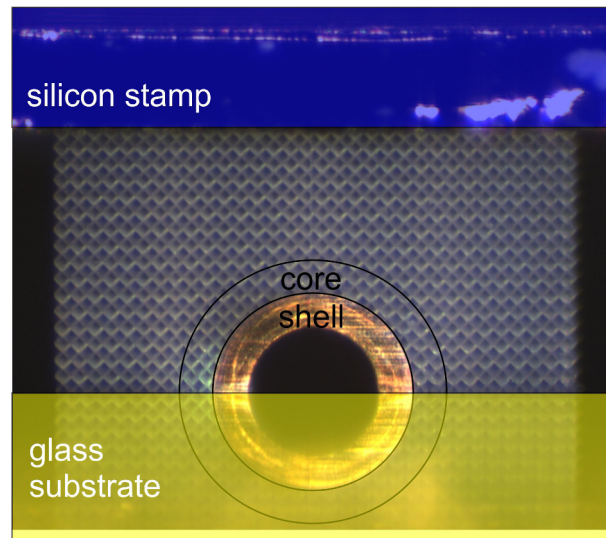


Figure 3: Illustration of a sample measurement of cloak sample number 3. The overlay illustrates the silicon stamp as well as the reflection of the glass substrate. The bump and cloaking shell are indicated. This helps to understand what is seen on the measurement images as shown in Figure 5.

In the main text an optimized cloak is discussed. To estimate the sensitivity of the design on the fabrication accuracy, an additional cloak is produced with smaller connection sizes d in the shell. This leads to a reduced bulk modulus in the shell, and thus to a larger displacement assuming the same acting force. Figure 4 shows the measurement of this cloak revealing an overcompensation of the solid core. As it is clear that the connection size is critical for the performance of the cloak, an estimation of the error allowable on lowering the connection size is quantified. Regarding an upper bound, one can compare the obstacle sample to the cloak. This leads to a variation between a too soft material and a too hard material in the overcompensated cloak and the obstacle sample. This reveals the fidelity of the designed cloak to the connection size.

2. B - Additional Information on the Core-Shell Cloak

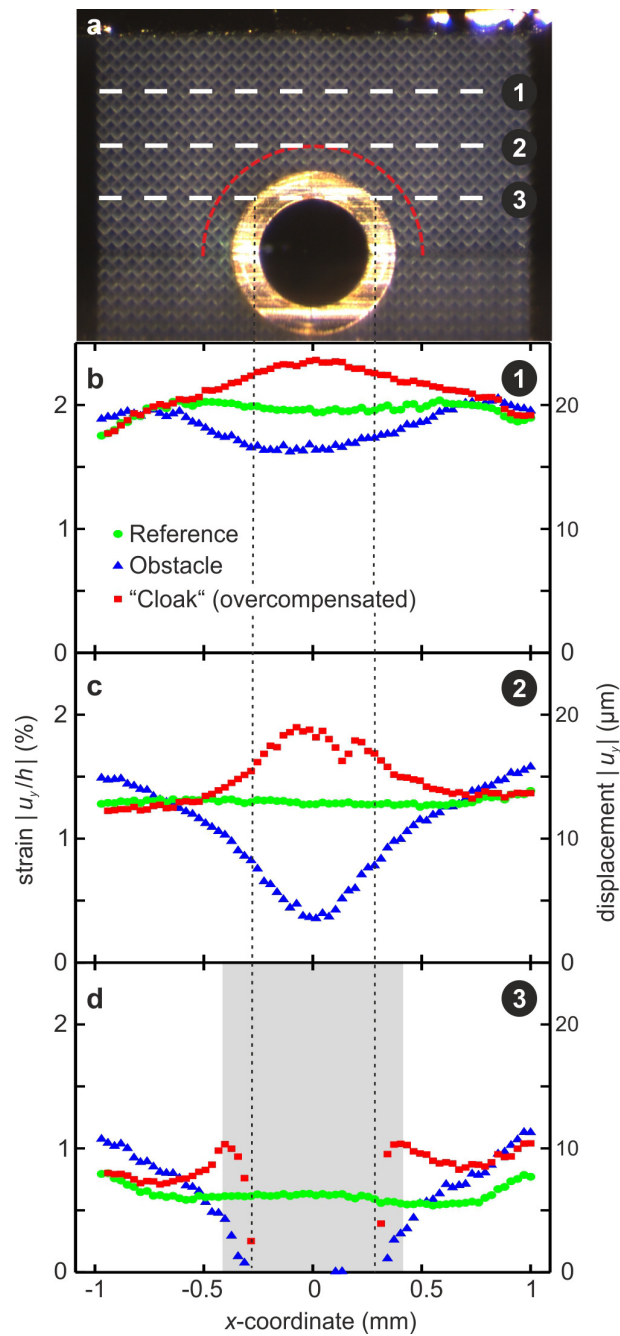
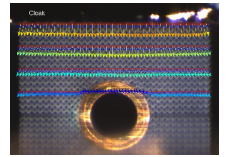


Figure 4: Evaluation of an overcompensated cloak. The displacements are larger than in the reference case indicating a too soft shell. The connection width is measured to be $3\ \mu\text{m}$. Figure in accordance to [139].

To estimate the directions and amplitude of the deformation, an image from the measurement is overlapped with the markers and arrows indicating the displacement vector (exaggerated by a common factor of 4) for each marker, see Figure 5. Here one gets a direct impression on the displacement field within the measured samples. The displacements of the individual parts of the samples are easy to compare and reveal the

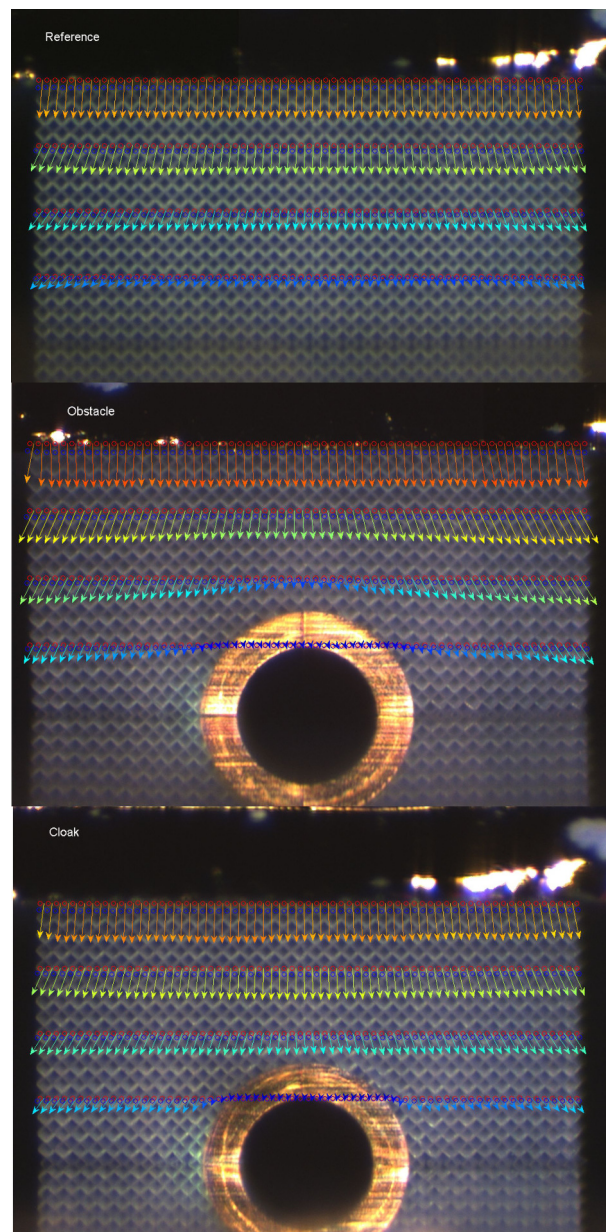
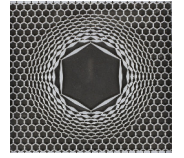


Figure 5: Comparison of the homogeneous, the obstacle and the cloak sample. Here the marker displacements are indicated by the arrows which represent exaggerated displacement field by a factor of four for the maximum strain. The representation gives an intuitive feeling on how the structures are deformed, and allows for a direct comparison of the strain fields.

cloaking performance. Especially the lower two evaluation lines show large displacement differences in the obstacle sample, which are compensated in the cloak.



3 C - Additional Information on the Lattice Transformation Cloak

3.1 Dependence of the Element's Width on its Length

Derivation of the width and length dependence for an element in the lattice transformation cloak.

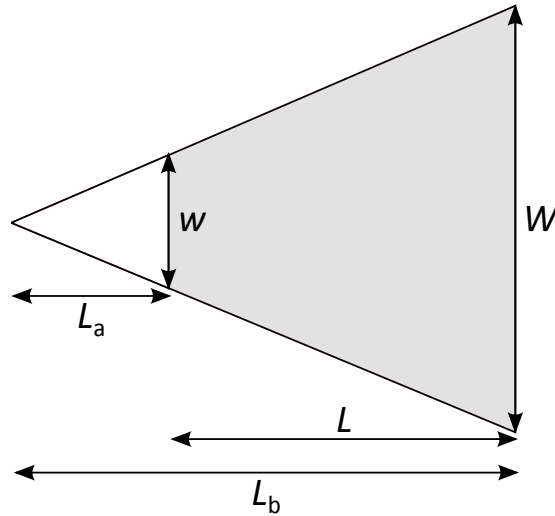


Figure 6: Basic elements of half a double cone used in the lattice transformation description.

First we define the dependencies:

$$L_a/L_b = w/W \quad (4)$$

$$d(x)/w = x/L_a, d(x) = wx/L_a \quad (5)$$

$$A(x) = wx/L_a \times T \quad (6)$$

$$L_a = wL/(W - w) \quad (7)$$

$$(8)$$

The different parameters can be seen in Figure 6. The thickness of the geometry is here set to an arbitrary value of $T = 1$. Now we calculate the displacement which is induced for a fixed pressure (kept constant over the width of the element)

$$\delta = \int_{L_a}^{L_b} PL_a \frac{dx}{EA(x)} = \frac{PL_a}{Ew} \int_{L_a}^{L_b} \frac{1}{x} dx = \frac{PL_a}{Ew} \ln \left(\frac{L_b}{L_a} \right) = \frac{PL}{E(W - w)} \ln \left(\frac{W}{w} \right) \quad (9)$$

As the spring constant D is proportional to the load and the displacement induced by this load one finds:

$$D = \frac{P}{\delta} = \frac{E(W - w)}{L(\ln(W/w))} \quad (10)$$

As a check we can calculate the well know result for a rod like structure. Using the above equation and the rule of L'Hopital one gets for $W \rightarrow w$:

$$\lim_{W/w \rightarrow 1} E \left(\frac{W}{w} - 1 \right) \frac{w}{L \ln(W/w)} \approx \lim_{W/w \rightarrow 1} \frac{Ew}{L} \left(\frac{1}{1/(W/w)} \right) \approx \frac{Ew}{L} \quad (11)$$

This is the result one would also expect for a simple bar. To keep a fixed spring constant on a double cone for a changed cone length L to L' we find the relation:

$$\frac{L'}{L} = \frac{W' - w' \ln \frac{W}{w}}{W - w \ln \frac{W'}{w'}} \quad (12)$$

Here we see that the changed length scaling can not directly be translated into an changed width, but the Young's modulus cancels out of this equation, making it independent of the constituent material. In the same fashion a calculation for conduction of each element can be performed, leading to the same equation relating the length L and L' with each other.

3.2 Different Parameters for the Lattice Transformation Cloak.

In this part of the appendix various other tests on the lattice transformation approach are performed. We divide the different tests into three main sub categories, namely testing the cloaks under different loading condition, changing the underlying transformation, and changing the initial material which is then transformed. This will give a good overview on how general the approach is, and what kind of performance is expected for different conditions. The comparison of different transformations and initial materials will give a hint on how the general realizations on the parameters scale regarding the cloak performance.

Changing the loading condition

In order to determine the general performance of the lattice transformation cloak, we have performed numerical calculations for different loading conditions. We have seen that the cloak works nicely for one particular loading direction, namely along the x -direction as shown in section 3.2. As we have performed the procedure on a hexagonal lattice there are two principle directions which are distinct from each other. As we have probed one of the directions in the main text, we can probe the other one by rotating the loading conditions (or the geometry) by 90° . Applying the same pressure and the same sliding boundary conditions on the boundaries we can probe the cloak under a rotation of 90° . The results of the calculations are plotted in the same manner and on the same scale as for the unrotated loading, see Figure 7. One can nearly see no difference in the performance of the cloak, only comparing the Δ values allows to reveal slight differences. We can conclude

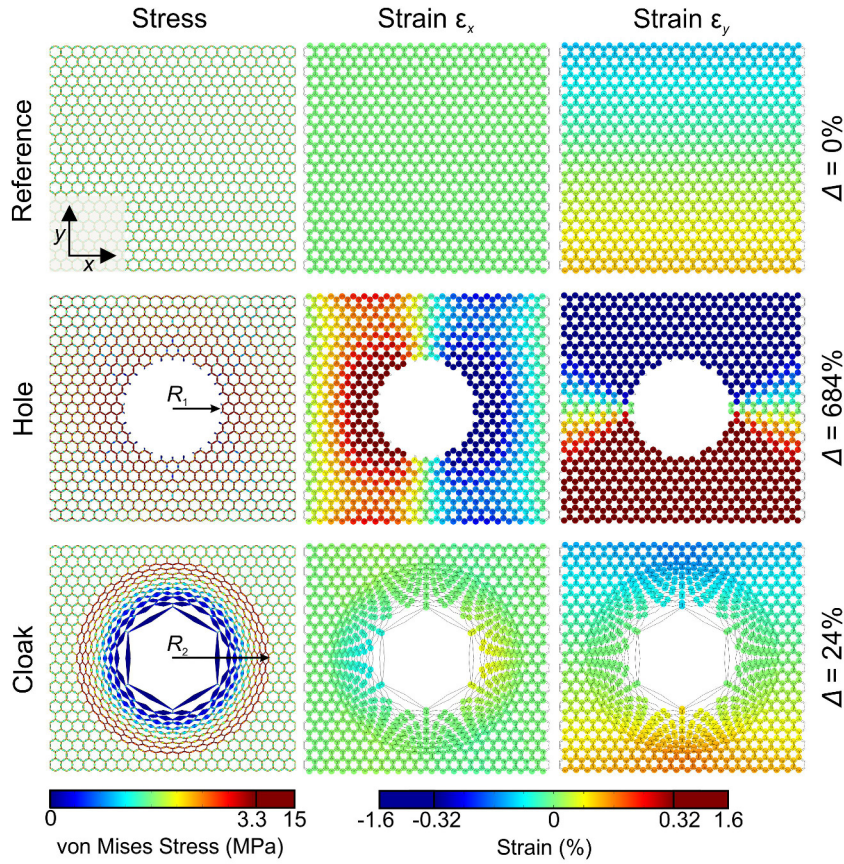
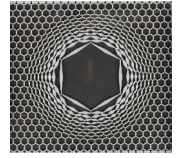


Figure 7: The same plot as Figure 3.12, but for loading conditions rotated by 90° . The cloak still shows an excellent performance close to the unrotated loading. The improvement factor of about 29 is comparable to the unrotated loading as well. Previously published in [140].

that the cloak works for loading conditions rotated from the initial direction by an angle of $0^\circ, 30^\circ, 60^\circ, \dots, 360^\circ$. As the cloak has nearly the same performance for at least all given angles before, and assuming a smoothly varying behavior between these angles, the cloak probably maintains its performance for all angles in general. This means that the cloak works at least for 12 different directions and is thus multi- if not omni-directional.

As we have sliding boundary conditions orthogonal to the loading direction, we probe the material in a way revealing mainly the bulk modulus of the material. The sliding boundaries transfer the unidirectional loading more into a compression type experiment. To be able to compare this behavior to other boundary conditions, one can think of various different ways of loading. To be able to compare the different loading situations, we will limit ourselves to some characteristic experiments. As a first example one can remove the sliding boundaries and set those boundaries to move freely. This is an experiment probing mainly the Young's modulus of the structure. The resulting calculations can be seen in Figure 8. Here the loading direction is along x and the upper and lower boundaries have no constraints. Even for the homogeneous material we get a strain along

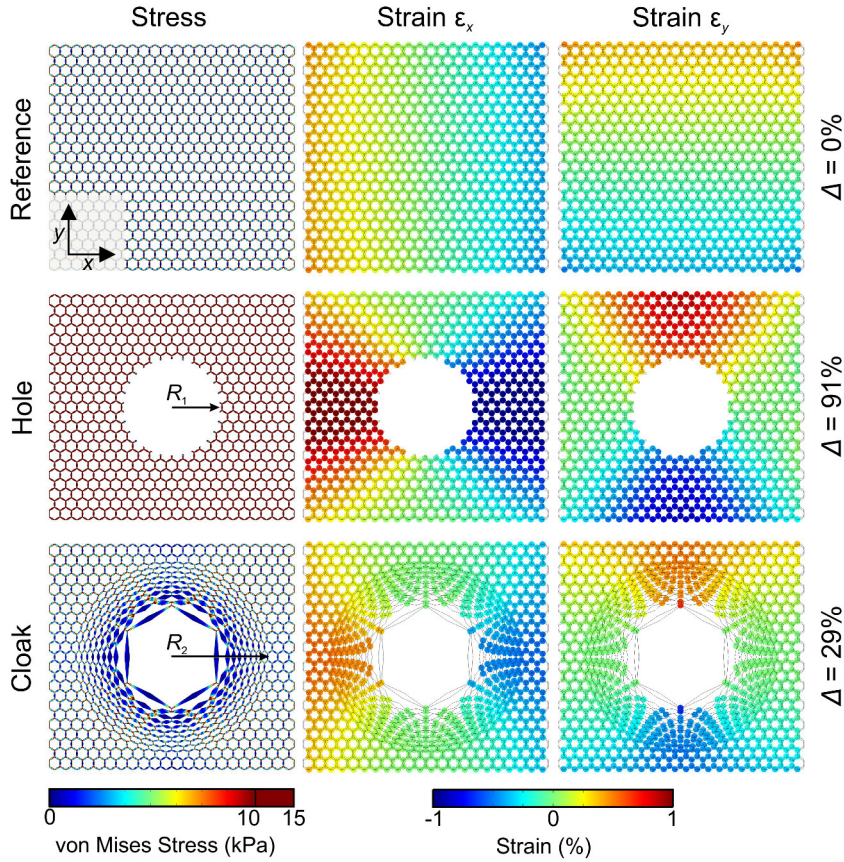


Figure 8: The same plot as Figure 3.12, but for a Young type of loading. Here the upper and lower boundaries are free to move, as a pressure is applied from the right and left. The deviations Δ are reduced in the hole case compared to the compression loading, reducing the improvement factor to about 3. Previously published in [140].

the y -direction, close in magnitude to the strain along x . This is due to the high Poisson's ratio of this particular effective material approaching $\nu = 0.5$. Considering the obstacle case we find that here a deformation takes place which leads to a deformation of the void and a not uniform deformation along the two shown strain directions. As the material is deformed out of the initial dimensions, as in the homogeneous case, the difference in the strain pattern is not as large as for the bound case. The deviations lead to $\Delta = 91\%$. The cloak recovers the deformation of the homogeneous material still better as the hole and can reduce the deviations by about a factor of 3 to $\Delta = 29\%$. The strains on the outer boundaries are not perfectly homogeneous. Nevertheless the cloak can provide a significant improvement with regard to the deformations in this case.

Comparing the loading under compression, probing the bulk modulus, and unidirectional loading, probing the Young's modulus, have shown that the lattice transformation cloak can improve the deformations in that it recovers the strain field of a homogeneous material. To probe a further general loading condition, a shear load is applied onto the sample. By applying a force on the top into the positive x -direction, and on the bottom into the

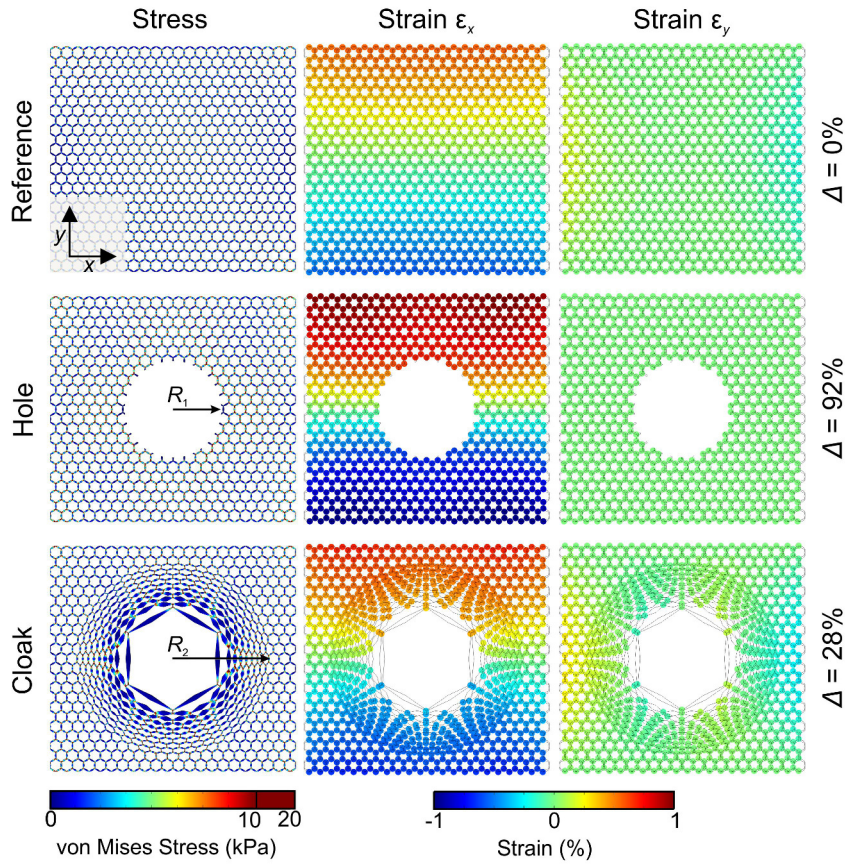
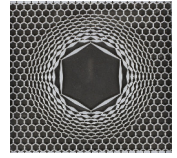


Figure 9: The same plot as Figure 3.12, but for a shear type of loading. Here a shear force is applied on the top and bottom boundaries. The other boundaries are set free to move. Here again the deviations are not as drastic in the Hole case reducing the improvement factor to a comparable value as in the Young's loading case of about 3. Previously published in [140].

negative x -direction, while fixing the vertical movements of these boundaries a shear loading is generated. The other boundaries are free to move. This loading leads to a shear like deformation of the effective material as depicted in Figure 9. The homogeneous material reveals the actual expected deformation. The top of the structure has a positive x component of the strain ϵ_x , whereas the opposite is the case at the lower boundary. As we have fixed the top and bottom boundaries in the vertical direction y , and we have a finite sample, we get a non zero strain in the y -direction on the right and left boundaries. In the obstacle case we find that the displacements along the x -direction are enlarged and thus the effective material is softer under shear loading because of the cut out material part in the center. The cloak again reduces this effect to a large extent and can recover the effective material properties of the homogeneous material. The improvement of a factor of about 3 is very similar to the Young's type of loading.

Considering different loading conditions reveals that the cloak improves the recovery of the strain field in all considered cases, but the effect is most drastic for a compression

type of loading. This is mainly due to the larger deviation of the obstacle case compared to the homogeneous material. The cloak has only small differences of a few % in the different loading conditions.

Changing the transformation

Changing the loading condition reduces the effectiveness of the cloak, but revealing undoubtedly that the cloak shows still a remarkably improvement compared to the obstacle or hole case. The next question would be how the performance of the cloak is changed when changing the transformation parameters. Here one has in general (staying with the Pendry transformation) two different parameters which could be changed, namely the two transformation radii R_1 and R_2 . As the later radius is responsible for the dimension of the cloak, and thus the ratio of the lattice period to the extends of the cloak, it determines how many unitcells take place in the cloaking procedure. As one increases the outer radius, the surrounding of the cloak would change as well, and one would have difficulties in comparing these results to the structures discussed so far. At the same time the numerical constraints are limiting us to a finite number of unitcells to be considered, limiting our variable. This is why we have not changed the radius R_2 here. A change in the inner transformation radius R_1 does not change the number of considered unitcells, and only changes the size of the inner void. This directly means though that the cells undergo a higher deformation and that the radial compression gets more drastic. A more drastic deformation also leads to longer unitcells, and thus more cells being limited by W_{max} .

As a start one can thus reduce the radius R_1 and relax these constraints. Figure 10 shows a cloak with a inner transformation radius of $R_1 = 15\text{mm}$. We have of cause no change in the homogeneous reference case, but the hole case changed, as there the obstacle radius is also determined by R_1 . This reduction in the obstacle has smaller strain deviations as a result leading to a reduced Δ of 264 %. Nevertheless the pattern is still the same, but the maximum strain has reduced to about half of what it has been before. Considering the cloak one can find that the changed transformation has lead to a structure which is showing smaller deformations of the unitcells, and thus it is harder to determine the outer radius R_2 by sight. The next feature that directly becomes visible, is the increased central width W towards the center. The more relaxed parameters of coarse lead to a better cloaking performance as before, showing only a deviation of about $\Delta = 6\%$. Comparing the improvement factor of 41 reveals that the cloak actually performs better, not only on the absolute error, but also on the improvement factor. The cloak improves performance, but the hole to be cloaked also reduces in size which leaves effectively more cloak area to void area or the ratio of the radii is reduced from formerly $R_1/R_2 = 0.5$ to now $R_1/R_2 = 0.25$. One more feature turns up very prominently, namely the stress distribution at the inner radius. Closer observation shows, that the stress is immensely reduced at the innermost double cones and that nearly no stress is present there. The imposed stress is guided around the void in the outer part of the cloak protecting the inner part of the cloak, and the void. This feature can be seen in all of the cloaks, but is most prominent here.

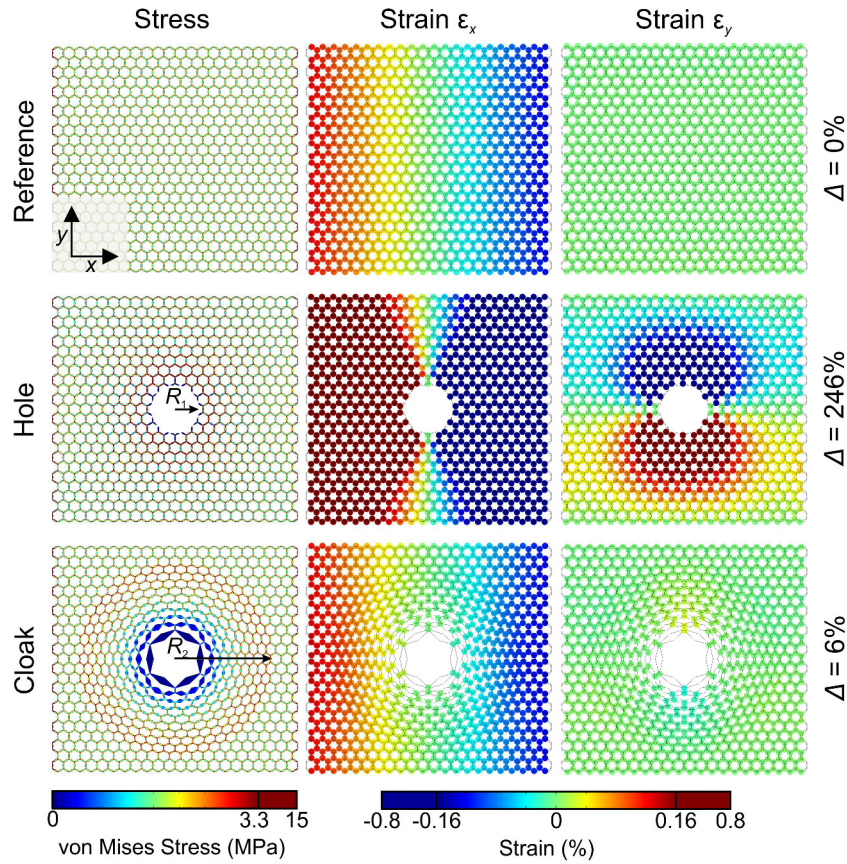
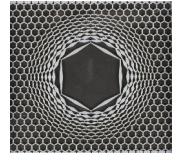


Figure 10: The same plot as Figure 3.12, but for a changed inner transformation radius of $R_1 = 15mm$. The hole and the cloak case have changed their geometry, as both depend on the radius R_1 . Note that the colorscale is always adjusted to the maximum strain obtained, which has been reduced by a factor of 2 compared to Figure 3.12 as the inner radius has been reduced by a factor of 2. Previously published in [140].

A reduction of the inner radius R_1 results in an even better cloak regarding the strain deviations and the improvement factor. One has to keep in mind that the ratio of the radii and the resulting space needed to cloak a certain sized object is also an interesting aspect, as one wants to have a large object and a cloak that is as thin as possible. So it is natural to explore the performance increasing the inner transformation radius R_1 . As the inner radius is bound at the upper side to the larger transformation radius R_2 , which we would like to keep fixed as described before, we cannot increase the inner radius by a factor of 2. Thus we start by increasing the inner radius in smaller steps of 5mm to first $R_1 = 35mm$ and later to $R_1 = 40mm$. This gives a good insight into what one can expect when changing the inner radius. First, an inner transformation radius of $R_1 = 35mm$ is examined. The resulting hole and cloak structure have been adapted to the changed transformation, depicted in Figure 11. Here the trend goes just the other way, as for a reduction of the inner radius. The absolute errors increase in both cases, as the unitcells

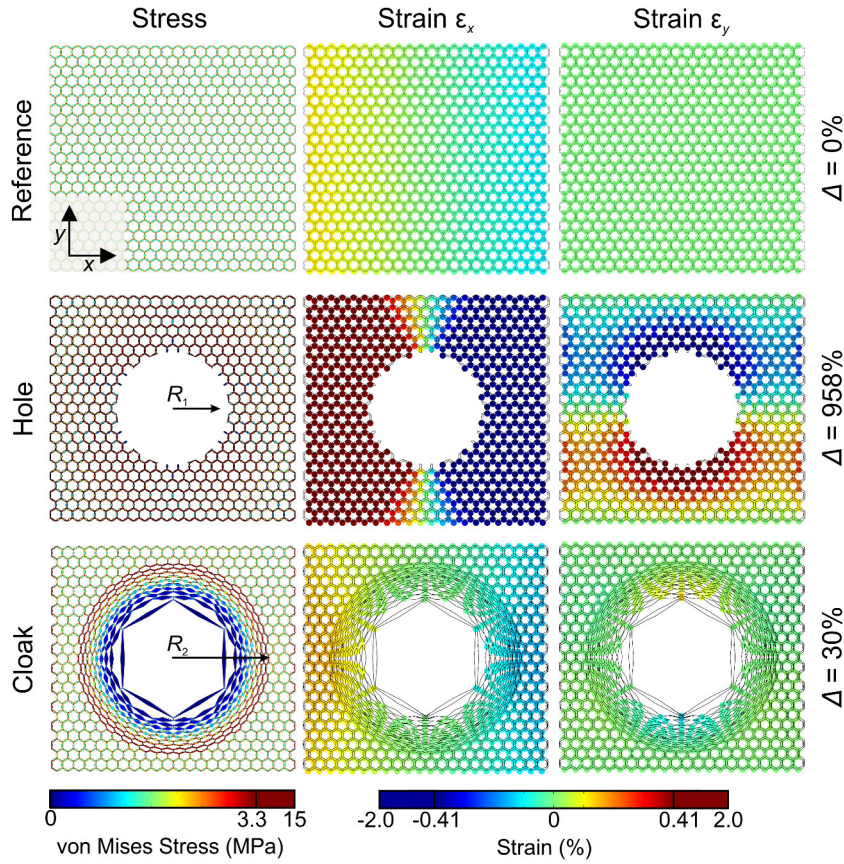


Figure 11: The same plot as Figure 3.12, but for a changed inner transformation radius of $R_1 = 35\text{mm}$. Previously published in [140].

get more deformed. The deviations Δ increase and the improvement factor is about 31. This shows the general trend as for a reduction of the cloaking shell thickness, the performance in absolute values goes down.

Further increasing the radius to $R_1 = 40\text{mm}$ underlines the dependence of the performance on the transformation parameter. The geometries and outcome of the calculations are shown in Figure 12. Here the transformation is already quite extreme and the cloaking area is reduced, as the ratio of radii is $R_1/R_2 = 2/3 = 0.\bar{6}$. This leads to a very dense cloaking area and a stronger (smaller) cut of width W_{max} . This can be seen especially on the innermost connecting double cones, which nearly turn into bars in this case. We find that the hole is showing a very large deformation as the Δ is increasing to about 1476%. This means that we find a very large deformation in the hole case, which we need to compare with the cloak showing only $\Delta = 47\%$. The improvement factor resulting from this is still as large as 31, rendering the performance of the cloak at least comparable to the initial case (showing an improvement factor of 34). The absolute deviation from the homogeneous reference case is though increased by about a factor of 2 showing a larger deviation from the initial homogeneous material.

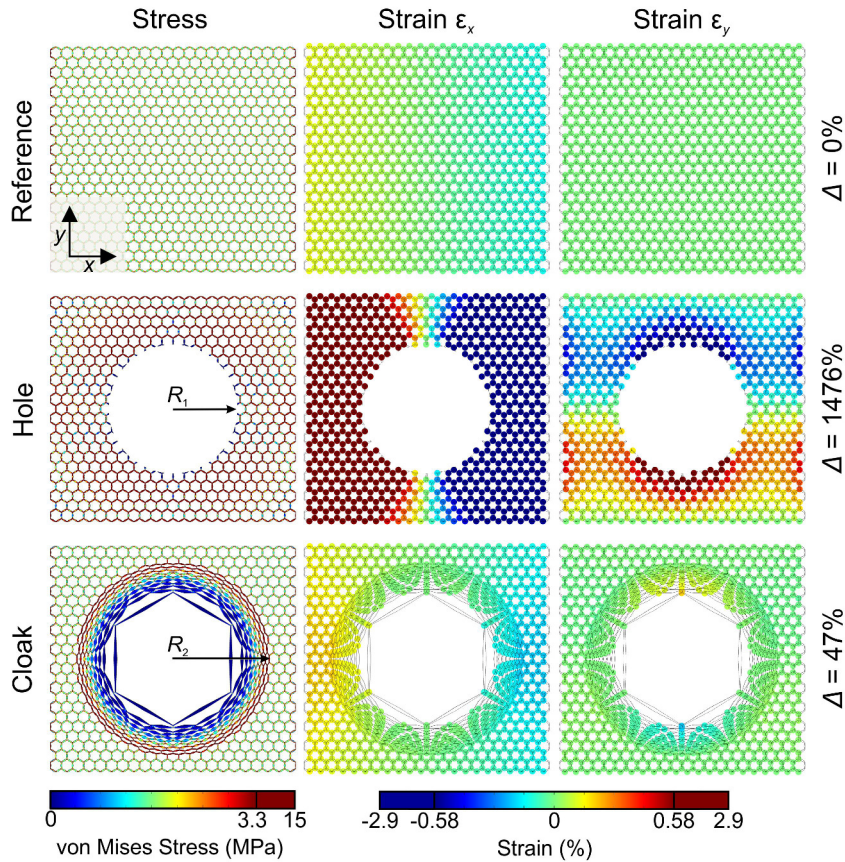
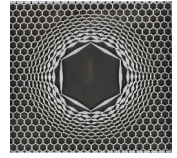


Figure 12: The same plot as Figure 3.12, but for a changed inner transformation radius of $R_1 = 40mm$. Previously published in [140].

These results lead to some conclusions regarding the change of the transformation, more precisely the inner transformation radius R_1 . At first the strain field shows larger deviations from the homogeneous reference for increased void size. This is somewhat natural expecting a better cloaking performance for a smaller void, and thus less deviations to start from. Further the cloak shows less extreme deformations of the unitcells, implying a less extreme gradient in the material properties, and thus a smoother geometry, generally connected to a better cloaking performance. A consideration of the improvement factor in comparison to the hole or obstacle case, leads to a slight change (also decreasing with increasing R_1) for the different geometries. The cloak did show an improvement factor of about 30 for all considered cloaks. This shows that the strain field can be recovered to a very large extent in all cases. As already pointed out in the beginning there are a lot more options to change the transformation. One could e.g. also change the outer radius R_2 , or use a totally different transformation. As pointed out before, due to numerical constraints these considerations are not done, but might lead to a improved performance, or a tailored solution to a specific problem.

One interesting fact not mentioned so far, is that the cloak is nearly stress free at the inner boundary. This feature prevents forces to penetrate into the inner most unitcells,

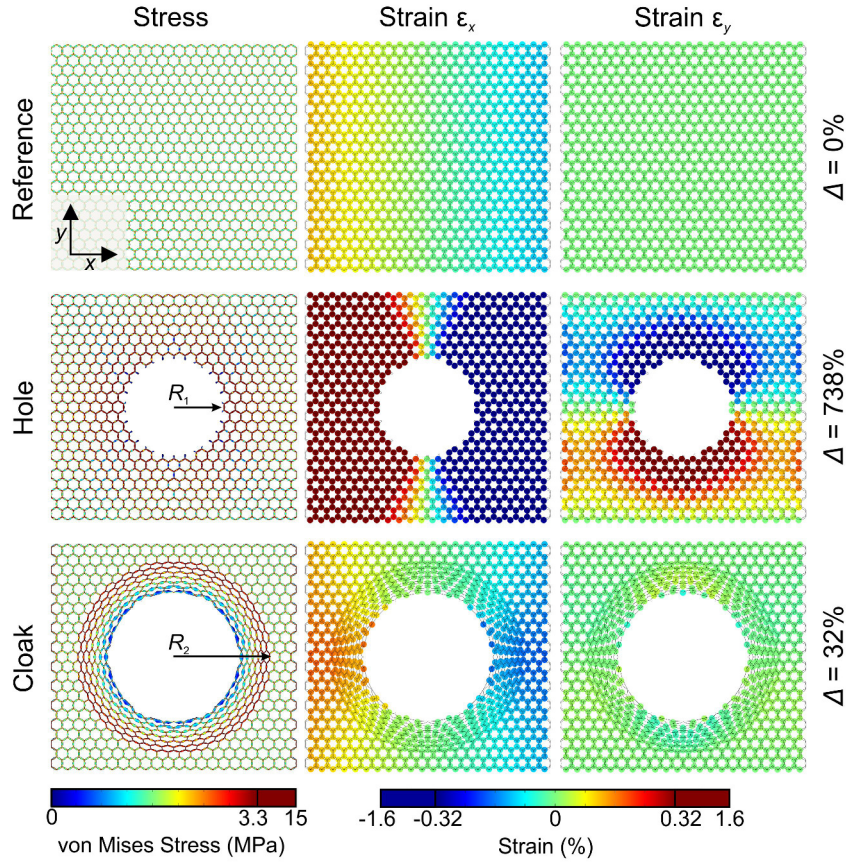
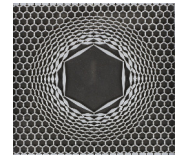


Figure 13: The same plot as Figure 3.12 with the same transformation radius of $R_1 = 30\text{mm}$. Further the inner part of the cloak is cut out at a radius of $R_{cut} = 40\text{mm}$. Previously published in [140].

and keeps the void protected. This specific feature could be used in principle to improve a cloaking performance with the regard of void size compared to the strain deviations. A less extreme transformation resulted in a better cloaking performance and the inner part of the cloak is still nearly stress free. This leads to the idea of cutting out part of the inner structure. As nearly no stress is present the performance should not deteriorate dramatically. To be able to compare the results a transformation based on an inner radius of $R_1 = 30\text{mm}$ is chosen and the inner part of the geometry is cut out in a circular fashion with a radius $R_{cut} = 40\text{mm}$. The cloak thus has a relaxed transformation, but an enlarged void in the central region, allowing to cloak larger objects. The resulting structure and calculations can be seen in Figure 13. The resulting performance is to be compared to the cloaks seen in Figures 3.12 and 12. We can see that the performance decreases as compared to the initial structure without cutting out the inner most part, but has improved in performance as compared to the more drastic transformation with a larger transformation radius R_2 . The improvement factor has changed comparing it to the hole of $R_1 = 30\text{mm}$ to 23, whereas comparing it to the enlarged hole size, which is actually present, of $R_1 = 40\text{mm}$ one gains on the improvement factor leading to 46.



This is a significant step to consider if searching for the optimum cloak for a certain given problem.

We have thus seen that different cloaks can be designed resulting in every case in an improved strain field recovery compared to the hole case. All of these considerations have taken the same homogeneous material as a starting point and have changed the void to cloaking area.

Changing the Initial Material

As the performance of the lattice transformation cloak has been explored with respect to changed transformation schemes, the initial material has not been changed. Initially we have just picked any reasonable combination of the diameters w and W . To explore if the cloaking performance is linked to the initial material, other homogeneous materials are considered. To simplify the concepts, we have changed the connection diameter w to larger, and smaller values, but kept the hexagonal lattice here (square lattices do work though, see Appendix Figure 16 and 17), as well as the double conical elements with the constant initial central width $W = 1$ mm for all length of elements (see Appendix Figure 18). To compare different materials, we have reduced the connection width to $w = 0.05$ mm and then increased it to $w = 0.8$ mm. Both cases are just two examples of the infinite number of possible materials based on a periodic lattice, but still give a good hint onto what can be expected when changing the material properties. As the connection width is changed, the transformation is fixed to $R_2 = 60$ mm and $R_1 = 30$ mm as in the initial case.

Reducing the connection width from $w = 0.4$ mm to a much lower value of $w = 0.05$ mm will lead to a material which is approaching the bimode material, the counter part of the pentamode material in two dimensions as discussed in Chapter 2.2. To estimate the material properties band structure calculations are performed, and the bulk to shear modulus are extracted, e.g. along the ΓX direction. This has been done for all three materials. The initial material returned a ratio of $B/G = 40$, relating to a material comparable to rubber rather than being already a bimode material. A reduction of the connection width to $w = 0.05$ mm enlarges the ratio to $B/G = 1300$ which definitely qualifies as a bimode material. Considering the opposite case and increasing the connection width to $w = 0.8$ mm, thus nearly the same value as the central width, rather normal material properties are found with a ratio of $B/G = 13$. By changing the initial material not only the material system one starts of with is alternated, but also the scaling of constant spring constant needs to be adapted. This is why the dependence of the width compared to the length, seen in Figure 3.11, is evaluated for the three different connection widths w . These different dependencies have to be taken into account when creating the cloak. The geometries created in this fashion, for $w = 0.05$ mm, are displayed in Figure 14. The strain has increased to very high values for this material, more than 1, leading in an actual sample to a complete filling of the hole structure. As the calculations performed are linear, we can thus still consider this case and compare it quantitatively to the other materials. The strain fields in the homogeneous and cloak geometry are with the set five fold saturation still quite close to zero, and only a slight strain can be seen

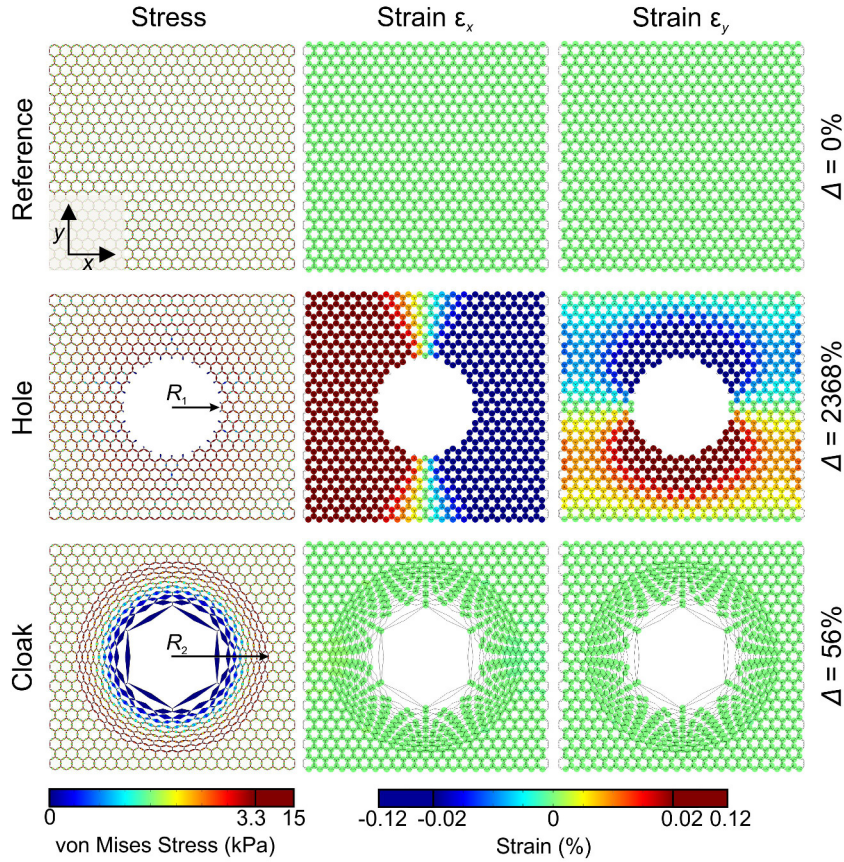


Figure 14: The same plot as Figure 3.12, but for a changed initial material. The connection width is reduced to $w = 0.05\text{mm}$, increasing the bulk to shear ratio to $B/G = 1300$. Previously published in [140].

on the outer side of the cloak. The deviations have increased to $\Delta = 2368\%$ for the hole and have also slightly increased for the cloak to $\Delta = 56\%$. This result means that we can still cloak a void in a material approaching a bimode material. The performance is not as good as in the initial material, but considering the improvement factor of 42, the relative improvement has even gained.

Reducing the connection width has obviously not hindered the cloak's performance in a significant way. It is thus interesting to consider a more natural and normal material. As described we have increased the connection width to $w = 0.8\text{mm}$ in the initial material. This reduces the bulk over shear modulus by two orders of magnitude and comes close to a material consisting of bar shaped elements. The resulting geometries, created as described earlier, can be seen in Figure 15. Here, just opposite of the decreasing width w case, the initial material gets more rigid and the induced strain is below one percent. As the shear modulus is enlarged in this material the hole case gets more stable and the deviations from the homogeneous sample are reduced to about $\Delta = 244\%$. The cloak has a deviation of $\Delta = 19\%$, leading to an improvement factor of about 13. This improvement is reduced

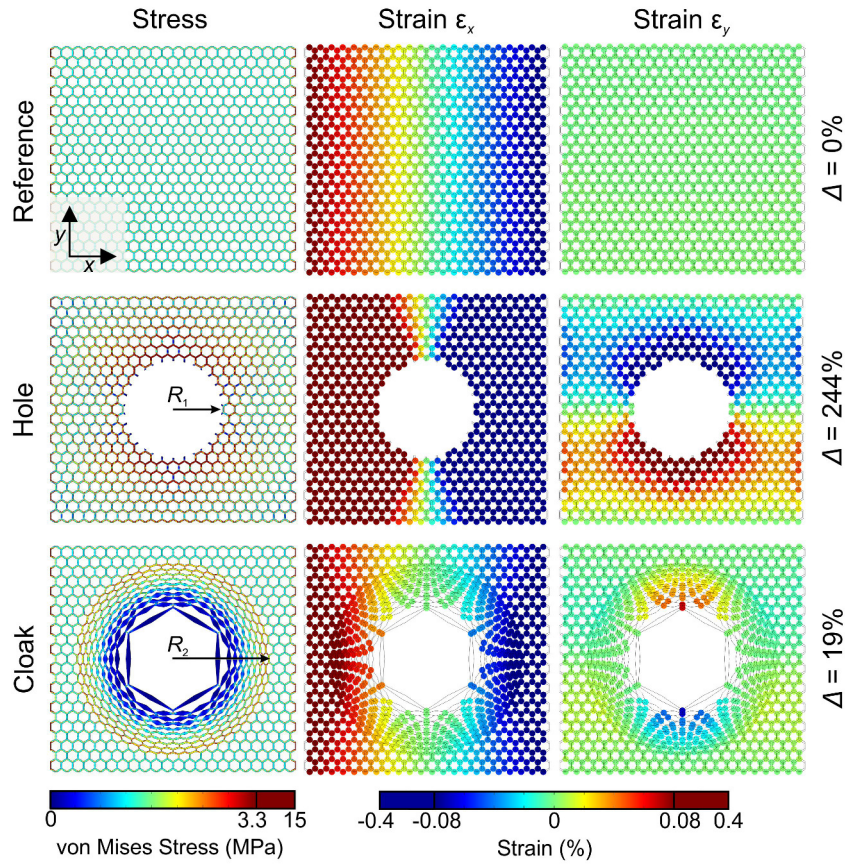
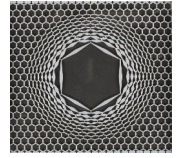


Figure 15: The same plot as Figure 3.12, but for a changed initial material. The connection width is reduced to $w = 0.8\text{mm}$, increasing the bulk to shear ratio to $B/G = 13$. Previously published in [140].

as compared to the initial or even the bimode material, but is still a large improvement considering the already reduced effect in the hole case.

The choice of different materials the lattice transformation cloak is based on, can change the performance of the cloak. The two shown examples prove that the concept of lattice transformation cloaking leads to a significant improvement for a variety of material systems, and is not limited to bimode materials. Here only hexagonal lattices are shown, but this concept should work in principle for all kind of lattice periodic materials, and seems to be also robust against changed material parameters in the cloaking region. In the Figures 16 and 17 a square lattice for different transformations is shown.

Here the deviation on the hole sample is more localized at the center and extends to about the width of the hole. The cloak though can guide the forces around the hole's site and perform comparable to the hexagonal design. As there are only a few lattice symmetries which can cover up the whole space only the triangular lattice is missing in this parameter sweep, but as it is related to the hexagonal lattice we assume no further gained insight by considering this lattice symmetry as a material system. As the hexagonal as well as the

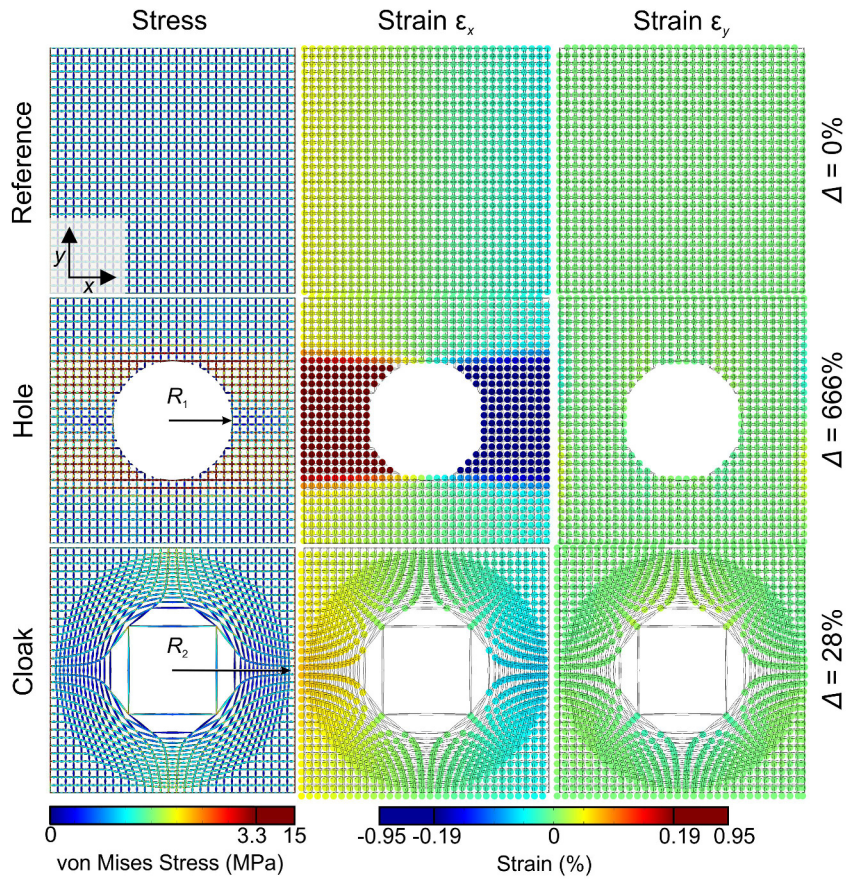


Figure 16: Lattice transformation cloak with $R_2 = 60\text{mm}$ and $R_1 = 30\text{mm}$, but for a square lattice.

square lattices have performed comparably and only deviated slightly in their performance we consider the approach to work for both of the initial lattice structures.

3. *C* - Additional Information on the Lattice Transformation Cloak

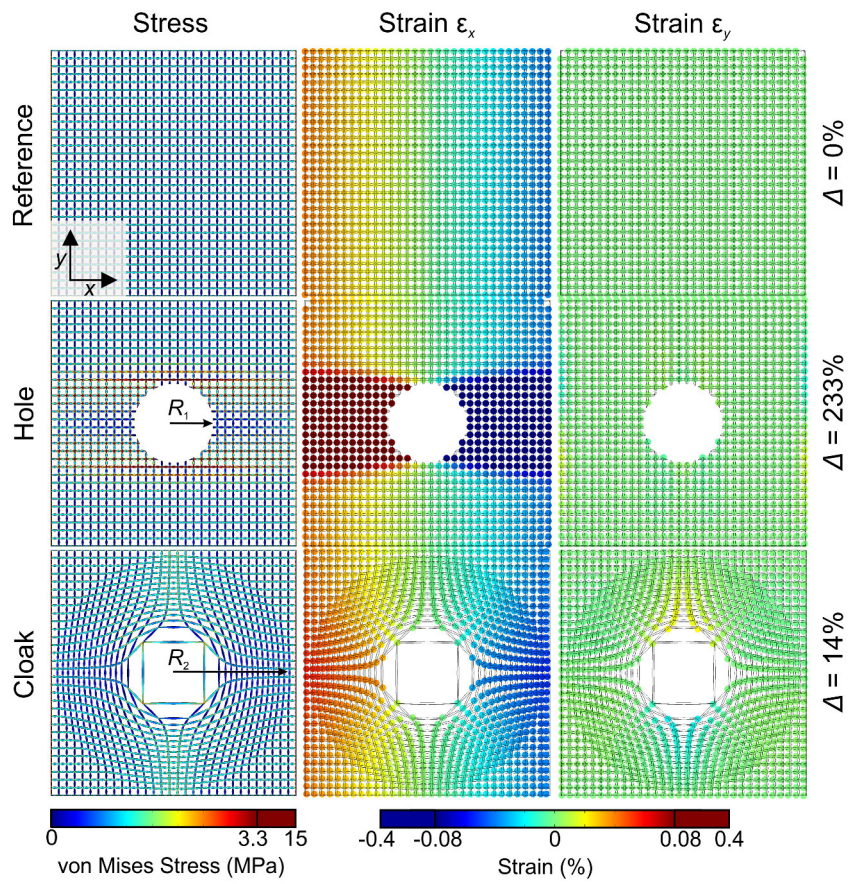
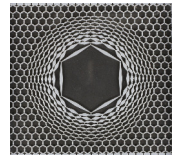


Figure 17: Lattice transformation cloak with $R_2 = 60\text{mm}$ and $R_1 = 20\text{mm}$, but for a square lattice.

To reduce the complexity of the design, one possible way is to place elements with the same width than the initial material everywhere in the cloak or even take bars for all of the elements, not changing the performance dramatically, rendering the concept very simple and useful for truss and scaffold systems or situations, where these simplifications are still performing good enough for a certain task, and simplifying the design.

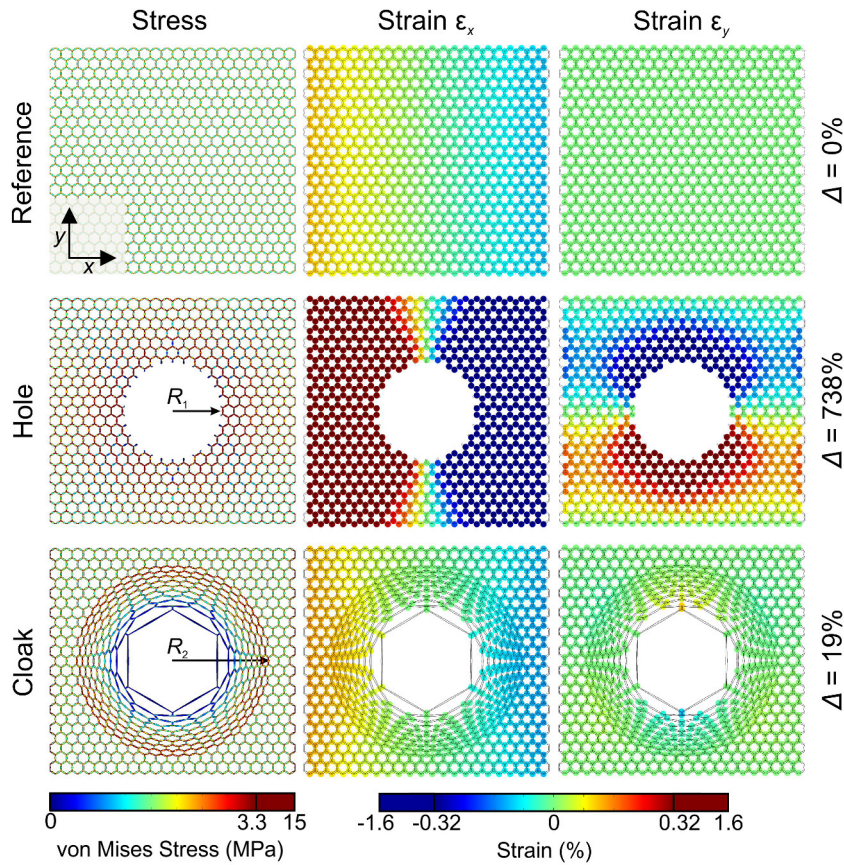
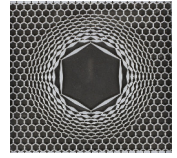


Figure 18: Lattice transformation cloak with $R_2 = 60\text{mm}$ and $R_1 = 30\text{mm}$. Here all central connection are fixed and the same $W = W' = 1\text{mm}$. The performance has not significantly changed from the adjusted width W' . This suggests, that the design is not sensitive at all to width changes, and rather is based on the directions and angle the different elements inscribe.

One can see in Figure 18 how this kind of cloak performs. The resulting performance is comparable to the adapted width case in the main text.



Additional Measurements on Other Transformations

To evaluate the performance of the cloaks further with regard to the measurement we have fabricated further structures for different transformation radii. As the sensibility of our measurement does not allow to detect the reasonable cloaking performance for smaller deviations, the radius R_1 was increased. As the constituent material of a new batch of VeroGrey is used the material is apparently stiffer leading to deviations especially prominent in the hole case.

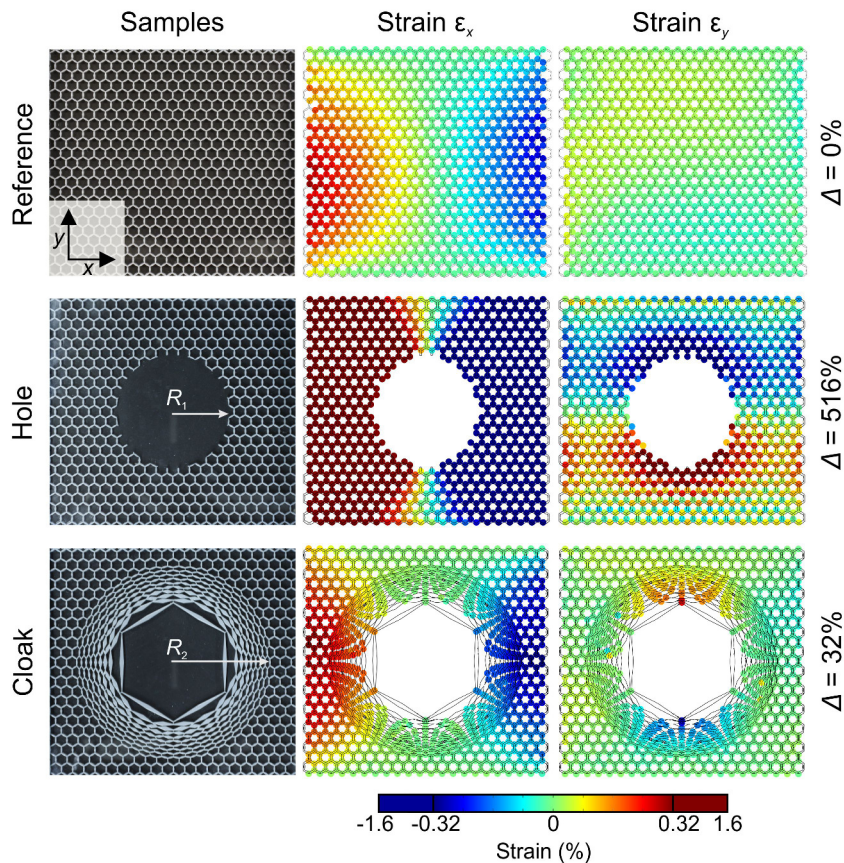


Figure 19: Measurement of a lattice transformation cloak with $R_2 = 60\text{mm}$ and $R_1 = 35\text{mm}$. The cloaking performance is comparable to the simulations. The hole sample is though stiffer than expected, eventually caused by a new batch of printing polymer.

Comparing the two measurements depicted in Figure 19 and 20 show the trend of slightly decreased cloaking performance as the transformation radius increases. This is even more prominent for the hole case. Both designs show a good improvement in the deformation as compared to the hole. Comparing the reference with the numerical calculations reveals that the boundary conditions are not perfect and friction is present at the top and bottom surface. There is also some movement along the vertical direction leading to strain along ϵ_y .

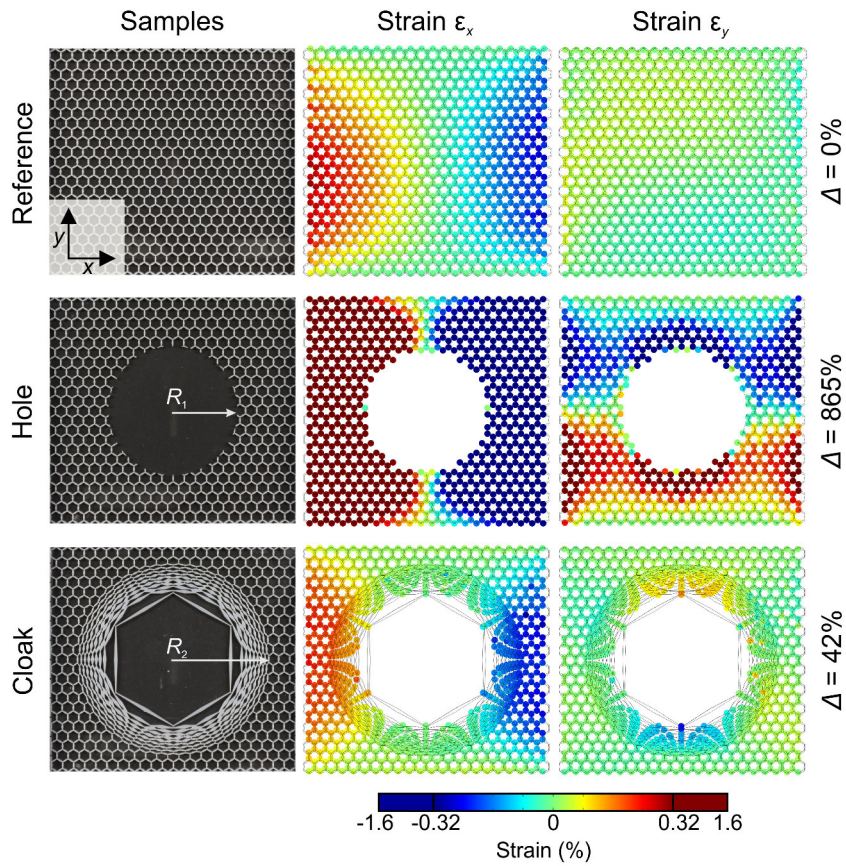
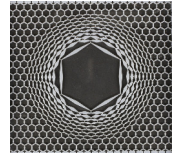


Figure 20: Measurement of a lattice transformation cloak with $R_2 = 60\text{mm}$ and $R_1 = 40\text{mm}$. Here the cloaking performance is close to the expected values. The hole case again is not showing a deformation as large as expected.

The cloaking concept can thus be applied to different settings and for various possible parameters of the transformation or the initial material. The theoretical concept is validated by numerical calculations as well as experiments.



Pulse-Shape Incident in the Dynamic Considerations

After the additional data shown for the static simulations and measurements dynamic considerations are performed. To be able to send a pulse into the mechanical domain, a displacement is assigned onto one boundary of the simulation space. The pulse is consisting of a sinusoidal enveloped by a gaussian as:

$$u(t) = A * \sin(\omega t) \times \exp\left(-\frac{(t - t_0)^2}{2\sigma^2}\right) \quad (13)$$

The absolute amplitude A was set to 1. The pulse is further shifted in time by $t_0 = 0.5$ s to be incident only at finite times. The displacement over time is plotted in Figure 21 for a frequency of $\omega = 80$ Hz and a width of $\sigma = 0.1$.

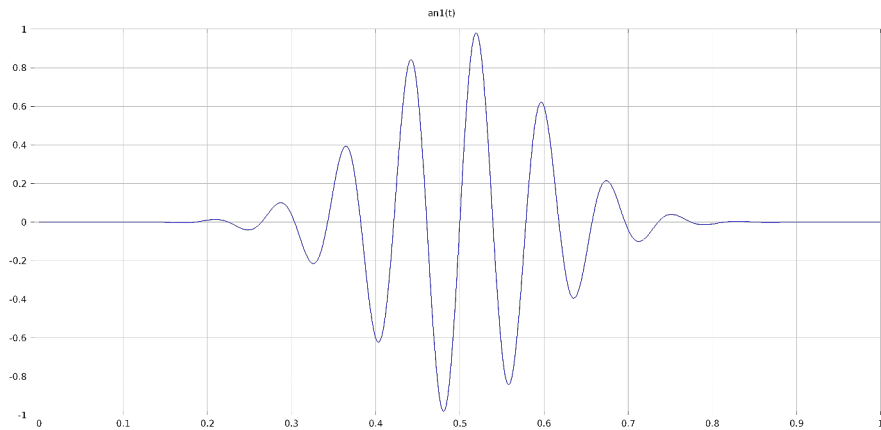


Figure 21: Pulse shape of the dynamic evaluation of the lattice transformation cloak. The amplitude is plotted over time.

4 D - Material Information

4.1 IP Photoresists

DATA SHEET



IP-PHOTORESISTS

Nanoscribe's family of negative-tone IP-photoresists is specifically designed for the demands of true 3D laser lithography by two-photon polymerization (2PP). IP-photoresists provide extraordinary resolution and high mechanical stability for structures in the micro and sub-micron range.

IP-L and **IP-L 780** are the liquid photoresist formulations showing the highest resolution achieved so far in combination with Nanoscribe's laser lithography systems *Photonic Professional* (see *Figure 1*).

IP-G and **IP-G 780** are the corresponding gel formulations of the acrylic photoresist. The high viscosity makes this resist ideal for complex writing tasks with arbitrary writing sequences and minimum feature sizes on the micro- and sub-micrometer scale (see *Figure 2*).

IP-Dip is the specially designed photoresist for Nanoscribe's novel Dip-in Laser Lithography (DILL) technology. IP-Dip serves as immersion and photosensitive material at the same time by dipping the microscope objective into this liquid photoresist. Due to its refractive index matched to the focusing optics IP-Dip guarantees ideal focusing and hence highest resolution for DILL (see *Figure 3*).



FEATURES

- Feature sizes down to 150 nm
- Low proximity effect
- Low stress
- Little shrinkage
- Good adhesion on glass substrates
- Easy handling: drop-casting of the photoresist

Features	IP-L (780)	IP-G (780)	IP-Dip
Refractive index at 780 nm unexposed	1.48	~ 1,50	1.52
Prebake	No	Yes	No
Cast process	Drop casting	Drop casting or spin coating	Drop casting
Exposure	780 nm for 2PP	780 nm for 2PP	780 nm for 2PP
Postbake	No	No	No
Developer	PGMEA / IPA	PGMEA / IPA	PGMEA / IPA

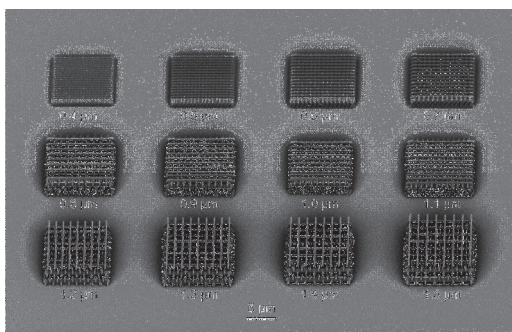


Fig.1: Woodpile structures consisting of parallel rods stacked upon another. The center-to-center rod distance is varied from 1.5 μm to 0.4 μm in steps of 100 nm. Resist: IP-L.

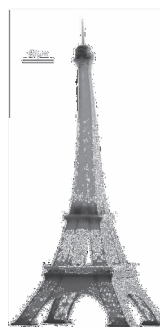


Fig.2: Eiffel tower, written with *Photonic Professional* (scale 1:3,000,000). Resist: IP-G.

Figure 22: IP Photoresist

4. D - Material Information

IP-Photoresists

RESOLUTION

- Down to 600 nm laterally in 3D
- 2½ D structuring with enormous design freedom
- 2D structuring with feature sizes down to 100 nm and resolution down to 300 nm
- DILL: Aberration constant writing in liquid resists for ultra-high and precise microstructures even on opaque substrates

APPLICATIONS

- Photonic crystals
- Photonic wire bonds
- Micro-optics
- Micro-/nano-fluidics
- Biomimetics
- Ultralight materials
- Mechanical metamaterials
- Scaffolds and tissue engineering
- Micro rapid prototyping
- And many others...

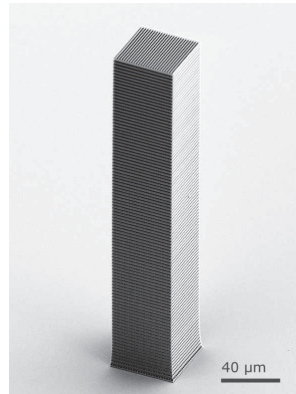


Fig.3: 280 μm tall woodpile structure written by means of the Dip-in laser lithography technology in IP-Dip photoresist.

REFERENCES

- S. Tottori et al., *Magnetic Helical Micromachines: Fabrication, Controlled Swimming, and Cargo Transport*, *Advanced Materials* 24, 709 (2012)
- R. Wittig et al., *Direct laser writing-mediated generation of standardized topographies for dental implant surface optimization*, *Journal of Laser Applications*, Vol. 24, 042011 (2012)
- M. Röhrig et al., *3D Direct Laser Writing of Nano- and Microstructured Hierarchical Gecko-Mimicking Surfaces*, *Small*, doi:10.1002/smll.201200308 (2012)
- M. Kadic et al., *On the practicability of pentamode mechanical metamaterials*, *Applied Physics Letters* 100, 191901 (2012)
- J. H. Atwater et al., *Microphotonic parabolic light directors fabricated by two-photon lithography*, *Applied Physics Letters* 99, (2011)



CONTACT

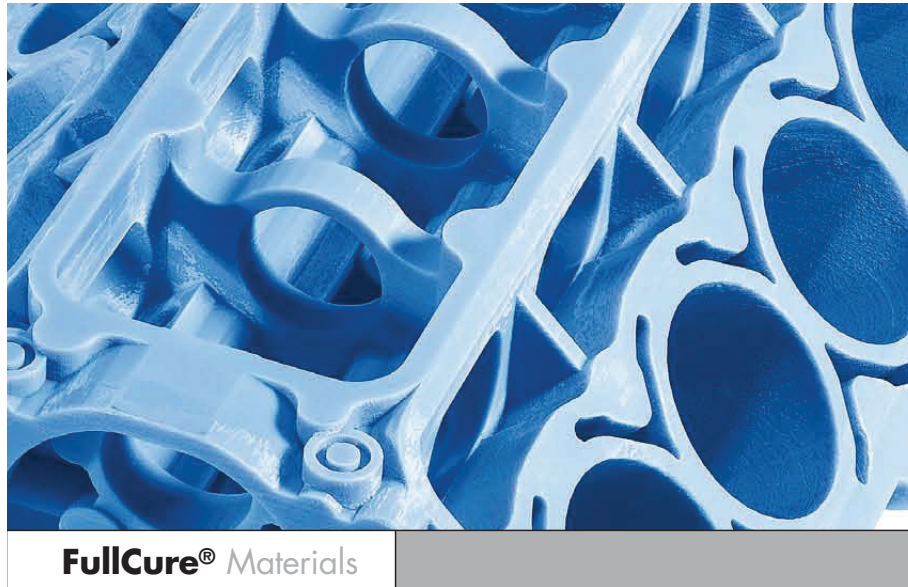
Nanoscribe GmbH
Hermann-von-Helmholtz-Platz 1
76344 Eggenstein-Leopoldshafen
Germany

Tel +49 721 60 82 88 40
Fax +49 721 60 82 88 48

E-Mail sales@nanoscribe.de
Web www.nanoscribe.de

Figure 23: IP Photoresist

4.2 Full-Cure Printing Materials



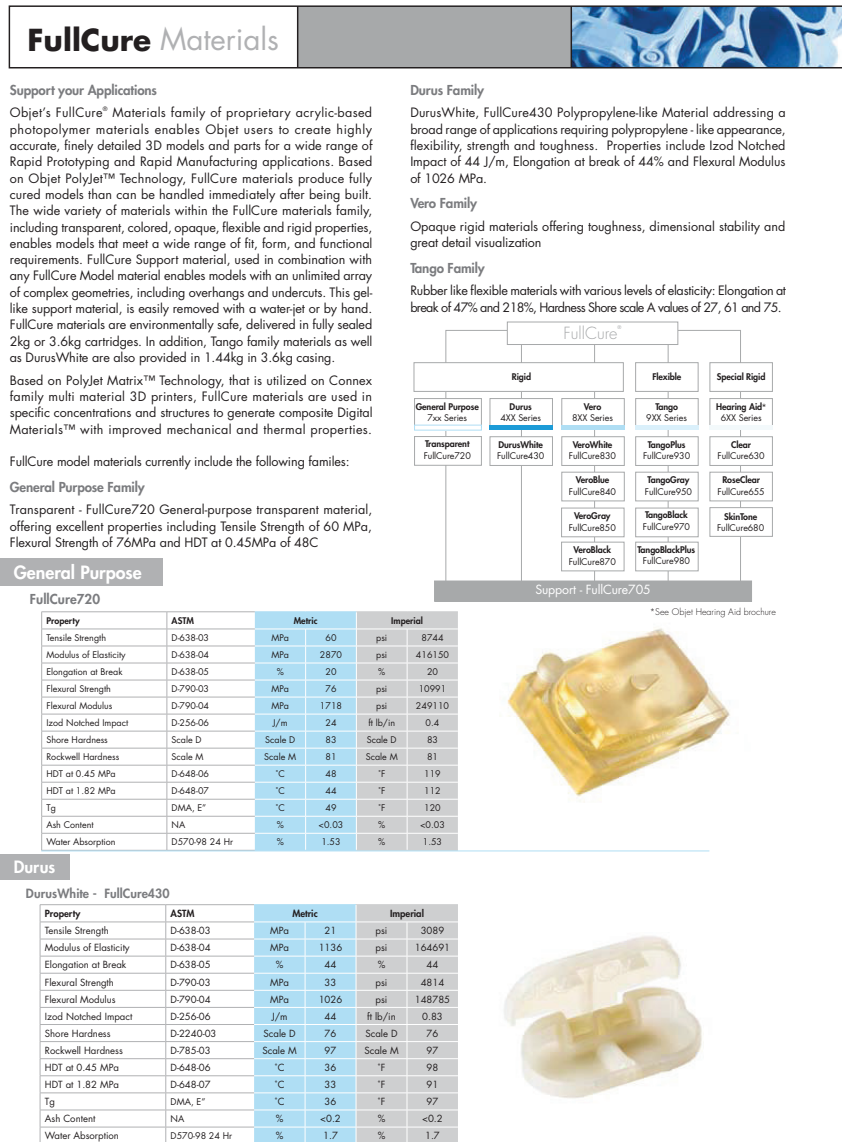
Support Your Application

- Choice of materials enables a wide variety of applications
- Excellent surface smoothness and fine details of the cured model
- Instant curing models ready to use
- Diversified Finishing
- Environmental Safety
- Easy to remove gel-like support material for all modeling materials



Figure 24: 3D printer materials

4. D - Material Information



Vero

VeroWhite - FullCure830

Property	ASTM	Metric	Imperial
Tensile Strength	D-638-03	MPa	psi
Modulus of Elasticity	D-638-04	MPa	psi
Elongation at Break	D-638-05	%	%
Flexural Strength	D-790-03	MPa	psi
Flexural Modulus	D-790-04	MPa	psi
Izod Notched Impact	D-256-06	J/m	ft lb/in
Shore Hardness	Scale D	Scale D	Scale D
Rockwell Hardness	Scale M	Scale M	Scale M
HDT at 0.45 MPa	D-648-06	°C	°F
HDT at 1.82 MPa	D-648-07	°C	°F
Tg	DMA, E"	°C	°F
Ash Content	USP 28	%	%
Water Absorption	D570-98 24 Hr	%	%



VeroBlue - FullCure840

Property	ASTM	Metric	Imperial
Tensile Strength	D-638-03	MPa	psi
Modulus of Elasticity	D-638-04	MPa	psi
Elongation at Break	D-638-05	%	%
Flexural Strength	D-790-03	MPa	psi
Flexural Modulus	D-790-04	MPa	psi
Izod Notched Impact	D-256-06	J/m	ft lb/in
Shore Hardness	Scale D	Scale D	Scale D
Rockwell Hardness	Scale M	Scale M	Scale M
HDT at 0.45 MPa	D-648-06	°C	°F
HDT at 1.82 MPa	D-648-07	°C	°F
Tg	DMA, E"	°C	°F
Ash Content	USP 28	%	%
Water Absorption	D570-98 24 Hr	%	%



VeroGray - FullCure850

Property	ASTM	Metric	Imperial
Tensile Strength	D-638-03	MPa	psi
Modulus of Elasticity	D-638-04	MPa	psi
Elongation at Break	D-638-05	%	%
Flexural Strength	D-790-03	MPa	psi
Flexural Modulus	D-790-04	MPa	psi
Izod Notched Impact	D-256-06	J/m	ft lb/in
Shore Hardness	Scale D	Scale D	Scale D
Rockwell Hardness	Scale M	Scale M	Scale M
HDT at 0.45 MPa	D-648-06	°C	°F
HDT at 1.82 MPa	D-648-07	°C	°F
Tg	DMA, E"	°C	°F
Ash Content	USP 28	%	%
Water Absorption	D570-98 24 Hr	%	%



VeroBlack - FullCure870

Property	ASTM	Metric	Imperial
Tensile Strength	D-638-03	MPa	psi
Modulus of Elasticity	D-638-04	MPa	psi
Elongation at Break	D-638-05	%	%
Flexural Strength	D-790-03	MPa	psi
Flexural Modulus	D-790-04	MPa	psi
Izod Notched Impact	D-256-06	J/m	ft lb/in
Shore Hardness	Scale D	Scale D	Scale D
Rockwell Hardness	Scale M	Scale M	Scale M
HDT at 0.45 MPa	D-648-06	°C	°F
HDT at 1.82 MPa	D-648-07	°C	°F
Tg	DMA, E"	°C	°F
Ash Content	USP 28	%	%
Water Absorption	D570-98 24 Hr	%	%



Figure 26: 3D printer materials

4. D - Material Information

Tango

TangoPlus - FullCure930 / TangoBlackPlus - FullCure980

Property	ASTM		Metric		Imperial	
Tensile Strength at Break	D-412	MPa	1.5	psi	211	
Modulus of Elasticity at 20% Strain	D-413	MPa	0.1	psi	21	
Modulus of Elasticity at 30% Strain	D-414	MPa	0.2	psi	27	
Modulus of Elasticity at 50% Strain	D-415	MPa	0.3	psi	38	
Elongation at Break	D-412	%	218	%	218.0	
Compressive Set	D-395	%	4	%	4.4	
Shore A Hardness	D-2240	Scale A	27	Scale A	27	
Ross Flex	D-1052		Above 150,000		Above 150,000	
Tensile Tear Resistance	D-624	Kg/cm	3	Lb/in	20	
Tg	DSC (80°C+100°C)	°C	-10	°F	15	



TangoGray - FullCure950

Property	ASTM		Metric		Imperial	
Tensile Strength	D-412	MPa	4	psi	632	
Elongation at Break	D-412	%	47	%	47	
Compressive Set	D-395	%	1	%	1	
Shore A Hardness	D-2240	Scale A	75	Scale A	75	
Tensile Tear Resistance	D-624	Kg/cm	10	Lb/in	54	
Tg	DSC (80°C+100°C)	°C	3	°F	37	



TangoBlack - FullCure970

Property	ASTM		Metric		Imperial	
Tensile Strength	D-412	MPa	2	psi	290	
Elongation at Break	D-412	%	48	%	48	
Compressive Set	D-395	%	1	%	1	
Shore A Hardness	D-2240	Scale A	61	Scale A	61	
Tensile Tear Resistance	D-624	Kg/cm	4	Lb/in	21	
Tg	DSC (80°C+100°C)	°C	-11	°F	13	



About Objet Geometries

Objet Geometries Ltd., the innovation leader in 3D printing, develops, manufactures and globally markets ultra-thin-layer, high-resolution 3-dimensional printing systems and materials that utilize PolyJet™ polymer jetting technology, to print ultrathin 16-micron layers.

The market-proven Eden™ line of 3D Printing Systems and the Alaris™ 30 3D desktop printer are based on Objet's patented office-friendly PolyJet™ technology. The Connex™ family is based on Objet's PolyJet Matrix™ Technology, which jets multiple model materials simultaneously and creates composite Digital Materials™ on the fly. All Objet systems use Objet's FullCure® materials to create accurate, clean, smooth, and highly detailed 3D parts.

Objet's solutions enable manufacturers and industrial designers to reduce cost of product development and dramatically shorten time-to-market of new products. Objet systems are in use by world leaders in many industries, such as automotive, electronics, toy, consumer goods, and footwear industries in North America, Europe, Asia, Australia, and Japan.

Founded in 1998, Objet serves its growing worldwide customer base through offices in USA, Europe and Hong Kong, and a global network of distribution partners. Objet owns more than 50 patents and patent pending inventions. Visit www.objet.com.

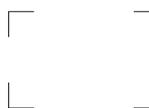
Objet Geometries Ltd.
Headquarters
 2 Holzman st.,
 Science Park,
 P.O. Box 2496,
 Rehovot 76124, Israel
 T: +972-8-931-4314
 F: +972-8-931-4315

Objet Geometries Inc.
North America
 5 Fortune Drive
 Billerica
 MA 01821
 USA
 T: +1-877-489-9449
 F: +1-866-676-1533

Objet Geometries GmbH
Europe
 Airport Boulevard B 210
 77836 Rheinmünster
 Germany
 T: +49-7229-7772-0
 F: +49-7229-7772-990

Objet Geometries AP
Asia Pacific
 Unit28, 10/F, HITEC
 1 Trademart Drive
 Kowloon Bay, Kowloon
 Hong Kong
 T: +852-217-40111
 F: +852-217-40555

Objet Geometries AP
Limited China Rep. Office
 Rm 1220, CIMIC Tower,
 1090 Century Blvd,
 Pudong Shanghai
 200120 P. R. China
 T: +86-21-5836-2468
 F: +86-21-5836-2469



info@objet.com www.objet.com

© 2009 Objet, Quadra, QuadraTempo, PolyJet, FullCure, SHR, Eden, Eden250, Eden260, Eden260V, Eden300, Eden350, Eden350V, Eden500V, Job Manager, Objet Studio, CADMatrix, Connex, Connex350, Connex500, Alaris, Alaris30, Polylog, TangoBlack, TangoGray, TangoPlus, TangoBlackPlus, VeraBlue, VeraWhite, VeraBlack, VeraGray, Duris, Digital Materials, PolyJet Matrix and ObjetGreen are trademarks of Objet Geometries Ltd. and may be registered in certain jurisdictions. All other trademarks belong to their respective owners.



OBJET

Figure 27: 3D printer materials

Bibliography

- [1] C. M. Soukoulis and M. Wegener, “Optical Metamaterials — More Bulky and Less Lossy,” *Science* **330**, 1633 (2010). (p. 1)
- [2] S. Guenneau, C. Amra, and D. Veynante, “Transformation Thermodynamics: Cloaking and Concentrating Heat Flux,” *Opt. Express* **20**, 8207–8218 (2012). (p. 1)
- [3] S. Narayana and Y. Sato, “Heat Flux Manipulation with Engineered Thermal Materials,” *Phys. Rev. Lett.* **108**, 214303 (2012). (p. 1)
- [4] R. Schittny, M. Kadic, S. Guenneau, and M. Wegener, “Experiments on Transformation Thermodynamics: Molding the Flow of Heat,” *Phys. Rev. Lett.* **110**, 195901 (2013). (p. 1, 16)
- [5] M. Maldovan, “Sound and heat revolutions in phononics,” *Nature* **503**, 209–217 (2013). (p. 1)
- [6] T. Han, X. Bai, D. Gao, J. T. L. Thong, and C. Li, B. and Qiu, “Experimental Demonstration of a Bilayer Thermal Cloak,” *Phys. Rev. Lett.* **112**, 054302 (2014). (p. 1)
- [7] R. V. Craster and S. Guenneau, *Acoustic metamaterials: negative refraction, imaging, lensing and cloaking* (Springer, Dordrecht, 2013). (p. 1, 12, 88, 94)
- [8] J. Li, Y. Gao, and J. Huang, “A bifunctional cloak using transformation media,” *J. Appl. Phys.* **108**, 074504 (2010). (p. 1)
- [9] F. Yang, Z. L. Mei, T. Y. Jin, and T. J. Cui, “dc Electric Invisibility Cloak,” *Phys. Rev. Lett.* **109**, 053902 (2012). (p. 1)
- [10] M. Liu, Z. L. Mei, X. Ma, and T. J. Cui, “dc illusion and its experimental verification,” *Appl. Phys. Lett.* **101**, 051905 (2012). (p. 1)
- [11] C. Naveau, D. Chan, A. Sanchez, and N. Del-Valle, “Magnetic properties of a dc metamaterial consisting of parallel square superconducting thin plates,” *Appl. Phys. Lett.* **94**, 242501 (2009). (p. 1)
- [12] F. Gömöry, M. Solovyov, J. Souc, C. Navau, J. Prat-Camps, and A. Sanchez, “Experimental Realization of a Magnetic Cloak,” *Science* **335**, 1466–1468 (2012). (p. 1)

Bibliography

- [13] F. Sun and S. He, “DC magnetic concentrator and omni-directional cascaded cloak by using only one or two homogeneous anisotropic materials of positive permeability,” *Prog. Electromagn. Res.* **142**, 683–699 (2013). (p. 1)
- [14] R. Schittny, M. Kadic, T. Bückmann, and M. Wegener, “Invisibility cloaking in a diffusive light scattering medium,” *Science* **345**, 427–429 (2014). (p. 1)
- [15] R. Schittny, A. Niemeyer, M. Kadic, T. Bückmann, and M. Wegener, “Transient behavior of invisibility cloaks for diffusive light propagation,” *Optica* **2**, 84–87 (2015). (p. 1)
- [16] H. Tzou and G. Anderson, *Intelligent Structural Systems* (Springer, New York, 1992). (p. 1)
- [17] G. W. Milton, *The theory of composites* (Cambridge Univ. Press, 2002). (p. 1, 13, 54, 98, 126)
- [18] T. A. Schaedler, A. Jacobsen, A. Torrents, A. Sorensen, J. Lian, J. Greer, L. Valdevit, and W. Carter, “Ultralight Metallic Microlattices,” *Science* **334**, 962–965 (2011). (p. 1, 59, 79, 81, 124)
- [19] G. W. Milton, “What nonlinear unimode metamaterials can one get using rigid bars and pivots?” *J. Mech. Phys. Solids* **61**, 1543–1560 (2013). (p. 1, 37)
- [20] L. Gibson and et al, *Mechanics of cellular solids* (Pergamon Oxford, Oxford, 1988). (p. 1)
- [21] G. N. Greaves, A. L. Greer, R. Lakes, and T. Rouxel, “Poisson’s ratio and modern materials,” *Nature Mater.* **10**, 823–837 (2011). (p. 1, 9, 10, 37)
- [22] J. Schwerdtfeger, F. Wein, G. Leugering, R. Singer, C. Körner, M. Stingl, and F. Schury, “Design of Auxetic Structures via Mathematical Optimization,” *Adv. Mater.* **23**, 2650–2654 (2011). (p. 1)
- [23] U. D. Larsen, O. Sigmund, and S. Bouwstra, “Design and fabrication of compliant micromechanisms and structures with negative Poisson’s ratio,” in *Proc. ‘An Investigation of Micro Structures, Sensors, Actuators, Machines and Systems’. IEEE Workshop The Ninth Annual Int Micro Electro Mechanical Systems, MEMS ’96* 1 pp. 365–371 (1996). (p. 1)
- [24] B. Xu, F. Arias, S. Brittain, X. Zhao, B. Grzybowski, and G. Torquato, S. and Whitesides, “Making Honeycomb Microcomposites by Soft Lithography,” *Adv. Mater.* **11**, 1186–1189 (1999). (p. 1)
- [25] D. Y. Fozdar, P. Soman, J. Lee, L. Han, and S. Chen, “Three-Dimensional Polymer Constructs Exhibiting a Tunable Negative Poisson’s Ratio,” *Adv. Funct. Mater.* **21**, 2712–2720 (2011). (p. 1)

Bibliography

- [26] T. Bückmann, N. Stenger, M. Kadic, J. Kaschke, A. Frölich, T. Kennerknecht, C. Eberl, M. Thiel, and M. Wegener, “Tailored 3D mechanical metamaterials made by dip-in direct-laser-writing optical lithography,” *Adv. Mater.* **24**, 2710–2714 (2012). (p. 1, 11, 26, 62)
- [27] W. F. Chen and A. F. Saleeb, *Constitutive equations for engineering materials*, Vol. 1 (Elsevier, 1994). (p. 5)
- [28] B. Banerjee, *An introduction to Metamaterials and Waves in Composites*, Vol. 1 (CRC Press Taylor Francis Group, 2011). (p. 5, 6, 13, 14)
- [29] L. Kinsler, A. Frey, A. Coppens, and J. Sanders, *Fundamentals of Acoustics* (John Wiley & Sons INC., 2000), 4 edn. (p. 7)
- [30] A. N. Norris, “Mechanics of elastic networks,” *Proc. R. Soc. B* **282**, 0140 522 (2014). (p. 8)
- [31] N. A. Fleck, V. S. Deshpande, and M. Ashby, “Micro-architected materials: past, present and future,” *Proc. R. Soc. A* **466**, 2495?2516 (2010). (p. 9, 10)
- [32] J. Bauer, A. Schroer, R. Schwaiger, I. Tesari, C. Lange, and O. Kraft, “Push-to-pull tensile testing of ultra-strong ceramic-polymer composites made by additive manufacturing,” *Extreme Mechanics Letters* (2015). (p. 9, 11, 79)
- [33] W. Bergmann, *Werkstofftechnik Teil 1: Grundlagen* (Carl Hanser Verlag, München Wien, 1984), 1 edn. (p. 11)
- [34] E. Cosserat and F. Cosserat, *Deformable Bodies* (Scientific Library A. Hermann and Sons, 1909). (p. 11)
- [35] R. Lakes and S. Saha, “Cement line motion in bone,” *Science* **204**, 501–503 (1979). (p. 11)
- [36] M. Brun, S. Guenneau, and S. Movchan, “Achieving control of in-plane elastic waves,” *Appl. Phys. Lett.* **94**, 061 903 (2009). (p. 12, 16)
- [37] J. Mei, Z. Liu, W. Wen, and P. Sheng, “Effective mass density of fluid-solid composites,” *Phys. Rev. Lett.* **96**, 024 301 (2006). (p. 12, 88)
- [38] Z. Liu, X. Zhang, Y. Mao, Y. Y. Zhu, Z. Yang, C. T. Chan, and P. Sheng, “Locally resonant sonic materials,” *Science* **289**, 1734–1736 (2000). (p. 12, 87)
- [39] D. Torrent and J. Sanchez-Dehesa, “Anisotropic mass density by two-dimensional acoustic metamaterials,” *New J. Phys.* **10**, 023 004 (2008). (p. 12)
- [40] M. Kadic, T. Bückmann, R. Schittny, and M. Wegener, “Metamaterials beyond electromagnetism,” *Rep. Prog. Phys.* **76**, 126 501 (2012). (p. 13, 16, 89, 94)
- [41] F. Fahy and P. Gardonio, *Sound and Structural Vibration* (Academic Press, 2007), 2 edn. (p. 14)

Bibliography

- [42] N. Stenger, M. Wilhelm, and M. Wegener, “Experiments on Elastic Cloaking in Thin Plates,” *Phys. Rev. Lett.* **108**, 014 301 (2012). (p. 14, 16, 98)
- [43] H. F. Tiersten, “Elastic Surface Waves Guided by Thin Films,” *J. Appl. Phys.* **40**, 770 (1969). (p. 14)
- [44] M. R. J. Wyllie, A. R. Gregory, and L. W. Gardner, “Elastic wave velocities in heterogeneous and porous media,” *Geophysics* **21**, 41–70 (1956). (p. 14)
- [45] J. B. Pendry, D. Schurig, and D. R. Smith, “Controlling Electromagnetic Fields,” *Science* **312**, 1780–1782 (2006). (p. 14, 109)
- [46] D. Schurig, J. J. Mock, B. J. Justice, S. A. Cummer, J. B. Pendry, A. F. Starr, and D. R. Smith, “Metamaterial Electromagnetic Cloak at Microwave Frequencies,” *Science* **314**, 977–980 (2006). (p. 14, 16, 109)
- [47] G. W. Milton, M. Briane, and J. R. Willis, “On cloaking for elasticity and physical equations with a transformation invariant form,” *New J. Phys.* **8**, 284 (2006). (p. 14, 15, 70, 87)
- [48] A. N. Norris and A. L. Shuvalov, “Elastic Cloaking Theory,” *Wave Motion* **48**, 525–538 (2011). (p. 15)
- [49] J. B. Pendry, A. Holden, W. J. Stewart, and I. Youngs, “Extremely Low Frequency Plasmons in Metallic Mesostructures,” *Phys. Rev. Lett.* **76**, 4773–4776 (1996). (p. 16)
- [50] J. B. Pendry, A. J. Holden, D. J. Robbins, and W. J. Stewart, “Magnetism from Conductors and Enhanced Nonlinear Phenomena,” *IEEE Transactions on Microwave Theory and Techniques* **47**, 2075–2084 (1999). (p. 16, 87)
- [51] J. Valentine, S. Zhang, T. Zentgraf, E. Ulin-Avila, D. A. Genov, G. Bartal, and X. Zhang, “Three-dimensional optical metamaterial with a negative refractive index,” *Nature* **455**, 376–379 (2008). (p. 16)
- [52] J. Yao, Z. Liu, Y. Liu, Y. Wang, C. Sun, G. Bartal, A. M. Stacy, and X. Zhang, “Optical Negative Refraction in Bulk Metamaterials of Nanowires,” *Science* **321**, 930 (2008). (p. 16)
- [53] J. Fischer, T. Ergin, and M. Wegener, “Three-dimensional polarization-independent visible-frequency carpet invisibility cloak,” *Opt. Lett.* **36**, 2059–2061 (2011). (p. 16)
- [54] S. Zhang, C. Xia, and N. Fang, “Broadband Acoustic Cloak for Ultrasound Waves,” *Phys. Rev. Lett.* **106**, 024 301 (2011). (p. 16, 97)
- [55] M. G. D. Geers, V. G. Kouznetsova, and W. A. M. Brekelmans, “Multi-scale computational homogenization: Trends and challenges,” *J. Comput. Appl. Math.* **234**, 2175–2182 (2008). (p. 20)
- [56] V. G. Kouznetsova, *Computational homogenization for the multi-scale analysis of multi-phase materials* (Eindhoven: Technische Universiteit, 2002). (p. 20)

Bibliography

- [57] S. Kawata, H. B. Sun, T. Tanaka, and K. Takada, “Finer features for functional microdevices,” *Nature* **412**, 697–698 (2001). (p. 22)
- [58] J. Fischer and M. Wegener, “Three-dimensional optical laser lithography beyond the diffraction limit,” *Laser Photonics Rev.* **7**, 22–44 (2013). (p. 22, 25)
- [59] M. Goeppert-Mayer, “Über Elementarakte mit zwei Quantensprüngen,” *Ann. Phys. (Berlin)* **9**, 273–294 (1931). (p. 23)
- [60] P. Soman, J. W. Lee, A. Phadke, S. Varghese, and S. Chen, “Spatial tuning of negative and positive Poisson’s ratio in a multi-layer scaffold,” *Acta Biomater.* **8**, 2587 – 2594 (2012). (p. 23)
- [61] “Nanoscribe GmbH, Karlsruhe Germany,” .
<http://www.nanoscribe.de> (p. 23, 25, 27)
- [62] J. Fischer, “Three-dimensional optical lithography beyond the diffraction limit,” *KIT-Library, Karlsruhe* (2012), <http://nbn-resolving.org/urn:nbn:de:swb:90-287048>. (p. 24)
- [63] E. Hecht, *Optics* (Addison-Wesley, Bonn, 2001). (p. 24, 31)
- [64] G. P. Agrawal and R. W. Boyd, *Contemporary nonlinear optics* (Academic Press, 1992). (p. 24)
- [65] W. Demtröder, *Experimentalphysik 1. Mechanik und Wärme* (Springer-Verlag GmbH, 1998), 2 edn. (p. 28)
- [66] M. Katz, *Introduction to geometrical optics* (World Scientific Publishing Co. Pte. Ltd., 2002). (p. 31)
- [67] C. Eberl, D. S. Gianola, X. Wang, M. Y. He, A. G. Evans, and K. J. Hemker, “A method for in situ measurement of the elastic behavior of a columnar thermal barrier coating,” *Acta Materialia* **59**, 3612–3620 (2011). (p. 32)
- [68] T. Bückmann, R. Schittny, M. Thiel, M. Kadic, G. W. Milton, and M. Wegener, “On three-dimensional dilational elastic metamaterials,” *New J. Phys.* **16**, 033 032 (2014). (p. 33, 39, 41, 42, 43, 44, 45, 46, 49, 51, 62, 125)
- [69] T. Tsang and H. Y. Park, “Sound velocity anisotropy in cubic crystals,” *Phys. Lett. A* **99**, 377–380 (1983). (p. 34)
- [70] R. Hill, “The Elastic Behaviour of a Crystalline Aggregate,” *Proc. Phys. Soc. A* **65**, 349–354 (1952). (p. 35)
- [71] F. Bowers, *Applied Mechanics of Solids* (Boca Raton, FL: CRC, 1992). (p. 35)
- [72] K. W. Wojciechowski, “Poisson’s ratio of anisotropic systems,” *Comp. Methods Sci. Technol.* **11**, 73–79 (2005). (p. 35)

Bibliography

- [73] R. Lakes, T. Lee, A. Bersie, and Y. C. Wang, “Extreme damping in composite materials with negative-stiffness inclusions,” *Nature* **410**, 565–567 (2001). (p. 36)
- [74] Y. S. Wang and R. Lakes, “Composites with Inclusions of Negative Bulk Modulus: Extreme Damping and Negative Poisson’s Ratio,” *J. Compos. Mater.* **39**, 1645–1657 (2015). (p. 36)
- [75] N. Fang, D. Xi, J. Xu, M. Ambati, W. Srituravanich, C. Sun, and X. Zhang, *Nature Mater.* **5**, 452–456 (2006). (p. 36)
- [76] J. Li and C. T. Chan, “Double-negative acoustic metamaterial,” *Phys. Rev. E* **70**, 055 602(R) (2004). (p. 36)
- [77] Y. Ding, Z. Liu, C. Qiu, and J. Shi, “Metamaterial with simultaneously negative bulk modulus and mass density,” *Appl. Phys. Lett.* **99**, 093 904 (2007). (p. 36)
- [78] A. Ballato, “Poisson’s Ratios of Auxetic and Other Technological Materials,” *IEEE Transactions on Ultrasonics, Ferroelectrics and Frequency Control* **57**, 7–14 (2010). (p. 36)
- [79] A. Y. Haeri, D. J. Weidner, and J. B. Parise, “Elasticity of α -cristobalite: a silicon dioxide with a negative Poisson’s ratio,” *Science* **257**, 650–652 (1992). (p. 36)
- [80] R. H. Baughman, J. M. Shacklette, A. A. Zakhidov, and S. Stafstrom, “Negative Poisson’s ratios as a common feature of cubic metals,” *Nature* **392**, 362–365 (1998). (p. 36)
- [81] R. H. Baughman, S. O. Dantas, S. Stafström, T. B. Zakhidov, A. A. and Mitchel, and D. H. E. Dubin, “Negative Poisson’s Ratios for Extreme States of Matter,” *Science* **288**, 2018–2022 (2000). (p. 36)
- [82] R. Hooke, *MICROGRAPHIA: or, Some Physiological Descriptions of minute bodies made by magnifying glasses*, Vol. 1 (J. Martyn and J. Allestry, London, 1665). (p. 36)
- [83] R. Lakes, “Foam Structures with a Negative Poisson’s Ratio,” *Science* **235**, 1038–1040 (1987). (p. 36)
- [84] R. Lakes, “Deformation mechanisms in negative Poisson’s ratio materials: structural aspects,” *J. Material Science* **26**, 2287–2292 (1991). (p. 37)
- [85] R. Lakes, “Advances in negative Poisson’s ratio materials,” *Adv. Mater.* **5**, 293–296 (1993). (p. 37)
- [86] R. Lakes and K. W. Wojciechowski, “Negative compressibility, negative Poisson’s ratio, and stability,” *Phys. Status Solidi B* **245**, 545–551 (2008). (p. 37)
- [87] J. B. Choi and R. Lakes, “Nonlinear properties of metallic cellular materials with a negative Poisson’s ratio,” *J. Material Science* **27**, 5373–5381 (1992). (p. 37)

Bibliography

- [88] G. W. Milton, “Composite materials with Poisson’s ratios close to -1,” *J. Mech. Phys. Solids* **40**, 1105–1137 (1992). (p. 37)
- [89] U. D. Larsen, O. Sigmund, and S. Bouwsta, “Design and fabrication of compliant micromechanisms and structures with negative Poisson’s ratio,” *IEEE J MEMS* **6**, 99–106 (1997). (p. 37)
- [90] D. Prall and R. Lakes, “Properties of a chiral honeycomb with a Poisson’s ratio -1,” *Int. J. of Mechanical Science* **39**, 305–314 (1996). (p. 37)
- [91] H. Mischke, J. Schwerdtfeger, F. Schury, M. Stingl, C. Körner, R. F. Singer, V. Robin, K. Mecke, and G. E. Schröder-turk, “Design of Auxetic Structures via Mathematical Optimization,” *Adv. Mater.* **23**, 2669–2674 (2011). (p. 37)
- [92] J. N. Grima and K. E. Evans, “Auxetic behavior from rotating squares,” *J. Mater. Sci. Lett.* **19**, 1563–1565 (2000). (p. 37)
- [93] O. Sigmund, “Materials with prescribed constituent parameters: an inverse homogenization problem,” *Int. J. Solids Structures* **17**, 2313–2329 (1994). (p. 37)
- [94] C. Andreassen, E. Andreassen, J. Jensen, and O. Sigmund, “On the realization of the bulk modulus bounds for two-phase viscoelastic composites,” *J. Mech. Phys. Solids* **63**, 228–241 (2014). (p. 37)
- [95] E. Andreassen, B. Lazarov, and O. Sigmund, “Design of manufacturable 3D extremal elastic microstructure,” *Mech. Mater.* **69**, 1–10 (2014). (p. 37)
- [96] J. Shim, C. Perdigou, K. Chen, E. R. Bertoldi, and P. Reis, “Design of Auxetic Structures via Mathematical Optimization,” *P. Natl. Acad. Sci. USA* **109**, 5978–5983 (2012). (p. 37)
- [97] K. Krieger, “Extreme mechanics: Buckling down,” *Nature* **488**, 146 (2012). (p. 37)
- [98] K. Bertoldi, P. Reis, S. Willshaw, and T. Mullin, “Negative Poisson’s Ratio Behavior Induced by an Elastic Instability,” *Adv. Mater.* **22**, 361–366 (2010). (p. 37)
- [99] J. Overvelde, S. Shan, and K. Bertoldi, “Compaction Through Buckling in 2D Periodic, Soft and Porous Structures: Effect of Pore Shape,” *Adv. Mater.* **24**, 2337–2342 (2012). (p. 37)
- [100] S. Babee, J. Shim, J. Weaver, E. Chen, N. Patel, and K. Bertoldi, “3D Soft Metamaterials with Negative Poisson’s Ratio,” *Adv. Mater.* **26**, 5044–5049 (2013). (p. 37)
- [101] J. Grima, G. Ruben, A. Alderson, and K. Evans, “On the Auxetic Properties of Rotating Rectangles with Different Connectivity,” *J. Phys. Soc. Jpn.* **74** (2005). (p. 37)
- [102] J. Grima, P. Farrugia, C. Caruana, R. Gatt, and D. Attard, “Auxetic behaviour from stretching connected squares,” *Journal of Materials science* **43**, 5962–5971 (2008). (p. 37)

Bibliography

- [103] D. Attard and J. Grima, “Auxetic behaviour from rotating rhombi,” *Phys. Status Solidi B* **245**, 2395–2404 (2008). (p. 37)
- [104] R. Gatt, L. Mizzi, J. Azzopardi, K. Azzopardi, D. Attard, A. Casha, J. Briffa, and J. Grima, “Hierarchical Auxetic Mechanical Metamaterials,” *Sci. Rep.* **5** (2015). (p. 37)
- [105] G. Milton, “Complete characterization of the macroscopic deformations of periodic unimode metamaterials of rigid bars and pivots,” *J. Mech. Phys. Solids* **61**, 1543–1560 (2013). (p. 38)
- [106] R. Schittny, T. Bückmann, M. Kadic, and M. Wegener, “Elastic measurements on macroscopic three-dimensional pentamode metamaterials,” *Appl. Phys. Lett.* **103**, 231 905 (2013). (p. 47, 53, 60, 61, 64)
- [107] G. W. Milton and A. V. Cherkaev, “Which Elasticity Tensors are Realizable?” *J. Eng. Mater. Technol.* **117**, 483–494 (1995). (p. 53, 54, 70, 77, 85)
- [108] M. Kadic, T. Bückmann, N. Stenger, M. Thiel, and M. Wegener, “On the feasibility of pentamode mechanical metamaterials,” *Appl. Phys. Lett.* **100** (2012). (p. 53, 55, 57, 58, 59, 60)
- [109] A. Martin, M. Kadic, R. Schittny, T. Bückmann, and M. Wegener, “Phonon band structures of three-dimensional pentamode metamaterials,” *Phys. Rev. B* **86**, 155 116 (2012). (p. 53, 65, 66, 67, 68, 69)
- [110] M. Kadic, T. Bückmann, R. Schittny, and M. Wegener, “On anisotropic versions of three-dimensional pentamode metamaterials,” *New J. Phys.* **15**, 023 029 (2013). (p. 53, 71, 73, 74, 75, 76)
- [111] P. G. Martinson and A. B. Movchan, “Vibrations of lattice structures and phononic band gaps,” *Q. J. Mech. Appl. Math.* **56**, 45–64 (2003). (p. 54, 65)
- [112] C. N. Layman, C. J. Naify, T. P. Martin, D. C. Calvo, and G. J. Orris, “Highly-anisotropic elements for acoustic pentamode applications,” *Phys. Ref. Lett.* **111**, 024 302 (2013). (p. 54)
- [113] A. N. Norris, “Acoustic metafluids,” *J. Acoust. Soc. Am.* **125**, 839–849 (2009). (p. 54)
- [114] P. Mott, J. R. Dorgan, and C. M. Roland, “The bulk modulus and Poisson’s ratio of “incompressible” materials,” *J. Sound Vib.* **312**, 572–575 (2008). (p. 56)
- [115] C. Kittel and P. McEuen, *Introduction to Solid State Physics*, Vol. 8 (Wiley, New York, 1967). (p. 65)
- [116] J. G. Berryman, “Long wavelength propagation in composite elastic media II. Ellipsoidal inclusions,” *J. Acoust. Soc. Am.* **68**, 1820–1831 (1980). (p. 69)
- [117] A. A. Krokhin, J. Arriaga, and L. N. Gumen, “Speed of sound in periodic elastic composites,” *Phys. Rev. Lett.* **91**, 264 302 (2003). (p. 69)

Bibliography

- [118] C. Cai, Z. Wang, Q. Li, Z. Xu, and X. Tian, “Pentamode metamaterials with anisotropic double-cone elements,” *J. Phys. D Appl. Phys.* **48**, 175 103 (2015). (p. 75, 77)
- [119] G. F. Mejica and A. D. Lantada, “Comparative study of potential pentamode metamaterials inspired by Bravais lattices,” *Smart Mater. Struct.* **22**, 115 013 (2013). (p. 77)
- [120] S. S. Kistler, “Coherent expanded Aerogels and jellies,” *Nature* **127** (1931). (p. 79)
- [121] T. M. Tillotson and L. W. Hrubesh, “Transparent ultralow density silica aerogels prepared by a two-step solgel process,” *J. Non-Cryst. Solids* **145** (1992). (p. 79)
- [122] F. Greer, D. Jang, L. R. Meza, and J. R. Greer, “Fabrication and deformation of three-dimensional hollow ceramic nanostructures,” *Nature Mater.* **12**, 893 (2013). (p. 79)
- [123] J. Bauer, S. Hengsbach, I. Tesari, R. Schwaiger, and O. Kraft, “High-strength cellular ceramic composites with 3D microarchitecture,” *P. Natl. Acad. Sci. USA* **111**, 2453–2458 (2014). (p. 79)
- [124] X. Zheng, H. Lee, T. H. Weisgraber, M. Shusteff, J. DeOtte, E. B. Duoss, J. D. Kunz, M. M. Biener, Q. Ge, J. A. Jackson, S. O. Kucheyev, N. X. Fang, and C. M. Spadaccini, “Ultralight, ultrastiff mechanical metamaterials,” *Science* **344**, 1373 (2014). (p. 79, 124)
- [125] A. Frölich and M. Wegener, “Spectroscopic characterization of highly doped ZnO films grown by atomic-layer deposition for three-dimensional infrared metamaterials,” *Opt. Mater. Express* **1**, 883–889 (2011). (p. 79)
- [126] M. Mecklenburg, A. Schuchardt, Y. K. Mishra, S. Kaps, R. Adelung, A. Lotnyk, L. Kienle, and K. Schulte, “Aerographite: Ultra Lightweight, Flexible Nanowall, Carbon Microtube Material with Outstanding Mechanical Performance,” *Adv. Mater.* **24**, 3486–3490 (2012). (p. 81, 124)
- [127] M. Kadic, T. Bückmann, R. Schittny, P. Gubsch, and M. Wegener, “Pentamode metamaterials with independently tailored bulk modulus and mass density,” *Phys. Rev. Applied* **2**, 054 007 (2014). (p. 83, 84, 85, 86, 88, 90)
- [128] C. T. Chan, J. Li, and G. K. H. Fun, “On extending the concept of double negativity to acoustic waves,” *J. Zhejiang Univ. Sci. A* **7**, 24–28 (2005). (p. 88)
- [129] R. Zhu, X. Liu, G. Hu, F. G. Yuan, and G. Huang, “Microstructural designs of plate-type elastic metamaterial and their potential applications: a review.” *International Journal of Smart and Nano Materials* pp. 1–37 (2015). (p. 88)
- [130] T. Bückmann, M. Kadic, R. Schittny, and M. Wegener, “Mechanical metamaterials with anisotropic and negative effective mass-density tensor made from one constituent material,” *Phys. Status Solidi B* (2015), doi:10.1002/pssb.201451698. (p. 88, 91, 92, 96)

Bibliography

- [131] Y. F. Wang and Y. S. Wang, “Complete Bandgap in Three-Dimensional Holey Phononic Crystals With Resonators,” *J. Vib. Acoust.* **135**, 041 009 (2013). (p. 90)
- [132] Y. Liu, X. Su, and C. T. Sun, “Broadband elastic metamaterial with single negativity by mimicking lattice systems,” *Journal of Mechanics and Physics of Solids* **74** (2015). (p. 90)
- [133] M. Farhat, S. Enoch, S. Guenneau, and A. B. Movchan, “Broadband cylindrical acoustic cloak for linear surface waves in a fluid,” *Phys. Rev. Lett.* **101**, 134 501 (2008). (p. 97)
- [134] B. I. Popa, L. Zigoneanu, and S. A. Cummer, “Experimental acoustic ground cloak in air.” *Phys. Rev. Lett.* **106**, 253 901 (2011). (p. 97)
- [135] L. Zigoneanu, B. I. Popa, and S. A. Cummer, “Three-dimensional broadband omnidirectional acoustic ground cloak,” *Nature Mater.* **13**, 352–355 (2014). (p. 97)
- [136] V. M. Garcia-Chocano, D. Torrent, and J. Sanchez-Dehesa, “Reduced acoustic cloaks based on temperature gradients,” *Appl. Phys. Lett.* **101**, 084 103 (2012). (p. 97)
- [137] L. Sanchis, V. Garcia-Chocano, R. Llopis-Pontiveros, A. Climente, J. Martinez-Pastor, F. Cervera, and J. Sanchez-Dehesa, “Three-dimensional Axisymmetric Cloak based on the Cancelation of Acoustic Scattering from a Sphere,” *Phys. Rev. Lett.* **110**, 124 301 (2014). (p. 97)
- [138] A. V. Amirkhizi, A. Tehranian, and S. Nemat-Nasser, “Stress-wave energy management through material anisotropy,” *Wave Motion* **47**, 519–536 (2010). (p. 98)
- [139] T. Bückmann, M. Thiel, M. Kadic, R. Schittny, and M. Wegener, “An elasto-mechanical unfeelability cloak made of pentamode metamaterials,” *Nature Com.* **5**, 5130 (2014). (p. 98, 101, 103, 104, 105, 106, 107, 126, 129)
- [140] T. Bückmann, M. Kadic, R. Schittny, and M. Wegener, “Mechanical cloak design by lattice transformation,” *P. Natl. Acad. Sci. USA* **112**, 4930–4934 (2015). (p. 98, 110, 111, 113, 117, 118, 133, 134, 135, 137, 138, 139, 140, 142, 143)
- [141] E. H. Mansfield, “Neutral holes in plane sheet - reinforced holes which are elastically equivalent to the uncut sheet.” *Quart. Journ. Mech. and Applied Math.* **6**, 370–377 (1952). (p. 98, 109)
- [142] E. H. Kerner, “The elastic and thermo-elastic properties of composite media,” *Proc. Phys. Soc. B* **69**, 808–813 (1956). (p. 98, 126)
- [143] E. G. Kirsch, “Die Theorie der Elastizität und die Bedürfnisse der Festigkeitslehre,” *Zeitschrift des Vereines deutscher Ingenieure* **42**, 797–807 (1898). (p. 109)
- [144] J. Silverberg, A. A. Evans, L. McLeod, R. C. Hayward, T. C. D. Hull, Santangelo, and I. Cohen, “Using origami design principles to fold reprogrammable mechanical metamaterials,” *Science* **345**, 647–650 (2014). (p. 124)

Bibliography

- [145] C. Lv, D. Krishnaraju, G. Konjevod, y. YuHong, and H. Jiang, “Origami based Mechanical Metamaterials,” *Scientific Reports* **4**, 5979 (2014). (p. 124)
- [146] B. Florijn, C. Coulais, and M. Van Hecke, “Programmable Mechanical Metamaterials,” *Phys. Rev. Lett.* **113**, 175 503 (2014). (p. 124)

Acknowledgments

I would like to thank Prof. Dr. Martin Wegener for his support, trust, and discussions throughout my work. He was always there to guide when problems occurred and left enough freedom to develop new ideas and concepts.

I am very grateful that Prof. Dr. Peter Gumbsch has kindly agreed to review my thesis and for the encouraging discussions during the collaborating projects.

I would also like to extend my thanks to the past and present members of our group, who helped me during my daily work regarding concepts and simulations as well as solving minor or major problems in the lab. Further I would like to emphasize my post-doctoral supervisors,

Dr. Nicolas Stenger, who helped me during the start of the project, and took a substantial part in developing the ideas of mechanical metamaterials.

Dr. Michael Thiel has helped me during the entire time of the thesis in relation to DLW, the project development, and helpful discussions.

Dr. Muamer Kadic has lead me throughout the various projects and publications. I would like to thank him for performed simulations throughout the thesis.

I would also like to thank my collaborators during this work, especially Prof. Dr. Graeme Milton for his theoretical support and design ideas, and Robert Schittny, for such a nice collaboration and exchange. Special thanks also go to the company Nanoscribe, as the collaboration and support was excellent allowing to be at the edge of DLW technology throughout my thesis. Thanks go further to Johannes Kaschke especially for taking SEM pictures with me and Andreas Frölich for coating samples with the ALD. The technical staff helped throughout countless discussions and supplied immediate support if problems occurred. Especially Johann Westhauser who has help with the design of measurement setups and the electronics workshop with Helmuth Lay, Michael Hippe, and Werner Gilde for the countless advises and support also during the maintenance of the group's servers.

I thank the proofreaders of this work for improving it and impressing it's final touch: Michael Thiel, Benjamin Richter, Johannes Kaschke, Robert Schittny and Muamer Kadic.

At last I would like to thank my family and friends for their support during the time of the thesis. Hereof I would like to point out Franziska Lambrecht, who has supported me every day during my thesis.

Prüfungserklärung

Hiermit versichere ich, dass ich die vorgelegte Arbeit selbstständig verfasst, noch nicht anderweitig für Prüfungszwecke vorgelegt, keine anderen als die angegebenen Quellen oder erlaubten Hilfsmittel benutzt, sowie wörtliche oder sinngemäße Zitate als solche gekennzeichnet habe.

Karlsruhe, den 18. Mai 2015

Declaration of Verification

I hereby testify, that the here presented work has been written by myself, has not been used for other assessments, that no other sources than the cited were used, and that citations are identified as such.

Karlsruhe, 18th of may 2015